Photoexcitation dynamics and disorder effects in organic donor/acceptor systems

DISSERTATION

zur
Erlangung des Doktorgrades
der Naturwissenschaften
(Dr. rer. nat)

dem
Fachbereich Physik
der Philipps-Universität Marburg

vorgelegt von

MARINA GERHARD

aus

Bad Arolsen

Marburg an der Lahn, 2016

Vom Fachbereich Physik der Philipps-Universität Marburg
als Dissertation angenommen am: 25.10.2016

Erstgutachter: Prof. Dr. Martin Koch
Zweitgutachter: Prof. Dr. Ulrich Lemmer

Tag der mündlichen Prüfung: 02.11.2016
Hochschulkennziffer: 1180

At some point, everything's gonna go south on you. [...] Now you can either accept that, or you can get to work. That's all it is. You just begin. You do the math. You solve one problem... and you solve the next one... and then the next. And If you solve enough problems, you get to come home.

Mark Watney

Aus der Verfilmung des Romans „*The Martian*“
von Andy Weir

Kurzfassung

Organische Halbleiter stellen eine vielversprechende Materialklasse für Anwendungen im Photovoltaik-Bereich dar, weil die Produktionskosten entsprechender Solarzellenmodule vergleichsweise gering einzuschätzen sind. In den vergangenen Jahren erzielten organische Solarzellen beachtliche Wirkungsgrade im Bereich von 10 % [1–3], doch trotz dieser Fortschritte sind die zugrundeliegenden Mechanismen der Ladungstrennung noch nicht ausreichend verstanden. In der vorliegenden Arbeit wird mit Hilfe der zeitaufgelösten Photolumineszenz-Spektroskopie die Lichtemission aus Rekombinationsprozessen untersucht, welche den Prozess der Ladungsseparation zwingend begleiten. Aufgrund der hohen Bindungsenergie von Elektron-Loch-Paaren, sogenannten Exzitonen, stellt deren Rekombination einen bedeutenden Verlustprozess dar. In einem organischen Donator/Akzeptor-Mischfilm, der in organischen Solarzellen typischerweise als aktive Schicht dient, können Exzitonen entweder in den jeweiligen Donator- oder Akzeptor-Domänen rekombinieren, wo sie zuvor durch Absorption eines Photons erzeugt wurden, oder sie können an internen Grenzflächen einen Ladungstransfer vollziehen. Dabei bildet sich ein Überganszustand (CT-Zustand für engl. „*charge transfer*“), in dem die Ladungen noch über die Grenzfläche hinweg miteinander korreliert sind. Der CT-Zustand kann entweder dissoziieren und damit freie Ladungen bilden, oder durch Rekombination in den Grundzustand übergehen. Die Rekombination von CT-Zuständen an inneren Grenzflächen kann den Wirkungsgrad einer organischen Solarzelle maßgeblich beeinträchtigen. In dieser Arbeit werden die Donator/Akzeptor-Systeme P3HT/PC$_{61}$BM und PTB7/PC$_{71}$BM untersucht. Diese Polymer/Fulleren-Mischfilme gelten im Bereich der organischen Photovoltaik als gut untersuchte Materialsysteme und haben vergleichsweise hohe Wirkungsgrade erzielt. Die Photolumineszenz (PL) dieser Materialien stammt sowohl von Rekombinationsprozessen der Exzitonen in den Donator- oder Akzeptor-Domänen, als auch von CT-Zuständen an den Grenzflächen.

Zunächst wird die PL reiner P3HT- und PTB7-Polymerfilme untersucht. Die beobachtete spektrale Rotverschiebung mit zunehmender Zeit nach der optischen Anregung ist ein typisches Merkmal organischer Systeme und ergibt sich aus überwiegend exothermen Hüpfprozessen der Anregungen in einer ungeordneten Zustandsdichte. Die Analyse und Interpretation der Messergebnisse orientiert sich an bereits publizierten Untersuchungen zu anderen Polymeren [4–6]. Die energetische Relaxation der PL-Emission in P3HT ist konsistent mit der Annahme einer zugrundeliegenden Gaußförmigen Zustandsdichte. Die energetische Relaxation der Anregungen in PTB7 fällt hingegen stärker aus, als man für eine Gaußförmige Zustandsdichte erwarten würde, was auf das Vorhandensein einer größeren Zahl niederenergetischer Zustände hinweist.

In einem nächsten Schritt werden die PL-Signaturen der P3HT/PCBM und PTB7/PCBM-Mischfilme untersucht. Neben der Emission von Singulett-Exzitonen,

die auch in den reinen Ausgangsmaterialien beobachtet wird, weisen die beiden untersuchten Materialsysteme eine weitere, vergleichsweise langlebige Signatur im Nahinfrarot-Bereich auf, die der Emission von CT-Zuständen an inneren Grenzflächen zugeordnet wird. Die Ergebnisse werden im Zusammenhang mit aktueller Literatur diskutiert, mit einem besonderen Schwerpunkt auf Untersuchungen zur Morphologie [7–12]. Es stellt sich heraus, dass die CT-Intensität und auch die Abnahme der Singulett-Emission im Gemisch mit der Präsenz einer stark durchmischten Donator/Akzeptor-Phase zusammenhängt. Darüberhinaus zeigen temperaturabhängige PL-Untersuchungen, dass ein großer Teil der CT-Emission bei moderater thermischer Energie verschwindet, was auf eine im Allgemeinen schwach ausgeprägte Bindung der CT-Zustände hinweist. Nur im Falle von P3HT/PCBM zeigt sich, dass ein gewisser Teil der CT-Zustände stärker gebunden ist, was zu höheren Verlusten in der stark durchmischten Phase führt. Die dargestellten Ergebnisse dienten als Grundlage für zwei Publikationen (Quellen [13] und [14]).

Im letzten Teil dieser Arbeit wird die Abnahme der PL-Intensität (Tilgung) bei Anlegen eines äußeren elektrischen Feldes an eine PTB7/PCBM-Solarzelle bei verschiedenen Temperaturen untersucht. Die Abnahme der PL-Intensität in einem elektrischen Feld ergibt sich durch die höhere Dissoziationsrate der Exzitonen. Das feldabhängige Auslöschen der PL hängt daher mit der Exziton-Bindungsenergie zusammen. Es zeigt sich, dass die Tilgung der Emission von CT-Zuständen bei niedrigeren Feldern als die Tilgung der Singulett-Exzitonen erfolgt, was darauf hindeutet, dass letztere stärker gebunden sind. Die zugrundeliegenden Bindungsenergien werden mit Hilfe eines kinetischen Modells quantifiziert, das von Rubel et al. vorgeschlagen wurde [15]. Diesem Ansatz liegt die Annahme zugrunde, dass sich die Dissoziation von Exzitonen in einem mehrstufigen Prozess vollzieht. Dabei vollführt eine der beiden Ladungen mehrere Hüpfprozesse zwischen jeweils benachbarten Chromophoren innerhalb des durch die andere Ladung verursachten Coulomb-Potentials. Das Modell ergibt eine gute Übereinstimmung mit den experimentellen Daten, wenn (i) die zugrundeliegende Unordnung berücksichtigt wird und wenn (ii) angenommen wird, dass das Coulomb-Potential an der Grenzfläche in hohem Maße abgeschirmt ist, zum Beispiel durch eine Dipol-Schicht [16]. Insgesamt zeigen die Ergebnisse, dass der energetisch relaxierte CT-Zustand in der PTB7/PCBM-Mischphase eine Vorstufe separierter Ladungen darstellt und nicht als Rekombinationszentrum angesehen werden sollte, welches den Wirkungsgrad begrenzt. Außerdem belegen die zeitaufgelösten Messungen der feldabhängigen PL-Tilgung, dass ein 'langsamer' von Diffusion getriebener Separationsprozess in der Tat die effiziente Erzeugung von Ladungen in organischen Solarzellen erklären kann. Eine Veröffentlichung der Ergebnisse ist in Planung [17].

Insgesamt wird in dieser Arbeit eine Kombination von Methoden präsentiert, die es ermöglicht, die relativ schwache Emission von CT-Zuständen in organischen Donator/Akzeptor-Mischsystemen zu identifizieren und zu charakterisieren. Die temperatur- und feldabhängigen Daten stellen eine fundierte Grundlage dar, um die Vorhersage von kinetischen Modellen zu überprüfen. Das im Rahmen dieser Arbeit verwendete kinetische Modell ergibt umgekehrt eine gute Übereinstimmung mit der experimentell beobachteten PL-Tilgung. Insbesondere zeigt sich, dass für eine angemessene Beschreibung des Separationsprozesses von Exzitonen Ansätze jenseits des üblicherweise verwendeten Onsager-Braun-Modells verfolgt werden sollten.

Abstract

Organic semiconductors are a promising material class for applications in photovoltaics, mainly due to the expected low manufacturing costs of solar modules. In recent years, considerable photoconversion efficiencies around 10 % have been reported for organic solar cell devices [1–3] but despite this progress, the underlying photophysical processes of charge generation still need to be understood in greater detail. This work addresses the radiative losses during the charge generation process, which are studied by means of time-resolved photoluminescence. According to the strong binding energy of electron-hole-pairs in organic systems, also termed as excitons, recombination from those geminate pairs has to be considered as a major loss process. In an organic donor/acceptor bulk heterojunction, typically representing the active layer in an organic solar cell device, gemiate pairs can either recombine in the donor or acceptor domains where they are created after absorption of light, or they can undergo charge transfer at the interface, thereby forming an intermediate so-called charge transfer (CT) state across the interface. The CT state either separates into free charges or recombines to the ground state. CT recombination can be a serious loss mechanism in organic solar cells. Here, two benchmark polymer/fullerene systems in organic photovoltaics (OPV) are studied, P3HT/PC$_{61}$BM and PTB7/PC$_{71}$BM, respectively. Photoluminescence (PL) arises from both excitons in the donor or acceptor domains (also referred to as *singlet* states), or from interfacial CT states. The signatures are investigated under various temperatures between 10 and 290 K and in the presence of an electric field.

First, the luminescence decay in the neat polymers P3HT and PTB7 is characterized. The observed time-dependent red shift of the signatures is typical for organic systems and results from preferential exothermic hops of the excitons between adjacent sites in a disordered density of states. The results are analyzed and discussed in the context of recent work on exciton relaxation in other polymers [4–6]. The energetic relaxation of the emission in P3HT is consistent with an underlying Gaussian density of states. The relaxation in PTB7 is however stronger than expected, which might be due to the presence of a higher number of low-energetic tail states with respect to a typically expected Gaussian profile.

In a next step, the PL of P3HT/PCBM and PTB7/PCBM mix films is studied. Beside the signatures of singlet excitons, which are also observed for the neat material, in both systems an additional long-lived feature in the near-infrared is identified and attributed to the emission of interfacial CT states. The results are discussed in the context of recent literature, in particular concerning the material morphology [7–12]. As a result, both the CT intensity and the quenching of singlet states are found to be correlated with the presence of an intimately mixed donor/acceptor phase. Furthermore, temperature-dependent PL studies show that in both material systems a high fraction of the CT emission is quenched with the help of thermal energy, suggesting that the CT binding

energy is rather weak. However, in case of P3HT/PCBM, a certain subset of the CT population seems to be more strongly bound, giving rise to higher losses in the P3HT/PCBM mix phase. Parts of the presented results have been published in Refs. [13] and [14].

In the final part of this work, the field-induced PL quenching of the singlet and CT emission is investigated under various temperatures. The decay of the PL intensity in an electric field arises from an enhanced dissociation rate of the excitons. The field-dependence of the PL quenching is thus related to the exciton binding energy. The quenching of CT states occurs at lower fields than the quenching of singlet states, indicating that the latter are more strongly bound. The binding energy is quantified using a kinetic model suggested by Rubel et al. [15]. The model is based on the assumption of a multi-step separation mechanism, where one of the charges performes several hops to escape the Coulomb potential of the other charge. It turns out that the model gives an appropriate description of the data when (i) the underlying disorder is taken into account and when (ii) it is assumed that the Coulomb potential at the interface is effectively screened, for example by an interfacial dipolar layer [16]. Overall, the results demonstrate that the energetically relaxed CT state in the PTB7/PCBM mix phase is a precursor state for charges rather than an efficiency-limiting trap. Moreover, the time-resolved and field-dependent measurements document that a diffusive and 'slow' separation mechanism of the CT excitons can account for the efficient charge generation in highly performing organic solar cells and a separation route via energetically excited intermediate states, which is often assumed, is not mandatory to drive charge separation. The results on field-induced luminescence quenching are planned to be published in Ref. [17].

Overall, a methodological framework is presented to identify and characterize emissive CT states in efficient OPV systems. The temperature and field dependent time-resolved data give a profund basis to test the validity of kinetic models and in turn, the applied kinetic model gives good agreement with the experimentally observed PL quenching, suggesting that for an appropriate description of the charge separation process it is necessary to go beyond the commonly applied Onsager-Braun theory.

Contents

Chapter 1

Introduction

A major challenge of this century is to meet worldwide growing energy demands while simultaneously reducing carbon dioxide emissions related to energy production. The tremendous influence of man-made carbon dioxide on the global climate has been recognized over the last decades [18] and time is getting short for effective intervention. In 2015, at the United Nation Climate Change Conference in Paris, 195 countries agreed to limit global warming to an extent of 1.5 K. This implies that Germany needs to reduce the carbon emissions generated by energy production to zero by the year 2040 [19]. In order to achieve this objective, it is essential to substantially increase the amount of renewable energy sources. At present, a fraction of 12.6 % of the primary energy in Germany is provided by renewable sources and the share of photovoltaics with regard to the total amount of energy produced is only 1 % [20]. These numbers suggest that there is still a long way to go. Nevertheless, the sun is a free primary source and the average terrestrial solar radiation intensity on a sunny day is about 1000 $\mathrm{Wm^{-2}}$ [21]. Decreasing prices for solar modules have let the worldwide market for photovoltaics grow and moreover, successfully implemented solar projects, in particular in Africa, demonstrate the capability of this technique to provide autonomous supply of energy in remote areas, thereby contributing essentially to their regional development [22, 23]. However, in order to support the fast establishment of photovoltaics, further efforts are necessary, involving political and economic commitment, but also further progress in engineering and fundamental research.

The discovery of the photovoltaic effect dates back to the year 1839 when Edmund Bequerel reported a light-induced electric current in a silver-coated platinum electrode [24], but it took until the 1950s before the upcoming silicon technology and the introduction of the pn-junction triggered the development of devices with notable photoconversion efficiencies. In this context, the report of Chapin et al. on a photovoltaic cell with 6 % power conversion efficiency in 1954 was a major breakthrough, after which photovoltaic devices were, for the first time, seriously considered for power generation [25]. Nowadays, silicon-based solar cells are produced on an industrial scale with photoconversion efficiencies beyond 20 %. In particular the 10-fold increase of Chinese production during the last decade has decreased module prices, making photovoltaics competitive with conventional energy production [26]. Beside silicon modules, a smaller segment of the market is affiliated to the so-called thin-film technologies, such as amorphous silicon, copper indium gallium selenide (CIGS) or cadmium telluride (CdTe), which are often referred to as second-generation photovoltaics. The particular advantage of these materials over silicon is their direct band gap, allowing for significantly less material consumption and a higher return of the energy invested during the production process. However, the availability of certain elements required for thin-film solar cells is limited, which in turn explains the faster growth of the silicon market [26].

Another material which is highly abundant on earth is carbon. This strongly motivates the development of a carbon-based solar cell technology. In fact, organic (i.e. carbon-based) semiconductors are promising candidates to meet the requirements for commercial photovoltaic devices [21, 26–28]. The current record efficiencies obtained under laboratory conditions are 10-11 % [1–3]. This is significantly less than the performance of their inorganic counterparts; however, organic solar cells can be profitable according to their lower manufacturing costs [27]. Most of the relevant materials can be processed from solution, enabling the use of standard techniques such as roll-to-roll processing and inkjet printing. Another interesting property of organic semiconductors is their flexibility, giving rise to application scenarios beyond those of rigid inorganic materials. These include for example lightweight and flexible foils on a variety of surfaces. Together with the dye-sensitized solar cells and the upcoming and impressively performing perovskites, organic solar cells are regarded as third-generation photovoltaic devices. However, long-term stability of these materials is the major issue that needs to be solved before one of these technologies can be commercialized on a large scale. Therefore, despite their interesting properties, these materials have been mainly limited to laboratory research until now.

Organic semiconductors are generally classified into molecular materials, either amorphous or crystalline, or polymers, the latter being composed of many repeating molecular building blocks. The semiconducting properties of molecular crystals have already been investigated in the 1960s [29–31] and intense research on semiconducting polymers began after the discovery of the high conductivity of polyacetylene upon doping in 1977 [32]. For their work on semiconducting polymers, Heeger, McDiarmid and Shirakawa were awarded with the Nobel Price in Chemistry in the year 2000. Later, reports on electroluminescence in relatively thin organic layers of a few 100 nm [33, 34] paved the way for the OLED technology, which is nowadays established in displays and large-area lightning panels. However, inverting the process of injected charge recombination is not trivial, because absorption of light in an organic solar cell does not directly lead to the formation of free charges. The relatively low dielectric constants of organic semiconductors ε_r typically range between 3 and 4. This results in poor screening and thus, strong Coulomb interaction between the charges. Therefore, the primary photoexcited species in organic semiconductors are neutral pairs comprised of a negative and a positive charge (*electron* and *hole*), which are bound by their mutual Coulomb attraction, forming so-called *excitons*. It took until the 1990s before the strong Coulomb interactions present in organic semiconductors and the implications for their optoelectronic properties were recognized. The exciton picture was in particular developed and supported by Bässler and coworkers [35–39]. In organic semiconductors, excitons are stable even at room temperature because the Coulomb interaction is particularly strong, typically several 100 meV. This is not the case for inorganic systems, where the exciton binding energies are on the order of 10 meV and thus, thermal energy at room temperature (about 25 meV) is sufficient to dissociate them. From this perspective, it appears surprising that charge generation in organic solar cells is possible at all.

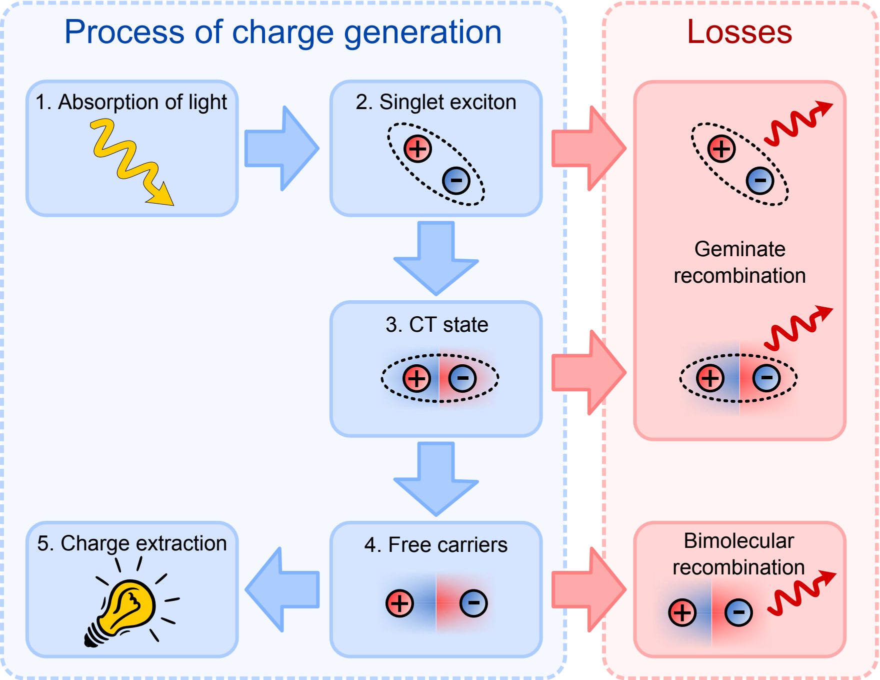

Figure 1.1.: Schematic of fundamental steps in the charge generation process and accompanying loss mechanisms. Both geminate and non-geminate recombination can occur radiatively or non-radiatively.

The excitonic nature of organic semiconductors was in fact the major drawback of the first organic solar cell devices that were composed of a monolayer of the active material, sandwiched between two electrodes [40, 41]. Excitons created in such a device could separate by transferring one charge to the electrode material. However, only a small number of the excitons could diffuse sufficiently close to an electrode within their lifetime, as the thickness of the active layer exceeded the average exciton diffusion length. Further progress was made by the discovery that upon blending the polymer with fullerene (C_{60}), electron transfer to C_{60} from photoexcitations created in the polymer is greatly enhanced [42, 43]. This is because the fullerene offers excellent electron accepting and transporting properties. The actual breakthrough regarding the efficiency of organic solar cell devices was achieved by intermixing the donor and the acceptor component with each other on a nanometer scale to form a so-called bulk heterojunction [44]. In such a device, excitons can reach a donor/acceptor interface with a high probability and the generated charges migrate to the electrodes in the spatially separated donor and acceptor domains. The major steps of the charge generation process in an organic donor/acceptor heterojunction can be summarized as follows (see Fig. 1.1): (1.) Absorption of light and creation of an exciton, (2.) diffusion of the exciton to an interface, (3.) electron transfer to the acceptor, leading to the formation of an interfacial charge transfer state, (4.) charge separation and (5.) charge extraction at the device electrodes. All of these processes are accompanied by losses, such as geminate (pairwise) recombination of excitons, which do not manage to overcome their mutual binding energy within their lifetime, or bimolecular recombination of free charges, either at the donor/acceptor interface or at the device electrodes.

Apparently, the donor/acceptor interface plays a decisive role in the charge generation process, as it helps the excitons to overcome their strong intrinsic binding energy. Charge separation at the interface occurs via intermediate so-called charge transfer (CT) states (step 3 in Fig. 1.1), where the charges are already in separate domains but assumed to be still weakly correlated via their mutual Coulomb force. The actual characteristics of the CT states and the underlying mechanisms of charge separation are however not yet sufficiently understood and subject of ongoing research. Delocalization of the charges might play a decisive role, and furthermore, the energetics at the interface or higher dielectric screening of the CT states are being considered as driving factors for charge separation. There is a strong fundamental interest in solving these questions and moreover, detailed knowledge about the processes at the donor/acceptor interface allows for a more rational design of novel material systems and devices.

The main objective of this work is to gain insight into the mechanisms relevant for charge generation at the donor/acceptor interface by studying the accompanying loss processes. This is done by time-resolving the photoluminescence emitted during charge separation, employing the streak camera technique. The measurements are sensitive to the radiative recombination of so-called *geminate pairs*, signifying pairs of charges which have not managed to overcome their mutual Coulomb attraction during their lifetime. The *bimolecular* recombination arising from free charges on the other hand is assumed to occur on a much slower time scale not covered by this experiment. Both singlet excitons and charge transfer states at the interface can give rise to geminate recombination and studying the decay dynamics under various temperatures and in an electric field allows to address questions such as (i) how fast is charge separation and (ii) how strong is the exciton binding energy. This work focuses on two benchmark systems in organic photovoltaics (OPV), based on two polymers P3HT and PTB7, which are blended with the fullerene derivative PCBM. The thesis is structured as follows:

- Chapter 2 is intended to provide a comprehensive background about the photophysical properties of organic solar cells and organic semiconductors in general, with a special focus on currently debated mechanisms of exciton separation at the donor/acceptor interface. Furthermore, the role of disorder and its influence on the optical properties will be discussed. The last part of the chapter gives a brief introduction into the characteristic parameters of organic solar cells and discusses some important design principles of semiconducting polymers for applications in OPV.

- Chapter 3 describes the experimental techniques of absorption and photoluminescence spectroscopy, providing a detailed description of the analysis procedure of the spectrally and time-resolved photoluminescence data. Furthermore, a brief description of the sample fabrication procedure is provided.

- Chapter 4 summarizes measurements of the PL decay in the neat polymers P3HT and PTB7. It appears useful to study the neat donor materials first, before turning towards the donor/acceptor blends. The PL characteristics of the neat polymer films are found to be consistent with the picture of exciton relaxation in a disordered system.

- In Chapter 5, the influence of intermixing with the fullerene derivative PCBM on the PL properties is investigated for blends with varying donor/acceptor compositions and compared to the emission of neat films. This allows for the identification of interfacial CT emission. The dynamics and intensity of the measured signatures are discussed in the context of recent studies on the blend morphology.
- Finally, the quenching of these features in the presence of an electric field under various temperatures is investigated in Chapter 6. The PL intensity is expected to decrease with increasing electric field and temperature, as the excitons are more likely to dissociate under such conditions. In a final step, a kinetic model is applied to gain a more sophisticated understanding of the separation process and to quantify the underlying exciton binding energies.
- The results and their implications are summarized in Chapter 7.

Overall, a strong correlation between the occurrence of interfacial CT emission and the presence of an intermixed polymer/fullerene phase is found for both investigated material systems. Furthermore, there is a strong influence of the underlying disorder on the PL characteristics, becoming apparent for example in the decay characteristics of the PL in the neat polymers and also in the context of field-dependent PL quenching studies. The luminescence quenching data in combination with kinetic modeling suggests that the binding energy of CT states at the donor/acceptor interface is much weaker than for singlet excitons either in the polymer or the fullerene. Thus, charges can separate efficiently from the energetically relaxed and weakly bound CT states via a diffusive hopping mechanism. This finding can be regarded as the major contribution of this work.

Chapter 2

Fundamental processes in organic photovoltaic devices

This chapter summarizes the most important aspects concerning the photophysics of organic solar cells. A more detailed description can be found in several monographs [21, 24, 28, 45–48]. The research on fundamental processes in OPV is a very active and highly interdisciplinary field and some phenomena, in particular the mechanisms leading to charge generation, are subject of ongoing debate. During the last years, however, several reviews have been published [27, 49–52], giving a comprehensive description of general concepts and open questions in the field. The introductory part of this thesis is oriented at the literature mentioned above.

Following the process of charge generation as illustrated in Fig. 1.1, this chapter is structured as follows: First, the electronic structure of organic semiconductors and some fundamental concepts for optical transitions between the electronic states will be introduced. The next section gives a detailed description of excitons in organic semiconductors and introduces some mechanisms of exciton transport. In organic solar cells, the excitons dissociate at the donor/acceptor interface, thus, underlying concepts of charge transfer and exciton separation will be introduced in the third section. The next part describes the influence of structural and energetic disorder in organic materials, with a special focus on conjugated polymers. Finally, the operation principle of organic solar cells stressing some fundamental limitations and common design principles of semiconducting polymers will be introduced.

2.1. The electronic structure of organic semiconductors

2.1.1. Molecular orbitals

Atomic or molecular orbitals, as sketched in Fig. 2.1, reflect the probability of finding an electron at a specific position relative to the positively charged nuclei. The electron configuration of atomic carbon is $1s^2 2s^2 2p^2$, signifying that the outer s and p orbitals are filled with four electrons (two in the 2s, one in the $2p_x$ and one in the $2p_y$ orbital). These *valence electrons* can form chemical bonds with adjacent atoms. The 2s and 2p orbitals of carbon are sketched in Fig. 2.1. When carbon undergoes chemical reactions, e.g. with other carbon atoms, the s and p orbitals mix to form isoenergetic orbitals, which are described by the concept of *hybridization*. For carbon,

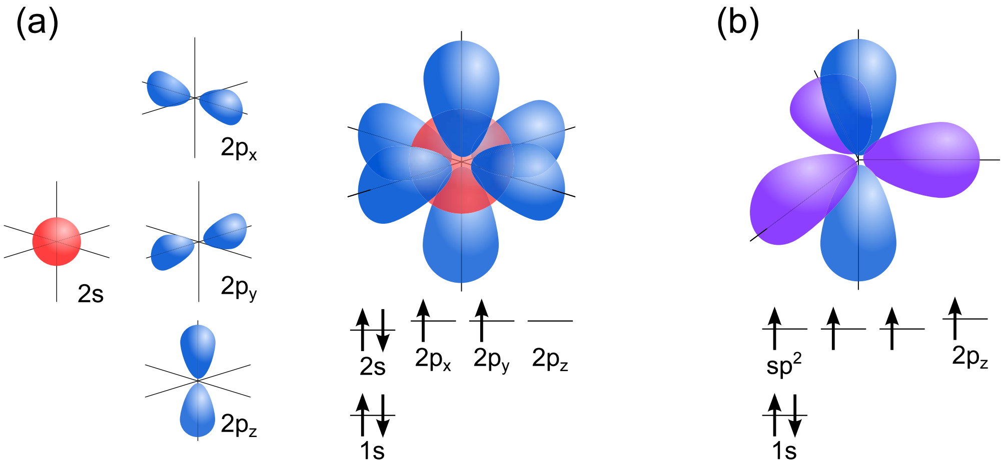

Figure 2.1.: Electronic structure of atomic carbon (a) and sp^2 hybridized carbon (b), which is the most relevant type of hybridization for organic semiconductors. The hybrid orbitals (violet) are oriented in the plane orthogonal to the remaining p$_z$ orbital (blue).

three types of hybridization are possible. When all 2s and 2p orbitals are involved, this leads to the formation of four sp^3 hybrid orbitals. For symmetry reasons, the sp^3 hybrid orbitals possess tetrahedral arrangement with respect to the nuclei, which is also reflected in the geometry of molecules based on sp^3-hybridized carbon. The second possible mechanism is sp^2-hybridization, where only the 2s, the 2p$_x$ and the 2p$_y$ orbitals are involved. sp^2-hybridization leads to three hybrid orbitals with planar geometry, whereas the remaining p$_z$ orbital is oriented perpendicular to this plane. This scenario (see Fig. 2.1(b)) is of particular relevance for organic semiconductors, where the bondings via the (parallel) p$_z$-orbitals account for their interesting optical and electronic properties. Finally, there is also the option that the 2s orbital combines with only one of the 2p orbitals, which is referred to as sp-hybridization, resulting in a molecular structure with linear arrangement of the involved atoms.

A possible way to approximate the geometry and energetics of molecular orbitals is the LCAO (*linear combination of atomic orbitals*) method [46]. The ground state orbitals of the simple molecule ethene are sketched in Fig. 2.2(a). Overlap of the atomic unbound sp^2 hybrid orbitals leads to preferential location of the contributed electrons between the two carbon atoms. The resulting probability distribution is referred to as σ-bond. Similarly, the p_z orbitals, each of them contributing one electron, overlap to form a π-bond. Molecular orbitals are formed by the entire distribution of σ-bonds (σ-*orbital*) and π-bonds (π-*orbital*), respectively.

The LCAO method also serves to calculate the orbital energies, which depend on three contributions [28]: The electron wave function overlap, the Coulomb interaction and the exchange interaction. The latter can be interpreted as an implication of the Pauli exclusion principle, which prohibits the existence of identical quantum states, when there is some coupling between the nuclei of the single atoms. As as consequence, the atomic energy levels split and the strength of this splitting depends on the strength of the exchange interaction between the respective orbitals. The splitting of atomic energy levels in the simple molecule ethene is exemplified in Fig. 2.2(b). The strong resonance interaction between the unbound sp^2 hybrid orbitals of the single atoms leads to a

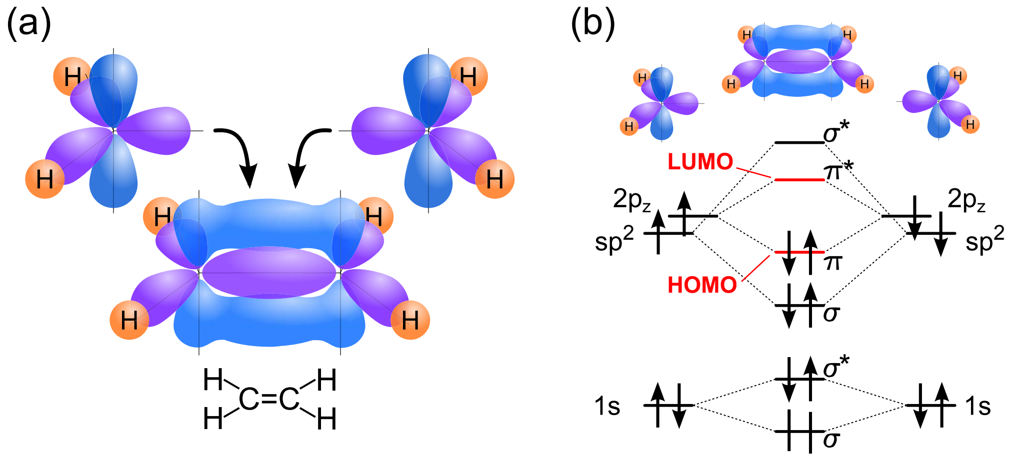

Figure 2.2.: Panel (a) shows the electronic structure of the molecule ethene in its ground state, resulting from the combination of two sp^2 hybridized carbon atoms and four hydrogen atoms. The energy levels and their occupation in the ground state is sketched in panel (b). Electrons involved in chemical bonds to hydrogen are omitted here. The arrows indicate the spin of the electrons. The HOMO and LUMO level (see text), corresponding to the π and π^* orbital, respectively, are highlighted in red.

rather large splitting of several eV between the σ and σ^* electronic states. According to the respective electron distribution, the energetically lower molecular orbital is also referred to as *bonding* orbital and the higher-energetic orbital is called *antibonding* orbital. For the π orbitals on the other hand, the splitting is smaller according to their weaker exchange interaction. In the electronic ground state of ethene, as presented in Fig. 2.2(b), molecular orbitals up to the π orbital are occupied with electrons, whereas the higher π^* and σ^* orbitals are unoccupied. The π-orbital in ethene is referred to as *highest occupied molecular orbital* (HOMO) and the π^* orbital is the *lowest unoccupied molecular orbital* (LUMO). The energetic difference between these orbitals determines the bandgap energy of the material. The photophysics of organic semiconductors are mainly governed by optical transitions between these π and π^* orbitals.

2.1.2. Conjugation

The optical gap of ethene, as presented in the previous section, is in the ultraviolet [46, 53], but this energy of the absorption edge is remarkably reduced in *conjugated* systems, where several sp^3 hybridized carbon atoms are linked to each other. The coupling of the p$_z$ orbitals in these systems leads to the formation of more delocalized electronic states and in particular to stabilization of the π^* excited states. As a consequence, the band gap is reduced. Schematically, conjugated molecules can be sketched by including a system of alternating single and double bonds into their molecular structure. However, according to the fact that the charges are delocalized, several electron configurations are possible, which can be expressed by several resonance structures, usually comprising different stability. Some examples of conjugated systems are summarized in Fig. 2.3. The aromatic poly(acenes) in panel (a) are a prominent group of conjugated molecules, which exemplify the decreasing optical gap, when the the number of benzene units, i.e. the size of the conjugated system is increased [47]. Figure 2.3(b) shows the chemical

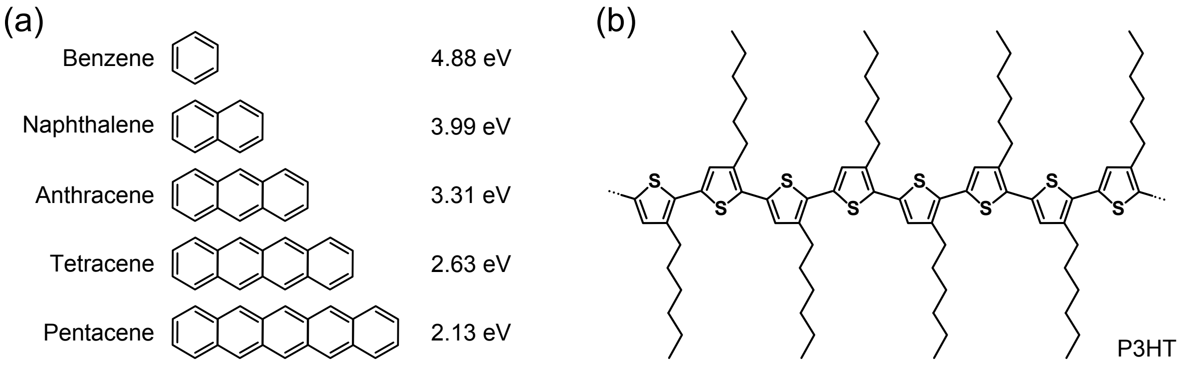

Figure 2.3.: Exemplary chemical structures of conjugated molecules. Panel (a) shows the poly(acenes) up to pentacene and their respective optical gap is given, according to Ref. [47]. Panel (b) shows the chemical structure of the polymer P3HT (poly(3-hexylthiophene), where conjugation is achieved by the alternating single and double bonds along the polymer backbone.

structure of the semiconducting polymer P3HT. Here, conjugation is achieved along the polymer backbone, which is formed by a chain of covalently linked thiophene rings. The material class of conjugated polymers will be introduced in greater detail in Ch. 2.4.

2.2. Optical transitions

The characteristic shape of optical spectra depends on the density of states (DOS) and on the individual transition probabilities between those states. It is a good approximation to assume that absorption or emission of light induces only small changes in the total energy of the system, such that the total energy of the system, described by the Hamilton operator H, is given by the energy of the initial system H_0, altered by a small perturbation H', i.e. $H = H_0 + H'$. A particular achievement of perturbation theory is Fermi's golden rule, which can be used to predict the transition rate k_{if} between an initial and a final state:

$$k_{if} = \frac{2\pi}{\hbar} \left| \langle \Psi_f | H' | \Psi_i \rangle \right|^2 \rho \ . \tag{2.1}$$

Here, Ψ_i and Ψ_f denote the wave functions of the initial and the final state and ρ is the density of final states. The molecular wave function can be written as $\Psi = \Psi_{el}\Psi_{spin}\Psi_{vib}$, signifying that the electronic, the spin and the vibronic contributions can be treated separately [28]. The perturbation H' induced by optical transitions is given by the dipole operator μ, which can be assumed to alter only the electronic wave function, but does not change the spin or the position of the nuclei. This is because the magnetic field of the incident or emitted light is too small to affect the spin state and because the nuclei are too heavy to follow the fast oscillations of the electric field of photons. The latter issue is often referred to as *Born-Oppenheimer approximation.* With these assumptions, Eq. 2.1 can be rewritten as [28]

$$k_{if} = \frac{2\pi}{\hbar} \rho \left| \langle \Psi_{el,f} | \mu | \Psi_{el,i} \rangle \right|^2 \left| \langle \Psi_{spin,f} | \Psi_{spin,i} \rangle \right|^2 \left| \langle \Psi_{vib,f} | \Psi_{vib,i} \rangle \right|^2 \ . \tag{2.2}$$

2.2.1. Transitions between electronic states

An optical transition is only allowed, when all factors in Eq. 2.2 are different from zero. The first integral in Eq. 2.2 $\langle \Psi_{el,f} | \mu | \Psi_{el,i} \rangle$ determines, whether a transition is *dipole-allowed* or not. Beside a change in parity between the initial and final state, it implies that the transition probability depends on the spatial overlap of the electron wave functions, leading to low probability of the transition, when the initial and final electron wave functions are located on different sites of the molecule. Furthermore, the probability of a transition is higher for more extended electronic states, as they offer a higher polarizability, to which the dipole operator can more efficiently couple.

Two common ways to sketch electronic states in a molecular system are presented in Fig. 2.4. Panel (a) shows the orbitals around the optical gap and their occupation with electrons, which are represented by arrows, according to their respective spin (either $+\frac{1}{2}$ or $-\frac{1}{2}$). The whole electron configuration of the system is referred to as *state*. Fig. 2.4 illustrates the configuration of the electronic ground state (S_0) and the lowest excited singlet (S_1, S_2) and triplet (T_1, T_2) states. Singlet and triplet states are distinguished among their total spin: For a singlet state, the sum over all electron spins is zero and for a triplet state it is one. The ground state usually exhibits singlet character, as all orbitals are occupied with electron pairs comprising opposed spin. As a consequence, optical transitions between the ground state and a triplet state are spin forbidden, because the spin state cannot be changed by the perturbing dipole operator. In Eq. 2.2, this is reflected by the factor $\langle \Psi_{spin,f} | \Psi_{spin,i} \rangle$, which is zero, when the spins of the initial and the final wave function are different. In real systems, however, the spin-orbit interaction gives rise to a certain probability for intersystem crossing (ISC),

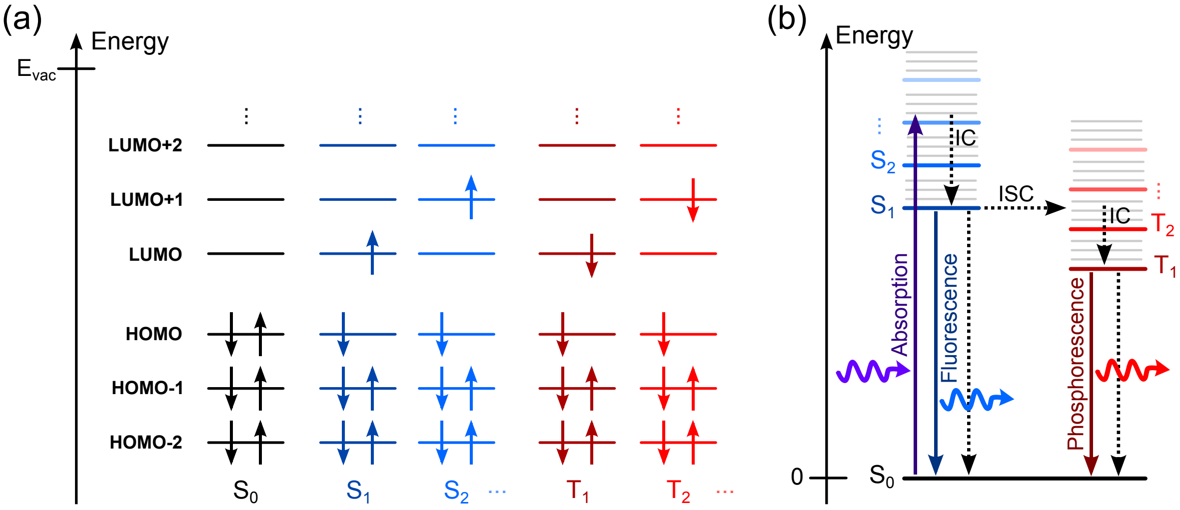

Figure 2.4.: Electronic ground state S_0 and excited singlet (S_1, S_2) and triplet (T_1, T_2) states in the energy level picture (a) and in a Jablonski diagram (b) (for more details see e.g. Ref. [47]). Optical transitions are shown as solid arrows, whereas non-radiative transitions are indicated by the dashed arrows. After excitation into a higher electronic state, internal conversion (IC) via vibronic sub-levels (gray) towards the lowest excited singlet or triplet state occurs typically on a sub-ps time scale. Transitions between the singlet and triplet states are spin-forbidden, but intersystem crossing (ISC) makes this process weakly allowed.

making singlet-triplet transitions weakly allowed. Optical emission spectra thus can comprise signatures of both singlet and triplet states. The singlet emission is termed *fluorescence*, and the triplet emission is known as *phosphorescence*. As a result of the overall weak transition probability, the decay of triplet states can last up to several seconds, whereas fluorescence decays on a nano to micro second time scale.

It should be noted that the energy level diagrams in Fig. 2.4(a) include some strong simplifications. Excitation of an electron into a higher orbital always changes *whole* molecular system, implying that the orbitals, which are usually approximated as one-electron orbitals, are subject to changes, too. In particular, the Coulomb and resonance interaction lead to a lowering of the energy gap [28]. For the description of optical transitions, it is more feasible to switch from the orbital diagram to a representation of the electronic states, also known as Jablonski-diagram, as shown in Fig. 2.4(b). Here, the ground state is at zero energy and the manifolds of singlet and triplet states are presented as separate energy level systems. Due to higher resonance interaction of the electrons in the HOMO and LUMO orbital for the case of triplet states, the triplet energy is generally below that of the singlet energy. Radiative and non-radiative transitions in the electronic state diagram are presented as solid and dashed arrows, respectively. The population of triplet states becomes efficient, when the rate of non-radiative intersystem crossing is comparable to the singlet decay rate to the ground state. Typically, the absorbed photons carry some excess energy with respect to the optical gap, leading to excitation into higher energetic states. This excess energy is, however, dissipated very fast via internal conversion (IC) processes, where the excited electron relaxes thermally via several intermediate electronic or vibronic levels to the S_1 state. The role of lattice vibrations will be discussed in greater detail below.

2.2.2. The role of lattice vibrations: Franck Condon priciple

The transition probability described by Eq. 2.2 also depends on the spatial overlap of the vibronic wave functions $\langle\Psi_{vib,f}|\Psi_{vib,i}\rangle$. The role of lattice vibrations in the absorption and emission process can be described in terms of Franck Condon principle [54, 55], which is based on the essential assumption, that the nuclear motion is slow compared to the absorption-induced change of the electron configuration (Born-Oppenheimer approximation). Furthermore, it has to be considered that the equilibrium configuration of the nuclei in the excited state is different from the configuration of the ground state, which is a plausible assumption, because exciting an electron from a bonding to an antibonding orbital reduces the screening between the nuclei and thereby increases their average separation. This can be illustrated by two displaced oscillator potentials, e.g. corresponding to the electronic ground state and the first excited state, as shown in Fig. 2.5(a) and (b). The vibrational modes of these oscillators are indicated by the gray sub-levels and numbered according to their energy. When the oscillator potential is approximated as harmonic, the energy levels are equidistantly spaced by the quantum $\hbar\omega_i$, where ω_i is the frequency of the involved phonon mode. The index i accounts for the fact that typically several vibronic processes are activated after excitation (e.g. C=C stretching, benzene breathing or C-H stretching), but typically, one mode i dominates the emission properties. The displacement of the respective

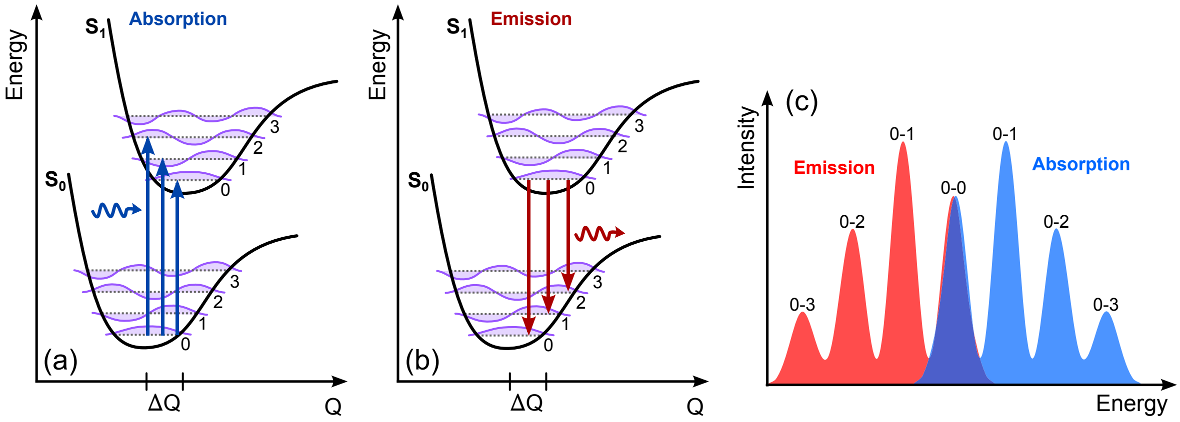

Figure 2.5.: Illustration of the Franck Condon principle, similar to Ref. [28]. The electronic ground and excited state are represented by two oscillator potentials as a function of nuclear coordinate Q. The equilibrium configurations are displaced by an amount ΔQ. As a consequence, transitions between the vibrational modes occur with different probabilities, depending on the vibronic wave function overlap. The typical shape of the resulting absorption and emission spectra is sketched in panel (c).

equilibrium constellations is quantified by the change in the configurational coordinate ΔQ_i. The Born-Oppenheimer approximation implies that optical transitions between these oscillators can be displayed as vertical arrows. The displacement of the oscillator potentials leads to the situation that transitions between certain vibronic states are more likely than others, because with $\Delta Q_i \neq 0$, the vibronic wave function overlap differs among the possible transitions. The intensity I_{0-m} of the transition between the vibronically relaxed ground state to the m^{th} vibrational mode in the electronic excited state is proportional to the squared overlap integral in Eq. 2.2, which can be further expressed by

$$|\langle\Psi_{vib,f}|\Psi_{vib,i}\rangle|^2 \propto I_{0-m} = \frac{S^m}{m!}\mathrm{e}^{-S} \quad \text{with} \quad S = \frac{1}{2}M\omega_m\frac{\Delta Q_i^2}{\hbar}\ . \tag{2.3}$$

The Huang-Rhys parameter S incorporates the potential displacement ΔQ_i and, as further important parameters, the reduced mass M and the frequency ω_m of the oscillating phonon mode. For emission (Fig. 2.5(b)) the situation is very similar to the absorption case. Here, it has to be considered that internal conversion leads to ultrafast depopulation of the higher vibronic levels and thus emission essentially occurs from the vibronically relaxed S_1 state. For the emission, again, the transition probability between the 0^{th} mode of the excited state and the different vibronic modes of the ground state varies, according to the different equilibrium coordinates of the ground an excited state potentials. The typical shape of absorption and emission spectra of organic systems is presented in Fig. 2.5(c): The 0-0 transition corresponds to optical transitions between the vibronically relaxed ground state and the excited states. Furthermore, the absorption and emission spectra exhibit a *vibronic progression* of peaks with equidistant spacing $\hbar\omega_i$ and intensities determined by the Franck-Condon-Factor (Eq. 2.3). In a first approximation, the signatures of the absorption and emission spectra are symmetric with respect to the 0-0 transition, however, in real systems several processes, such as conformational changes, non-radiative transitions or spectral relaxation processes, which will be discussed in greater detail in Ch. 2.4.2, can lead to significant differences between the absorption and emission spectra.

2.3. Excitons

Excitons are neutral photoexcitations, comprising an excited electron and a positively charged vacancy (*hole*), which are correlated via their mutual Coulomb attraction. A simple way to classify excitonic states in solids arises from the spatial volume they occupy. According to the high dielectric constants of inorganic semiconductors, the mutual Coulomb interaction of electron-hole-pairs in these materials is efficiently screened, leading to binding energies only on the order of $k_B T$ and delocalization over several unit cells of the lattice. This type of exciton is called *Mott-Wannier-exciton*. The other extreme case is the *Frenkel exciton*, emerging for the case of poor dielectric screening and with a spatial extension not exceeding the volume of the unit cell. Of particular relevance for this work is also the situation where the electron and hole wave functions are located on different molecules, also referred to as *charge transfer* (CT) exciton. For all three species, the degree of delocalization is sketched in Figure 2.6, employing a simple point-charge picture.

In solid state physics, excitons are traditionally defined as excited states of an ensemble of coupled atoms or molecules. The photoexcitation is thus not affiliated to a specific center, it is rather described by a coherent wave packet, which is delocalized over the whole ensemble of coupled building blocks. The superposition of many atomic states results in a continuous band structure with a specific energetic dispersion. In the field of organic semiconductors, the term *exciton* is used in several contexts. Band structures, which are well known from inorganic semiconductors, have also been reported for excitons in organic solids [28, 47, 56]. Experimental observations also include coherent excitonic states on a macroscopic scale [57]. However, due to the weak intermolecular coupling in a molecular crystal lattice, usually originating from van-der-Waals-interactions, these exciton bands are energetically narrow, typically on the order of 100 cm^{-1} [47] (12 meV). As a consequence, quantum coherence of the excitonic states

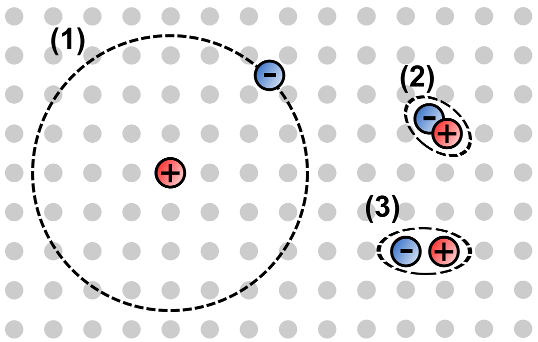

Figure 2.6.: Point-charge model for different types of excitons: (1) Mott-Wannier exciton, (2) Frenkel exciton and (3) Charge transfer exciton.

is easily lost, for example due to scattering with phonons or structural defects, both implying changes in momentum and energy. Such incoherent electron-hole-pairs are localized to single molecules, or to interfaces between them, and hence they do not fulfill the exciton picture in terms of delocalized collective excitations. Nevertheless, they are often referred to as *excitons* and this nomenclature will also be used in this work.

The material systems studied herein comprise high portions of disorder and hence, incoherent processes play an important role. However, even in highly disordered systems, quantum coherence emerges on a microscopic scale, for example due to the formation of nanoaggregates or the coupling of adjacent p_z-orbitals on a conjugated molecular chain. In the limit of weak coupling between the contributing building blocks, coherent photoexcitations can be described by the concept of Frenkel-excitons [58], which shall be briefly sketched in the following section. Afterwards, the underlying mechanisms of exciton transport will be introduced. Here, the focus is on incoherent processes such as Förster- and Dexter-type exciton transfer, as they are more relevant for disordered organic solids.

2.3.1. The concept of Frenkel Excitons

The theoretical framework presented here is conceptually similar to the tight binding approximation in solid state physics. However, the quasiparticles treated in this approach are excitons and not single particles. The exciton model was first introduced by Frenkel in the early 1930s [58] and later, Davydov applied this framework to excitonic states in organic crystals [59]. In order to keep the formalism simple, a one-dimensional crystal lattice with N repeat units and one molecule per unit cell can be considered [28, 45], likewise it is instructive to neglect any influences of lattice vibrations or spin on the total energy of the system. With these simplifications, the Hamilton operator (*Hamiltonian*) is given by the sum of the individual molecular Hamiltonians H_i and the molecular interactions V_{ij}:

$$H = \sum_{i=1}^{N} H_i + \frac{1}{2} \sum_{\substack{i,j=1 \\ i \neq j}}^{N} V_{ij} \tag{2.4}$$

In the limit of weak intermolecular interactions, the ground state wave function of the system Ψ^0 can be approximated by the product of the individual molecular wave functions ψ_i^0. However, the coupling term implies that electrons can be exchanged between the molecular states and hence the wave functions become indistinguishable. In order to satisfy the Pauli exclusion principle, the antisymmetrization operator $\mathcal{A}$ has to be applied to construct wave functions fulfilling Equation 2.4:

$$\Psi^0 = \mathcal{A} \prod_{i=1}^{N} \psi_i^0 \tag{2.5}$$

To describe the collective excited states, one may now be tempted to replace one of the molecular ground state functions in Equation 2.5 by the molecular wave function of the excited state ψ'_j, giving

$$\Psi'_j = \mathcal{A}\psi'_j \prod_{\substack{i=1\\i\neq j}}^{N} \psi_i^0 \ . \tag{2.6}$$

However, this wave function Ψ'_j is not an eigenfunction of the Hamiltonian in Equation 2.4, as it is localized to site j and does not account for the intermolecular coupling. A general solution of the Schrödinger equation needs to consider that the molecules of the ensemble are identical, therefore the excited state has to be described by the superposition of N wave functions Ψ'_j with $j = 1...N$. Assuming periodic boundary conditions for the linear array of molecular building blocks with spacing a and taking into account only nearest neighbor interactions, appropriate wave functions can be found by using the LCAO method [28, 45], giving

$$\Psi'(k) = \frac{1}{\sqrt{N}} \sum_{j=1}^{N} e^{ikaj}\Psi'_j \qquad \text{with} \qquad k = 0, \pm\frac{2\pi}{Na}, \pm\frac{4\pi}{Na}, \ \dots\ , \pm\frac{\pi}{a} \ . \tag{2.7}$$

This type of wave function defines a Frenkel-type excitonic state. It is conceptually similar to a Bloch wave function, which is used to describe electron or hole states in inorganic semiconductors. The energy of an optical transition is given by the energy difference between the ground state and the excitonic state energies. Both are obtained from calculating the eigenenergies of the Hamiltonian in Equation 2.4. The ground state energy of the wave function in Equation 2.5 is given by

$$E^0 = \left\langle \Psi^0 \left| H \right| \Psi^0 \right\rangle = \left\langle \Psi^0 \left| \sum_{i=1}^{N} H_i \right| \Psi^0 \right\rangle + \left\langle \Psi^0 \left| \frac{1}{2} \sum_{\substack{i,j=1\\i\neq j}}^{N} V_{ij} \right| \Psi^0 \right\rangle = \sum_{i=1}^{N} E_i^0 + D, \tag{2.8}$$

where the first part is the sum over all single molecule ground state energies and the negative term D, resulting from the (typically van-der-Waals-type) interactions between the molecules, is also referred to as *polarization energy*. For the excited states, the wave functions $\Psi'(k)$ (Equation 2.7) yield the eigenvalues [28]

$$\begin{gathered} E'(k) = \left\langle \Psi'(k) \left| H \right| \Psi'(k) \right\rangle = \sum_{\substack{i=1\\i\neq j}}^{N} E_i^0 + E_j^* + D' + 2\beta\cos(ka) \\ \text{with} \quad D' = \left\langle \Psi'_j \left| \frac{1}{2} \sum_{\substack{i,j=1\\i\neq j}}^{N} V_{ij} \right| \Psi'_j \right\rangle \quad \text{and} \quad \beta = \left\langle \Psi'_j \left| \frac{1}{2} \sum_{\substack{i,j=1\\i\neq j}}^{N} V_{ij} \right| \Psi'_i \right\rangle \ . \end{gathered} \tag{2.9}$$

The expression for the excited state energy contains the sum over all single molecule ground state energies, but it is considered that one molecule j is in the excited state with the energy E_j^*. Similar to the treatment above, D' denotes a polarization shift, resulting from the interaction term in the Hamiltonian. Again, D' is negative and usually the energy level shift is larger than that of the ground state, i.e. $|D'| > |D|$. The factor β denotes an interaction energy between adjacent molecules. As the excited state energy is a function of the wave number k, the exciton band possesses a dispersion, which is schematically sketched in Figure 2.7. From the maximum and minimum values of the cosine function in Equation 2.9 it becomes evident that the band width is given by 4β. Subtracting the ground state energy in Equation 2.8 from the excited state energy (Equation 2.9) yields the transition energy:

$$\Delta E = E_j^* - E_j + D' - D + 2\beta \cos(ka) \tag{2.10}$$

For optical transitions it has to be taken into account that light carries only small momentum $\hbar k = 2\pi/\lambda$. As a consequence, optical transitions are limited to a small interval around $k = 0$, to fulfill momentum conservation.

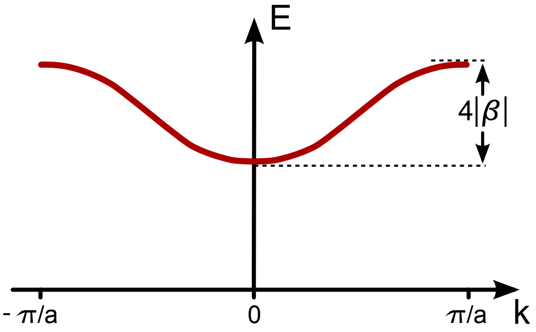

Figure 2.7.: Exciton band in one dimension.

2.3.2. Transport mechanisms

In organic solar cells, efficient transport of excitons towards donor-acceptor interfaces is an important driving factor for charge separation. Both coherent and incoherent transport mechanisms are possible and are explained in greater detail in this section. Coherent mechanisms are generally more efficient than incoherent processes and the interplay between both is considered to govern the exciton transport properties in organic systems [21, 60, 61]. In this section, the principle of both coherent and incoherent exciton transport mechanisms will be briefly sketched.

Coherent exciton transport

Coherent energy transfer occurs in two different ways [21]: In the previous section, the exciton has been treated as a collective excitation, giving rise to ultrafast energy transfer according to the delocalized nature of the excited state. In addition, the energetic dispersion in Equation 2.9 implies that the exciton can be treated as a coherently propagating wave packet. When the cosine function in Equation 2.9 is expanded to the quadratic term, the dispersion relation is given by

$$E(k) = \epsilon + 2\beta - \beta a^2 k^2 \quad \text{with} \quad \epsilon = \sum_{\substack{i=1 \\ i \neq j}}^{N} E_i^0 + E_j^* + D'. \tag{2.11}$$

From this, it is possible to assign an effective mass m^* and a group velocity v_g to the exciton:

$$m^* = \hbar^2 \left(\frac{\partial E}{\partial k^2} \right)^{-1} = -\frac{\hbar^2}{2\beta a^2} \quad \text{and} \quad v_g = \frac{1}{\hbar} \frac{\partial E}{\partial k} = -\frac{2\beta a^2 k}{\hbar} \tag{2.12}$$

Conceptually, such a coherent wave packet is a quasi particle, for which the momentum k is conserved. In organic semiconductors, however, k-conservation is easily disturbed by scattering events, e.g. with phonons, defects or other photoexcited species.

Incoherent exciton transport

When quantum coherence is lost, the exciton migrates via incoherent mechanisms, which are generally less efficient than coherent processes. Here, several mechanisms need to be discussed. The most trivial type of energy transfer is recombination of the exciton via emission of a photon and subsequent reabsorption of this photon by another chromophore. This process does not require any interaction between the involved chromophores, however, its efficiency is limited by the average exciton recombination rate and the absorption of the accepting chromophore needs to overlap spectrally with the emission of the exciton donor.

Furthermore, radiationless incoherent transport between adjacent chromophores is possible when there is some quantum chemical coupling between them. The exciton transfer (XT) rate is then given by Fermi's golden rule [28]

$$k_{XT} = \frac{2\pi}{\hbar} \left| \langle \Psi_f \left| H' \right| \Psi_i \rangle \right|^2 \rho_E, \tag{2.13}$$

where Ψ_i and Ψ_f denote the wave functions of the initial and final state, respectively. The Hamiltonian H' describes the coupling between the chromophores and ρ_E denotes the density of states, which depends on the spectral overlap of the donor emission spectrum with the absorption spectrum of the exciton accepting chromophore. The overlap integral is usually presented as a function of wavelength

$$\rho_e \propto J = \int I_D(\lambda) \epsilon_A(\lambda) \lambda^4 d\lambda, \tag{2.14}$$

where $I_D(\lambda)$ is the donor emission spectrum, normalized to unit area, and $\epsilon_A(\lambda)$ is the molar extinction coefficient. Depending on the type of coupling, two mechanisms of incoherent exciton transfer are prominent and commonly described in the literature, i.e. Förster- and Dexter-type exciton transfer.

When the donor and acceptor chrompohores are oriented in a manner that allows dipole-dipole interactions, exciton transfer is likely to occur via *Förster resonant energy transfer (FRET)* [62]. In this concept, the donor and acceptor sites are treated as point dipoles and any other type of electrostatic interaction is neglected. The interaction energy $\beta = \langle \Psi_f | H' | \Psi_i \rangle$ then depends on the transition dipole moments of the donor and acceptor sites μ_D and μ_A, their separation R and the relative orientation of the chromophores, respectively, which is described by the orientation factor κ:

$$\beta_{FRET} \propto \frac{|\mu_D|\,|\mu_A|}{R^3}\kappa \tag{2.15}$$

The orientation factor reaches a maximum value of 4 for collinear arrangement of the interacting dipoles and it is zero when they are perpendicular to each other. For a system with randomly distributed dipoles, κ has a value of 2/3. According to Equation 2.13, the transfer rate is thus proportional to the inverse of R^6. A commonly used representation is

$$k_{FRET} = \frac{1}{\tau_D^0}\left(\frac{R_0}{R}\right)^6 \quad \text{with} \quad R_0^6 = 8.77 \cdot 10^{-5} \cdot \kappa^2 \Phi_D J, \tag{2.16}$$

where τ_D^0 is the lifetime and Φ_D the quantum efficiency of the donor PL, J is the spectral overlap integral (Equation 2.14) and the numeric factor results from relating the measurable parameters in Equation 2.16 to the Einstein coefficients [28]. The quantity R_0 defines the *Förster radius*, corresponding to the donor-acceptor separation, at which the Förster transfer rate equals the recombination rate.

The second transfer mechanism, referred to as *Dexter energy transfer* (DET) [63], is based on exchange interactions between the donor and acceptor chromophores and does not require dipolar coupling. For Dexter-type transfer, the transfer rate k_{DET} decreases exponentially with increasing site separation R:

$$k_{DET} \propto \mathrm{e}^{-\frac{2R}{L}} J \tag{2.17}$$

Here, L is related to the average chromophore size. Due to the exponential dependence, Dexter transfer is only efficient for relatively small separations of the chromophores ($< 1\,\mathrm{nm}$), whereas Förster transfer emerges on a length scale up to 10 nm. However, for certain orientations Förster transfer is dipole-forbidden. Furthermore, triplet excitons cannot be transported via Förster mechanism, as the corresponding electronic transitions in Figure 2.8 would be inconsistent with the Pauli exclusion principle. Under such circumstances, Dexter transfer governs the transport properties.

The different types of coupling are illustrated in Figure 2.8. Dexter transfer can be illustrated in terms of an *exchange* of electrons and holes between the chromophores, whereas Förster transfer denotes the transfer of excitation energy from a donating to an accepting site.

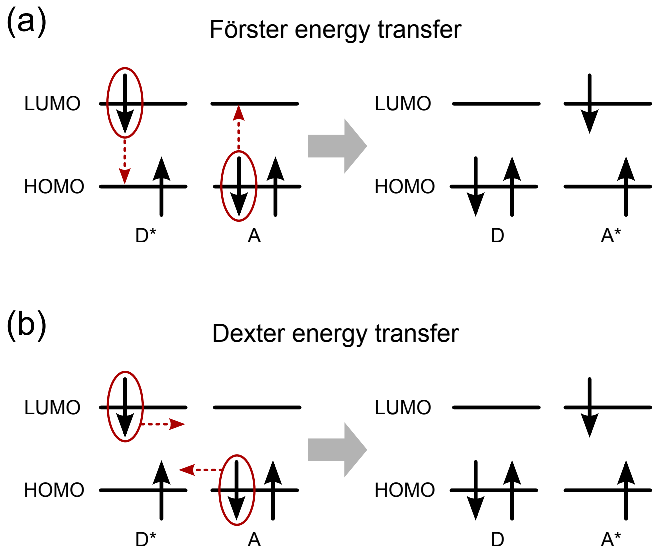

Figure 2.8.: Schematic representation of (a) Förster resonant energy transfer and (b) Dexter-type exciton transfer between a donor (D) and an acceptor (A) chromophore.

2.4. Real systems: Conjugated polymers

After having introduced important concepts of the underlying photophysics in organic semiconductors, the properties of *real* materials will now be discussed in greater detail, exemplified for conjugated polymers, which are of particular relevance for this work. The discovery of conductive polymers dates back to the late 1970s. In their pioneering work, Heeger, MacDiarmid and Shirakawa demonstrated that doping increases the photoconductivity of polyacetylene over a range of eleven orders of magnitude [32]. For these findings and subsequent developments, they were awarded with the Nobel prize in chemistry in the year 2000. Early theoretical approaches to describe the electronic structure of this new material class were based on the classical semiconductor band picture, in combination with strong polaronic effects. A major drawback of this framework developed by Su, Schrieffer and Heeger (SSH model) [64–66] was, however, that it did not account for the strong interactions between the charges. Nowadays, it is commonly accepted that dielectric screening in organic semiconductors is weak and hence it is extremely important to take Coulomb interactions into account. As a consequence, the excited species in organic semiconductors are described as Frenkel-type excitons. The exciton picture is in good agreement with experimental results obtained from optical spectroscopy. For example the presence of excitons explains the large discrepancy between the optical and the electronic band gap in organic semiconductors [38] and the typically observed red shift of the PL in these materials with respect to the absorption edge, also known as *Stokes shift*[1], can be interpreted in terms of exciton diffusion towards low-energetic tail states in a disordered system [4, 6, 35, 67]. This phenomenon of *spectral relaxation* and the consequences for the optical properties will

---

[1] Here, the Stokes shift denotes the energy difference between the 0-0 transitions in absorption and emission, consistent with the IUPAC definition [28]. This should not be confused with the energy difference between the maxima of the absorption and emission spectra, which is not always the same but in some contexts also referred to as Stokes shift.

be discussed in this section, after a general overview over the electronic structure of conjugated polymers.

2.4.1. Electronic structure of conjugated polymers

Conjugated polymers consist of many repeating monomer units, forming a backbone with the essential character of alternating single and double bonds. Along this backbone, charges can be delocalized. It is not intuitive, why there should be a band gap at all in such a system. When the photoexcited electron (or hole) is for example considered as a free particle on a chain of N conjugated carbon atoms, solving the corresponding Schrödinger problem ("particle-in-a-box-model") yields that the energy difference between the highest occupied and the lowest unoccupied eigenstates scales with $\frac{1}{N}$. In this simple approach (see e.g. Refs. [28] or [68]), the band gap energy thus approximates zero for long chains. It is therefore not applicable to polymers, which typically comprise several hundreds of monomer units and possess a band gap, though. The actual origin of the band gap in polymer systems is under ongoing debate. To resolve this issue in the SSH model, it was argued that dimerization of the carbon chain leads to doubling of the unit cell and thus gives rise to an energy gap [64, 65]. This assumption is based on earlier calculations, which have demonstrated that a dimerized chain with an electron configuration comprising alternating single and double bonds is in fact energetically favored compared to a non-dimerized chain, where the negative charge is equally distributed [69]. This behavior was also predicted for the potential energy of one-dimensional metals, where the energetically favored dimerization is referred to as *Peierls distortion* [70]. However, beside bond length alternation, further explanations are required, as an optical gap is also observed in systems with equal spacing of the atoms, such as for example for poly(silylene) [28].

A good way to test the validity of a model for the polymer band gap is to extrapolate the electronic properties of oligomers to the polymer limit, where the optical gap converges to a constant value and does no longer depend on N. It turns out that good agreement between experimental findings and theoretical predictions is achieved with a simple empirical oscillator model, developed by Lewis, Calvin [71] and Kuhn [72]. In their approach, the polymer chain is treated as a series of coupled oscillators, which are represented by the C=C double bonds, whereas the coupling is provided by the C-C single bonds. The energy E_0 of the individual oscillators is given by [71]

$$E_0 = \hbar\sqrt{\frac{k_0}{\mu_0}}, \tag{2.18}$$

where k_0 denotes the restoring force constant and μ_0 is the reduced mass of the oscillator. When N of these oscillators are correlated via a coupling constant k', the energy of the optical transition is given by the lowest energy difference between the resulting eigenmodes. From these considerations, Kuhn derived the following expression for the optical gap [72]:

$$\Delta E = E_0\sqrt{1 + 2\frac{k'}{k_0}\cos\frac{\pi}{N+1}} \tag{2.19}$$

This relation can be used to fit experimental data of the optical gap of oligomers using the parameters E_0 and $\frac{k'}{k_0}$, which allows for prediction of the polymer band gap. Kuhn's phenomenological approach has been demonstrated to be quite accurate for diverse polymer systems [68, 73]. Exemplarily, the shifting of the optical gap according to Equation 2.19 in oligo(enes) is illustrated in Figure 2.9(a). More recent work concerning the energy gap of conjugated polymers is based on quantum chemical calculations [73]. Here, particular difficulties arise from the manifold of influences on the energy of the optical gap E_g. These can be summarized as [73, 74]

$$E_g = E_{bb} + E_{dist} + E_{sub} + E_{solv} + E_{cryst}, \tag{2.20}$$

where E_{bb} is the optical gap of the polymer backbone, E_{dist} denotes a blue shift (hypsochromic shift) according to distortions of the polymer chain, E_{sub} accounts for an offset caused by the electronegativities of different substituents, E_{solv} is an energy shift induced by the polarization of the surrounding, and the contribution of E_{cryst} becomes relevant, when the material tends to form aggregates with considerable intermolecular interactions. From this it becomes evident that the optical gap size depends significantly on the dielectric environment.

Microscopically, a polar environment stabilizes the energy levels of the ground state and the excited state. The excited state is however more strongly influenced, as it comprises a higher polarizability. The resulting red-shift of the optical gap with increasing polarity of the surrounding is known as *bathochromic shift* (see Figure 2.9(b)). One important implication of this polarization effect is that the absorption signatures related to the optical gap of a disordered polymer film are energetically broadened, because each excited state is created in an individual dielectric environment with varying degrees of polar stabilization. The presence of structural disorder has also important consequences for the quantum coherence and transport characteristics of photoexcitations. Excitons or charges can only delocalize along several segments of a conjugated chain in a coherent manner, as long as the polarization-induced variation of the energy levels is small compared to the coherent coupling [28]. However, structural disorder leads to variation of the polarization energy over spatial position and thus results in the formation of coherently coupled regions, which are separated by zones where this interaction is weak (see Figure 2.9(c)). Due to the parallel arrangement of the π-orbitals, coherence can also be disturbed by torsions or kinks of the chain. The photophysics of polymer films is thus not governed by the intrinsic band gap corresponding to their backbone configuration and substituents, it rather results from the individual energetics of these small segments of high quantum coherence, which are referred to as *chromophores* or *sites*.

Beside the above-made considerations about the microscopic environment, it is of great importance to take into account the interactions between the photoexcited species for an appropriate description of the excited state energetics. As a consequence of the poor dielectric screening of charges in organic semiconductors ($\varepsilon_r \approx 3 - 4$), optically excited electrons are typically Coulombically bound to the positively charged remaining vacancy in the valence band (hole), thereby forming a bound quasi-particle, the exciton.

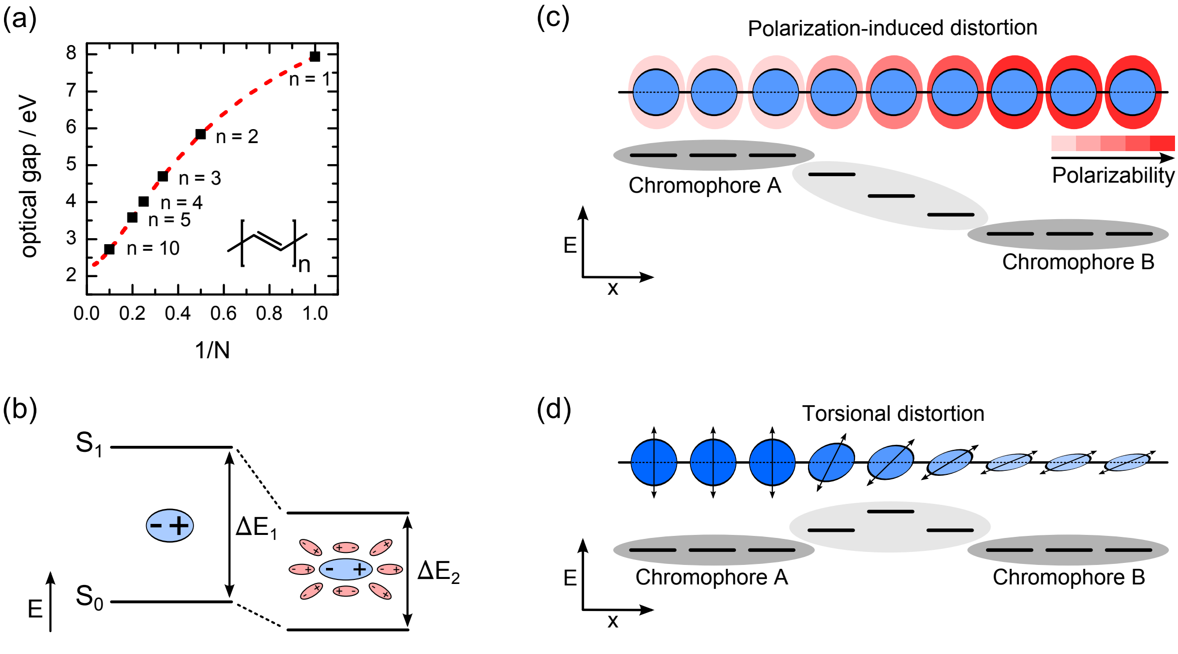

Figure 2.9.: Intrinsic and extrinsic influences on the optical gap of conjugated polymers, oriented at Ref. [28]. Panel (a) shows the dependence of the optical gap on the oligomer size exemplified for polyethylene, as predicted by the coupled oscillator model. The curve is obtained from Eq. 2.19 with the parameters E_0= 7.94 eV and $\frac{k'}{k_0}$= 0.46 [28]. The stabilizing influence of the dielectric environment is illustrated in panel (b). Coherent coupling between the covalently linked monomer units can either be disturbed by a change in the surrounding polarization (c) or by torsion or kinks of the polymer backbone (d).

The binding energies involved are on the order of several 100 meV [38, 75, 76], leading to remarkable reduction of the excited state energy [77].

2.4.2. Exciton transport in a disordered system

The above-made considerations about structural disorder and a varying polar environment imply that the energy levels of the chromophores and their spatial positions are randomly distributed. As a consequence, the signatures of optical transitions are significantly broadened with regard to the homogeneous linewidth of a single chromophore. It is commonly accepted that the spatial positions of the sites are uncorrelated, whereas the energy-dependent density of states $g(\epsilon)$ can be described by a Gaussian distribution [78]:

$$g(\epsilon) = \frac{1}{2\pi\sigma} \exp\left(-\frac{(\epsilon-\epsilon_0)^2}{2\sigma^2}\right) \tag{2.21}$$

The Gaussian profile together with a scheme of the corresponding spatial and energetic site distribution are presented in Fig. 2.10. The energy levels of the individual sites spread around an average energy ϵ_0, which is determined by the average bathochromic shift with regard to the site energy in a non-polar environment. The parameter σ is the standard deviation of this distribution and characterizes the amount of energetic disorder. Equation 2.21 is valid for both excitons and charges. However, the energy levels of charges should not be confused with the excitonic energy levels or the distribution of the ground state energies, as all of them are described by different, specific parameters ϵ_0 and σ.

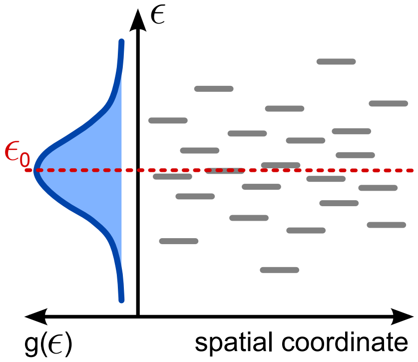

Figure 2.10.: Scheme of the energetic and spatial distribution of sites in a real disordered polymer system.

Within the chromophores, the excitons can delocalize in a coherent manner, but transport between the sites is governed by incoherent hopping. The precise mechanisms of incoherent exciton transport in conjugated polymers are subject to ongoing research [4, 6, 79, 80]. Generally, the transfer rate between two sites depends on their spatial separation, on the difference of their energies and on temperature, which may enable thermally activated hops to sites with a higher energy. This can be expressed as [81]

$$a_{ij} = \nu_0 f\left(|r_j - r_i|\right) \times \begin{cases} exp\left(-\frac{|\epsilon_j - \epsilon_i|}{k_B T}\right) & \epsilon_j > \epsilon_i \\ 1 & \epsilon_j \leq \epsilon_i \end{cases} . \tag{2.22}$$

The hopping rate a_{ij} from site i to site j is thus weighted with a thermal activation factor, which is one for hops downwards in energy and less than one, when the target site j has a higher energy. The parameter ν_0 denotes the attempt-to-escape frequency. The function $f\left(|r_j - r_i|\right)$ incorporates the spatial distance of the sites and depends on the underlying transport mechanisms. As already pointed out in Ch. 2.3.2, fundamental differences arise for the transport of singlet and triplet excitons. Singlet excitons can migrate via multipole interactions, i.e.

$$f\left(|r_j - r_i|\right) = \left|\frac{R_0}{r_j - r_i}\right|^S , \quad \frac{R_0}{|r_j - r_i|} < 1 . \tag{2.23}$$

For dipole interaction, as described in the Förster model (see Eq. (2.16)), the exponent S is 6 and R_0 denotes the Förster radius. However, for conjugated polymers, the chromophore size is comparable to their separation and thus, the point dipole approximation in Förster theory might be too simplistic to describe coupling-induced exciton transport. A more sophisticated description is obtained when the actual shape of the involved wave functions is taken into account [79, 80].

For triplet excitons and charges as well, transport occurs via short-range exchange interaction, leading to an exponential factor

$$f\left(|r_j - r_i|\right) = exp\left(-\frac{2\,|r_j - r_i|}{\alpha}\right) \,. \tag{2.24}$$

Exciton transport in a disordered system has important consequences for the PL properties. A phenomenon, which is typically observed in disordered systems and related to downward hops in the density of states is *spectral relaxation* [4, 6]. Figure 2.11(a) summarizes different possible relaxation processes. In a system, where exciton transport is efficient, the interplay between exothermic downward hops and thermally activated upward hops within the density of states leads to an overall red-shift of the PL emission maximum as a function of time after excitation through a laser pulse. This red-shift saturates at a certain energy ϵ_∞ , where a dynamic equilibrium between upward and downward hops is reached, see process number 1 in Fig. 2.11(a). Quantitatively, the equilibrium energy ϵ_∞ can be derived by calculating the average energy of an ensemble of excitations within a Gaussian distribution of site energies $g(\epsilon)$ (see Eq. 2.21 with $\epsilon_0 = 0$), following Boltzmann statistics [28, 78, 81]:

$$\epsilon_\infty = \frac{\int_{-\infty}^{\infty} \epsilon g(\epsilon) \exp(-\epsilon/k_B T)\, \mathrm{d}\epsilon}{\int_{-\infty}^{\infty} g(\epsilon) \exp(-\epsilon/k_B T)\, \mathrm{d}\epsilon} = -\frac{\sigma^2}{k_B T} \tag{2.25}$$

The equilibrium energy thus depends on the disorder parameter σ and decreases with decreasing temperature. The expected slope of ϵ_∞ as a function of temperature is sketched in Fig. 2.11(b). As a consequence of this slope, saturation of the disorder-induced red shift is faster reached for higher temperatures [4, 6]. In the low temperature regime, the required time to reach thermal equilibrium may even exceed the average recombination time, implying that the spectral red shift saturates below a critical temperature, see process number 2 in Fig. 2.11(a). The energetic shift of the PL maximum as a function of temperature and its evolution in time are sketched by the blue curves in Fig. 2.11(b) and (c). For the time-dependent energetic shift of the PL emission $\epsilon(t)$, Monte Carlo studies based on the Gaussian DOS have evidenced that $\epsilon(t)/\sigma \propto \log \nu_0 t$ [4, 28], with the attempt-to-escape-frequency ν_0.

When the transition rates are low, this may give rise to so-called *frustration* of the relaxation process, in particular at low temperatures [4, 6]. Instead of saturation or a continuous red shift of the PL emission maximum with decreasing temperature, kinetic frustration leads to a blue shift of the PL emission maximum, when the temperature is decreased below a critical value T_C (see Fig. 2.11(b)). This is due to the fact that in case of limited transport, only a small number of target sites is available for each exciton and thermally activated hops become relevant to assist spectral relaxation into energetically lower sites, as illustrated by process number 3 in Fig. 2.11(a). At low temperatures, thermally activated downward hops in the DOS are inhibited, leading to an overall blue-shift of the PL maximum below T_C, see process number 4 in Fig. 2.11(a). Such behavior has in particular been experimentally evidenced for phosphorescent triplet excitons, as they migrate via exchange interaction, which is of short-range and thus

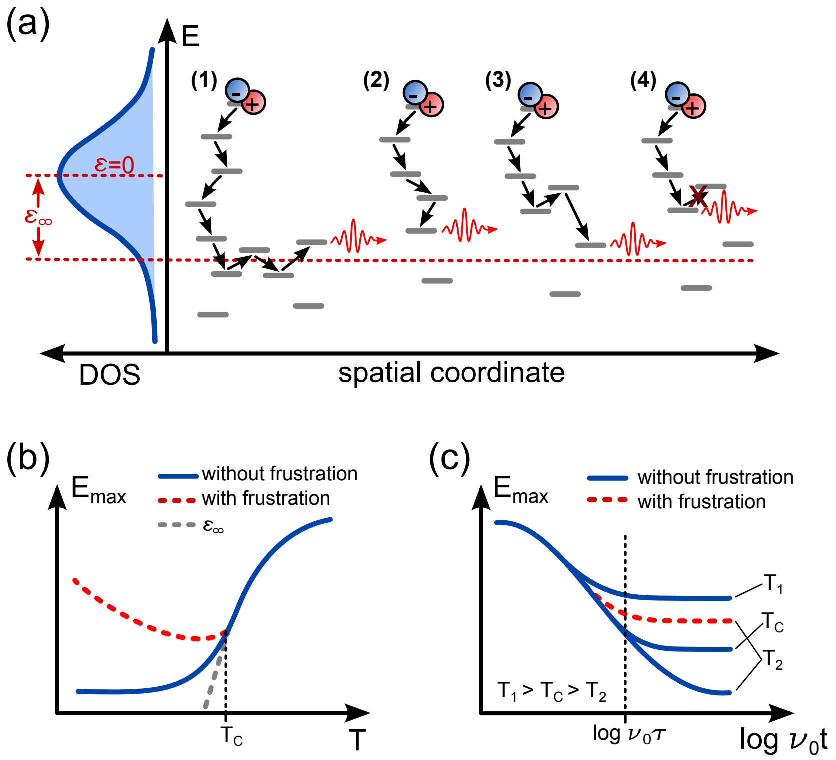

Figure 2.11.: Spectral relaxation in a disordered organic system with a Gaussian DOS [4]. Panel (a) summarizes different relaxation processes: (1) Relaxation towards an equilibrium energy ϵ_∞; (2) recombination before reaching equilibrium conditions; (3) spectral relaxation assisted by thermally activated hops and (4) frustration of the relaxation process. Panel (b) shows the expected temperature-dependent shift of the PL maximum in a system without kinetic frustration (solid blue curve) and in a system with inhibited exciton transport below a critical temperature T_C. The slope of the equilibrium energy ϵ_∞ is indicated as dashed gray curve. Panel (c) sketches the time-dependent red-shift of the PL maximum for different temperatures. The red-shift saturates, when thermal equilibrium is reached after the recombination time τ. The parameter ν_0 denotes the attempt-to-escape frequency.

yields a smaller number of target sites in the hopping process with respect to Förster coupling of singlet excitons [4].

2.5. Exciton separation at the donor/acceptor interface

One of the key questions investigated in this work is how excitons separate efficiently at a donor/acceptor heterojunction. After diffusion towards the interface, the actual electron or hole transfer leading to the population of a CT state can occur very efficiently on a sub-picosecond time scale [49]. This process can be described in the framework of semi-classical Marcus theory [28, 49, 75]. However, the subsequent step of exciton dissociation is not yet so well understood and there is an ongoing discussion among researchers about the underlying mechanisms. This section will introduce some of the concepts that have been developed to understand charge separation. A more detailed discussion of recent literature in this field will be given in Ch. 6.2, in the context of experimental findings on field- and temperature dependent CT emission presented in this work.

2.5.1. Marcus theory of electron transfer

In his publication from 1956, Marcus described the electron transfer between a donor and an acceptor molecule as a transition between two intersecting potential curves with minima at different configuration coordinates [82] (see Fig. 2.12). The first potential curve corresponds to the *reactant*, i.e. to the initial situation comprising the excited donor and the acceptor molecule D^*/A. The second potential curve describes the *product* CT state D^+/A^-. According to the Born-Oppenheimer approximation, the equilibrium coordinates of the potentials do not change during the electron transfer process. Therefore, an electron in the potential of the donor molecule must be in a vibrationally excited state to overcome an activation barrier ΔG^*, which depends on the intersection point of the potentials. For parabolic potential curves, the activation barrier is given by

$$\Delta G^* = \frac{(\lambda + \Delta G^0)^2}{4\lambda} \; , \tag{2.26}$$

where ΔG^0 is the energy offset between the potential surfaces of the initial and the final state and λ is the *reorganization energy.* This amount of energy would be necessary for the reactant to reach the equilibrium configuration of the product state. The rate of electron transfer k_{ET} can be expressed by Fermi's golden rule, yielding [49]

$$k_{ET} = \frac{2\pi}{\hbar\sqrt{4\pi\lambda k_B T}} V^2 \exp\left(-\frac{(\lambda + \Delta G^0)^2}{4\lambda k_B T}\right) \; . \tag{2.27}$$

The exponential factor accounts for the activation barrier and V denotes the transition matrix element, reflecting the electronic coupling between the reactant and the product state. In the classical treatment of Marcus, the matrix element V needs to be small, otherwise the coupling would lead to non-negligible energetic splitting of the potential curves. The limit of weak coupling is referred to as *nonadiabatic* approximation, whereas splitting of the energy levels at the intersection point would imply an *adiabatic* transfer reaction, signifying that the electron remains in the same electronic state after the transfer [21]. Another limitation of the classical treatment arises from the fact that at lower temperatures, the thermal energy in the system becomes comparable to the energy of the phonon modes involved. As a consequence, the vibrational energy can no longer be treated as a continuum, i.e. the potential energies the electron become discrete, according to the dominating phonon modes, which is illustrated by the equidistantly spaced energy levels in Fig. 2.12. In a semi-classical approach, Jortner suggested to treat the vibrational modes of the donor and acceptor molecules quantum mechanically [83], but to consider the vibrational energy provided by the environment to be a continuum. The electron transfer (ET) rate can then be expressed by [21, 28, 83]

$$k_{ET} = \frac{2\pi}{\hbar\sqrt{4\pi\lambda k_B T}} V^2 \mathrm{e}^{-S} \sum_{m=0}^{\infty} \frac{S^m}{m!} \exp\left(-\frac{(\lambda + \Delta G^0 + m\hbar\omega)^2}{4\lambda k_B T}\right) \; . \tag{2.28}$$

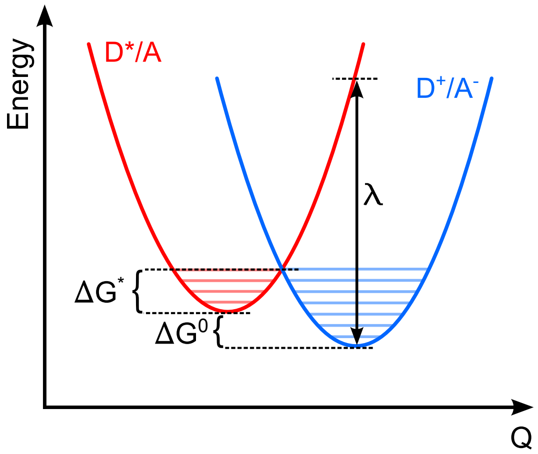

Figure 2.12.: Schematic of intersecting potentials according to Marcus theory of nonadiabatic electron transfer [82]. The parabolas signify potential energy surfaces of the reactant and the product state, which are plotted as a function of the configurational coordinate Q. Energy levels inside the potential curves indicate discrete phonon modes, according to Jortner's semi-classical extension [83]. ΔG^* is the activation barrier, ΔG^0 the ground state energy offset and λ the reorganization energy, as described in the text.

This semi-classical transfer rate is not applicable at very low temperatures, where also the phonon modes of the environment are on the order of k_BT [21]. Furthermore, the picture of intersecting potentials is challenged by recent studies on the coherent nature of the charge separation mechanism [51, 84, 85], which imply larger coupling between the adjacent molecules.

2.5.2. The process of exciton separation: Hot versus cold mechanisms

After electron an or hole transfer, the singlet exciton is transferred into a *charge transfer* (CT) state and the characteristics of this CT state strongly influences the performance of an organic solar cell, as the CT state can either be a precursor for charge separated (CS) states or act as a trap for interfacial electron-hole-pairs, giving rise to substantial losses in the charge generation process. Figure 2.13 sketches potential separation mechanisms, as suggested by Clarke and Durrant [49]. In principle, the variety of underlying separation mechanisms [51, 52] can be divided into two classes: (i) Charge separation via energetically excited CT states (CT*), often referred to as a "hot" process, or (ii) charge separation via the relaxed CT_1 state, which is also termed a "cold" process. The former process implies that the kinetic competition between the rate of CT* separation k_{CS^*} and the rate of thermal relaxation k_{therm} is decisive for the yield of CS states. When, on the other hand, charge separation from the relaxed CT states via k_{CS} is efficient, charge separation competes with transitions from the CT_1 to the ground state. Furthermore, triplet generation from the CT_1 state ($^3\mathrm{CT} \rightleftharpoons {}^3\mathrm{CT} \rightarrow \mathrm{T}_1$) has to be considered as a loss, when the triplet energy of either the donor or the acceptor component is below that of the CT state.

In the literature, there are good arguments for both types of separation processes, based on experiments and calculations. A more detailed discussion of recent studies will be given in Ch. 6.2, in the context of field-dependent luminescence quenching

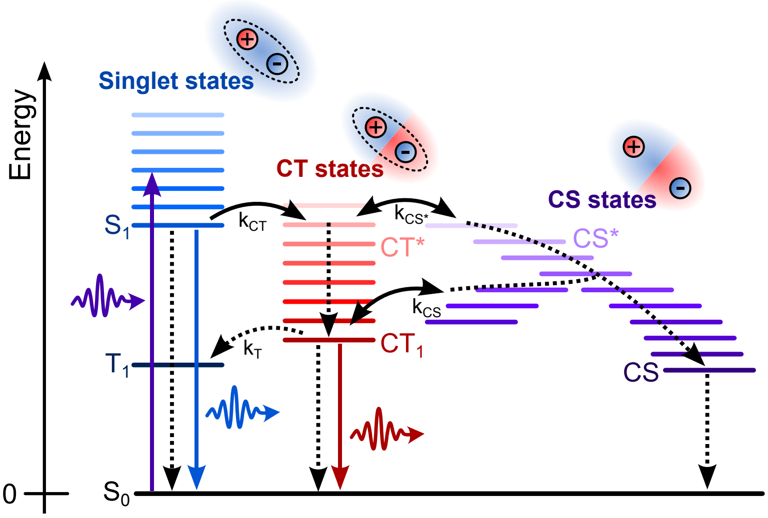

Figure 2.13.: Charge generation and loss mechanisms after Clarke and Durrant [49]. Photoexcitation of the system leads to population of singlet states S_1, which can create CT states with the rate k_{CT}. The excess energy of the initially formed CT* state either drives charge separation (CS) via k_{CS^*} (hot process), or the excess energy is dissipated in the system, leading to population of the energetically relaxed CT_1 state. When dissociation of the relaxed CT state via k_{CS} (cold separation mechanism) is possible, this process competes with recombination and conversion into triplet states, provided that the T_1 level of the donor or acceptor component is energetically below the CT level.

studies. Concepts of charge separation via energetically excited CT states are based on the fact that the initial CT state, when created from a singlet exciton, must carry some excess energy, according to the offset of the donor and acceptor energy levels at the interface. Furthermore, this is also a direct implication of Marcus theory, which states the excess energy of the CT state must at least correspond to the activation barrier induced by the intersection point of the potential surfaces. This excess energy leads to the population of vibrationally excited or even higher electronic CT states, both denoted by CT*, which may couple more efficiently to CS states, either due to the better matching of energy levels or according to the more delocalized nature of the CT* states. Energetic relaxation towards the CT_1 state on the other hand implies that the charges have to separate in a diffusive manner and it is reasonable to assume that they are still Coulombically bound across the heterointerface during this process. Despite these apparent drawbacks, there is experimental evidence that this process can be very efficient [86, 87]. A reasonable argument for efficient charge separation from relaxed CT states arises from the assumption that the screening of charges, i.e. the dielectric constant, at the heterointerface is actually much higher than in the neat donor or acceptor domains, according to the presence of a static dipolar layer at the donor/acceptor interface [16, 88, 89]. This issue will be further detailed in Ch. 2.5.5.

For this work, field and temperature dependent PL quenching studies indicate that a diffusion-related quenching mechanism can in fact consistently explain the observed PL dynamics of the CT emission under various electric fields for one of the material systems. To gain further insight, an appropriate kinetic model needs to be applied to the data. As further detailed in Ch. 6, it turns out that a hopping process involving

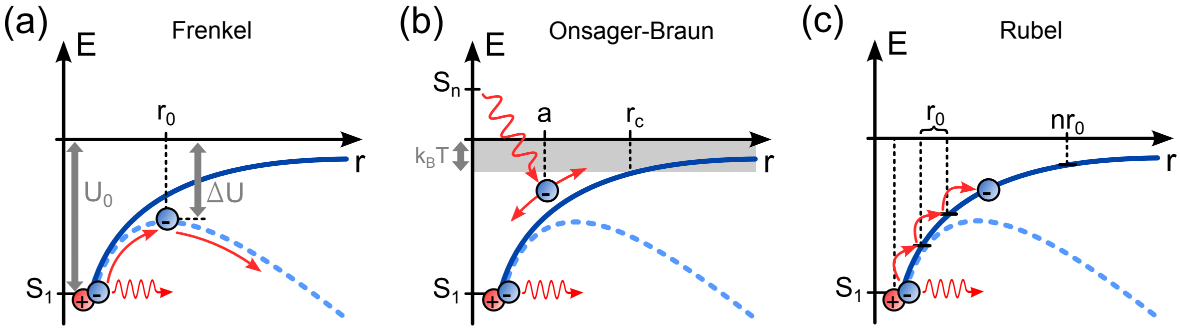

Figure 2.14.: Schematic representation of the different kinetic models for field-induced dissociation of the S_1 state described in Ch. 2.5.3 and Ch. 2.5.4. Blue solid (dashed) curves describe the Coulomb potential one of the charges has to escape from without (with) applied electric field. The model of Frenkel [90] in (a) describes charge separation as a one-step process, where an activation barrier $U_0 - \Delta U$ has to be overcome. The Onsager-Braun model (b) is based on the assumption that after excitation one of the charges thermalizes at a distance a from the origin and undergoes classical diffusion [92]. The charges are considered to be free when their distance exceeds r_c. Panel (c) sketches dissociation via a hopping mechanism [15]. The hopping sites have a spacing r_0 and dissociation is complete at a critical distance nr_0.

several intermediate steps during charge separation is in good agreement with the experimental data. This approach suggested by Rubel et al. [15] is in principle an extension of classical Onsager-Braun theory and the Poole-Frenkel model for exciton dissociation. All three concepts shall be briefly introduced in the next sections. In each case, the field and temperature dependent dissociation rate $k_D(F,T)$ yielded by the respective model is of particular interest, as it can be used to describe the luminescence quenching, which is related to the amount of excitons dissociated in the presence of an electric field $\eta_D(F,T)$. Therefore, it has to be taken into account that there is always a kinetic competition between field-induced dissociation and recombination via k_{rec}, i.e.

$$\eta_D(F,T) = \frac{k_D(F,T)}{k_{rec} + k_D(F,T)} \; . \tag{2.29}$$

2.5.3. Classical descriptions: Poole-Frenkel and Onsager-Braun model

In a simple, but comprehensive approach, Frenkel considered exciton separation as a one-step process [90] (Fig. 2.14(a)). He suggested that charge separation occurs when one of the mutually bound charges is thermally activated above the ionization barrier, which is lowered in the presence of an electric field. According to this assumption, the dissociation rate can be expressed as [90, 91]

$$k_{D[Frenkel]}(F,T) = \nu_0 \exp\left(-\frac{E_b - \Delta U}{k_B T}\right) \; , \tag{2.30}$$

where ν_0 denotes an attempt-to-escape frequency, E_b is the exciton binding energy and $\Delta U = 2\sqrt{e^3 F / 4\pi\varepsilon_0\varepsilon_r}$ is the lowering of the potential well, when an electric field F is applied.

Another classical theory has been developed in the 1930s by Onsager, originally to describe the dissociation of ion pairs in weak electrolytes [93], but later he adapted his work for the case of optically created electron-hole pairs [94]. His main idea was that excess energy from the excitation process gives the electron-hole pair some initial separation distance a (see Fig. 2.14(b)). When this separation exceeds a certain extent, the charges are considered to be free. This critical separation distance is known as the *Coulomb capture radius* r_c and it defines the distance, at which the potential energy equals the amount of thermal energy k_BT in the system, i.e. [49]

$$r_c = \frac{e^2}{4\pi\varepsilon_0\varepsilon_r k_B T} \ . \tag{2.31}$$

When the thermalization radius is smaller than the Coulomb capture radius r_C, the charge is 'captured' and undergoes Brownian diffusion in the Coulomb potential of the other charge, which is assumed to be immobile. The electron-hole-pair may then either recombine or dissociate. The probability for dissociation is enhanced by an externally applied electric field. In his original treatment, Onsager did not consider the possibility that a charge can make several attempts to escape from the Coulomb potential during its lifetime. The model was later extended by Braun [92], who considered the interplay between field-induced exciton dissociation and recombination, as presented in Eq. (2.29). For the field-dependent dissociation rate, Braun used the original expression from Onsager's theory [93]

$$k_{D[Onsager]}(F,T) = \frac{3e\mu}{4\pi r_0^3\varepsilon_0\varepsilon_r} \exp\left(-\frac{E_b}{k_B T}\right) \frac{J_1(2\sqrt{-2b})}{\sqrt{-2b}} \ , \tag{2.32}$$

where μ denotes the carrier mobility and r_0 is the initial separation of the charges. The exciton binding energy is given by $E_b = e^2/4\pi\varepsilon_0\varepsilon_r r_0$ and J_1 is the first order Bessel function with the parameter $b = e^3F/8\pi\varepsilon_0\varepsilon_r(k_BT)^2$.

2.5.4. Hopping dissociation on a one-dimensional chain

The model of hopping dissociation has been proposed by Rubel et al. [15]. In this concept, a carrier either escapes from the mutual Coulomb potential via a multi-step hopping process or it recombines with the opposite charge. In principle, Frenkel and Onsager theory can be interpreted as special cases of Rubel's approach: The model of Frenkel considers exciton dissociation as a one-step process and in the Onsager-Braun concept, the carrier undergoes a classical diffusion process, which would correspond to an infinitely small spacing between the hopping sites. However, from the previous discussion on the chromophores in semiconducting polymers acting as energetically and spatially separated sites, and regarding the mechanisms of incoherent hopping transport between them, it appears reasonable to go beyond Onsager's approach, which treats the material as a homogeneous medium. This also appears plausible, as disorder turns out to have a strong influence on the observed field-induced PL quenching characteristics. Both spatial and energetic disorder can be easily implemented in the kinetic model introduced herein.

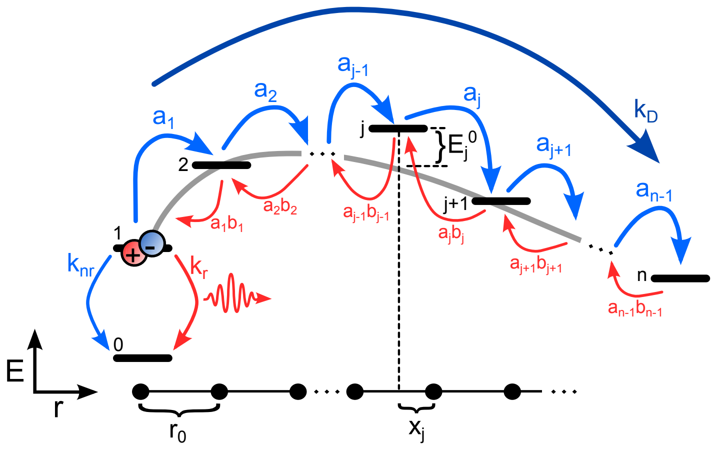

Figure 2.15.: Schematic of a disordered model potential according to Eq. 2.40, from which a charge may escape via hopping. From site 1, the exciton can either dissociate or recombine. All sites have random spatial and energetic offsets x_j and E_j^0 from the ideal slope of the Coulomb potential represented by the gray curve. The overall dissociation rate k_D results from the individual forward and backward hopping rates between adjacent sites a_j and $a_j b_j$, respectively, and is calculated from Eq. 2.38.

The general idea of the model and the important parameters are sketched in Fig. 2.15. The photogenerated hole is considered to be immobile at the first site, whereas the electron can migrate via hopping between discrete sites in the attractive Coulomb potential. The choice of the hole at the origin is arbitrary and the inverse situation with an immobile electron may apply as well. Transport between two sites j and $j+1$ occurs via phonon-assisted tunneling, as described by a Miller-Abrahams-type hopping rate [95]

$$a_j = \nu_0 \exp\left(-\frac{2\,|r_{j+1}-r_j|}{\alpha}\right) \times \begin{cases} \exp\left(-\frac{|E_{j+1}-E_j|}{k_B T}\right) & E_{j+1} > E_j \\ 1 & E_{j+1} \leq E_j \end{cases} . \tag{2.33}$$

Here, r_j is the distance of site number j from the first site, α denotes a localization parameter and E_j is the site energy in the Coulomb potential caused by the opposite charge at the origin. The potential can be lowered by an electric field F:

$$E_j(F) = -\frac{e^2}{4\pi\varepsilon_0\varepsilon_r r_j} - eFr_j \tag{2.34}$$

Beside transport away from the first site, the charge can also migrate backward and recombine with the opposite charge at the first site. The specialty of the model considered here is the assumption of a certain asymmetry in the forward and backward transition rates. In the approach of Rubel et al., the backward transition rate from site $j+1$ to site j is given by the product $a_j b_j$ with the asymmetry factor b_j defined as

$$b_j = \exp\left(\frac{E_{j+1}-E_j}{k_B T}\right) . \tag{2.35}$$

The time $\tau_D(F,T)$, that a carrier needs to dissociate, can be expressed as the sum over all inverse hopping rates a_j, weighted by the probability for back transfer. Starting from site 1 and with dissociation fulfilled at site n, this yields

$$\begin{aligned}\tau_D(F,T) &= \frac{1}{a_1}+\frac{1}{a_2}\cdot\frac{a_1 b_1}{a_1}+...+\frac{1}{a_{n-1}}\cdot\frac{a_{n-2}b_{n-2}}{a_{n-2}}\cdot...\cdot\frac{a_1 b_1}{a_1} \\ &= \frac{1}{a_1}+\sum_{j=2}^{n-1}\frac{1}{a_j}\prod_{k=1}^{j-1} b_k \ . \end{aligned} \tag{2.36}$$

Due to advantageous definition of the asymmetry factor (see. Eq. 2.35), the product in Eq. 2.36 can be expressed as

$$\prod_{k=1}^{j-1} b_k = \exp\left(\frac{E_j - E_1}{k_B T}\right) \ . \tag{2.37}$$

The field- and temperature dependent dissociation rate $k_D = \tau_D^{-1}$ for a carrier starting at the first site can thus be expressed as

$$k_{D[Rubel]}(F,T) = \left[\sum_{j=1}^{n-1}\frac{1}{a_j}\exp\left(\frac{E_j(F)-E_1}{k_B T}\right)\right]^{-1} \ . \tag{2.38}$$

The site energies E_j are given by Eq. 2.34. Here, the energy of the first site E_1 is defined as

$$E_1 = -\frac{e^2}{4\pi\varepsilon_0\varepsilon_r r_0} - eFr_0 \ , \tag{2.39}$$

to avoid divergence of the potential at the origin. The parameter r_0 defines the spacing between the sites and thus the distance of each site from the origin is given by $r_j = jr_0$ (see Fig. 2.15).

In real systems, however, the sites are not equally spaced and the site energies are statistically distributed, following the discussion in Ch. 2.4.1. These effects can be included into the model by adding a random offset to the position and energy of each site in the dissociation path [15]. The dissociation process is thus unique for each photogenerated electron-hole-pair and an adequate number of simulation runs has to be performed to mediate sufficiently between the characteristics of the individual dissociation paths. To account for spatial disorder, a random offset x_j is created from an interval $\pm\delta$. Energetic disorder is implemented using the random energy offset $E_j^0(\sigma)$, which is normally distributed quantity around zero with standard deviation σ, according to the Gaussian DOS in organic systems. The parameters δr and σ are used to quantify the portions of spatial and energetic disorder in the system. In the presence of disorder, the spatial and energetic positions of the sites turn into

$$\begin{aligned} r_j &= x_j + j r_0 \ , \ x_j \in \pm \delta r \\ E_j(F) &= E_j^0(\sigma) - \frac{e^2}{4\pi\varepsilon_0\varepsilon_r r_j} - eFr_j \ . \end{aligned} \tag{2.40}$$

A schematic representation of the resulting model potential including the relevant parameters is given in Fig. 2.15. In analogy with the other introduced models, the portion of energy a carrier needs to overcome the potential barrier created by the opposite charge can be interpreted as the exciton binding energy and is given by the energy level of the first site E_1 in Rubel's approach. In a disordered system, this is however an average value, because also the initial site is subject to disorder. Furthermore, the threshold for exciton separation is mainly determined by the largest energy difference between two adjacent sites on the one-dimensional chain, and in the presence of disorder, this is not necessarily the difference between E_1 and E_2.

2.5.5. Impact of delocalization and dipoles at the donor/acceptor interface

It should be noted that Eq. 2.34 is only a very rough approximation for the potential energy, because it does not account for the delocalization of charges or quantization effects. Furthermore, it is unsuitable for the description of heterointerfaces, because the predicted Coulomb binding energy would be too large to account for the efficient charge

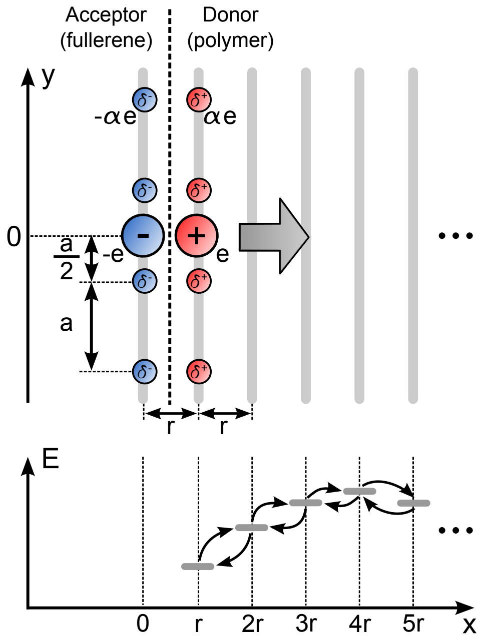

Figure 2.16.: Illustration of the separation mechanism of CT states, suggested by Arkhipov et al. [16]. The hole can escape from the Coulomb potential of the (localized) electron via several hops between adjacent polymer chains. The escape direction is indicated by the gray arrow and the potential energy of the hole on the polymer chains is sketched in the lower plot. Interfacial dipoles are implemented via partial charges $\pm\alpha e$ at the donor/acceptor interface, corresponding to the distribution suggested in Ref. [96] and applied in Ref. [97].

separation observed in many OPV systems. In a more rigorous treatment, Arkhipov et al. [16] calculated the electrostatic potential based on the following assumptions (see Fig. 2.16): At the donor/acceptor interface, typically a polymer/fullerene heterojunction, the hole is delocalized on a polymer chain, which is oriented parallel to the interface. To overcome the Coulomb attraction of the electron, the hole performs inter-chain hops in a direction perpendicular to the interface, while the electron remains localized at the acceptor molecule. Beside delocalization of the hole, the second essential assumption is an interfacial layer of discrete dipoles, which is present even in the ground state. The model has been further developed by Nenashev et al., who derived an analytic approximation for the potential energy [98] and by Wiemer et al. [96], who reconsidered the distribution of interfacial dipoles, thereby strerssing their potential importance in the charge separation process. When the problem is treated quantum mechanically, the energy of the hole on the nth polymer chain can be calculated from solving the Schrödinger equation

$$-\frac{\hbar^2}{2m^*}\frac{\mathrm{d}^2\Psi(y)}{\mathrm{d}y^2}+U_n(y)\Psi(y)=E_n\Psi(y)\ , \tag{2.41}$$

where m^* is the hole effective mass and $\Psi(y)$ is the hole wave function, assuming that its delocalization is constrained to the one-dimensional polymer chain. The potential energy $U_n(y)$ of the hole on the nth chain is determined by the Coulomb well, lowered by the electric field, which is applied perpendicular to the interface, yielding

$$U_n(y)=-\frac{e^2}{4\pi\varepsilon_0\varepsilon_r\sqrt{y^2+x_n^2}}-eFx_n \quad \text{with} \quad x_n=nr\ . \tag{2.42}$$

For this potential, Eq. 2.41 cannot be solved analytically, but an analytic approximation suggested by Nenashev et al. [98] is to use the second order expansion of the position-dependent factor, leading to

$$\frac{1}{\sqrt{y^2+x_n^2}}\approx-\frac{1}{x_n}+\frac{1}{2x_n^3}y^2\ . \tag{2.43}$$

Solving Eq. 2.41 with the approximated potential then yields two essential contributions [97]

$$\begin{aligned} E_n=E_{pot}+E_{kin} \quad &\text{with} \quad E_{pot}=U_n(y)|_{y=0} \\ &\text{and} \quad E_{kin}=\left.\sqrt{\frac{\hbar^2}{4m^*}\frac{\mathrm{d}^2}{\mathrm{d}y^2}U_n(y)}\right|_{y=0} \end{aligned} \tag{2.44}$$

The first term corresponds to the potential energy, which has already been given in the classical description in Ch. 2.5.4 (see Eq. 2.34). Inserting the second quadratic term of Eq. 2.43 into Eq. 2.41 is equivalent to the quantum mechanical formulation of the harmonic oscillator. The energy E_{kin} corresponds to the ground state energy $\hbar\omega/2$, which raises the hole energy above the value resulting from classical treatment. Thus, these *zero point oscillations* effectively add to the dissociation probability and the impact increases with decreasing effective mass of the hole.

Assuming that a number of N equidistantly spaced dipoles is located at the donor/acceptor interface (see Fig. 2.16(a)) and with the distribution of interfacial dipoles presented in Fig. 2.16, the potential energy of the hole on the nth polymer chain is given by [96]

$$U_n(y) = -\frac{e^2}{4\pi\varepsilon_0\varepsilon_r}\left(\frac{1}{\sqrt{x_n + y^2}} + \sum_{j=-N/2}^{N/2}\frac{\alpha}{\sqrt{(x_n - r)^2 + (y - (j + \frac{1}{2})r)^2}}\right.$$
$$\left. + \sum_{i=-N/2}^{N/2}\frac{-\alpha}{\sqrt{x_n^2 + (y - (i + \frac{1}{2})r)^2}}\right) - eFx_n \ . \qquad (2.45)$$

The parameter α is a measure for the dipole strength. It turns out that even for relatively small values of α on the order of 0.1 and for an effective hole mass similar to that of the electron, the calculated threshold field for exciton dissociation is reduced by a factor of 10^3 [96], giving substantial evidence that charge separation at the interface can be efficient, even when the excitation has relaxed into the emissive CT_1 state. In the framework of this thesis, no detailed calculations of the carrier energy following Eqns. 2.44 and 2.45 have been carried out, however, the concept presented in this section allows for a well-grounded discussion of the results presented in Ch. 6.

2.6. Organic solar cells

2.6.1. The bulk heterojunction concept

A general requirement for the operation of solar cells is a built-in asymmetry, driving electron migration towards the cathode and hole transport towards the anode. In inorganic devices, this is achieved by a pn-junction, however, organic bilayer devices are not efficient [43, 99], according to the excitonic nature of the photoexcitations. Organic solar cells are thus based on a different concept, where donor and acceptor are intimately mixed to form a so-called *bulk heterojunction* (BHJ), serving as active layer in devices [44]. In such a device, excitons, created either in the donor or the acceptor component, can efficiently dissociate at the donor/acceptor interface and charges are transported towards the device electrodes in the respective domains. This implies, that a compromise between a large heterointerface for exciton separation on the one hand, and sufficiently large donor and acceptor domains for efficient transport on the other hand has to be found. Thus, device optimization is not trivial and the overall morphology plays a decisive role for the performance of organic solar cell devices. The general concept of a BHJ device is illustrated in Fig. 2.17. Charge generation follows

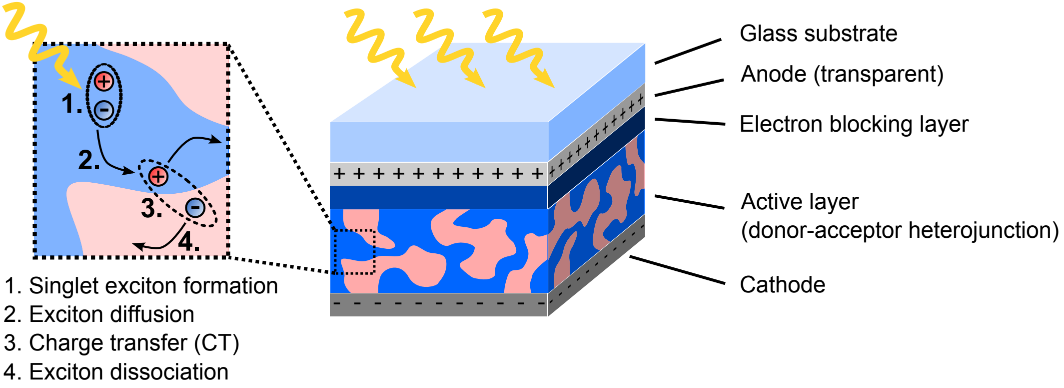

Figure 2.17.: Operation principle of a bulk heterojunction device.

the previously discussed steps, i.e. absorption of light, singlet exciton diffusion towards a heterointerface, charge transfer, CT dissociation and eventually charge extraction. For selective extraction of charges, electrodes of different work functions are used, as sketched in Fig. 2.18. For simplicity, the energy level diagram corresponds to the arrangement of a bilayer device, but in a BHJ the situation is similar. When the device is operated as a solar cell, the potential difference induces a built-in field, which drives charge separation. The energy level arrangement at the donor/acceptor interface of a BHJ represents a so-called *type-II-heterojunction*, which promotes the separation of excitons.

For operation as a solar cell, one of the contacts has to be transparent. Typically, indium tin oxide (ITO) is used, which is deposited on a glass substrate. A common material for the back side contact is aluminum (Al), which can be deposited via evaporation on the active layer. The efficiency of charge extraction can be further enhanced by introducing electron or hole transporting layers between the active layer and the respective electrode. Beside the standard device geometry, inverted device structures have proven successful [1, 27]. In contrast to the design sketched in Fig. 2.17, the transparent electrode in an inverted structure serves as cathode, collecting the electrons, whereas the holes are collected at the metal contact. The fabrication procedure of the devices investigated in the framework of this thesis is further detailed in the appendix 3.4.

2.6.2. Characteristic parameters of organic solar cells

The efficiency of organic solar cells is determined from their current-density-voltage (JV) characteristics, which is recorded under standardized illumination conditions. By convention, the intensity and the spectrum of the illumination source corresponds to the air mass (AM) 1.5 spectrum[2]. The important parameters extracted from a JV curve are shown in Fig. 2.19(a). In the chosen representation, a negative voltage corresponds

---

[2] The air mass factor 1.5 corresponds to the 1.5-fold thickness of the atmosphere, giving a measure for the typical attenuation of light in the atmosphere.

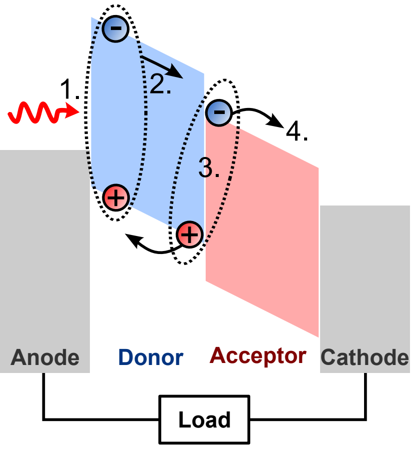

Figure 2.18.: Energy level scheme and charge generation mechanism of an organic solar cell under operation conditions. The steps of the charge generation process are numbered similar to Fig. 2.17.

to a bias in *reverse direction*, where the applied field adds to the built-in field. In this regime, the energy level offset inhibits charge injection from the electrodes and the measured current is essentially the drift current driven by the built-in field of the device. The current measured at zero external field is defined as short circuit current J_{sc}. Further increase of the voltage eventually leads to compensation of the built-in field at the open circuit Voltage V_{oc}, where the net current is zero. At higher forward bias, charges are injected into the device, leading to a strong increase of the current. The energy level arrangements for open circuit and short circuit conditions are sketched in Fig. 2.20. The bias range between short circuit and open circuit conditions is equivalent to typical operation range of a solar cell. The supplied power can be calculated from the product of the current and the voltage at a given point of the JV curve. From the slope of the JV curve it becomes apparent, that the power delivered by the device depends on the current extracted by a connected load resistance. The maximum power point defines the operation point, where the power supplied by the device reaches a maximum.

The power conversion efficiency (PCE) η is given by the ratio between the maximum output electrical power P_{max} and the incident power P_{sun}, provided by the absorbed sunlight

$$\eta = \frac{P_{max}}{P_{sun}} \ . \tag{2.46}$$

The maximum power P_{max} can be expressed by the open circuit voltage V_{oc}, the short circuit current J_{sc} and the fill factor FF. The latter is useful to quantify the deviation of the JV curve from the idealized slope, which would be a rectangular curve intersecting the axes at J_{sc} and V_{oc}. The fill factor is defined by

$$FF = \frac{J_{MPP} \cdot V_{MPP}}{J_{sc} \cdot V_{oc}} \ , \tag{2.47}$$

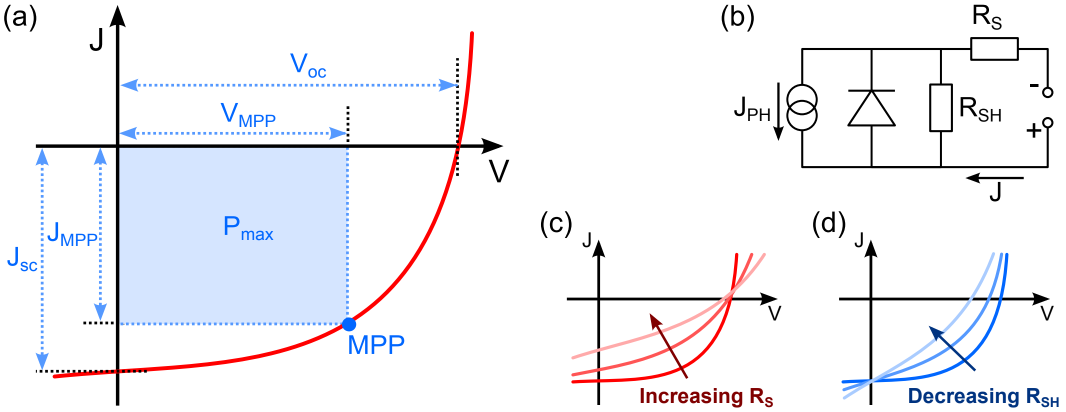

Figure 2.19.: Current-density-voltage characteristics and of a solar cell device. Panel (a) illustrates the parameters, which are extracted from a JV curve (red) to determine the solar cell efficiency: J_{sc} is the short circuit current density, V_{oc} the open circuit voltage and MPP the operation point where the device delivers the maximum amount of power P_{max}. Panel (b) shows an equivalent circuit of a real device, including a serial resistance R_S and a shunt resistance R_{SH}. The influences of a non-zero serial resistance and a finite shunt resistance are illustrated in (c) and (d), after Ref. [28].

where J_{MPP} and V_{MPP} are the current and the voltage at the operation point with maximum power. An idealized device would have a fill factor of one, but the fill factor of real devices is below that value. With the fill factor, Eq. 2.46 can be expressed as

$$\eta = \frac{FF \cdot I_{sc} \cdot V_{oc}}{P_{sun}} \; . \tag{2.48}$$

The JV characteristics of a real device can be described by considering the equivalent circuit presented in Fig. 2.19(b), comprising an effective serial resistance R_S and a shunt resistance R_{SH}. In an ideal device, the serial resistance is zero and the shunt resistance is infinity. However, in real devices, in particular the electrode contacts can increase the overall resistance, thereby limiting the extracted current. A reason for finite shunt resistance is recombination inside the device. The influences of these parasitic resistances on the JV curves can be described by adapting the Shockley equation for an ideal diode [100] using Ohm's law. This leads to

$$J = J_{dark}\left[\exp\left(\frac{e}{nk_BT}(U - JR_S)\right) - 1\right] + \frac{U - JR_S}{R_{SH}} - J_{ph} \; , \tag{2.49}$$

where J_{dark} is the dark current, e the elementary charge, n is the diode ideality factor and J_{ph} is the photo current. In accordance with the expectations, increasing the serial resistance reduces the supplied current. Reduction of the shunt resistance on the other hand leads to a smaller open circuit voltage.

2.6.3. Limitations on the performance

A fundamental limitation on the performance of solar cells has been postulated in 1961 by Shockley and Queisser [101]. Their considerations were based on the fact that there

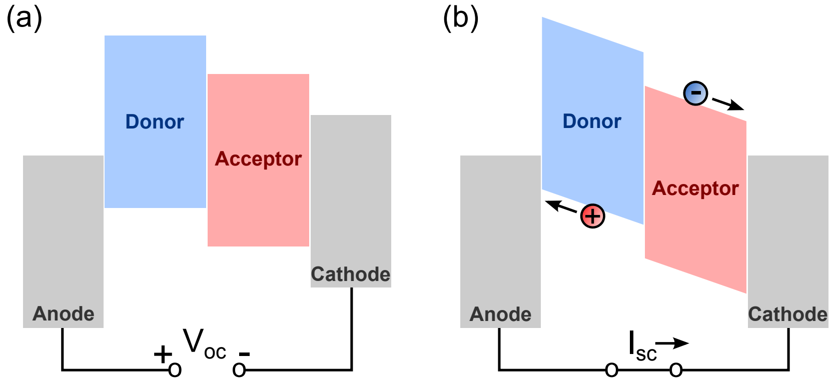

Figure 2.20.: Schematic representation of the energy level alignment in an organic donor/acceptor heterojunction. In panel (a) the built-in field of the device is compensated by the external bias Voc and in (b) the device is operated under short circuit conditions.

is always a trade off between reducing the band gap of a semiconductor material for efficient light harvesting and thereby increasing J_{sc} on the one hand, and retaining a sufficiently large band gap on the other hand, because the band gap is directly related to V_{oc}. This correlation results from the fact, that photogenerated charges relax very quickly to the band edges, even when they have been created with a high portion of excess energy with respect to the band gap. Based on similar considerations and taking into account the AM 1.5 spectrum, more recent work reports an optimum band gap of 1.34 eV and a corresponding theoretical efficiency of 33 % [102]. For bulk heterojunction devices it has to be taken into account that the effective band gap of the material corresponds to the energy difference between the HOMO of the donor and the LUMO of the acceptor material. Based on these considerations and applying Shockley Queisser theory, Kirchartz et al. [103] estimated the maximum achievable PCE in the radiative limit[3] to 23 %. Apparently, there is still a high discrepancy between this theoretical limit and the efficiencies achieved nowadays in real devices. Particular losses in organic solar cell devices are attributed to [27, 103]:

1. Reduction of the impinging light intensity at the device surface and due to parasitic absorption layers
2. Incomplete exciton dissociation at the donor/acceptor interface
3. Recombination at interfaces or defects
4. Insufficient collection of charges at the electrodes

Empirically, it is found that the open circuit voltage of organic solar cell devices is diminished by an amount $\Delta = 0.3 - 0.6\,\mathrm{eV}$ with respect to the value of V_{oc} expected from the energy level offset [28, 104, 105], i.e.

$$V_{oc} \approx \frac{1}{e}\left(\left|E^{D}_{HOMO}\right| - \left|E^{A}_{LUMO}\right|\right) - \Delta \; . \tag{2.50}$$

---

[3] The *radiative limit* corresponds to an idealized device without any non-radiative recombination related to traps. Radiative recombination on the other hand is intrinsic and cannot be avoided.

As a particular reason for this discrepancy, non-radiative losses, such as interfacial recombination, triplet generation and diffusion currents at the electrodes are being considered [27, 103–105]. In order to increase the performance of organic solar cell devices, it is necessary to identify the precise origins of these losses experimentally and to find ways to reduce them.

2.6.4. Design principles of conjugated polymers for organic photovoltaics

Semiconducting polymers typically consist of a π-conjugated backbone with alkyl chains or other side groups attached to it. The chemical, structural and photophysical requirements for their application as donor materials in OPV are manifold. Polymer solar cells are fabricated via diverse solution processing techniques, thus the side groups should be large enough to enable good solubility in the organic solvent. On the other hand, the side groups should not disturb molecular packing in the spin-cast films, which would affect the exciton or charge transport properties. Thus, optimizing procedures focus a lot on the selection of appropriate side groups. A prominent example for the impact of side-group arrangment in spin-cast films is the polymer P3HT. The side chains can have *regiorandom* (RRa) or *regioregular* (RR) arrangement. The random orientation of the alkyl groups in RRa-P3HT impedes crystallization of the polymer and thereby reduces the intermolecular interactions, which tremendously alters the optical properties and affects the performance of electronic devices [8, 106].

Another key challenge is to optimize the energy levels of the molecular orbitals with respect to the energetics of the acceptor material. A certain offset between the donor and acceptor HOMOs and LUMOs is necessary to drive charge separation, however due to thermalization effects, this excess energy is finally dissipated in the system and the open circuit voltage is related to the offset between the HOMO energy of the polymer and the LUMO energy of the acceptor material, as discussed in Ch. 2.6.3. Thus, lowering the HOMO energy of the donor or raising the LUMO level of the acceptor generally leads to a higher open circuit voltage. On the other hand, it has to be considered that reducing the band gap of the polymer is beneficial in terms of better light harvesting. The only way to raise the open circuit voltage and increase the absorption of light simultaneously is to lower both the HOMO and the LUMO level of the polymer [107].

Several strategies are employed to reduce the polymer band gap. Generally, polymers with a high planarity have a smaller optical gap compared to polymers with a high degree of torsional distortions, because parallel arrangement of the non-hybridized p_z-orbitals leads to the formation of larger chromophores. A higher planarity of the polymers can be achieved by increasing the double bond character between the building blocks, which are typically composed of aromatic monomers, such as benzene or thiophene. In the ground state, such polymers comprise two nondegenerate resonance structures, i.e. the *aromatic* and the *quinoid* form. In many polymers, the aromatic form where the electrons are located inside the building blocks is energetically favored, but leads to a higher band gap than the quinoid form. The latter comprises double bonds between the monomers, thus giving rise to higher planarity and a reduced band gap [48, 108]. The aromatic and quinoid resonance structures of polythiophene are presented in figure 2.21.

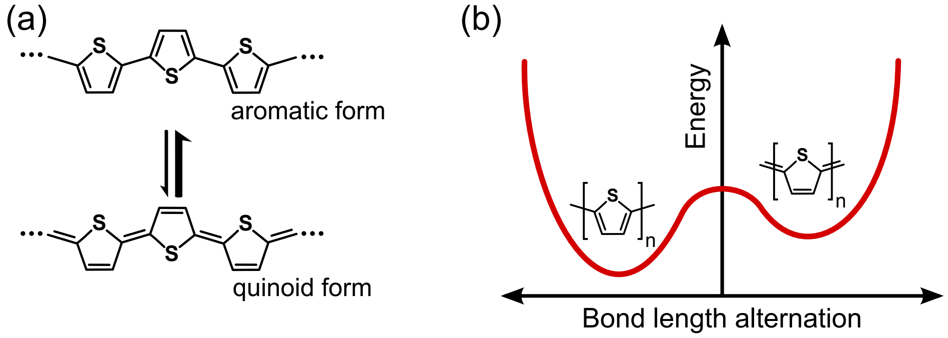

Figure 2.21.: Aromatic and quinoid resonance structures of polythiophene. The thick arrow in panel (a) indicates that the aromatic form is the dominating resonance structure. Panel (b) sketches the corresponding potential energy curve.

Two major strategies have been developed to stabilize the quinoid structure: The most common approach is to employ alternating building blocks with different electronegativities [109–111], as illustrated in Fig. 2.22(a). When electron-donating and electron-accepting monomers are linked via copolymerization, partial charge transfer from donor to acceptor units enhances the electron density between the building blocks, thereby improving the planar character. Furthermore, coupling of the individual molecular orbitals leads to the formation new HOMO and LUMO orbitals in the polymer [108, 111, 112], yielding a reduced band gap.

The other approach, also referred to as *quinoid*-approach, makes use of monomers, which inherently stabilize the quinoid structure of the polymer [113–115]. This is typically achieved with polycyclic monomers, which are composed of different aromatic rings with individual resonance energies[4]. A prominent example is isothianaphthene [108, 113, 115], which consists of a benzene and a thiophene ring, as shown in Fig. 2.22(b). The resonance energy of the benzene ring is much higher than that of the thiophene ring, thus the thiophene ring is dearomatized. Polymerization is performed via linking of the thiophene rings, giving rise to a backbone, which is clearly dominated by the quinoid structure. Compared to the donor-acceptor-approach, this strategy has been less often employed. However, it has been argued that the quinoid approach is beneficial for the hole mobility in conjugated polymers, as the alternating electron density in donor-acceptor copolymers could also lead to carrier trapping [115].

Structural formulas of some popular semiconducting polymers for OPV are presented in Fig. 2.23 and some important material parameters are summarized in Tab. 2.1. The poly(p-phenylenevinylene)s (PPVs) were the first class of conjugated polymers considered for applications in organic electronics. A PPV-derivative was also the first polymeric material, for which electroluminescence has been demonstrated [34]. The PPV derivative MDMO-PPV (poly[(2-methoxy-5-(3',7'-dimethyloctyloxy))-1,4-phenylenevinylene]) has been widely used in early OPV devices. A general drawback of this material class is, however, the incorporation of several defects such as cis-

---

[4] The *resonance energy* quantifies the stabilization of the aromatic ring structure due to electron delocalization with respect to the (hypothetical) structure, in which the electrons are localized to specific bonds.

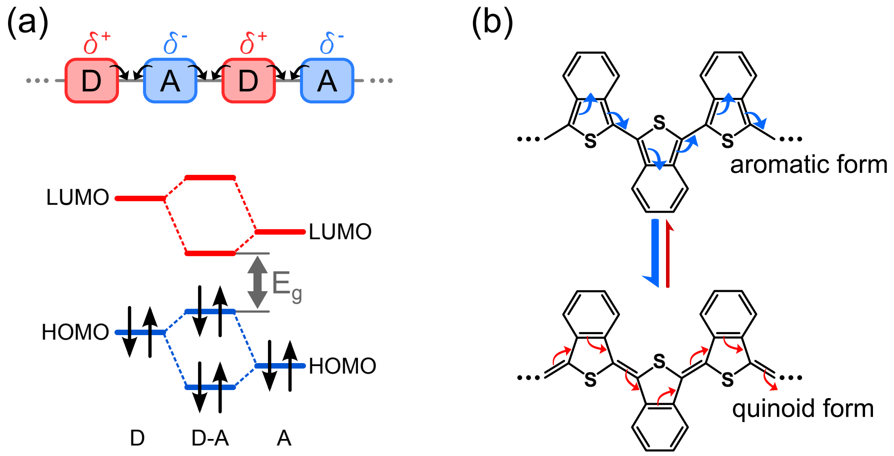

Figure 2.22.: Strategies to lower the band gap in conjugated polymers according to Ref. [108]. In the donor-acceptor approach, the 'push-pull-character' increases the double bond character between the donor and acceptor monomers (a). The 'quinoid' approach (b) exploits different resonance energies, e. g. of benzene and thiophene rings in poly(isothionaphthene), as presented here, to stabilize the quinoid structure. Blue (thick) arrows indicate transfer of the electron distribution to the preferred resonance structure.

linkages[5], loss of conjugation or the incorporation of oxygen leading to the formation of *keto-defects*. These defects act as traps, giving rise to non-radiative recombination [28].

Polythiophenes comprise a much higher chemical stability and represent an important material class for organic electronics. Here, the derivative P3HT (poly(3-hexylthiophene) is of particular relevance. Bulk heterojunction devices based on P3HT blended with the fullerene derivative $PC_{61}BM$ (see Ch. 2.6.5) were regarded as the benchmark system in OPV for many years [116]. Extensive research on P3HT and on BHJ devices based on it has resulted in a high number of publications over the last decade and has significantly contributed to the understanding of both the photophysics of the polymer [8, 75, 106, 117–120] and the morphological issues in bulk heterojunction devices [7, 9, 121, 122]. It turns out that a peculiarity of P3HT is its tendency to crystallize, which has a strong influence on the optical properties and is found to be beneficial for the performance of BHJ devices. This is because crystallization leads to a significant lowering of the optical gap and improves the transport properties. However, the optical band gap of rr-P3HT is still as high as 1.9 eV [75], which limits the achievable photoconversion efficiency and motivates the development of polymers with a more suitable lower band gap.

An optical gap similar to that of P3HT, but a lower HOMO energy was realized in the copolymer PCDTBT (poly[N-9-heptadecanyl-2,7-carbazole-alt-5,5-(4,7-di-2-thienyl-2,1,3-benzothiadiazole)]) [123]. Accordingly, higher open circuit voltage and photoconversion efficiency have been reported and, interestingly, an internal quantum efficiency close to 100 % has been demonstrated in the same study [124]. Further efforts have led

---

[5] *Cis*-configuration denotes one of two possible configurations of functional groups linked to a double bond. Cis-linkage of monomers in the backbone of a semiconducting polymer leads to 'kinks' in the backbone and thus give rise to structural distortions.

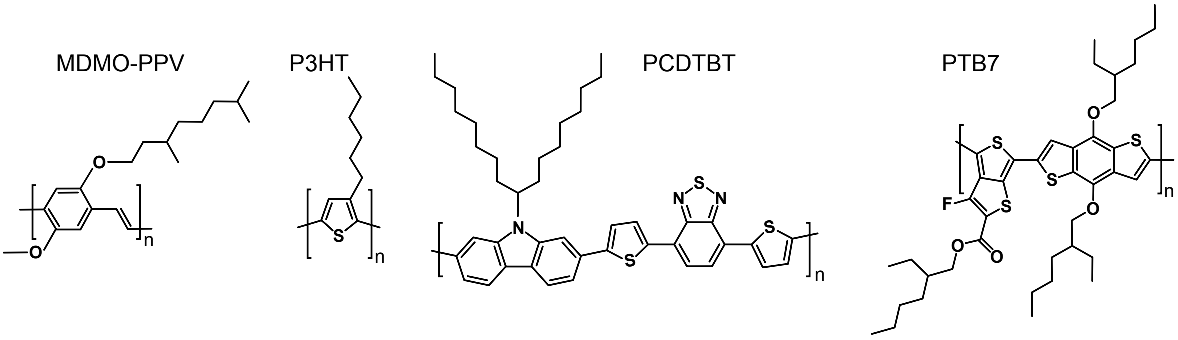

Figure 2.23.: Structural formulas of polymers used for OPV devices. P3HT and PTB7 were studied in the framework of this thesis.

Table 2.1.: Material parameters of selected conjugated polymers relevant for OPV applications. The PCE values denote typical efficiencies for the respective polymers measured in blends with PCBM.

Name	E_{HOMO}	E_{LUMO}	Optical gap	PCE
MDMO-PPV	−5.0 eV [129]	−2.8 eV [129]	2.1 eV [130]	3.1 % [131]
P3HT	−5.2 eV [118]	−3.5 eV [118]	1.9 eV [75]	3.0-4.0 % [116]
PCDTBT	−5.5 eV [123]	−3.6 eV [123]	1.9 eV [123]	6.0-6.1 % [124]
PTB7	−5.2 eV [125]	−3.3 eV [125]	1.6 eV [125]	7.4 % [125]; 9.2 % [1]

to a variety of copolymers with reduced band gaps, among them PTB7 [125, 126], which is of particular relevance for this work. PTB7 resulted from rational optimization of a series of polymers with backbones comprising alternating electron rich benzodithiophene (BDT) and electron deficient thienothiophene (TT) units. Furthermore, the TT blocks were found to stabilize the quinoidal structure [126], leading to a reduced band gap. Similar structures comprising the BDT building block have yielded comparable efficiencies in blends with PC$_{71}$BM, such as PBDTTPD [127] and PBDTTT [128].

2.6.5. Acceptor materials

Over the last years, many efforts have been made to optimize the polymeric donor component in organic bulk heterojunctions, but only little attention has been paid to the acceptor material. Fullerenes, such as C_{60} and C_{70} reveal a high electron affinity and good electron transport properties. These benefits for applications in OPV have already been recognized two decades ago with the discovery of ultrafast electron transfer from a semiconducting polymer to C_{60} [42]. Neat fullerenes are, however, not well-suited for solution-processed devices, according to their poor solubility in commonly used solvents. State-of-the-art acceptors in organic solar cells are thus fullerene derivatives, such as $PC_{61}BM$ or $PC_{71}BM$ (phenyl-C_{61}-butyric acid methyl ester or phenyl-C_{71}-butyric acid methyl ester), which comprise a much better solubility. Both materials also served as acceptor component for the bulk heterojunction devices studied in this work and their molecular structures are sketched in Fig. 2.24.

A major drawback of the fullerenes is their large band gap, which limits efficient harvesting of the solar spectrum. On the other hand, charge separation in polymer/fullerene systems is very efficient and internal quantum efficiencies near unity have been reported [86, 124]. It has been proposed that crystallization of the fullerenes is one of the key factors for efficient charge separation [132–134] and it is challenging to develop non-fullerene acceptor materials fulfilling these conditions. Potential alternative acceptor materials are for example n-type polymers, small molecules or inorganic materials [48]. In recent years, remarkable progress has been made in the development of acceptor materials based on small molecules. Their particular advantage with regard to the fullerenes is that their absorption coincides well with the solar spectrum and recently, a photoconversion efficiency of 11 % has been reported for a fullerene-free organic solar cell [3]. At present, many state-of-the-art polymers are optimized for bulk heterojunction devices with fullerene acceptors. However, appropriate selection of the donor polymer with respect to the non-fullerene acceptor material can lead to further improvement [135, 136].

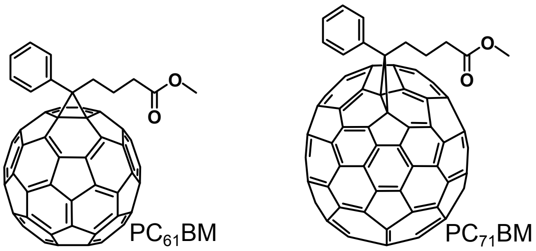

Figure 2.24.: Molecular structures of the fullerene derivatives $PC_{61}BM$ and $PC_{71}BM$, which have also been employed for the devices studied in this work.

Chapter 3

Experimental details

3.1. Linear absorption

Optical attenuation spectra are recorded with the experimental setup sketched in Fig. 3.1. A tungsten lamp driven at a DC bias of 15 V serves as white light source. The light is first guided through a pinhole in order to improve the quality of the intensity profile. Afterward, the light is focused on the sample, which is mounted in a Helium-flow cryostat[1] to protect the organic film from ambient oxygen. The residual pressure in the cryostat is typically $10^{-5} - 10^{-6}$ mbar. Moreover, an integrated heating element and liquid helium can be used to vary the sample temperature between 10 and 300 K. The light transmitted through the sample is recorded with an optical spectrum analyzer[2], comprising a maximum spectral resolution of 0.05 nm and covering a spectral range from 350 to 1750 nm. The spectral range in the experiments is however limited to the spectrum covered by the white light, thus, only wavelengths above ca. 400 nm are accessible.

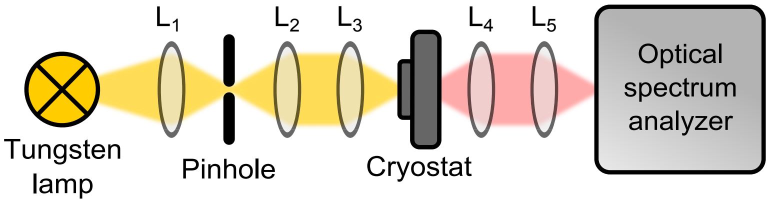

Figure 3.1.: Schematic of the experimental setup for absorption measurements. L_1-L_5 denote collimating and focusing lenses, respectively.

The intensity of the light transmitted through the sample can be quantified by Beer's law

$$\frac{I(z,\lambda)}{I_0(\lambda)} = \mathrm{e}^{-\alpha(\lambda)z}, \tag{3.1}$$

where I_0 denotes the intensity of the incident light and z is the thickness of the absorbing layer. The extinction coefficient $\alpha(\lambda)$ accounts for the attenuation of the light resulting from absorption, scattering and reflection. The absorption curves presented in

---

[1] "Microscopy cryostat", *Cryo Vac*

[2] Model AQ-6315A, *Ando/Yokogawa*

this work show the optical attenuation, which is calculated via subtracting the percentage of transmitted light from one. Each absorption curve requires three measurements: A transmission measurement of the respective material $I(\lambda)$, a reference measurement $I_0(\lambda)$, typically through the transparent glass substrate, and a measurement of the background noise $I_{BG}(\lambda)$, which is subtracted from $I(\lambda)$ and $I_0(\lambda)$. The fraction of absorbed light $I_{abs}(\lambda)$ is then given by

$$I_{abs}(\lambda) = \frac{I_0(\lambda) - I(\lambda)}{I_0(\lambda) - I_{BG}(\lambda)} \ . \tag{3.2}$$

3.2. Time-resolved photoluminescence

The main part of this work is based on time-resolved photoluminescence (TRPL) studies employing the streak camera technique, therefore the corresponding methodology will be introduced in greater detail in the following sections. The experimental setup is sketched in Fig. 3.2. For time-resolved measurements, a pulsed laser source is necessary, yielding pulses with a duration much shorter than the decay time of the signature to be measured. The laser used for TRPL studies is a titanium:sapphire (Ti:Sa) laser[3], which can be operated in the spectral range between 700 and 1000 nm. The gain medium is a sapphire crystal (Al_2O_3) doped with titanium ions, which is pumped by a frequency-doubled neodym-doped yttrium aluminium garnet (Nd:YAG)[4] laser at 532 nm with a maximum pump power of 11 W. In standard experiments the pump power is typically reduced to 9.5 W, to increase the lifetime of the pump source. For pulsed operation, the Ti:Sa laser is passively mode locked with the sapphire crystal acting as a non-linear Kerr medium. The Ti:Sa laser emits pulses with a duration of 100 fs and a repetition rate of 80 MHz, corresponding to a time delay of 12.5 ns between two laser pulses. The output power ranges between 2 W at an operation wavelength of 800 nm and 0.5 W at the edge zones of the tuning curve at 700 and 1000 nm, respectively. For excitation of the materials under study, the laser intensity is attenuated by the combination of a $\lambda/2$ wave plate and a polarizing beam splitter. When the wave plate is rotated, the laser polarization changes with respect to the polarization transmitted by the beam splitter. With this configuration, the excitation power can be varied over more than two orders of magnitude.

The range of accessible excitation wavelengths is extended by a so-called *tripler*[5], which enables second and third harmonic generation employing non-linear crystals. For the experiments carried out in the framework of this thesis, only the second harmonic generation (SHG) is relevant, which can be selected from the spectral range between 350 and 500 nm, according to the tuning range of the fundamental laser mode. Inside the tripler, the red laser light is focused onto a lithium triborate crystal, which can be rotated to establish phase match between the fundamental and the second harmonic laser pulse. The resulting second harmonic blue laser beam is then spectrally separated

---

[3] "Tsunami", *Spectra Physics*

[4] "Millenia", *Spectra Physics*

[5] "SuperTripler", *CSK Optronics*

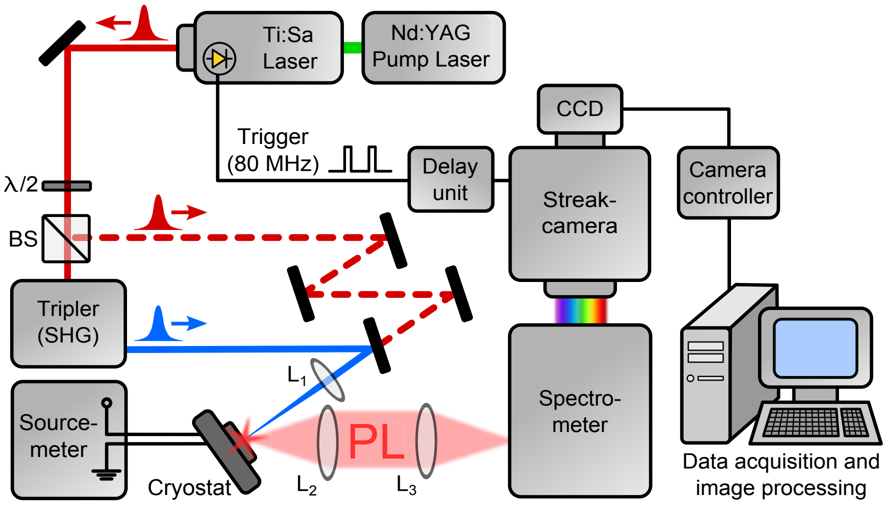

Figure 3.2.: Schematic of the experimental setup for time-resolved photoluminescence studies. The abbreviation $\lambda/2$ denotes a wave plate, BS is polarizing beam splitter and L_1-L_3 signify focusing and collimating lenses, respectively.

from the fundamental mode and yields an intensity up to 300 mW. The experimental setup is designed in a way that easily allows to switch between red and blue excitation, as indicated by the blue and the red dashed beam path in Fig. 3.2.

The laser beam is focused to the sample by the lens L_1, which has a focal length f of 15 cm. The diameter of the laser spot corresponding to the full width at half maximum value is approximately 30 µm. When the time-averaged laser power in front of the sample is measured with a standard optical power meter, the excitation fluence can be calculated. The procedure is described in the appendix (see section A). Typical values of the excitation fluence in the experiments presented in this work range between 0.1 and 0.5 $\mu\mathrm{Jcm}^{-2}$. The sample is mounted in a helium flow cryostat similar to that described in Ch. 3.1, yielding ultrahigh vacuum conditions and allowing for variation of the sample temperature in the range between 10 and 300 K. Additionally, the electronic feed-through of the cryostat comprising eight separate contacts can be used for field-dependent studies of the solar cell devices. Bias is supplied by a source measure unit[6], which can simultaneously measure the current. The details on field-induced luminescence quenching studies are given in Ch. 6. The photoluminescence emitted by the sample is collected by lens L_2 (f=10 cm) and focused to the vertical entrance slit of the spectrometer by lens L_3 (f=20 cm). The spectrometer[7] comprises various gratings, but for the measurements of the spectrally broad PL signatures presented in the following chapters, only the coarsest grating with a lattice parameter of 33 µm (300 lines/cm) was used.

After passing through the spectrometer, the spectrally resolved light is transmitted through the horizontal entrance slit of the streak camera[8]. The operation principle of the streak camera tube is illustrated in Fig. 3.3. First, the photons emerging from the

---

[6] Model 238, *Keithley*

[7] Model 25015, *Bruker*

[8] Model C5680, *Hamamatsu Photonics*, equipped with Synchroscan Unit M5675

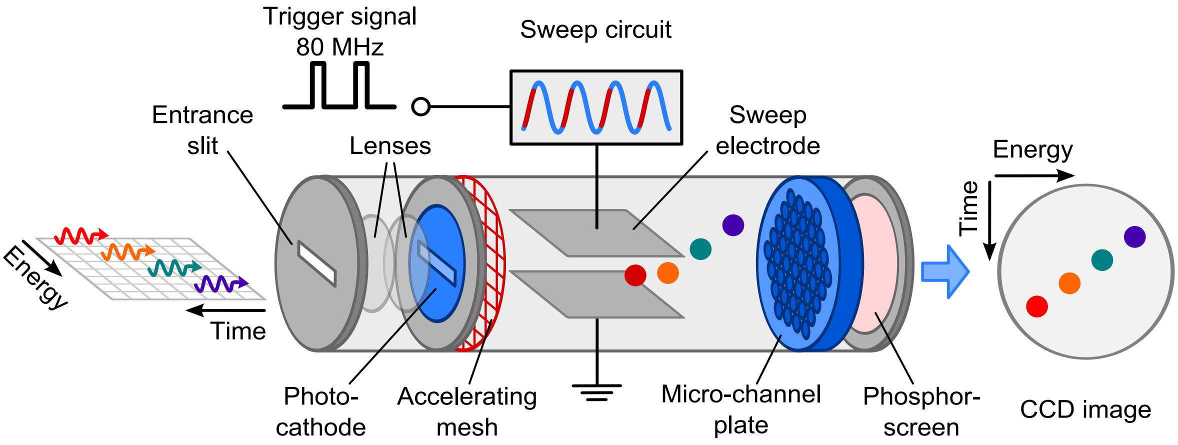

Figure 3.3.: Operation principle of the streak camera tube, after Refs. [137] and [138]

luminescence experiment impinge on a photosensitive cathode, where photoelectrons are created. These electrons are then accelerated following the direction of the streak tube, where they next pass an AC field between two capacitor plates, which is oriented perpendicular to the direction of their propagation. This procedure is essential for the time-resolved experiments, as it gives the electrons a vertical deflection, depending on the time of their transit. The field is modulated by a sine wave function, which is triggered to the 80 MHz repetition frequency of the Ti:Sa oscillator. The trigger signal is obtained from the internal photo diode of the laser. To generate the vertical deflection of the electrons in the streak tube, the linear edge of the sine wave is used as sketched in Fig. 3.3. The vertical deflection is thus proportional to the time delay of the photons entering the instrument. This operating principle of the streak camera is referred to as *synchroscan mode*, as the deflection voltage is synchronized to the repetition rate of the optical phenomenon to be measured. Depending on the purpose, the signal can be monitored over various time windows ranging between 150 ps and 2200 ps. The delay unit is used to adjust the delay between the trigger signal and the synchroscan bias manually, in order to adapt the studied time window to the measured signature. After passing the capacitor field, the electrons hit a micro channel plate, consisting of many small capillaries with diameters ranging between 10 and 20 µm. Each of these channels is coated with a secondary electron emitting material [137]. The micro channel plate serves to multiply the impinging electrons and the amplification increases exponentially with the applied bias. With the highest amplification (*gain*), an impinging electron can create up to 10^4 secondary electrons. These secondary electrons are then re-converted into light, when they bump against a phosphor screen, yielding an optical image, which is recorded by a high sensitivity CCD camera. Finally, the signal is read out by a computer via a frame grabber. Data acquisition is controlled by the software HPDTA (*High Precision Digital Temporal Analyzer*), provided by *Hamamatsu*.

The spectral and temporal resolution in the experiment mainly depends on the aperture sizes of the vertical entrance slit of the spectrometer and the horizontal entrance slit of the streak camera, respectively. Here, a compromise between incoming light intensity and achievable resolution has to be made. For small aperture sizes below 30 µm, the time resolution of the streak camera is about 2-3 ps, when the shortest time window of 150 ps is selected. This is a fundamental limitation of the streak camera arising from the accuracy of the electron beam, whereas the pulse duration of the excitation laser is much shorter. Further impairment of the time resolution may be given by the trigger frequency. The streak camera is configured for operation in the frequency range of 80±0.5 MHz, but the laser frequency should be excactly 80 MHz for optimum performance. For the experiments carried out in this work, an appropriate signal-to-noise ratio of the weak PL emission obtained from the solar cells could only be achieved with aperture sizes larger than 30 µm. Typically, the size of the entrance slits was set to 60 µm or even 100 µm in field-dependent experiments with short integration times. The corresponding time resolution was empirically determined from the rise time of the recorded PL signatures, yielding ca. 10 ps for the 800 ps time window and 35 ps for the 2200 ps time window. It is assumed that no delayed PL formation contributes to the rise time of the signal.

The maximum achievable spectral resolution of the setup is on the order of 0.1 nm [138]. With the coarsest grating, however, a very broad spectral range typically larger than 400 nm is displayed on the CCD chip and the resulting image is converted to a size of 512×512 pixel. This translates into a spectral accuracy of about 1 nm and an energetic resolution of 2 meV at a wavelength of 800 nm.

3.3. Analysis of streak camera images

In a first step, a background resulting from noise and ambient light is subtracted from the data. The background is recorded in a separate measurement under conditions similar to the PL measurement, but without PL signal. Afterward, the intensity profile of the streak camera image needs to be corrected by the spectral sensitivity of the setup, resulting from the spectral response of the cathode, but also from the input optics. The spectral sensitivity of the cathode is plotted in Fig. 3.4. Beyond 1000 nm, the sensitivity decreases by roughly one order of magnitude per 100 nm. The detection limit of the streak camera used for this work is around 1200-1300 nm. Beside the

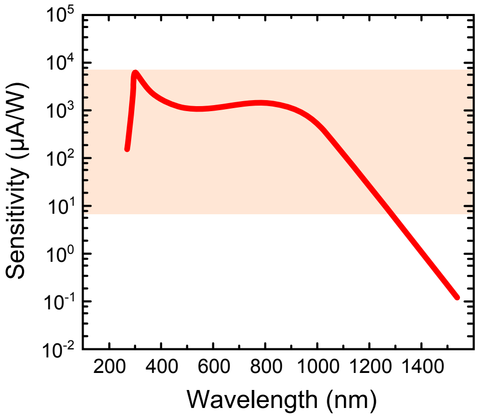

Figure 3.4.: Spectral sensitivity of the cathode employed in the streak camera, after Ref. [139]. The highlighted region corresponds to the dynamic range accessible in experiment.

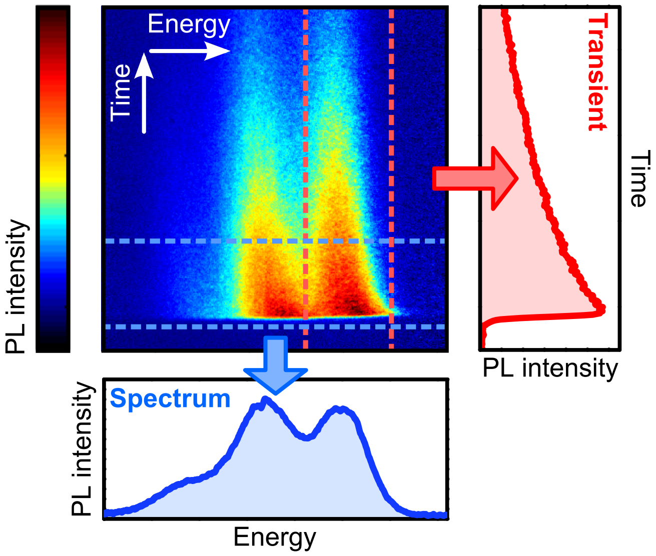

Figure 3.5.: Exemplary two-dimensional false color plot of the streak camera data set. From this data, spectra and transients can be extracted by integrating over a certain number of columns or rows, respectively.

spectral dependence, there is also a variation of the sensitivity in vertical direction, i.e. along the time axis of the recorded streak camera image, resulting from the deflection of the electron beam. The corresponding correction function in vertical direction depends on the time window chosen for the measurement. Furthermore, the micro channel plate, phosphor screen and CCD chip do not reveal a homogeneous sensitivity profile, mainly as a consequence of artifacts resulting from long-term use. For an accurate measurement of the PL intensity, all these influences need to be considered. Both background subtraction and the correction functions are implemented in a home-built *LabVIEW*-tool, allowing for fast processing of the binary data sets provided by the streak camera.

The spectral and time-resolved information in the streak camera data can be further evaluated by extracting PL-spectra and transients from the two-dimensional streak camera images. This is exemplified in Fig. 3.5. A spectrum describes the wavelength-dependent PL intensity and is obtained from summing over the rows contained in a certain time interval or over all rows of the data matrix. A transient on the other hand provides information about the time-dependent decay of the PL intensity. It is obtained from the data matrix via summation over the columns in a specific interval of wavelengths or over the whole spectral range covered by the measurement.

Depending on the purpose, the PL intensity can be plotted either as a function of wavelength or energy. The PL intensity measured by the CCD chip is proportional to the inverse of the wavelength. In order to show the PL intensity as a function of emission energy E, the energy axis is calculated from the wavelength λ via $\mathrm{E(eV)} = \frac{hc}{\lambda} = \frac{1240\,\mathrm{eVnm}^{-1}}{\lambda}$ and the PL intensity needs to be scaled by a factor proportional to λ^2.

Further methodological issues, such as extraction of PL decay times and peak energies from the data are addressed in the following chapters. It should be noted that for a precise determination of the decay constants a more sophisticated analysis becomes necessary, when the decay of the investigated signature is longer than the time window of 12.5 ns between two laser pulses. The presence of such accumulation effects can be identified by signatures emerging before the laser-induced rise of the PL intensity. The signatures investigated in this work decay on time scales below 2 ns, therefore no evidence for any longer-lived signatures was found. However, a very detailed and comprehensive description of this issue is given in Ref. [138].

An important experimental parameter that will be discussed in several contexts in the next chapters, is the *quenching* of the luminescence. For the organic solar cell materials studied in this work, quenching arises in particular from dissociation of the luminescent excitons, which is driven either by thermal energy, by an applied electric field, or it may occur spontaneously at a donor/acceptor interface. The quenching is quantified by comparing the PL emission in the absence of the quenching effect to the emission, where the quenching channel is present. TRPL studies allow for closer investigation how the quenching evolves in time. When the quenching builds up on a time scale shorter than the time resolution in the measurement, this will be referred to as *static* quenching in the following chapters. When on the other hand the quenching channel induces a faster measurable decay of the PL signature, this will be termed *dynamic* quenching. In the latter case, the PL decay time depends on both the intrinsic radiative lifetime τ_r and the decay time associated with the non-radiative channel τ_{nr}, i.e.

$$\frac{1}{\tau_{PL}} = \frac{1}{\tau_r} + \frac{1}{\tau_{nr}} \,. \tag{3.3}$$

3.4. Sample fabrication

This work focuses on two benchmark material systems: The first one is based on the polymer P3HT and the second one incorporates the copolymer PTB7. Both polymers were studied as pure compounds and blended with the fullerene derivatives $PC_{61}BM$ and $PC_{71}BM$. Devices of P3HT/$PC_{61}BM$ and PTB7/$PC_{71}BM$ were fabricated under inert atmosphere, as described in Refs. [13] and [14]. The major fabrication steps, device geometry and device parameters obtained from the current-density/voltage (JV) characteristics are briefly summarized below. In order to study the influence of the blend composition on the PL characteristics, the fullerene content in the active layers of the devices was varied. Additionally, reference samples comprised of a neat polymer or fullerene layer were processed in the same manner as the blend devices.

3.4.1. P3HT/PCBM

A scheme of the P3HT/PCBM solar cell devices studied in this work is presented in Fig. 3.6. Structured indium tin oxide (ITO) glass served as a substrate. Before processing, the substrate was cleaned in an ultrasonic bath and subsequently

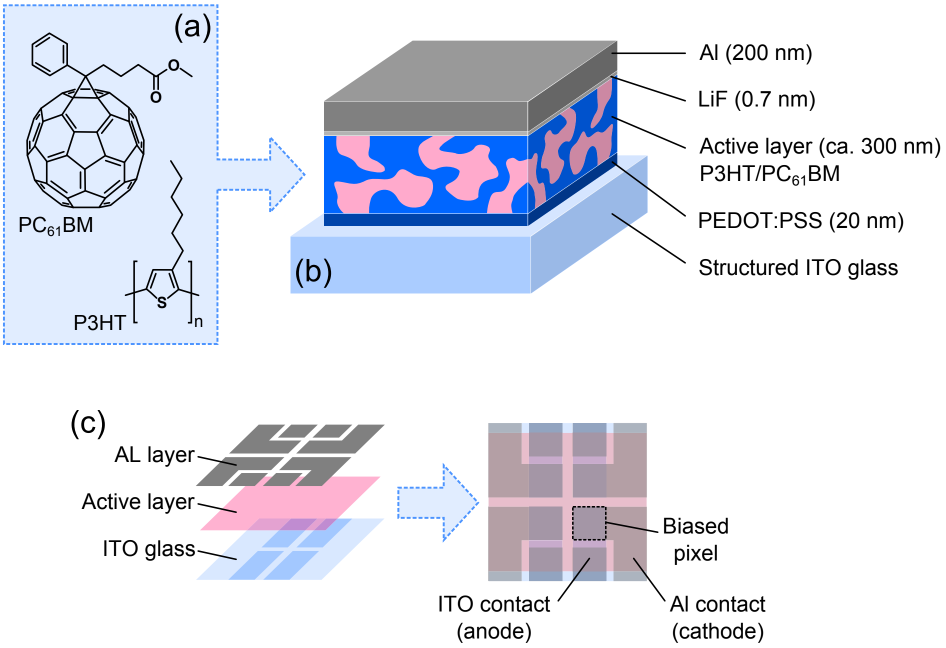

Figure 3.6.: (a) Structural formulas of the donor polymer P3HT and the electron-accepting fullerene-derivative PCBM; (b) scheme of the layer structure and (c) scheme of the electrode structures of ITO glass and the evaporated aluminum layer.

using oxygen plasma. Afterward, a 20 nm layer of poly(3,4-ethylenedioxythiophene)-poly(styrenesulfonate) (PEDOT:PSS) was spin cast to the substrate and annealed for 10 min at 130 °C, serving as hole-selective transporting layer. The components of the active layer were P3HT (poly(3-hexylthiophene)), purchased from Rieke Metals, and PC$_{61}$BM ([6,6]-phenyl-C$_{61}$-butyric acid methyl ester), purchased from Solenne BV. The structural formulas of P3HT and PC$_{61}$BM are summarized in Fig. 3.6(a). The active layer (ca. 300 nm) was deposited from dichlorobenzene solution at a rotation speed of 1000 rpm (for 40 s) and slowly dried under solvent atmosphere. This method is known as *solvent annealing* and has been found to be beneficial for the self-organization of the components in the condensed phase [140]. The active layer is followed by an evaporated 0.7 nm layer of lithium fluoride (LiF). Finally, a 200 nm structured layer of aluminum (Al) was evaporated, serving as the cathode, when the device is operated as a solar cell. A scheme of the layer structure is presented in Fig. 3.6(b).

Table 3.1.: Parameters for the P3HT/PCBM solar cells derived from JV curves in a solar simulator. V_{OC} denotes the open circuit voltage, J_{SC} is the current density at short circuit conditions, FF is the fill factor and PCE is the photoconversion efficiency.

Sample	V_{OC} (V)	J_{SC} (mA/cm^{-2})	FF (%)	PCE (%)
P3HT/PCBM [1:0.5]	0.54	5.09	41.3	1.14
P3HT/PCBM [1:0.9]	0.59	6.26	65.4	2.4
P3HT/PCBM [1:2]	0.65	2.06	27.2	0.36

According to the structural design of the Al and the ITO electrodes, the devices are subdivided into four pixels, each of them ca. 3x3 mm in size, which can be biased separately (see Fig. 3.6(c)). Representative JV-curves for the three blend devices with different contents of PCBM are shown in the appendix (see Fig. B.1). The measurements under illumination were performed in a solar simulator to determine the device efficiencies, which are summarized in Tab. 3.1 together with some other relevant parameters.

3.4.2. PTB7/PCBM

PTB7-based devices (Fig. 3.7) were fabricated in an inverted structure, where the electrons are collected at the ITO contact and holes migrate towards the aluminum contact. In such a device geometry, the efficiency of PTB7/PCBM could be improved by almost 1 % [1]. An electron-selective layer or zinc acetate dihydrate (ZAD) was deposited on the ITO-structured glass substrate and annealed at 200 °C for 40 min. Then, the bulk heterojunction layer comprising the polymer PTB7 (thieno-[3,4-b]thiophene-*alt*-benzodithiophene) and the fullerene-derivative $PC_{71}BM$ ([6,6]-phenyl-C_{71}-butyric acid methyl ester) was spin cast from chlorobenzene solution (ca. 75 nm). Additionally, the solution contained 4 % of the solvent additive diiodooctane (DIO). PTB7 was purchased from 1-Material Inc- and $PC_{71}BM$ was obtained from Solenne BV. Two blend films were fabricated with different fractions of PCBM: One film had a PCBM fraction of 75 % and the other film contained 60 % PCBM, the latter percentage corresponding to the reported optimized stochiometric ratio [125]. After deposition, the active layer was annealed for 10 min at 60 °C. Finally, the anode material was deposited, comprising a

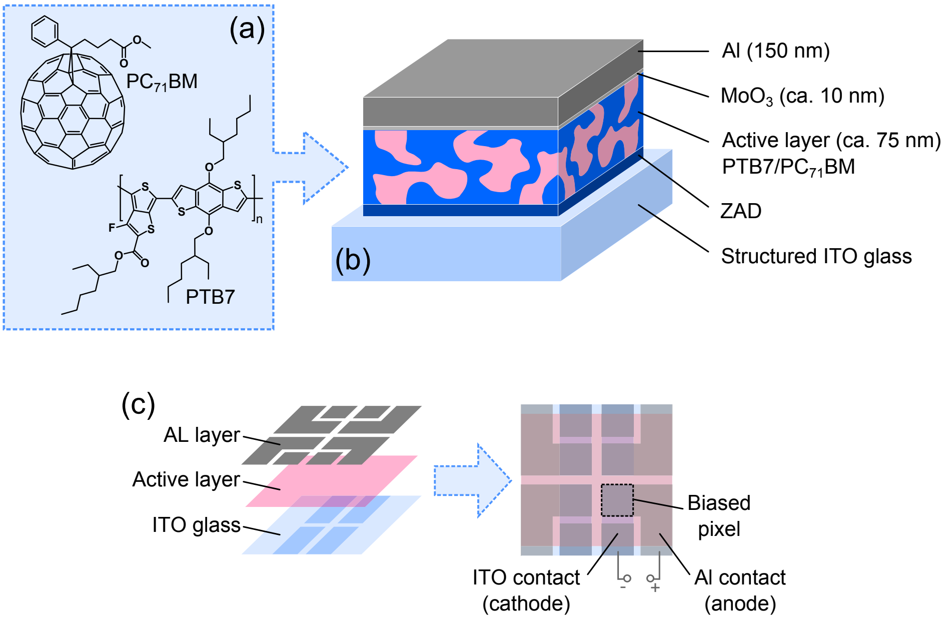

Figure 3.7.: (a) Molecular structures of the polymer PTB7, acting as electron donor, and the acceptor fullerene derivative $PC_{71}BM$. (b) Schematic of the deposited layers forming the inverted device, as described in the text. Panel (c) stekches the electrode structure and the positive and negative contacts signify a reverse bias, which was applied to the devices for field-dependent PL quenching studies.

thin (10 nm) layer of molybdenium oxide MoO_3 (electron blocking layer) and a 150 nm layer of aluminum. The electrode geometry was similar to that of P3HT/PCBM, but according to the inverted device geometry, the ITO-contact in the PTB7-based devices is the cathode and the Al contact represents the anode, when the device is operated as a solar cell (see Fig. 3.7(c)).

Efficiencies of the studied devices are listed in Tab. 3.2. For the field-dependent PL studies presented in Ch. 6, a second batch of devices with a PTB7/PCBM ratio of 1:1.5 was fabricated, yielding efficiencies higher than those of the first batch. The corresponding JV curves can be found in the appendix. For field-dependent PL studies, a reverse field was applied to the samples, as indicated by the contacts in Fig. 3.7(c).

Table 3.2.: Parameters derived from JV curves of the PTB7/PCBM devices. V_{OC} denotes the open circuit voltage, J_{SC} is the current density at short circuit conditions, FF is the fill factor and PCE is the photoconversion efficiency. The parameters of the sample highlighted with (*) was obtained for the second batch of samples fabricated for field-dependent PL quenching studies.

Sample	V_{OC} (V)	J_{SC} (mA/cm^{-2})	FF (%)	PCE (%)
PTB7/PC$_{71}$BM [1:1.5]	0.72	15.9	43.4	4.98
PTB7/PC$_{71}$BM [1:3]	0.71	14.9	37.1	3.95
PTB7/PC$_{71}$BM* [1:1.5]	0.73	15.7	68.5	7.50

Chapter 4

Exciton relaxation in conjugated polymers

Optical spectroscopy is a useful tool to study the exciton transport properties, that are of particular relevance for semiconducting polymers in OPV, where exciton diffusion towards a donor-acceptor interface should be efficient to avoid excitonic recombination. Furthermore, the spectral relaxation characteristics of the PL emission allows conclusions about the underlying density of states (DOS) to be made. The goal of this chapter is to characterize the luminescence of the neat polymers P3HT and PTB7, with a special focus on the complex PL decay characteristics. Both of these polymers are state-of-the-art materials for OPV devices. The temperature dependence and the dynamics of the polymer emission can be consistently explained with the picture of exciton relaxation in a disordered system as introduced in Ch. 2.4.2, however, in case of PTB7, the Stokes shift is found to be particularly strong, which is inconsistent with the expectations for a Gaussian DOS. This chapter is organized as follows: The results section comprises a detailed analysis of the time- and temperature-dependent Stokes shift of the polymers P3HT and PTB7. Both polymers are benchmark materials in OPV devices. Afterwards, the experimental findings are discussed in the context of recent studies on exciton relaxation in other polymer systems [4–6].

4.1. Luminescence decay in high-performance polymers for organic photovoltaics

The excitation wavelength in the experiments was set to similar values of 450 nm for P3HT and 460 nm for PTB7 (corresponding to energies of 2.70 and 2.76 eV). This implies that the excited states comprise some vibronic excess energy, which is, however, dissipated on a 100 fs time scale [21]. According to this fast thermalization, vibronic excess energy is not relevant for the phenomena described herein, because the best time resolution provided by the streak camera is about 3 ps, whereas the exciton lifetimes in the investigated polymers are much longer (on the order of 500 ps).

PL spectra of the polymers at a temperature of 10 K are plotted in Fig. 4.1, together with the respective absorption spectra at 10 K and at room temperature. The energetic offset $\Delta\epsilon$ between the absorption and emission of the 0-0 mode is referred to as Stokes shift (see Ch. 2.4). Both polymers exhibit a pronounced Stokes shift, which could in principle result from several phenomena: The altered electron configuration of the excited state could induce conformational changes, leading to a reduced emission energy with respect to the absorption. Another phenomenon of high relevance for disordered systems is migration of the excitons towards tail states in the DOS

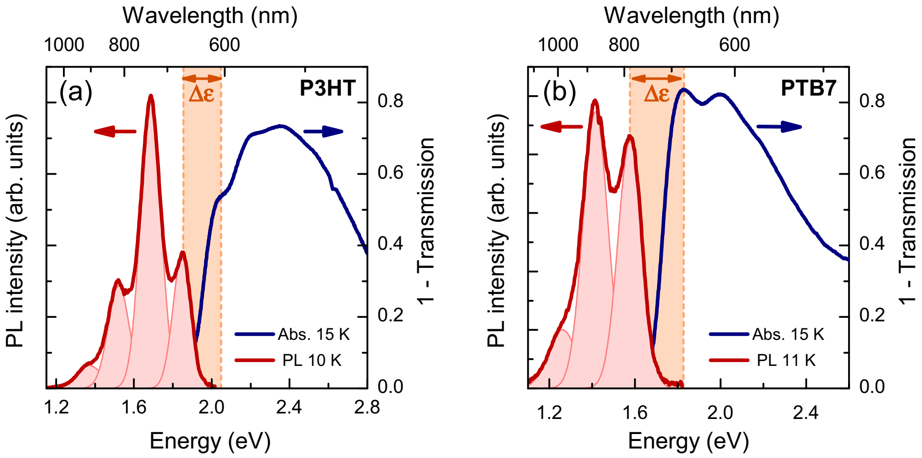

Figure 4.1.: Low-temperature absorption and emission spectra of P3HT (a) and PTB7 (b). The energy difference $\Delta\epsilon$, which is marked by the gray lines, indicates the Stokes shift. To extract the peak energies, a series of 4 (3) Gaussians was fit to the P3HT (PTB7) spectra.

and subsequent emission from those low-energetic sites. A particular advantage of time-resolved spectroscopy is that the temporal evolution of the Stokes shift can be monitored and compared to theoretical concepts, to gain insight into the underlying processes. A more detailed analysis of the PL dynamics and the temperature dependence of the emission, as performed herein, will substantiate that exciton relaxation towards tail states in a disordered system is the most probable cause for the observed complex time- and temperature-dependent PL characteristics.

4.1.1. Energy-dependent PL dynamics

When temperature is increased from 10 K to room temperature, the PL intensity does not change remarkably and also the decay characteristics of the integrated transients, as presented in Fig. 4.2, is only slightly altered. These findings imply that for both investigated polymers, thermal activation of non-radiative decay channels plays only a minor role. An important finding is, however, that at low temperatures, the transients in Fig. 4.2 exhibit more strongly pronounced non-exponential decay characteristics.

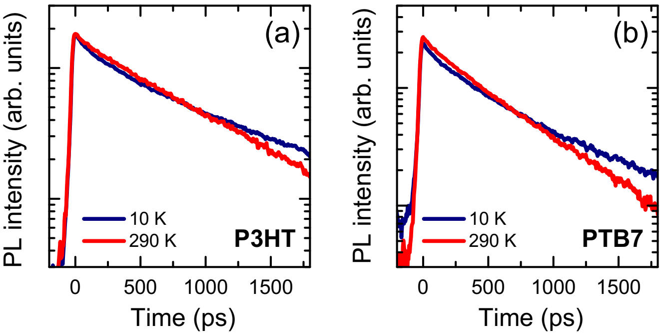

Figure 4.2.: Spectrally integrated transients of P3HT (a) and PTB7 (b) at room temperature and at 10 K.

This effect appears to be small regarding the spectrally integrated transients, but a closer look at the energy-resolved PL dynamics presented in the two-dimensional plots in Fig. 4.3 reveals substantial differences between the dynamics of the room temperature PL and the emission at 10 K. This is further detailed in Fig. 4.4, which shows transients extracted from different energy intervals of the 0-1 transition at 10 K. The corresponding $1/e$ decay times are presented in panels (c) and (d), together with the decay times extracted from measurements at 290 K. With increasing temperature, these dispersive decay characteristics become less pronounced. The findings for the low-temperature PL imply that the interplay between energetic downward hops and thermally activated upward hops in the DOS is important to understand the process of exciton diffusion in disordered polymer systems. Such dispersive PL decay in the low temperature regime is also known from disordered inorganic systems [141–143]. However, before discussing the phenomenon of spectral relaxation and in particular its temperature dependence in greater detail, it appears reasonable to exclude other influences on the PL dynamics, such as higher order non-radiative processes, which become important at high excitation fluence.

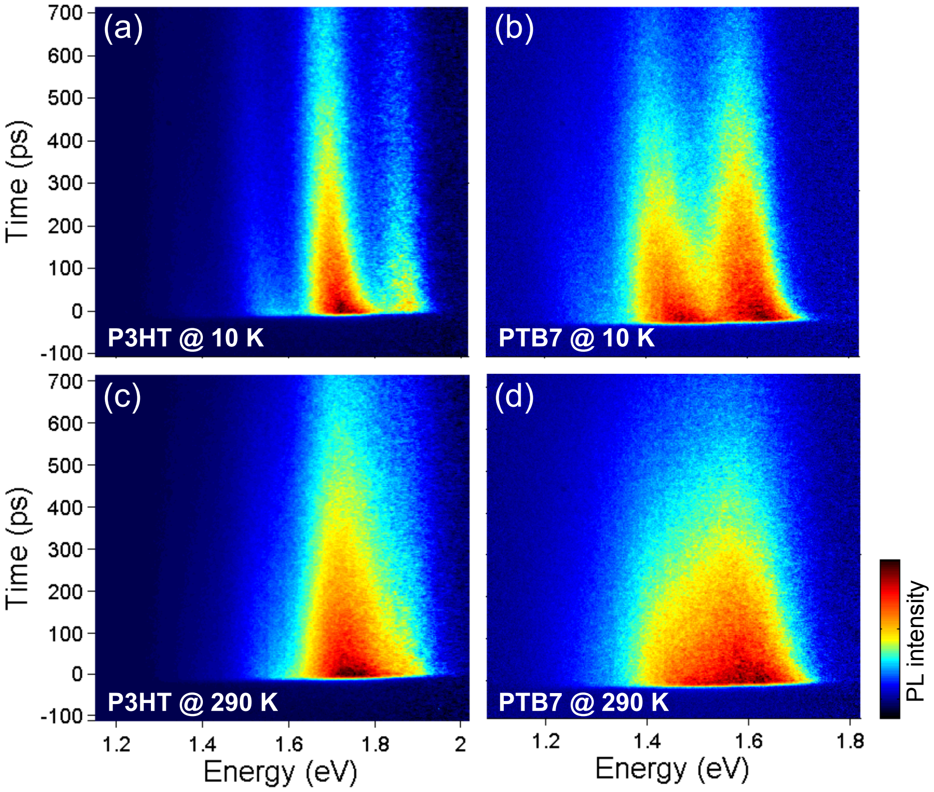

Figure 4.3.: Two-dimensional plots of TRPL data acquired for P3HT and PTB7 at 10 K and at room temperature.

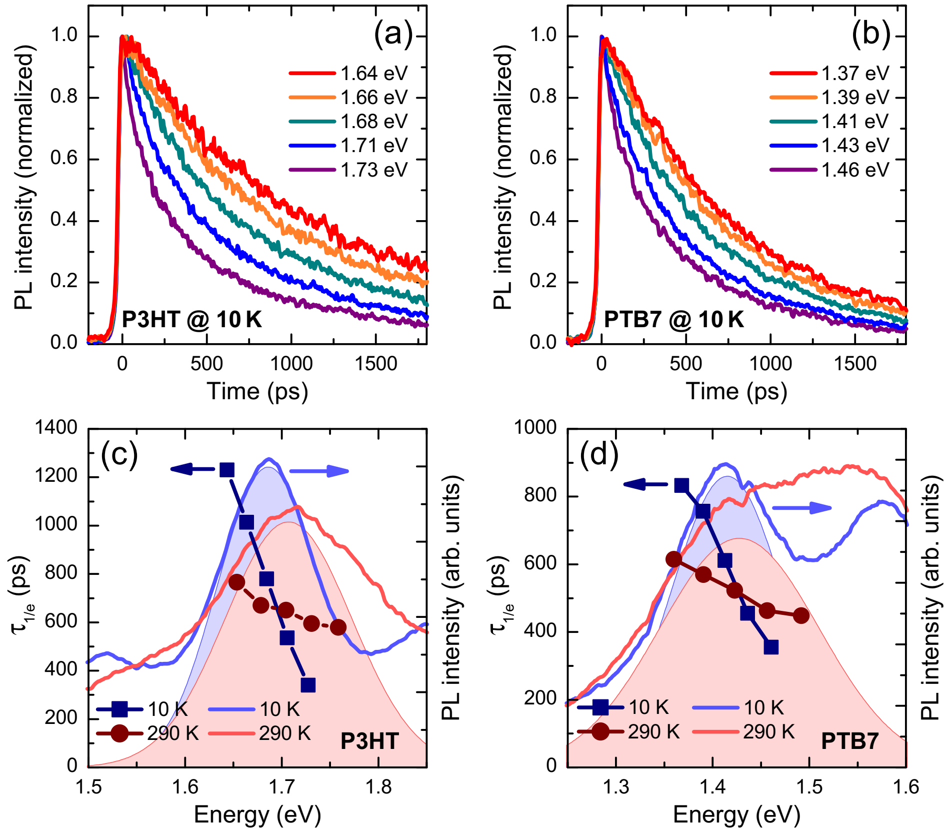

Figure 4.4.: PL transients for different emission energies. For closer analysis, transients were extracted from different energy intervals within the 2σ with of the 0-1 emission of P3HT (a) and PTB7 (b). The labeled energies correspond to the central wavelength of the selected energy intervals. Panels (c) and (d) show the $1/e$ decay times extracted from the transients at 10 K and at room temperature. As a guide to the eye, the PL spectra and the Gaussians obtained from the fit belonging to the 0-1 transition are shown as well.

4.1.2. Power-dependent measurements

Panels (a) and (b) in Fig. 4.5 show spectrally integrated PL transients for different excitation intensities at room temperature. Generally, the relation between the PL intensity I and the excitation intensity P can be expressed by a power law

$$I(P) = P^{\alpha} \ , \tag{4.1}$$

where the exponent α describes the functional interrelation. A value of $\alpha = 1$ signifies linear increase of the PL intensity with increasing excitation power, indicating that the contribution of non-radiative channels does not increase in the investigated range of excitation intensities. A sublinear increase of the PL intensity with increasing fluence ($\alpha < 1$) is expected, when the contribution of higher order non-radiative processes, such as exciton-exciton or exciton-charge annihilation or Auger processes become significant. Some systems also reveal $\alpha > 1$. This is for example observed for saturation of non-radiative decay centers or stimulated emission. As indicated by the dotted blue curves ($\alpha = 1$) in Fig. 4.5 (c), the correlation between P and I is linear up to a certain

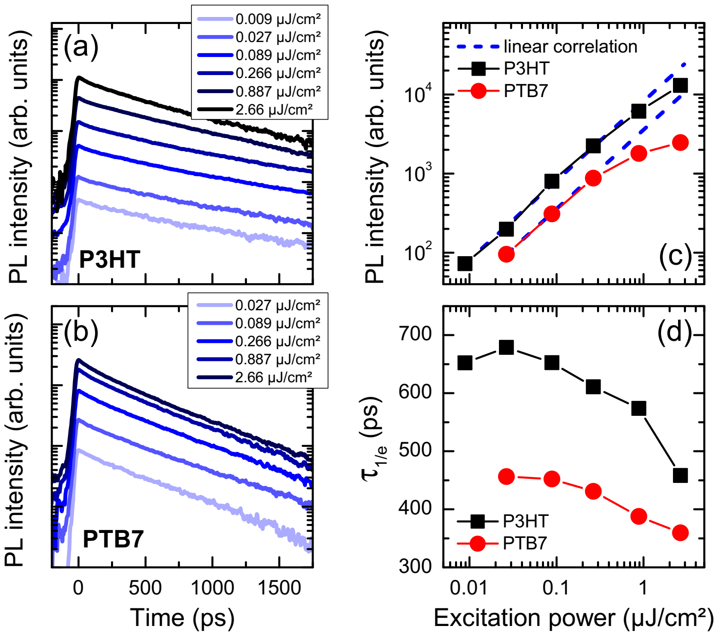

Figure 4.5.: Variation of the excitation power. Panels (a) and (b) show spectrally integrated transients of P3HT and PTB7 for different excitation fluences. Panels (c) and (d) show the integrated PL intensities and 1/e decay times extracted from those measurements. The dotted lines in panel (c) correspond to a linear correlation between excitation fluence and PL intensity.

threshold fluence for both investigated polymers. Deviations from $\alpha = 1$ beyond an excitation fluence of about $0.3\,\mu\text{Jcm}^{-2}$ could be due to enhanced non-radiative decay via exciton-exciton annihilation. It should be mentioned that long exposure to higher fluences beyond $1\,\mu\text{Jcm}^{-2}$ was also found to cause a non-reversible faster decay of the PL emission, which is related to the enhanced formation of defect states, giving rise to non-radiative decay. In the fluence-dependent measurements presented in Fig. 4.5, however, exposure times were kept short and after the highest excitation power, a control measurement was performed at lower fluence to verify the reversibility of the observed process. The raising impact of non-radiative decay channels is also reflected by the decrease of the overall PL lifetime with increasing excitation fluence, as presented in panel (d) of Fig. 4.5. To avoid higher order phenomena and degradation, an excitation fluence of $0.09\,\mu\text{Jcm}^{-2}$ was selected for both polymers studied herein.

4.1.3. Time-integrated PL spectra

Temperature-dependent integrated PL spectra of P3HT and PTB7 are presented in Fig. 4.7(a) and (b). At low temperatures, the PL of both polymers exhibits a pronounced fine structure, resulting from one or several [117] Franck Condon progressions. To quantify the temperature-induced energetic shift of the signatures and the temperature dependence of the disorder parameter σ, the data was fit by a series of Gaussians, as exemplarily shown in Fig. 4.1:

$$I(E) = \sum_{i=1}^{n} A_i \exp\left(\frac{(E - E_i)^2}{2\sigma_i^2}\right) \tag{4.2}$$

Here, E_i denotes the energetic position and σ_i is the disorder parameter, corresponding to the standard deviation. The whole set of parameters $E_i(T)$ and $\sigma_i(T)$, together with the integrated PL intensities, is summarized in the appendix (see Fig. B.3). Again, it should be emphasized that no remarkable change of the overall PL intensity is observed. The fits however document, that with increasing temperature, the PL features broaden significantly and the maxima of the spectra undergo a blue shift. In earlier work it has been argued that such behavior could be a consequence of the interplay between decreasing conjugation length due to thermally induced distortions, leading to a blue shift (see Ch. 2.4.1) and thermal expansion of the polymer matrix, inducing a red shift [117]. On the other hand, it has been demonstrated for several polymers that exciton diffusion in a Gaussian DOS, as introduced in Ch. 2.4.2, is the dominant process, leading to an overall blue shift of the CT emission with increasing temperature. In order to estimate the impact of 'static' effects such as thermal expansion or reduction of the chromophore sizes, temperature-dependent measurements of the optical absorption have been carried out for the studied polymers. The resulting spectra are presented in Fig. 4.6. In fact, there is a temperature-induced blue shift of the absorption signatures on the order of 30 meV for both polymers, indicating that the underlying conjugation lengths are affected by temperature. Thus, for an accurate description of the temperature-dependent Stokes shift, the temperature-dependent shift of the absorption maxima explicitly has to be taken into account.

For closer analysis, the 0-1 transition in the respective emission spectra was selected for several reasons: In both polymers, this peak was the one with the highest intensity and thus is expected to give the most accurate fitting results. Furthermore, the emission of the 0-0 transition might be affected by re-absorption according to the partly overlapping 0-0 absorption band [4]. The temperature-dependent disorder parameter $\sigma(T)$ obtained for the 0-1 band is plotted in panel (c) of Fig. 4.7. Generally, the disorder parameter of PTB7 is above that of P3HT, which can be attributed to the higher tendency of P3HT to crystallize, whereas the morphology of pristine PTB7 is amorphous to a higher degree, giving rise to a higher amount of structural and energetic disorder. The amorphous character of PTB7 has been confirmed in particular for blends with

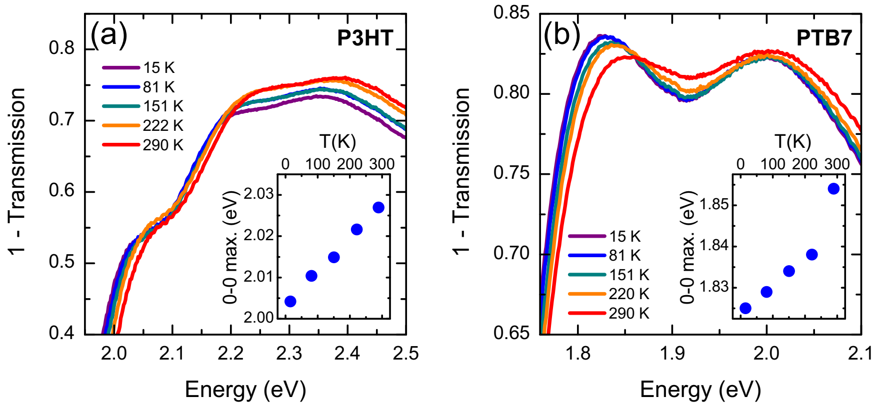

Figure 4.6.: Temperature-dependent absorption curves in the range of the 0-0 and 0-1 transition for P3HT (a) and PTB7 (b). Based on these spectra, the insets show the estimated peak energies of the 0-0 transition as a function of temperature.

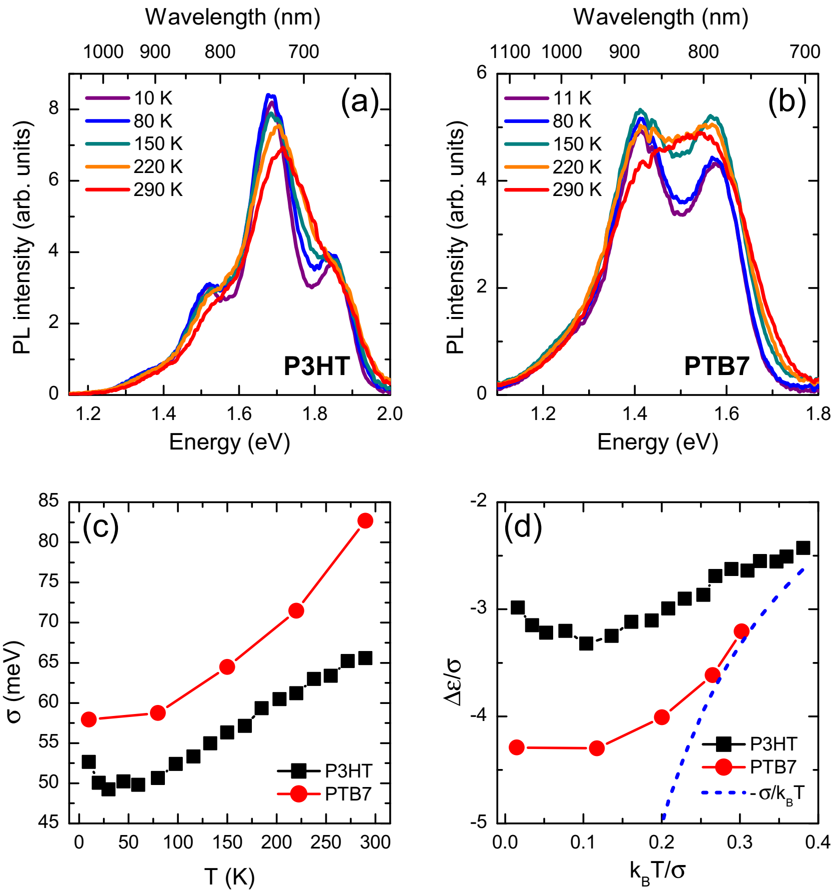

Figure 4.7.: Panels (a) and (b) show time-integrated PL spectra of P3HT and PTB7, recorded for different temperatures. The spectra of P3HT (PTB7) were fit by a series of 4 (3) Gaussians to extract the disorder parameter σ, which is plotted in (c) for the 0-1 transition. The disorder-normalized energetic shift with regard to the 0-0 absorption band $\Delta\epsilon$ is presented in (d), together with the slope of the equilibrium energy $\Delta\epsilon_\infty/\sigma = -\sigma/k_BT$ (blue dotted line).

PCBM [144]. The disorder parameter can be used to calculate the disorder-normalized energetic shift of the PL maximum $\Delta\epsilon/\sigma$. The parameter $\Delta\epsilon$ is the energetic offset between the absorption and emission energy of the 0-0 transition (see Fig. 4.1) and normalizing this quantity by $\sigma(T)$ allows for comparison of both polymers regarding the temperature-dependent Stokes shift $\Delta\epsilon$. Similar to the analysis performed in Ref. [4], $\Delta\epsilon$ was not directly determined from the energetic difference between the 0-0 absorption and emission. Again, the emissive 0-1 transition was used, because the emissive 0-0 transition could be affected by re-absorption. The Stokes shift $\Delta\epsilon$ is then given by the energetic difference between the 0-0 absorption and the 0-1 emission band, diminished by the energy of the dominating vibronic mode, which corresponds to the energy offset between the emissive 0-0 and 0-1 features.

The resulting values of $\Delta\epsilon/\sigma$ are presented in Fig. 4.7(d), together with the expected temperature-dependent slope of the thermal equilibrium energy ϵ_∞. It becomes evident that thermal equilibrium is only reached at room temperature, whereas with decreasing temperature most of the excitons recombine before reaching ϵ_∞, and, consequently, $\Delta\epsilon/\sigma$ saturates in the low temperature regime. The slight increase of $\Delta\epsilon/\sigma$ for P3HT at low temperatures could be due to a growing influence of frustration, i.e. localization of excitons. The Stokes shift of PTB7 on the other hand does not evidence any growing influence of frustration in the low temperature regime. Typical saturation values for $\Delta\epsilon/\sigma$ between 3 and 4 have been reported for several polymers [4]. The temperature-dependent slope of the disorder-normalized Stokes shift of P3HT and PTB7 is in good agreement with these results.

4.1.4. Characterization of spectral diffusion

PL spectra integrated over different time intervals after optical excitation are presented in Fig. 4.8(a) and (b). At low temperatures, the peaks of the vibronic progression exhibit a clearly visible red-shift with proceeding time after excitation. Fits using a series of Gaussians according to Eq. 4.2 were performed to characterize the time-dependent shift of the PL maxima. The energetic shift of the 0-1 band for P3HT and PTB7 is shown in Fig. 4.8(c) and (d), respectively. With the logarithmic time scale, the slope of the energetic shift is linear, indicating that $\Delta\epsilon(t) \propto \log \nu_0 t$ is fulfilled, as predicted for a Gaussian DOS. The dotted lines in Fig. 4.8 mark the $1/e$ decay times of the room temperature transients (Fig. 4.2). From this representation it becomes clear why the Stokes shift of the time-integrated PL spectra saturates in the low temperature regime (Fig. 4.7): For both P3HT and PTB7, spectral relaxation is not terminated at times when most of the excitons have already recombined. An exception is the emission of P3HT at room temperature, where the red-shift of the PL maximum saturates, suggesting that thermal equilibrium between upwards and downwards hops is reached at early times ($< \tau_{1/e}$). The experimentally observed saturation energy is about 10 meV above the saturation energy E_∞ predicted for a Gaussian DOS. The saturation energy of the 0-1 emission can be calculated by subtracting the equilibrium energy $\epsilon_\infty = -\sigma^2(T)/k_B T$ and the energy of the dominating phonon mode from the energy of the 0-0 absorption signature. The resulting values of E_∞ are indicated as dark red dotted lines in Fig. 4.8(c) and (d). The discrepancy between the saturation energy of the P3HT signature at room temperature and the calculated value of E_∞ could arise from the fact that even at room temperature, thermal equilibrium is not entirely reached. Furthermore, local heating of the excitation laser could play a role. Additionally, certain inaccuracies may arise simply due to the fact that E_∞ is determined from three independent experimental parameters: The 0-0 absorption maximum, the phonon energy corresponding to the energetic difference between the emissive 0-0 and 0-1 transition and the equilibrium energy ϵ_∞, which incorporates the disorder parameter $\sigma(T)$.

From the time- and temperature dependent PL spectra it can be concluded that spectral relaxation of excitons in P3HT is consistent with the expectations for a Gaussian DOS [4, 6]. For PTB7, however, certain peculiarities arise, which should be discussed in greater detail. In contrast to P3HT, spectral relaxation in PTB7 is not terminated at an equilibrium energy, but continues following a $\propto \log \nu_0 t$ slope without showing any tendency to saturate for all investigated temperatures and over the whole studied time window. In a similar way as for P3HT, the saturation energy E_∞ at room temperature was calculated from the absorption and emission spectra and is highlighted in Fig. 4.8(d). From this it becomes evident that the Stokes shift in PTB7 is much stronger than expected from the concept of quasi-equilibrium in a Gaussian DOS. Here, a particular advantage of TRPL with respect to steady state measurements of the luminescence is, that the actual time-dependent slope of the Stokes shift can be directly investigated, in particular at longer time delays after excitation, where the remaining PL intensity is weak and superimposed by earlier emission in steady state experiments. Thus, time-resolved studies provide valuable information about the actual relaxation characteristics.

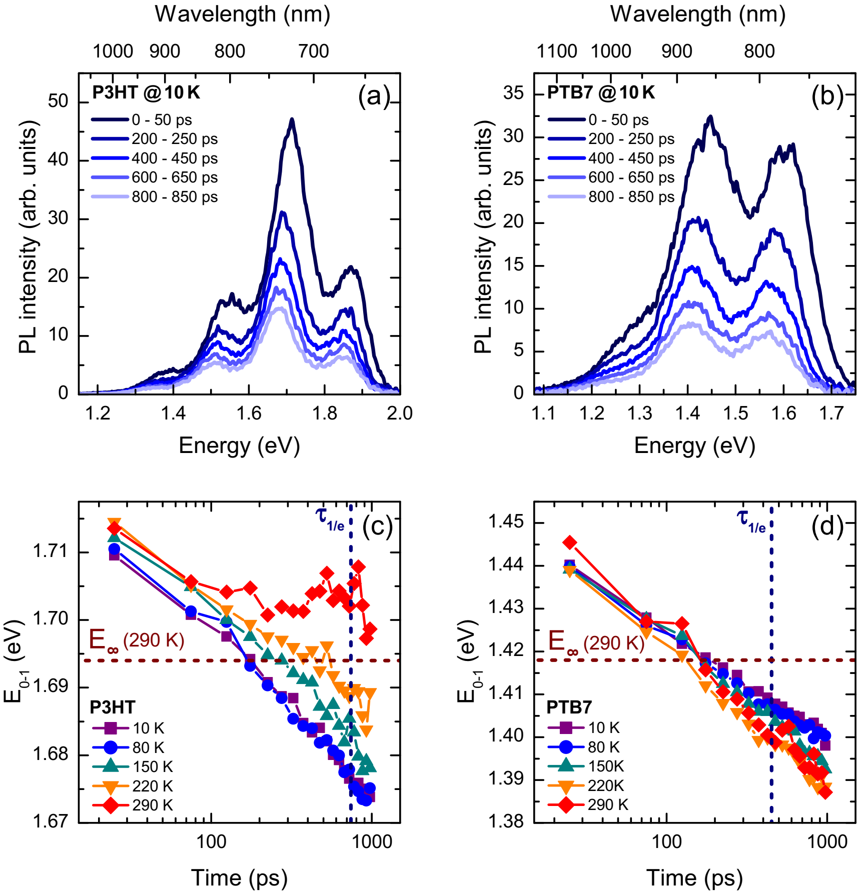

Figure 4.8.: Time-dependent PL spectra of P3HT (panel (a)) and PTB7 (panel (b)). To extract the spectra from the two-dimensional data sets, the spectra were integrated over several time intervals as labeled. The resulting spectra were fit by a series of Gaussians. The time-dependent shift of the emissive 0-1 transition, characterized by E_{0-1}, is plotted in panels (c) and (d). The dotted red lines correspond to the expected saturation of the time-dependent red-shift at room temperature, assuming a Gaussian DOS. The dotted blue lines signify the $1/e$-decay times, where the excitonic population has decreased to a fraction of $1/e$ with respect to the initial amount.

4.2. Discussion

Up to now, the precise origin of the strong Stokes shift in PTB7 is not clear. However, the observations provoke the question if the underlying DOS in polymer systems is mandatorily Gaussian. Although the Gaussian DOS appears to describe the PL and also the electronic properties in many systems correctly, it is hard to access the actual profile of the DOS directly in experiments. For example, it has been argued that the oscillator strength in absorption measurements is not necessarily equal for all probed energies [145]. Thus, the spectroscopically obtained signatures do not imply the same shape for the DOS. The hypothesis of a DOS, which is more heavily tailed towards lower energies has also recently been investigated in systems with molecular aggregates [146]. In this study, efficient exciton transfer towards low-energy sites, so-called Lévy-states, has been evidenced by means of single molecule spectroscopy. Furthermore, a commonly made assumption for disordered organic systems is that the site positions and their respective energies are uncorrelated [78]. This is however not entirely true, because in conjugated systems the energies of neighboring sites are correlated due to polarization effects [28] and the energy of the $\pi - \pi^*$ transition depends on the spatial extension of the chromophore. This could have further implications for the characteristics of spectral relaxation. Another well studied example for a distribution with a more heavily weighted portion of tail states compared to a Gaussian profile is the exponential DOS, which is of particular relevance for inorganic systems [141, 142, 147, 148]. For model systems with an exponential distribution of tail states it turns out that an equilibrium situation, where the rate of exothermic downward hops equals the amount of thermally activated hops does not exist [145]. This is in stark contrast to the theoretical predictions for a Gaussian DOS. Excitons within an exponential DOS undergo continuous relaxation until they recombine, resulting in a continuous red-shift of the PL emission, following a $|E(0) - E(t)| \propto k_B T \log \nu_0 t$ law [145, 147]. Hence, in contrast to the Gaussian DOS, the slope of the spectral shift is predicted to be temperature-dependent for the case of an exponential DOS. In fact, such behavior is observed here for the spectral shift of PTB7 (Fig. 4.8(d)), where the spectral shift gets faster with increasing temperature. However, this dependence is weaker than expected for an exponential tail and could also originate from other phenomena. For example, the Förster transfer rate in conjugated polymers can have a significant temperature dependence due to inhomogeneous broadening and thus better spectral overlap of the single chromophore absorption and emission bands with increasing temperature [149].

4.3. Summary

This chapter has provided insight into the fundamental photophysics of two state-of-the-art-polymers for OPV applications, P3HT and PTB7, respectively. The luminescence in both polymers exhibits a pronounced Stokes shift. Detailed analysis of the temperature- and time-dependent Stokes shift has shown that the experimental observations are consistent with the phenomenon of spectral relaxation, i.e. incoherent and exothermic hopping processes of excitons within a manifold of sites being subject to spatial and energetic disorder. For both polymers, the Stokes shift increases with decreasing temperature but saturates in the low-temperature regime. These characteristics corroborate recent findings for other polymers [4, 6] and can be attributed to the interplay between relaxation and thermally activated upward hops. In a Gaussian DOS, this interplay eventually leads to an equilibrium situation, where the upward and downward hopping rates are equal. As a consequence, the Stokes shift saturates at a specific energy. This equilibrium energy decreases with decreasing temperature. For $T \rightarrow 0\,\mathrm{K}$, most of the excitons recombine before they have relaxed towards the equilibrium energy, leading to the observed saturation of the Stokes shift.

For P3HT it has been demonstrated that the relaxation process reaches equilibrium conditions only at room temperature. With decreasing temperature, excitons recombine before reaching thermal equilibrium and in the low-temperature regime, the blue shift of the disorder-normalized Stokes shift indicates the growing influence of exciton localization. For the excitons PTB7 on the other hand neither frustration of the relaxation process, nor the presence of an equilibrium situation could be evidenced. Instead, spectral relaxation of the PL emission was found to proceed trough the whole analyzed time window. A potential reason for this observation could be the DOS itself, which could comprise more tail states in PTB7 and thus decay less abruptly than a Gaussian DOS. As a consequence, there is always a higher probability for the excitons to perform hops towards sites with lower energies and thermal equilibrium is never reached.

Chapter 5

Intermixing effects in polymer/fullerene systems

In state-of-the-art OPV devices, polymer and fullerene molecules are intimately mixed, forming a bulk heterojunction [44] as active layer. The general concept of such a device can be easily explained (see Ch. 2.6.1), but profound guidelines for the rational design of novel polymer/fullerene systems have not yet been developed. Due to its complexity, this topic is subject of ongoing research. One challenge is to optimize the donor and acceptor energy levels with respect to each other, i.e. to minimize the amount of excitation energy, which is dissipated in the system due to the energy level offset. On the other hand, a certain offset energy is required to avoid backward charge transfer [27, 104]. Beside energetic considerations, the nanomorphology of the devices is decisive for their performance. As charge generation is assumed to occur via CT states at the donor/acceptor interfaces, the CT rate can in principle be increased by reducing the size of the donor and acceptor nanodomains. This leads to an increase of the interfacial area and better harvesting of singlet excitons. However, when the nanodomains are too small, this limits the transport of charges to the device electrodes. For optimized PTB7/PCBM devices it has been found that the domain sizes are on the order of the exciton diffusion length [12]. Furthermore, a general problem regarding device optimization arises from the fact that the actual process of exciton separation at the interface is not yet fully understood. Ultrafast separation mechanisms via energetically excited CT states [84, 119, 120, 150–154] or due to delocalization effects resulting from the formation of aggregates [84, 85, 132, 134, 155] concur with the idea of efficient charge separation through energetically relaxed and weakly bound CT states [16, 86, 87, 97, 156]. The suggested mechanisms are not mutually exclusive, however, each of them implies different guidelines for the design of a BHJ in terms of nanomorphology and energy level alignment.

A general discussion of recent studies focusing on the problem of exciton dissociation at the donor/acceptor interface (which is not a problem at all in efficient OPV devices) will be given in Ch. 6.2, in the context of the experimental results on field dependent luminescence quenching studies. First, however, it is important to understand the interrelation between the morphology of polymer/fullerene blends and the resulting optical properties. Therefore, the relevant luminescence signatures arising from intermixing need to be identified. For efficient OPV devices, it can be expected that the emission of singlet states in the neat components is significantly quenched due to interfacial CT reactions in the blend material. Furthermore, recombination may arise from the interface itself, giving rise to the PL signature from an interfacial CT state. This feature is expected to be energetically below the emission of singlet states and its dynamics reveal valuable information about the dissociation and recombination processes at the donor/acceptor interface.

This chapter will first provide a general overview of the intermixing effects in the polymer/fullerene systems P3HT/PC$_{61}$BM and PTB7/PC$_{71}$BM. Each material system has been implemented in devices with varying blend composition and was studied under various excitation conditions, allowing for identification of singlet and CT states. In the second section, the quenching of singlet states with varying donor/acceptor ratio and sample temperature is investigated in greater detail. The third part focuses on the thermal quenching of the CT emission. The subsequent discussion aims at relating the spectroscopic results to reports on the morphology of the respective material systems. It turns out that a consistent interpretation of the results in terms of the underlying morphology is possible. In this context, an important result is that a higher portion of emissive CT states is formed when the donor and acceptor phases are intimately mixed. Parts of the results presented in this chapter have been published in Refs. [13] and [14].

5.1. Sample morphology and optoelectronic properties

In the framework of this thesis, no detailed studies of the blend morphology have been carried out. The spectroscopically investigated material systems P3HT/PC$_{61}$BM and PTB7/PC$_{71}$BM are however prominent model systems in OPV research and thus, the blend morphology and implications for the device performance have been intensely investigated by others [7–12]. It turns out that the fabrication methods are decisive for the device performance and the processing steps depend strongly on the material system. The devices studied in this work were processed under conditions similar to previous reports but with varying acceptor concentration. The fabrication procedure and the sample geometries for both investigated material systems are described in greater detail in the appendix (section 3.4). To provide a general overview over the investigated materials, it appears instructive at this point to summarize briefly their basic photophysical and electronic properties and discuss them in the context of recent literature on the material morphology. This is extremely relevant to understand subsequent TRPL measurements.

Absorption spectra of the investigated polymer/fullerene systems with varying blend composition are presented in Fig. 5.1. The absorption features of the P3HT blends in Fig. 5.1(a) are attributed to the polymer component, whereas the PC$_{61}$BM absorption signatures are mainly located in the UV. With increasing fullerene fraction, the shape of the P3HT absorption signatures changes. Importantly, the low-energetic shoulder at 600 nm is remarkably reduced, when the fullerene content is increased to 66 %. This feature has been attributed to an interchain transition in highly-ordered π-stacked polymer chains [117]. The decrease in intensity with increased PCBM content thus indicates that the amount of P3HT crystallites is remarkably reduced in the blend with 66 % PC$_{61}$BM. This observation is consistent with previous work, in which the

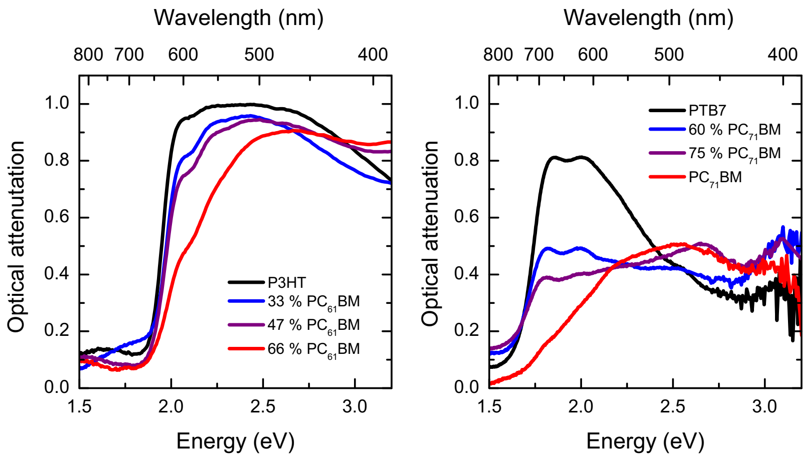

Figure 5.1.: Absorption spectra of the neat polymers P3HT (a) and PTB7 (b) and of blend films with different portions of PCBM.

structural and optical properties have been correlated with each other [7, 10]. For the P3HT/PCBM system it has been found that thermal annealing enhances the device performance [7, 10, 121, 140, 157, 158], but it is significantly reduced when the PCBM content is increased beyond ca. 60 % [10, 157]. This can be understood by taking into account the impact of the nanomorphology. In this context, Collins et al. [9] have reported that the morphology of P3HT/PCBM bulk heterojunctions is composed of three phases: A pure and crystalline polymer phase, a pure fullerene phase and an amorphous polymer-rich phase, which is intermixed with fullerene molecules. This is in agreement with previous suggestions by Erb et al. [7]. The effect of increasing the PCBM content and connected with this the enhanced formation of amorphous and intermixed polymer phases in P3HT/PCBM is illustrated in Fig. 5.2(a).

For the P3HT-based devices investigated in this work, substantial changes of the morphology in the sample with excess PCBM are further indicated by the JV curves (see Appendix B). The drift current of the device with a PCBM content of 66 % is found to be relatively low and, moreover, depends on the applied voltage. In agreement with the optical investigations and literature reports on different stochiometric P3HT/PCBM ratios, the investigated device with a medium PCBM fraction of 47 % reveals the highest efficiency of 2.4 %, whereas increasing the fullerene content to 66 % leads to remarkably reduced PCE of 0.36 %. This discrepancy cannot solely be explained by the reduced absorption of the polymer. Thus, the presence of an extended amorphous phase comprising poor transport properties appears to be a plausible assumption. The relevant parameters for the OPV performance of the studied P3HT/PCBM devices devices are summarized in Ch. 3.4.1.

For the polymer PTB7, it has been demonstrated that the tendency to crystallize in blends with PCBM is much less pronounced than for P3HT, suggesting that crystallization of the polymer is not the key factor for high performance of a BHJ device [11]. Another important aspect for fabrication of efficient OPV devices is however the use of solvent additives during the spin coating process [125, 159–162]. For PTB7/PCBM [11, 12, 125], and also for blends based on a very similar polymer PBDTTT-C [163],

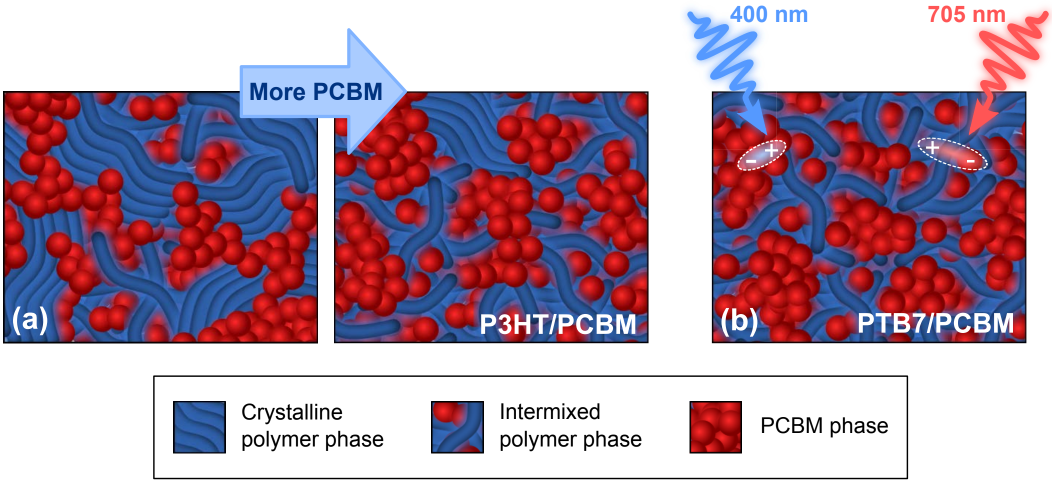

Figure 5.2.: Schemes of the blend morphology of (a) P3HT/PCBM and (b) PTB7/PCBM. In P3HT/PCBM, increasing the fullerene content reduces the formation of P3HT crystallites. In PTB7/PCBM, the polymer is to a large extent in an intermixed phase with PCBM, which coexists with clusters of pure fullerene [11, 12]. A laser wavelength of 400 nm preferentially creates excitations in the fullerene phase, whereas an excitation wavelength of 705 nm allows for selective excitation of the intermixed polymer phase.

the usage of the PCBM-selective solvent diiodooctane (DIO) has proven successful. Employing X-ray scattering experiments, Collins et al. [11] found that usage of DIO in the fabrication process drastically reduces the domain sizes, leading to an improved nanomorphology. This is consistent with complementary work of Hedley et al. [12], who investigated the morphology of PTB7/PCBM combining TRPL with photoconductive atomic force microscopy. Both studies evidence a two-phase morphology of PTB7/PCBM: Amorphous and polymer-rich intermixed phases alternate with pure PCBM domains on a 10 nm scale. However, when the blend is processed without DIO, large PCBM agglomerates are formed and exciton dissociation becomes inefficient [11, 12]. The PTB7-based devices produced for studies of the intermixing effects were processed with DIO, as described in Ch. 3.4.2, giving reasonable performances of 4.98 % (60 % PCBM) and 3.95 % (75 % PCBM). The corresponding JV curves are shown in the Appendix B.

The range of excitation wavelengths accessible in TRPL experiments allows to make use of the spectrally separated absorption signatures of PTB7 and PCBM. According to the absorption spectra presented in Fig. 5.1, a wavelength of 705 nm can be used to selectively probe the polymer phase, because the absorption of PCBM in this range of wavelengths is negligible. On the other hand, an excitation wavelength of 400 nm leads to preferential excitation of the PCBM domains. Both excitation scenarios are illustrated in Fig. 5.2(b).

5.2. Composition dependence of excitonic signatures

5.2.1. Time-resolved photoluminescence of P3HT/PC$_{61}$BM

Two-dimensional plots of the TRPL data recorded from the P3HT/PCBM devices at a temperature of 290 K are presented in Fig. 5.3. Additionally, data of devices comprising neat films of P3HT and PC$_{61}$BM is shown. The excitation wavelength in all measurements shown throughout this section was set to 440 nm and the excitation power was 5 mW, translating into an excitation fluence of 2.7 µJcm^{-2}. The overview illustrates that blending of P3HT with PCBM drastically changes the PL properties. As further evidenced in the plots of the time-dependent spectra in Fig. 5.4 (upper row), the emission in the blends is dominated by P3HT, but the decay time of the PL is significantly reduced with regard to the neat P3HT device. This can be attributed to the quenching of excitons at the donor/acceptor interfaces, which represent an additional non-radiative decay channel in the blend. On the other hand, no contribution of PCBM to the PL emission can be observed in the blends, not even in the sample with excess fullerene. However, beside the signature of P3HT, a weaker, but longer-lived feature peaking around 1.34 eV is present in the TRPL data of the [1:0.9] and the [1:2] device, leading to longer decay times of the PL emission in the spectral range beyond 800 nm. The fact that this feature is not present in the neat films suggests that it arises from recombination of charge transfer (CT) states at the donor/acceptor

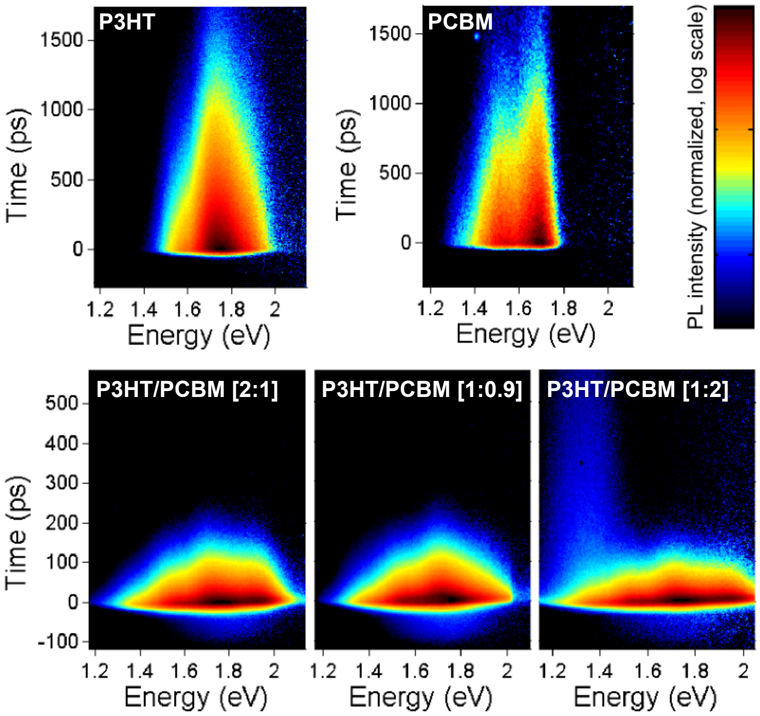

Figure 5.3.: Two-dimensional plots of the TRPL data recorded for neat P3HT and PCBM (upper row) and the blend devices with different polymer/fullerene mixing ratios as labeled (lower row). All measurements were carried out at room temperature. The PL intensity is normalized and a logarithmic scale is chosen (see colored bar), allowing for identification of the long-lived and faint CT emission.

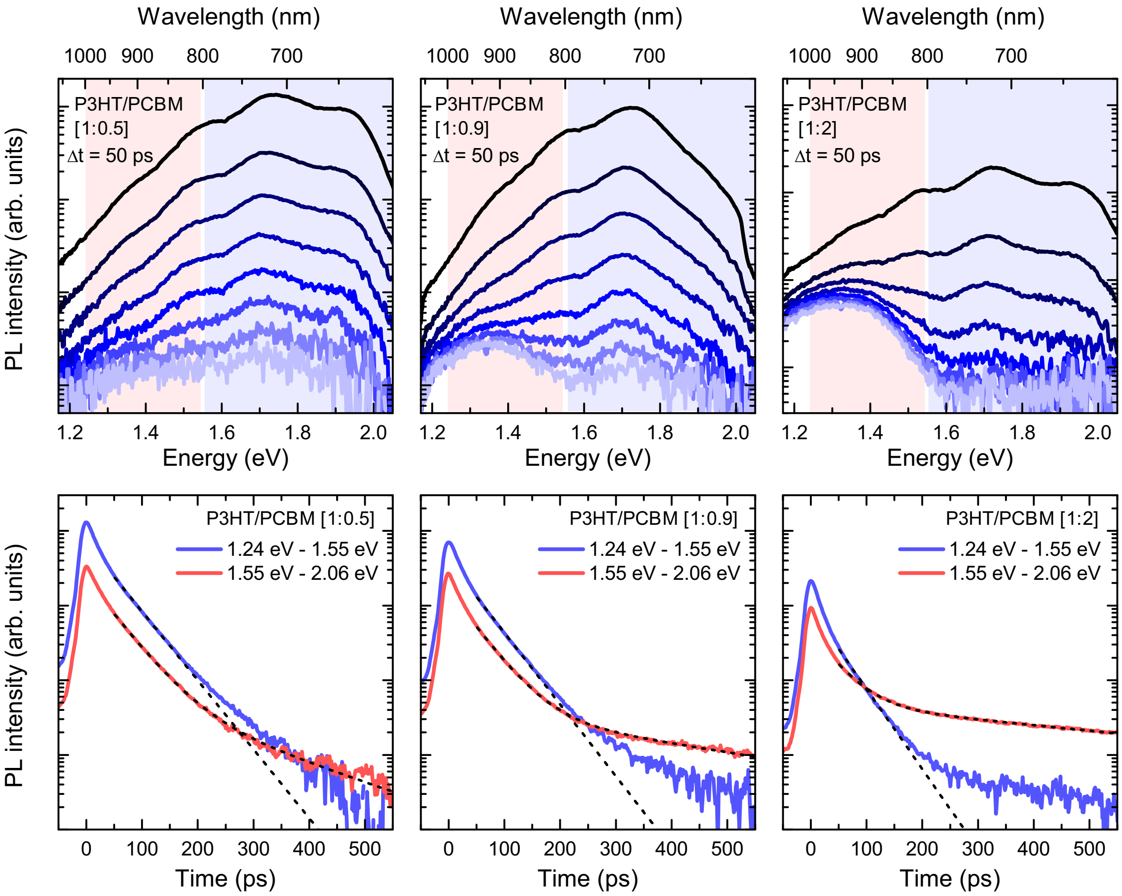

Figure 5.4.: Time-dependent spectra (upper row) and transients derived from different spectral ranges of the PL emission (lower row) for the devices with varying PCBM fraction. The data was extracted from the room temperature TRPL images presented in Fig. 5.3. The spectra were obtained from integrating the PL data over time intervals of 50 ps, starting at the time, where the PL emission is at its maximum. The 'earliest' spectra in the plots thus correspond to the time interval from 0 to 50 ps and the 'latest' spectra represent the time range from 350 to 400 ps. The transients plotted in the row below show the PL decay for the two highlighted energy ranges of the PL spectra. Monoexponential fits of the high-energy emission and biexponential fits of the low-energy range are shown as dotted curves.

interface. The temperature-dependent measurements of the CT emission (Ch. 5.4) and further discussion of the results in connection with the device morphology (Ch. 5.5) will further support this statement. Additionally, the emission energy of the presumable CT feature is roughly in line with the energy level difference between the LUMO of PCBM (-3.75 eV [118]) and the HOMO of P3HT (-5.20 eV [118]), yielding an energy of 1.45 eV for the transition between them. However, this simplistic consideration does not include any effects of the CT binding energy, disorder or changes of the molecular orbitals at the donor/acceptor interface.

For closer analysis of the underlying decay times, PL transients were integrated over the spectral range between 600 to 800 nm, where the emission is dominated by singlet excitons, and from 800 to 1000 nm, corresponding to superimposed singlet and CT emission. The different regimes are highlighted by the colored regions in the plots of the spectra in Fig. 5.4. Transients obtained from these intervals are plotted below the time-dependent spectra. The singlet decay times were estimated from monoexponential fits of the PL transients integrated from 600 to 800 nm. It should be mentioned that the PL of singlet excitons in polymers reveals multiexponential decay characteristics, which is a consequence of exciton migration and spectral relaxation, as demonstrated in Ch. 4. Thus, the applied monoexponential fit deviates from the recorded transients at longer delay times after excitation, where the PL intensity is low. Nevertheless it is useful to quantify the decay, allowing for comparison of the different blends. The CT decay times are obtained from biexponential fits of the emission between 800 and 1000 nm. The short-lived component of the transients in this region is attributed to singlet emission and the long-lived component is used to 'measure' the actual CT lifetime. This approach may be oversimplified, but in the investigated time window of 800 ps, good matches with the experimental data are obtained. The fits are shown as black dotted curves in the transients in Fig. 5.4. The resulting fitting parameters were found to vary slightly with the fitted time range of the transient. Due to the superimposed rise function of the instrument and time resolution limited to ca. 15 ps, it is unfavorable to fit the transient data from $t = 0$. Here, the starting point of the data evaluated by the fits was set to 50 ps after the transient maximum.

Singlet and CT decay times τ_{S1} and τ_{CT} resulting from the fits are summarized in Tab. 5.1, together with the decay times of the singlet emission in the neat P3HT and PCBM films, which were obtained by monoexponential fits in the same manner as described above. Furthermore, for direct comparison an overview over the transients of neat P3HT and the blends is presented in Fig. 5.5(a). The decay of the singlet emission in the blends becomes faster with increasing fullerene content. This can be explained in terms of exciton diffusion towards the donor/acceptor interface, becoming more efficient when the sizes of the polymer domains are small. Reflecting the summary of morphological studies in Ch. 5.1, it is reasonable to assume that the average size of the polymer domains decreases with increasing fullerene content, in favor of an increasing amorphous and intimately mixed polymer/fullerene phase. The diffusion-picture is also consistent with the temperature dependence of the singlet exciton decay (Fig. 5.5(b)): With increasing temperature, the decay becomes faster, because thermal energy enhances the diffusion rate inside the domains. For neat P3HT (Ch. 4.1), no such thermal quenching of singlet states has been observed. The efficiency of the diffusion-related quenching mechanism can be estimated from comparing the decay times of the polymer emission in the blends to that of a neat P3HT film via

$$Q_D = 1 - \frac{\tau_{S1}[Blend]}{\tau_{S1}[P3HT]} \ . \tag{5.1}$$

The values of Q_D obtained for the blends at room temperature are listed in Tab. 5.1. The efficiency of the diffusion-related quenching mechanism is on the order of 90 % for all mixing ratios, demonstrating that this process is efficient already for PCBM concentrations smaller than required for the optimum mixing ratio. Assuming similar intensity and overall-decay of the P3HT emission at low temperatures (see Fig. 4.2), Q_D of excitons in the [1:2] blend at 10 K is ca. 85 %. The room temperature result is consistent with previous studies employing transient absorption spectroscopy: Piris

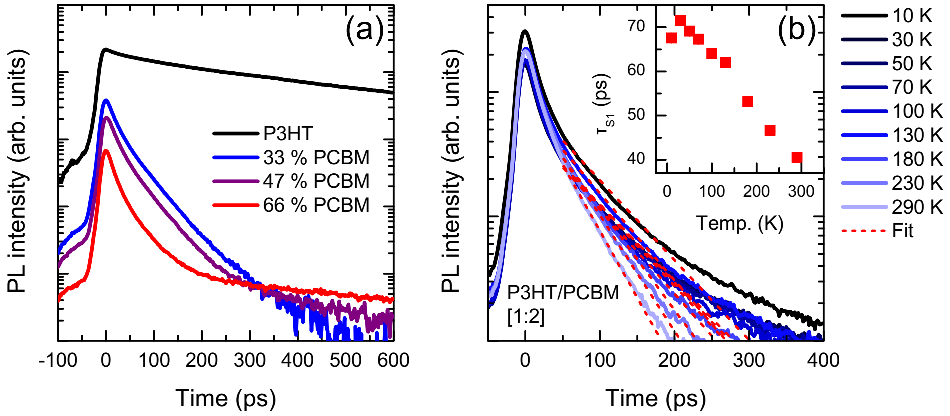

Figure 5.5.: Compositional and temperature-dependent quenching of singlet excitons in the blends. Panel (a) shows transients recorded for the blends with different PCBM content and a PL transient recorded for neat P3HT. In panel (b), temperature-dependent transients obtained from the spectral range between 600 and 800 nm of the [1:2] blend are presented. The inset shows decay times obtained from monoexponential fits, which are included as red curves in the plot.

et al. [164] found a value of 90 % and Guo et al. [119] obtained a dynamic quenching efficiency of 89%. Both investigated annealed BHJ films with a PCBM content of 50 %.

From direct comparison of the PL transients recorded for neat P3HT and the blend devices (Fig. 5.5), it becomes however evident that the dynamic quenching mechanism is not the decisive one, because a high fraction of the singlet emission in the blends is quenched on a time scale falling below the temporal resolution of the experimental setup. The initial amplitudes of the transients recorded for the [1:0.5] and the [1:0.9] device are decreased by a factor of 10 compared to the amplitude of the transient recorded for neat P3HT. In the [1:2] blend, the amplitude is even more drastically reduced by a factor > 30. Such a strong variation in intensity over more than one order or magnitude cannot be solely explained by the differing donor/acceptor ratios or by inaccuracies of the layer thickness. A potential reason for the strong decrease of the initial PL amplitudes in the blends is the presence of a second, ultrafast quenching mechanism. Considering the varying polymer fraction of the devices c_p, the efficiency of this ’static’ Q_S quenching process can be estimated from the initial amplitudes of the transients via

$$Q_S = 1 - \frac{A_{S1}[Blend]}{c_p A_{S1}[P3HT]} \,, \tag{5.2}$$

yielding 74 % for the [1:0.5], 82 % for the [1:0.9] and 91 % for the [1:2] device. Again, this finding complements the results of transient absorption studies, where charge formation via two channels has been evidenced: An ultrafast process on a sub-picosecond timescale, potentially emerging from excitations close to the donor-acceptor interface, and a slower dissociation channel (few 10s of ps), resulting from exciton diffusion towards a donor/acceptor interface in more extended pristine domains [119, 120, 164].

The CT decay times range between 171.2 ps for the [1:0.5] blend and 588.0 ps for the [1:2] blend. Thus, they are significantly longer than the decay times derived for the

Table 5.1.: Summary of parameters describing the PL decay in neat P3HT and PCBM films and in the blends with varying mixing ratios. The parameter A_{S1} denotes the maximum of the transients, Q_S is the portion of static quenching calculated from Eq. 5.2, τ_{S1} is the decay time of the singlet excitons obtained from monoexponential fits, Q_D is the efficiency of the diffusion-related quenching mechanism (Eq. 5.1) and τ_{CT} denotes the lifetime of the CT state obtained from biexponential fits.

Sample	A_{S1} (a.u.)	Q_S	τ_{S1} (ps)	Q_D (%)	τ_{CT} (ps)
P3HT	218.1	-	444.8 ± 1.9	-	-
blend [1:0.5]	38.0	73.6	47.1 ± 0.1	89.4 ± 0.1	171.2 ± 4.9
blend [1:0.9]	20.9	81.9	45.2 ± 0.2	89.8 ± 0.1	365.2 ± 9.7
blend [1:2]	6.8	90.1	40.5 ± 0.3	90.8 ± 0.1	588.0 ± 5.5
PCBM	-	-	876.6 ± 4.1	-	-

singlet emission. This is not unexpected, because the oscillator strength is reduced when the charges are located on different molecular sites. Furthermore, the measured CT decay times are consistent with complementary transient absorption studies, where a monomolecular signature has been assigned to the decay of CT states [119, 120]. It should be noted that for the [1:0.5] blend studied in this work no clearly shaped CT signature is observed in the time-dependent spectra plotted in Fig. 5.4. This might be due to the superimposed emission of the singlet excitons decaying on a similar time scale. However, the presence of this feature in the blend with excess polymer remains speculative, as the only indication is the slightly longer-lived emission observed in the spectral range between 800 and 1000 nm. It is found that the blend composition has a strong influence on the decay of the CT emission such that increasing the fullerene fraction leads to a longer decay time and higher intensity. Beside, there is also a slight red-shift of ca. 30 meV between the CT feature in the [1:0.9] blend, peaking around 1.35 eV, and the signature in the [1:2] blend, which has a maximum at ca. 1.32 eV. However, in both cases the emission is very broad.

Regarding the decay time of the CT signature, Guo et al. [119] made similar observations employing transient absorption spectroscopy. They investigated annealed and as-cast P3HT/PCBM blends with a PCBM fraction of 50 % and found that the CT population decays with a time constant of 500 ps in the as-cast material, which reduces to 250 ps after annealing. It is assumed, that P3HT crystallization is to a large degree suppressed in non-annealed P3HT/PCBM BHJ devices [7, 10, 157, 158], similar to the blend with excess PCBM studied in this work. Based on these results, Guo et al. suggested that the emissive CT states could be destabilized by enhanced hole mobility in a vicinity of higher crystallinity. The CT states could then undergo quenching via transfer of holes from the amorphous polymer phase towards a crystalline phase where they are more delocalized [119]. Consequently, the long-lived and intense CT emission in the [1:2] blend is indicative for higher losses emerging from geminate recombination in the amorphous polymer phase. This is in line with steady state PL studies by Hallermann et al. [8], who evidenced a particularly strong emissive CT feature in blends based on regiorandom P3HT[1] with PCBM, whereas the CT emission in an

---

[1] Regiorandom arrangement of the side chains suppresses crystallization of P3HT, see Ch. 2.6.4

annealed blend comprising regioregular P3HT was found to be very weak and barely distinguishable from the superimposed singlet emission. The picture of interfacial traps arising from the amorphous and intermixed phase is also consistent with the measured external quantum efficiency, which is 50 % for the as-cast films and 80 % for annealed P3HT/PCBM [119].

5.2.2. Time-resolved photoluminescence of PTB7/PC$_{71}$BM

For PTB7/PC$_{71}$BM it is of particular interest to study the PL properties of both the intermixed polymer phase and the fullerene phase separately. This is possible within the given experiment due to the partially separated absorption features of PTB7 and PCBM (see Fig. 5.1(b)) and because the excitation wavelength can be tuned to either 400 nm, where the major faction of the impinging light is absorbed by the fullerene, or to 705 nm, allowing for selective excitation of PTB7. Exemplary PL images resulting from these excitation scenarios at a sample temperature of 10 K are presented in Fig. 5.6. In this work, two blend devices with polymer/fullerene mixing ratios of [1:1.5] (60 % PCBM) and [1:3] (75 % PCBM) were studied and compared to the PL properties of neat films of PTB7 and PCBM. For 400 nm excitation, the PL of the blends is clearly dominated by the fullerene emission and no substantial differences arise with regard to the neat material. For 705 nm excitation on the other hand, the PL signatures are tremendously altered in the blend, yielding a broad and almost featureless emission decaying within the time resolution of the experiment, followed by a longer lived signature peaking around 1.32 eV. Due to the fact that the laser excites only the PTB7 molecules when tuned to 705 nm, it is reasonable to attribute the short-lived initial signature to the polymer emission, which decays rapidly, because PTB7 is in an intimately mixed phase with PCBM [11]. The long-lived signature after excitation of the intermixed phase presumably arises from CT emission, due to its decay on a timescale of 1 ns and according to the emission energy, which is, similarly to P3HT/PC$_{61}$BM, in rough agreement with the energy level offset at the interface[2].

The time-dependent spectra and spectrally integrated PL transients presented in Fig. 5.7 allow for a more detailed characterization of the intermixing phenomena. The assignment of the blend signatures under different excitation conditions to either the fullerene (400 nm excitation) or the polymer (705 nm excitation) is further supported by the variation of the PL intensities with the mixing ratio: Under 400 nm excitation the intensity of the PL signatures increases with increasing fullerene content, indicating that the emission is related to PCBM, whereas for 705 nm excitation, the PL intensity increases with decreasing PCBM content, as expected for emission from the polymer. Under 400 nm excitation, the emissive features of PCBM at 1.73 and 1.55 eV are clearly visible in the blends. However, in the [1:1.5] blend the intensity ratio of the higher and the lower energy peak is different from the emission of the neat film. This could arise from the higher polymer fraction in the [1:1.5] blend. The absorption of PTB7 overlaps with the high-energetic emission of PC$_{71}$BM (see Fig. 5.1(b)), thus it is likely that some of the PCBM excitons undergo Förster transfer to PTB7 or the emitted light from PCBM is re-absorbed by the polymer, both leading to a reduced intensity

---

[2] $E_{HOMO}[PTB7] = -5.15\,\mathrm{eV}$[125]; $E_{LUMO}[PC_{71}BM] = -3.9\,\mathrm{eV}$[165]; $\Delta E = 1.25\,\mathrm{eV}$

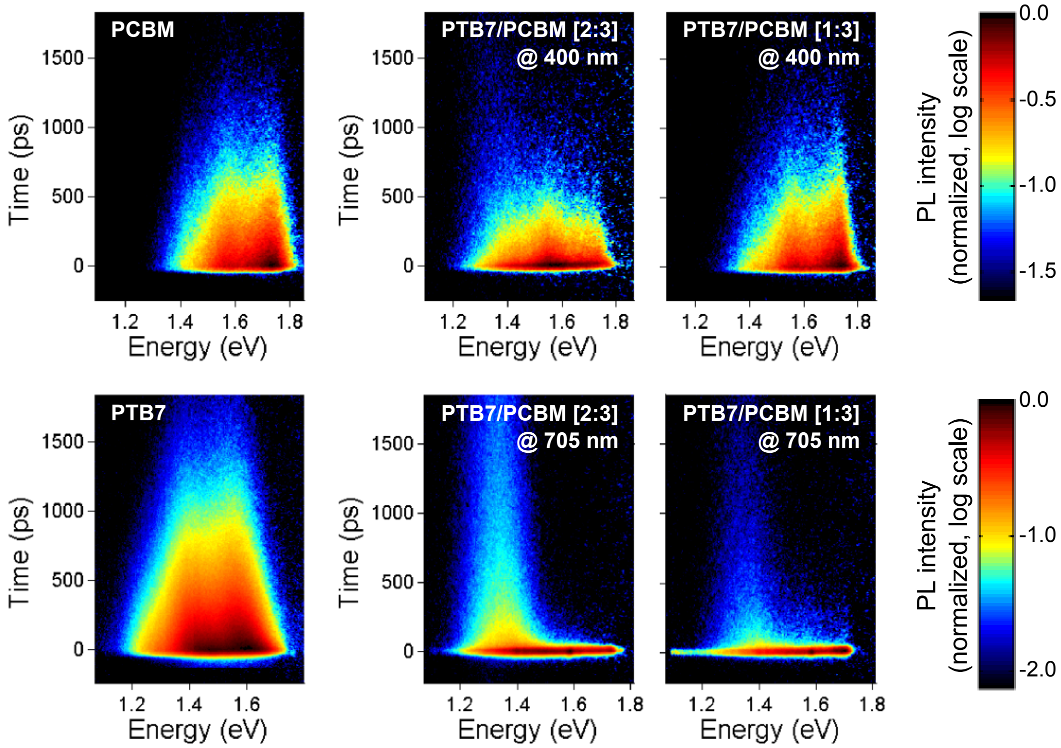

Figure 5.6.: Overview over the TRPL data recorded for pristine PTB7 and $PC_{71}BM$ and blends, as labeled, at a temperature of 10 K. The excitation wavelength was set to 400 nm for preferential excitation of PCBM in the blend films (upper row) and to 705 nm for selective excitation of the polymer phase (lower row). The data is normalized and the intensity is color-coded on a logarithmic scale, as indicated by the color legends on the right.

of the high-energetic emission band of PCBM. Another peculiarity arising from the time-dependent spectra of the [1:1.5] blend plotted in Fig. 5.7(a) is the long-lived and broad emission around 1.32 eV, which is similar to the presumable CT feature observed after 705 nm excitation, but much weaker in intensity. Comparing the intensities of the long-lived emission, thereby considering the wavelength-dependent absorptivity of the material and the different photon fluxes at 400 and 705 nm, the CT yield under 705 nm excitation is by a factor of 3 higher than after 400 nm excitation. Recalling the material morphology, this could arise from losses during the exciton diffusion process in PCBM, after which a smaller portion of excitons reaches the interface where CT states are formed. On the other hand, there is also the possibility that the dissociation efficiency of CT states depends on the environment, where they are created. This issue can be further addressed by investigating the actual quenching efficiency of excitons created in PCBM.

In order to investigate the emissive losses of excitons in the PCBM phase, PL transients recorded for neat material are compared to those of the blends. The corresponding data obtained after 400 nm excitation is presented in Fig. 5.7(e). In addition to the measurements at 10 K, transients recorded at room temperature are shown as dotted curves. For neat PCBM, the decay characteristics does not remarkably change with temperature. In the blends on the other hand, the decay becomes faster. This is consistent with the picture of exciton diffusion, because thermal energy enhances the

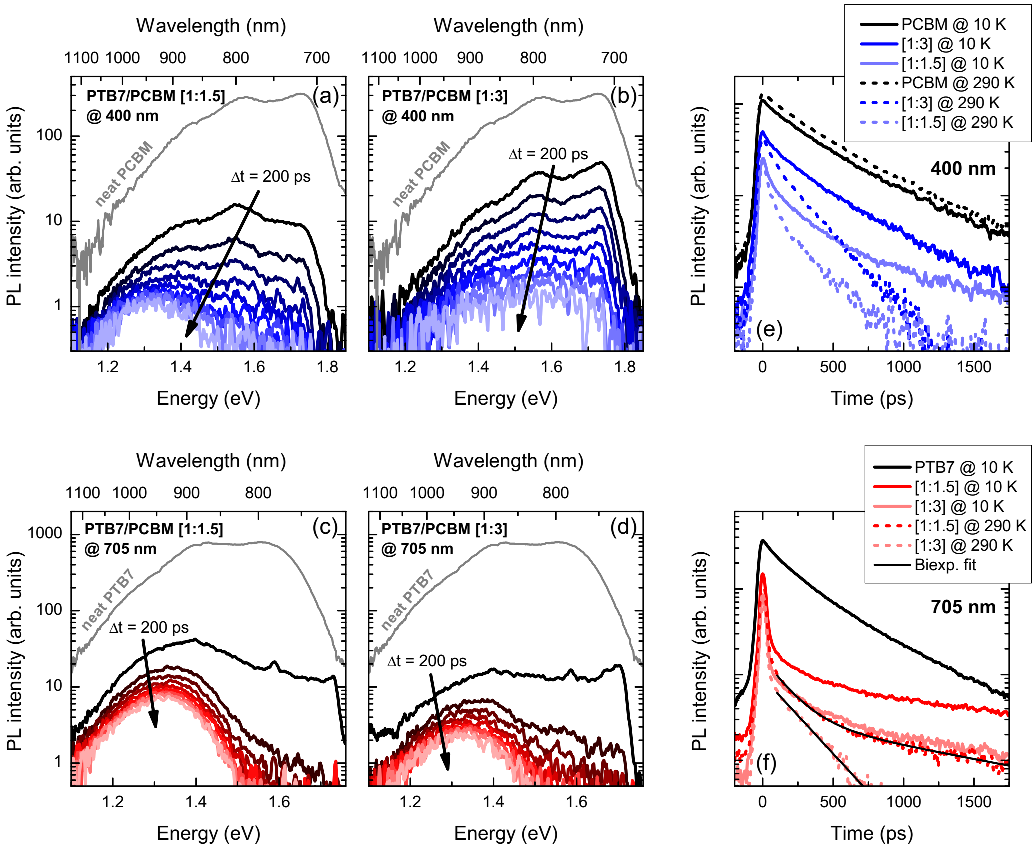

Figure 5.7.: Time-dependent PL spectra and spectrally integrated PL transients extracted from the measurements at 10 K. Spectra were obtained from integrating the data over time intervals of 200 ps, starting at the maximum of the PL emission. The 'latest' spectrum in this representation corresponds to the time range between 1600 and 1800 ps after the transient maximum. Data recorded for 400 nm excitation is shown in panels (a) and (b), together with the time-integrated PL spectrum of neat PCBM (gray curve), and data for 705 nm excitation is presented panels (c) and (d), including the time-integrated PL-spectrum of neat PTB7. Panels (e) and (f) show the PL transients recorded under different excitation conditions. Dotted curves correspond to room temperature measurements. The long-lived component in the blend emission investigated under 705 nm excitation is attributed to CT emission. The room temperature data of the CT decay was approximated with a biexponential fit function as indicated by the thin black curves.

diffusivity and hence, the excitons need on average less time to reach a quenching donor/acceptor interface. In neat PCBM on the other hand, no such quenching channel is present. Similar to the analysis carried out for P3HT/PCBM (Ch. 5.2.1), the initial amplitudes and decay times are used to quantify the quenching yield. The initial amplitudes A_{S1} and 1/e decay-times τ_{S1} obtained for sample temperatures of 10 and 290 K are listed in Tab. 5.3. The observed decrease of τ_{S1} with decreasing fullerene fraction can be attributed to a decrease of the average PCBM domain size. From Eq. 5.1, the efficiency of the diffusion-related quenching mechanism is estimated to 26 % in the [1:3] blend and 62 % in the [1:1.5] blend at 10 K. However, as indicated by the amplitudes of the PL transients, only a small fraction of excitons in the blend undergoes the observed long-lived decay and a much higher percentage is quenched on a time scale <3 ps. From the given experiment, the contribution of this ultrafast process can only

Table 5.2.: Overview over the extracted decay parameters derived from the PL decay of the PTB7/PCBM blends and neat PCBM under different excitation conditions for a sample temperature of 290 K. The amount of static quenching Q_S was calculated from the initial amplitudes of the transients in Fig. 5.7(e) via Eq. 5.2. The parameter τ_{S1} denotes the 1/e-decay time of the PCBM excitons obtained from the same transients. Together with the decay time of neat PCBM, these values can be used to calculate the efficiency of the diffusive quenching mechanism Q_D via Eq. 5.1.

Sample	A_{S1} (a.u.)	Q_S (%)	τ_{S1} (ps)	Q_D (%)	Q_T (%)
PCBM (10 K)	1.10 ± 0.12	-	367.7 ± 4.9	-	
PCBM (290 K)	1.33 ± 0.12	-	367.7 ± 4.9	-	
PTB7/PCBM [1:3] (10 K)	0.50 ± 0.05	39.5 ± 8.2	273.1 ± 4.9	25.7 ± 2.3	55.0 ± 5.6
PTB7/PCBM [1:1.5] (10 K)	0.26 ± 0.03	61.2 ± 5.6	141.0 ± 4.9	61.7 ± 1.8	85.1 ± 2.6
PTB7/PCBM [1:3] (290 K)	0.42 ± 0.04	57.5 ± 5.9	156.3 ± 4.9	57.5 ± 3.7	82.0 ± 2.4
PTB7/PCBM [1:1.5] (290 K)	0.23 ± 0.02	70.7 ± 5.8	75.6 ± 4.9	79.4 ± 6.8	94.0 ± 0.9

be estimated from comparing the initial amplitudes of the PL transients obtained from neat PCBM to those of the blends. For the efficiency of the fast quenching mechanism, Eq. 5.2 yields an increasing value with increasing temperature and additionally, strong influence of the fullerene fraction on the quenching is observed. It is found that the quenching is more efficient, when the fullerene fraction is reduced, which is consistent with the assumption that the higher PTB7 fraction offers more quenching sites for excitons created in PCBM. Both the fast PL quenching on a sub-ps time scale and the long lived decay, which is 75 ps at room temperature, are in agreement with the findings of Hedley et al. [12].

Here, the overall quenching efficiency Q_T resulting from the concurrence of both static and dynamic processes is of particular interest. It can be calculated either from comparing the PL intensities or with the calculated parameters Q_S and Q_D via

$$Q_T = Q_S + (1 - Q_S)Q_D \ . \tag{5.3}$$

The values of Q_T listed in Tab. 5.3 were calculated from Eq. 5.3. Importantly, the total quenching of the [1:1.5] blend at a temperature of 10 K is still 85 %, suggesting that the diffusion-related losses of PCBM excitons in the blend are rather small, even in the low-temperature regime. Based on the assumption, that the non-radiative decay mechanism is mainly due to interfacial quenching, which is supported by the measurements of neat PCBM, it can thus be concluded that most of the excitons created in PCBM reach the interface, where they form CT states. This finding supports the hypothesis that CT states that are populated from more extended PCBM domains are in fact less stable than CT states created in the polymer phase, where the PCBM agglomerates are presumably smaller, leading to higher localization of the electron. This finding is in contrast to the results on P3HT/PCBM, where tuning of the excitation wavelength to either preferential excitation of the polymer or the fullerene did not lead to significant changes in the CT yield [13].

The CT emission can be characterized in greater detail using the data obtained for 705 nm excitation. Transients recorded from neat PTB7 and the blends at 10 K and at room temperature are presented in Fig. 5.7(f). The CT signature in the blend with a higher fullerene fraction decays faster and likewise, increasing the sample temperature leads to faster decay. To quantify the CT lifetime, the CT component in the blend emission at room temperature is approximated with a biexponential fit function, starting at a time of 100 ps after the transient maximum to avoid contributions from superimposed singlet emission. For the [1:1.5] blend, the CT decay can be described by a shorter component ($\tau_{CT,1} = 167$ ps) and a longer-lived component ($\tau_{CT,2} = 1399$ ps). In case of the [1:3] blend, the decay is monoexponential and only one contribution with a time constant of $\tau_{CT,1} = 244$ ps can be extracted from the data. Similar to the findings for P3HT/PCBM, the intensity and decay time of the CT emission are correlated with the blend composition. Based on the argumentation of Guo et al [119], the faster decay of the CT emission in blends with higher P3HT content has been attributed to the enhanced probability of hole transfer to regions of P3HT with higher ordering and thus a higher dissociation probability of the CT state. Likewise, in PTB7/PCBM, a higher supply of PCBM sites and more extended PCBM domains offering more efficient separation pathways for interfacial states could be the reason for the faster decaying CT signature in the [1:3] blend, which is consistent with the underlying picture of the material morphology [11, 12]. The strong temperature dependence of the CT emission will be discussed in Ch. 5.4 and in greater detail in Ch. 6.1.5, in combination with field-dependent PL experiments.

5.3. Localization effects

5.3.1. Localized excitons in the PTB7/PCBM mix phase

An interesting detail in the initial PL spectra of the PL emission in the PTB7/PCBM mix phase (see Fig. 5.7(c) and (d)) is the narrow and short-lived feature peaking around 1.58 eV (785 nm). This line-narrowing occurs to a similar extent in both investigated blends but not in neat PTB7 (see Fig. 5.8(a)), and without any noticeable temperature-dependence. The energy difference between the narrow feature and the excitation laser at 705 nm (1.76 eV) is 0.18 eV, which is similar to the energy reported for the most prominent Raman mode in neat PTB7, which is a stretching mode of the C=C bonds in the thiophene rings of the benzoditiophene unit peaking at 1489 cm^{-1}(0.184 eV) [166]. Accordingly, the weaker narrow feature observed for all the blends at 1.40 eV could be the second side band of the same vibronic progression. Such line-narrowing is a phenomenon rather known from resonant excitation of tail states in the low-temperature regime [167]. In such a situation, sites that energetically coincide with the laser energy are excited and the excitons created on these sites are trapped on a time scale exceeding their lifetime. The emission of the zero phonon line cannot be investigated experimentally, as it coincides with the excitation energy, but the line-narrowing also occurs in the phonon branches emitted by the localized excitons. In principle, this phenomenon can be exploited for site-selective spectroscopy to investigate the properties of individual chromophores, when the linewidth of the exciting laser is sufficiently

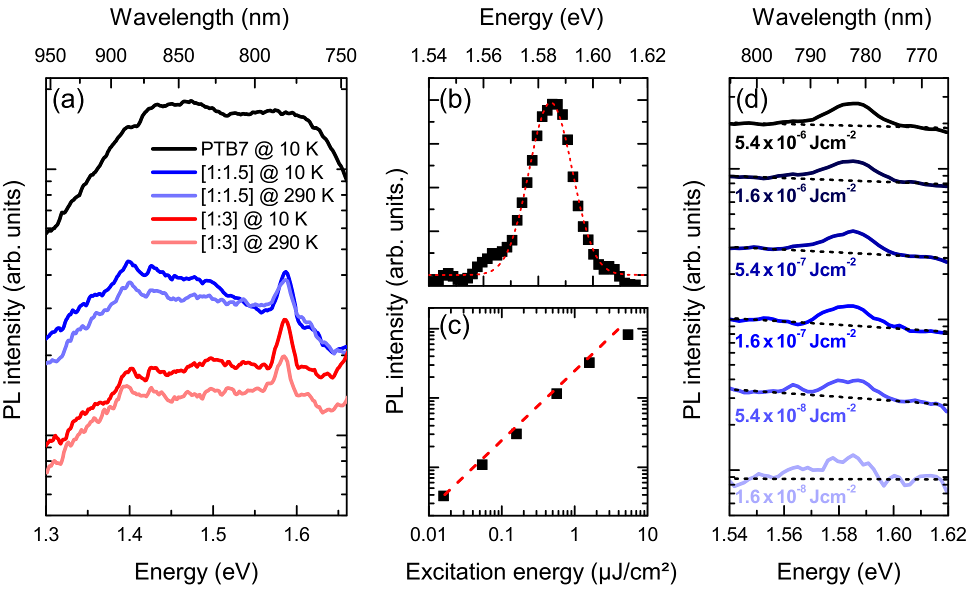

Figure 5.8.: Investigation of the narrow features observed in the PTB7/PCBM blends after selective excitation of the polmer phase at 705 nm. Panel (a) shows a comparison between low temperature and room temperature spectra of the [1:1.5] and the [1:3] blend in the region of the narrow emission features, which are plotted together with the spectrum of neat PTB7. In panel (b), the narrow feature recorded for an excitation power of 6.4 µJcm^{-2} is shown in greater detail. Panels (c) and (d) summarize the results of power-dependent measurements: The intensity of the narrow features was approximated with the integral over the respective spectral region, diminished by a linearly interpolated background as shown in (d).

narrow [39]. The linewidth of the narrow signatures in the experiments was extracted from a Gaussian fit (see Fig. 5.8(b), yielding a standard deviation of 7.9 meV, which translates into a FWHM of 7.4 nm at the excitation wavelength of 705 nm. This is in good agreement with the linewidth of the pulsed excitation laser, indicating, that a laser pulse creates an ensemble of localized states, whereas the homogeneous linewidth of the individual chromophores is smaller and cannot be resolved in the experiment.

The observed line narrowing could also result from stimulated emission of sites with energies resonant to the excitation energy. The probability of this process is expected to increase with increasing laser fluence. However, the intensity of the narrow feature, which was approximated via the peak area corrected by a linearly interpolated background (see Fig. 5.8(d)), is found to be linearly correlated with the excitation fluence, as shown in Fig. 5.8(c). Thus, it appears implausible that stimulated emission is the underlying phenomenon of the observed line narrowing. This is further supported by the fact that no narrow features are observed in neat PTB7.

It should be noted that in the PL decay, no evidence for longer-lived emission resulting from the localized subset of excitons is observed, indicating that long-range exciton migration is not mandatory for efficient exciton separation in the investigated blends. In fact, the probability for an exciton to get localized on a polymer chain is expected to be higher, when it is surrounded by larger portions of PCBM, which reduce the amount of available polymer sites it can hop to. On the other hand, the CT rate is enhanced with more acceptor sites in the vicinity. Thus, especially the excitons located on rather isolated polymer sites could undergo particularly fast CT, giving rise to the overall situation that for some polymer sites in the PTB7/PCBM mix phase, the CT rate is faster than the hopping rate to adjacent sites in the polymer.

5.3.2. Localization of charge transfer states

Considering the nature of CT states, it is straightforward to assume that they are localized, as their migration would be limited to sites at the interface between the donor and acceptor component. Furthermore, the underlying transport mechanism of CT excitons is expected to be less efficient than that of singlet states. The latter can migrate via long-range Förster transfer or Dexter mechanism. It is however questionable, if these processes are also feasible for CT states, first of all due to the poor oscillator strength of the CT transition to the ground state, which inhibits Förster transfer. Furthermore, the exchange coupling between adjacent CT sites enabling Dexter transfer is expected to be weak, when the interface is subject to disorder. However, Deotare et al. have recently reported experimental evidence for mobile CT states, based on their observation of a gradual red-shift of the PL emission in TRPL studies and accompanying Monte Carlo simulations [168]. They propose a transport mechanism based on asynchronous motion of the electron and hole, which remain correlated via their mutual Coulomb interaction during the migration process. If present, such a process could enhance the exciton separation rate in OPV materials, because CT excitons could diffuse into regions where they can be more easily separated (e.g. towards interfaces of domains with a higher degree of crystallinity).

Despite these striking results reported in Ref. [168], the analysis carried out for the CT emission in the P3HT/PCBM and PTB7/PCBM system indicates that CT mobility is not the underlying phenomenon leading to the observed PL characteristics. A consistent interpretation of the results is rather possible, when the weak Coulomb interaction of CT states and consequently a small activation barrier to get separated are explicitly taken into account. The statement of weakly bound CT states will be further corroborated in Ch. 5.4 and Ch. 6.1.5. The CT states investigated by Deotare et al. on the other hand were found to be strongly bound, allowing the authors to rule out any influence of CT dissociation in the system they investigated.

The ambiguity arising from the interpretation of TRPL data in the presence of weakly bound CT states becomes evident from the time-dependent PL spectra shown in Fig. 5.9 and the decay characteristics at different emission energies summarized in Fig. 5.10. For better comparison, the time dependent PL spectra in Fig. 5.9 are normalized to the dominating signature in the respective time interval after excitation (either singlet or CT). Recalling the PL characteristics arising from spectral relaxation of singlet excitons reported in the previous chapter (see section 4.1.4), the red-shift observed for the CT emission in PTB7/PCBM could in principle be due to the migration CT excitons towards tail states in the CT DOS. This would also be in agreement with the highly dispersive decay characteristics of the long-lived component of the CT emission in the low-temperature regime, as summarized in Fig. 5.9. However, both

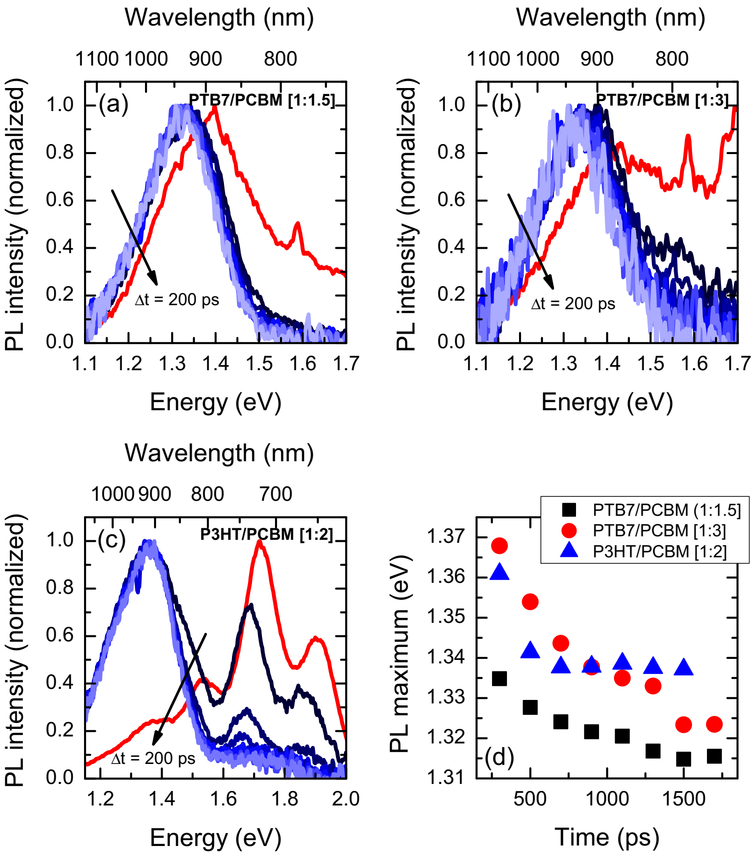

Figure 5.9.: Time-dependent spectral characteristics of the CT emission for PTB7/PCBM (panels (a) and (b)) and for P3HT/PCBM (c) at a sample temperature of 10 K. The signatures were obtained from integrating the PL emission over time intervals of 200 ps, starting at the maximum of the corresponding PL transient. The spectra were normalized to their maximum and the red curves correspond to the 'initial' PL spectra (0-200 ps), which are dominated by singlet emission. Blue curves correspond to dominating CT emission, whereas lighter color indicates later time intervals after excitation. Panel (d) summarizes the time-dependent shift of the CT maxima, which were approximated by a Gaussian fit function.

observations can also be interpreted in terms of an energy-dependent quenching mechanism, e.g. CT dissociation. The observation that the high-energy tail of the CT emission exhibits faster decay is consistent with the assumption of an underlying manifold of CT binding energies, giving rise to a variation in dissociation probabilities. The binding energy of the CT state is correlated with the emission energy such that Coulombic attraction between the charges decreases the CT energy level [77], leading to a red shift of the PL emission. Based on the hypothesis of dissociation and a manifold of binding energies, the CT states corresponding to high-energy emission are thus more weakly bound and more likely to get dissociated than the low-energy CT states. In fact, for a temperature of 10 K, the decay time of the long-lived CT component is found to saturate below a certain threshold energy (see Fig. 5.10(d)-(f)), indicating that in this regime the dissociation rate is smaller than the recombination rate.

Regardless of the actual process leading to the dispersive decay characteristics of the CT emission in PTB7/PCBM, no significant spectral shift is observed in the TRPL data of the CT emission in P3HT/PCBM (see Fig. 5.9(c)). For quantification, the spectral shift was estimated from Gaussian fits to the CT spectrum and the resulting peak energies are summarized in Fig. 5.9(d). The initially higher emission energy of the CT spectrum in P3HT/PCBM may result from superimposed singlet emission. However, importantly, there is no continuous red-shift with proceeding time after excitation, which is a strong indicator for CT localization and likewise evidences that the high energy subset of the CT population, which is able to dissociate irrespective of thermal energy, is negligibly small in the P3HT/PCBM [1:2] sample.

A further observation is the decrease of the long CT decay times with increasing temperature. This effect is more strongly pronounced in case of the PTB7/PCBM blends. In order to retain the methodology, the decay times obtained from fitting the data recorded at 240 K are presented in panels (e) and (f) of Fig. 5.10, because the long-lived component of the CT emission at room temperature was too weak for an appropriate biexponential fit. For P3HT/PCBM, however, the long-lived component of the CT decay remains even at room temperature. The decrease of the decay times with increasing temperature suggests that thermal energy assists the dissociation of those CT states, which are too strongly bound to get separated at low temperature. This

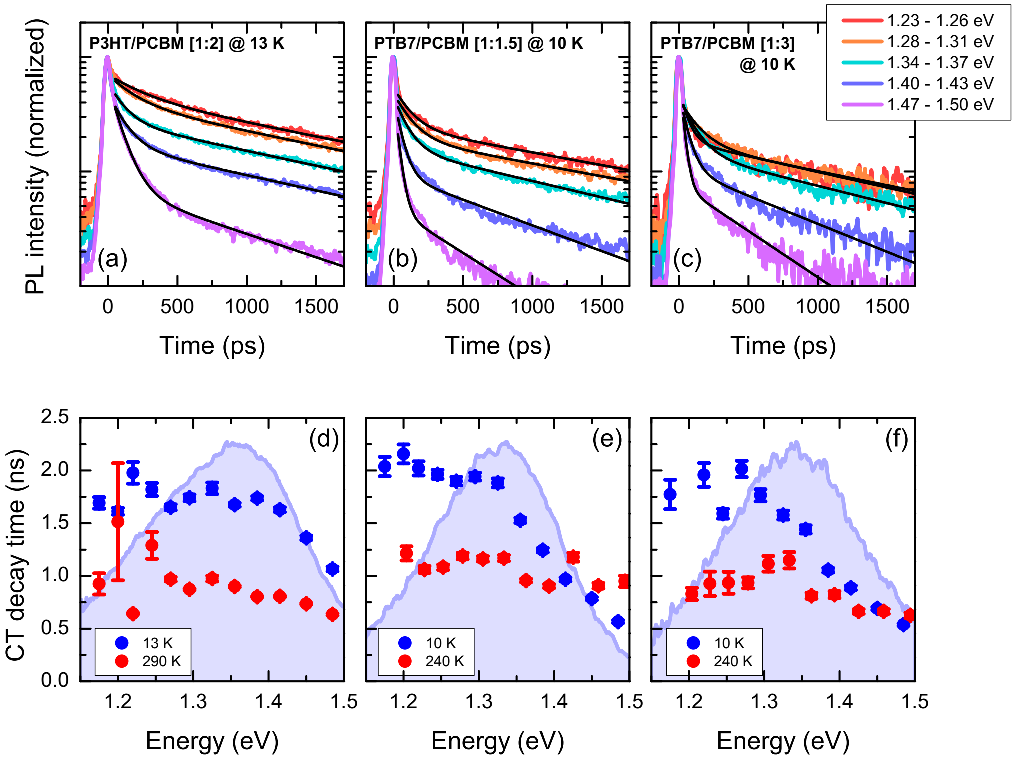

Figure 5.10.: Energy-dependent decay characteristics of the CT emission. Panels (a)-(c) show exemplary transients integrated over different spectral ranges of the CT emission as labeled at a temperature of 10 K. Panels (d)-(f) summarize the decay times of the long-lived component of the CT emission, which was extracted via biexponential fits (see black curves in the in the transient data panels). In addition, the decay times of the CT emission obtained for higher temperatures are shown. The low-temperature CT spectra of the respective samples are indicated as light-blue filled curves in panels (d)-(f).

effect is particularly strong for PTB7/PCBM, but in the P3HT/PCBM [1:2] sample, a remarkable subset of the CT population remains bound on a longer time scale even at room temperature. The temperature dependence of the CT emission with a special focus on its dynamics will be discussed in greater detail in the next section.

In order to further substantiate the picture of localized CT states, the CT emission is investigated under various excitation fluences. The spectra extracted from the time range dominated by CT emission are presented in Fig. 5.11. In the spectra of P3HT/PCBM, a small contribution of the P3HT singlet emission remains in the PL spectra. When the excitation fluence is increased, the relative intensity of the singlet feature decreases with regard to the CT emission. A sub-linear increase of the singlet exciton emission with increasing excitation fluence, presumably due to exciton-exciton annihilation, has already been observed for pristine P3HT (see Ch. 4.1.2) above a threshold fluence of ca. $0.3\,\mu\mathrm{J cm}^{-2}$. The CT emission on the other hand seems to be less affected by higher-order effects, which is consistent with the assumption that they are localized on a length scale where they do not interfere with each other.

The intensity of the CT emission in the PTB7/PCBM blends on the other hand tends to saturate with higher fluence (Fig. 5.11(b) and (c)). Beside the saturation, a signature around 800 nm arises from the PL spectra with increasing excitation fluence. According to its similarity to the PTB7 emission, the signature is attributed to singlet excitons in the polymer. The growing fraction of this longer-lived singlet population with increasing excitation fluence could arise from the filling of the CT states. As the CT states are longer lived, in particular in the low temperature regime, singlet excitons may undergo diffusion in the polymer phase until they reach an unoccupied CT quenching site. On the other hand, the occurence of a longer-lived singlet population at high fluences is also consistent with previous reports on the re-generation of singlet states via triplet-triplet annihilation [169].

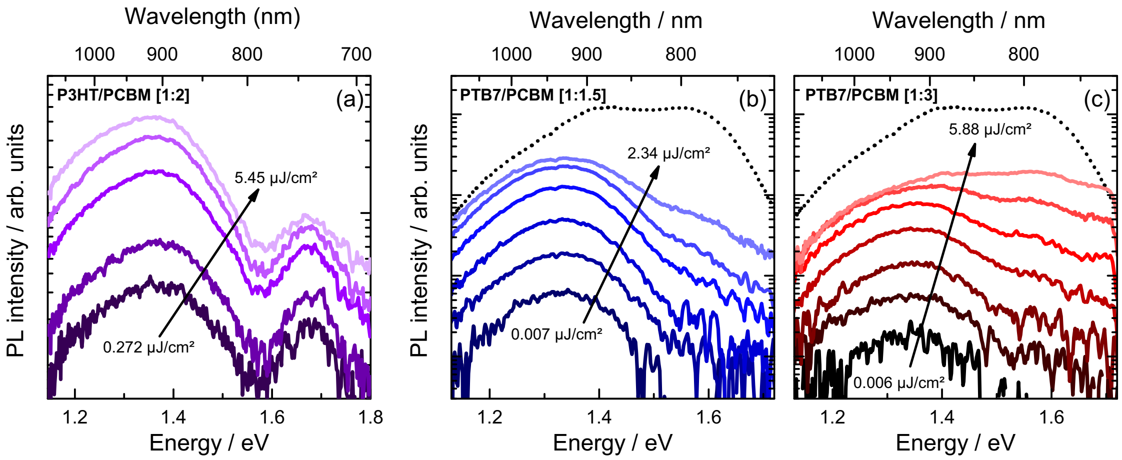

Figure 5.11.: Fluence dependent PL spectra recorded at 10 K and integrated over the time range, which is dominated by CT emission. Panel (a): P3HT/PCBM, integrated over the time range after 400 ps; Panels (b) and (c): PTB7/PCBM integrated over the time range after 50 ps. The dotted curves in panels (b) and (c) correspond to the PL spectrum of neat PTB7, recorded over the same time window.

Based on the assumption that the high-energy emission in PTB7/PCBM results from singlet states in the polymer, the spectral characteristics of the CT signature do not change, when the laser fluence is varied. However, if the CT states were mobile, increasing the laser fluence would presumably lead to an energetic shift of the CT emission towards higher energies. This is expected, because mobile CT states could undergo spectral relaxation. Thus, low excitation fluence would lead to preferential population of the low-energy CT states, whereas a higher excitation fluence would also populate the energetically higher CT states, when the low-energy sites are filled. The fact, that such behavior is not observed, not even in the regime where the overall CT intensity saturates, strongly suggests that the CT emission spectrum mainly reflects the initial population without any evidence of spectral migration.

The PL transients in Fig. 5.12 further confirm the absence of diffusion-related annihilation effects of CT excitons, as they reveal similar decay up to high fluences (the

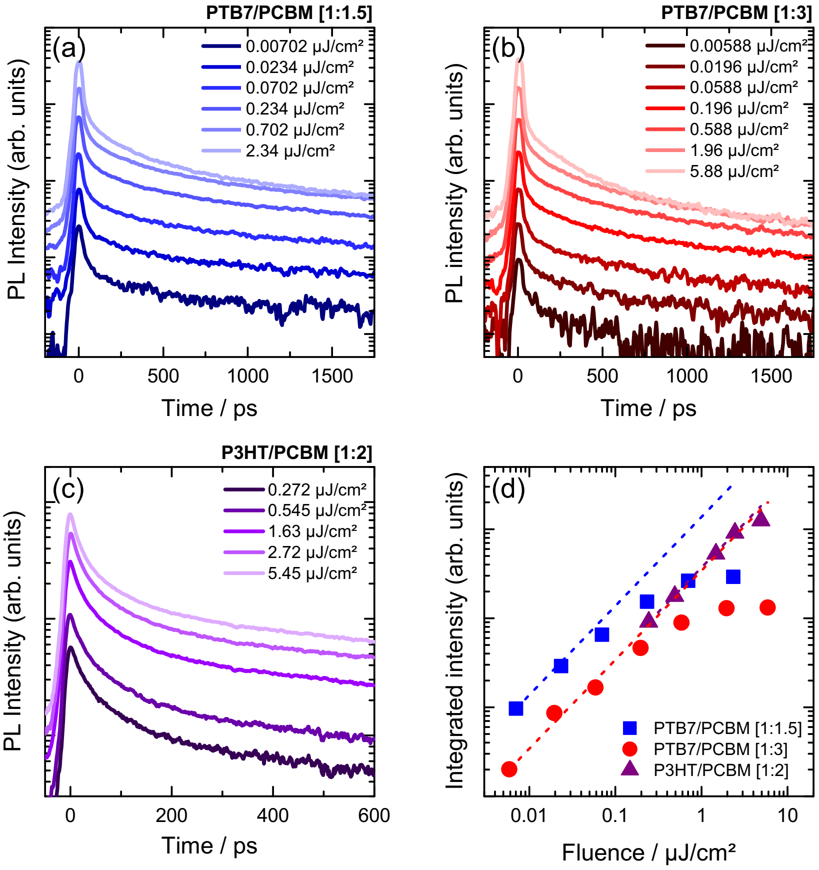

Figure 5.12.: PL transients recorded under variation of the excitation fluence at a sample temperature of 10 K for PTB7/PCBM (panels (a) and (b)) and for P3HT/PCBM (panel(c)). The transients in panel (c) were obtained by integrating the PL emission over the spectral range between 800 and 1000 nm, in order to show the PL decay in the region, which is dominated by CT emission. For all investigate samples, the CT intensity was approximated by the long-lived component of a biexponential fit function, yielding the intensities presented in panel (d). The dotted lines signify the slope expected for a linear correlation between the excitation fluence and CT intensity.

faster component arising at high fluences in PTB7/PCBM is attributed to longer-lived singlet excitons in the polymer). For the three analyzed samples, the CT intensity was estimated from the long-lived component of a biexponential fit function $I(t) = A_1 \exp(-t/\tau_1) + A_2 \exp(-t/\tau_2)$, where the intensity is given by the product $A_2\tau_2$. The resulting intensities are shown as a function of the excitation fluence in Fig. 5.12(d). The CT intensity of PTB7/PCBM shows a clear tendency to saturate at higher fluences, which is most likely related to the filling of CT states and not due to higher-order annihilation phenomena, as indicated by the similar decay characteristics up to high fluences. In P3HT/PCBM on the other hand, no saturation of the CT DOS is observed in the investigated range of excitation fluences.

5.4. Thermal quenching of charge transfer states

Finally, the thermal quenching of the CT states is investigated in greater detail. Temperature-dependent spectra of the CT emission are presented in Fig. 5.13. In all blends, the CT signature exhibits a systematic spectral shift with increasing temperature, but the direction of this shift is different for the two investigated material systems. In case of PTB7/PCBM, the maximum of the CT emission is blue-shifted with increasing sample temperature, whereas the signature of P3HT/PCBM reveals a red shift. The observed blue shift is consistent with the idea that thermal energy assists charge separation. Increasing the temperature leads to a larger average separation of the electron-hole pairs, thereby reducing their Coulomb interaction. The weaker coupling between the charges in turn raises the CT energy with respect to the ground state. The more pronounced temperature-induced blue shift of the CT emission in the PTB7/PCBM [1:3] blend is in line with the faster decay of the CT emission compared to the [1:1.5] blend, indicating, that the CT states formed in the material with a higher excess of PCBM are on average more weakly bound, which is related to a larger average separation and a higher dissociation rate. The red shift of the CT emission in the P3HT/PCBM blend on the other hand contrasts with the results for the PTB7 blends. One reason for the red shift could be the spectral overlap of CT emission with a vibronic side band of the singlet emission, which is present in the long-lived PL emission in the low temperature regime. However, the red-shift is continued even at temperatures above 130 K, where the contribution of the singlet emission becomes negligibly small due to its faster decay. The precise reason of the observed red shift of the CT emission in P3HT/PCBM with increasing temperature remains unclear. Potentially, the reduced stiffness of the molecular matrix or fluctuations of the excitonic coupling at room temperature could enhance the stability of the emissive CT states with increasing temperature [13, 170]. However, regardless of the underlying cause for the thermally induced red shift, the absence of a blue shift suggests that thermal energy does not remarkably lower the binding energy of the emissive CT states in the P3HT/PCBM system.

The above-made statement concerning P3HT/PCBM is further supported by the decay characteristics of the CT emission, which is not significantly altered with increasing temperature, in contrast to the CT dynamics of PTB7/PCBM (see Fig. 5.14(a)-(c)). Nevertheless, significant quenching of the CT emission is also observed in case of

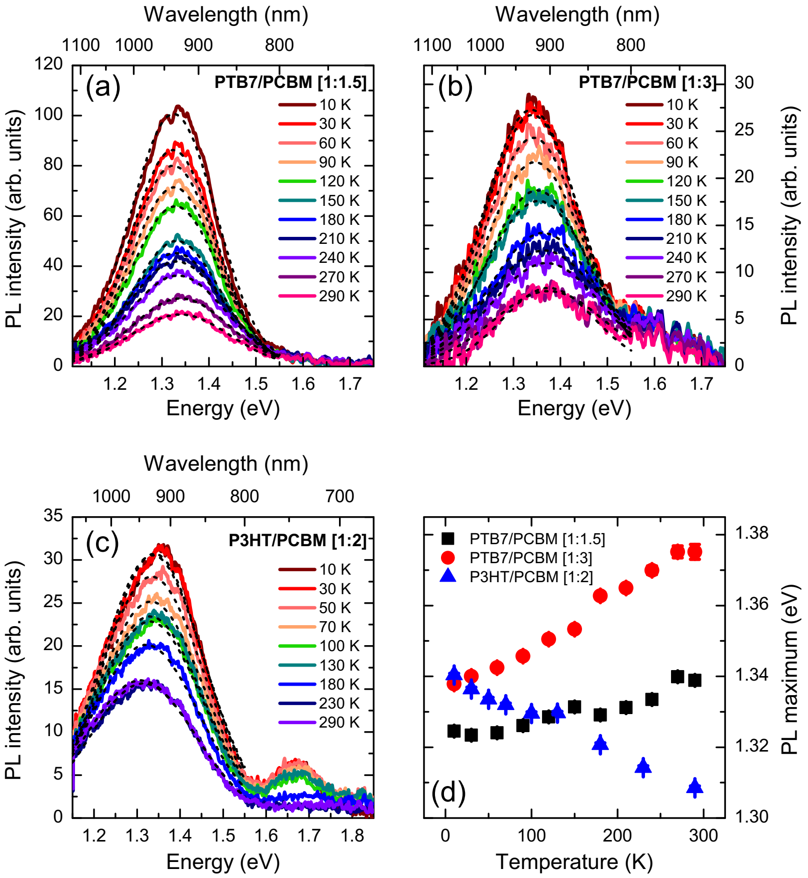

Figure 5.13.: Temperature-dependent spectra of the CT emission. Spectra were integrated over the time range, where the PL emission is dominated by the CT signature. In case of PTB7/PCBM (panels (a) and (b)), the spectra were integrated over the time range beyond 200 ps after the PL maximum and in case of P3HT/PCBM (panel (c)), CT spectra were extracted from a time range starting at 400 ps after the PL maximum. The maxima of the CT signatures were approximated with a Gaussian fit and the resulting peak energies are presented in panel (d).

P3HT/PCBM, suggesting that the actual quenching process of the CT states occurs on a time scale, which is much shorter than the decay of the CT state. This finding suggests that the emissive CT states in P3HT/PCBM should be interpreted as interfacial traps, from which charge separation by means of thermal energy is unlikely. This finding corroborates the work of Jarzab et al. [171], who found that the dynamics of the CT emission in the OPV system PCPDTBT/PCBM is not altered by temperature, in contrast to the overall amplitude. Based on this result, they suggested the presence of a 'hot' precursor state, which can either promote charge generation or relax into an emissive CT state with trapping character. The hypothesis of high-energetic precursor state is also consistent with other work evidencing charge generation via energetically excited or delocalized intermediate states [85, 153, 154, 164, 172]. On the other hand, the result challenges classical Onsager theory [94] and other kinetic models, in which the electron-hole pairs are assumed to overcome their mutual Coulomb interaction in a diffusive manner. A different picture arises for the PTB7/PCBM blends: Here, the

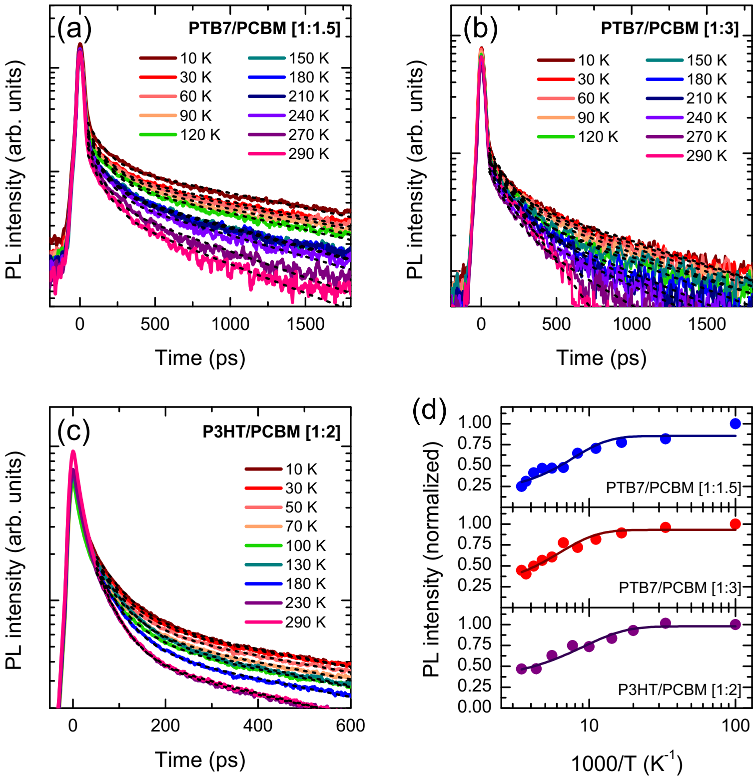

Figure 5.14.: Temperature-dependent PL transients of PTB7/PCBM (a) and (b) and P3HT/PCBM (c). The CT intensities were quantified with a biexponential model function as described in the text. The resulting values normalized to the emission at 10 K are plotted in panel (d) as a function of reciprocal temperature. The solid curves correspond to fits employing a thermal activation model (see Eq. 5.4).

CT emission reveals multiexponential decay dynamics, which depend strongly on temperature, suggesting that a diffusive mechanism starting from the energetically relaxed CT states leads to efficient quenching of the CT population. This dynamic quenching mechanism is more efficient in the [1:3] blend, as indicated by the stronger temperature dependence and the overall faster decay PL of the PL transients, suggesting that CT dissociation is in particular driven by electron migration. However, the optimized stochiometric ratio in the PTB7/PCBM system is 1:1.5 [125], where the higher polymer fraction establishes more efficient hole transport.

In order to quantify the CT intensity, the transients shown in Fig. 5.14 were fitted with a biexponential model function $I(t) = A_1 \exp(-t/\tau_1) + A_2 \exp(-t/\tau_2)$. In case of PTB7/PCBM, the fit matches the multiexponential decay of the CT emission well, when the initial singlet emission in the time range below the first 50 ps after the PL maximum is excluded from the fit range. The integral over the CT emission is then given by $I_{CT} = A_1\tau_1 + A_2\tau_2$. The CT emission in P3HT/PCBM on the other hand overlaps to a larger extent with the signatures of singlet emission in P3HT. Thus, in this case, the short-lived component is attributed to singlet emission and the CT intensity is approximated with the intensity of the long-lived contribution, which is given by the product $A_2\tau_2$. From the slope of the PL intensity as a function of temperature, an activation barrier for the quenching of CT states can be estimated via

$$I(T) = \frac{a}{1 + b\exp(-\frac{E_a}{k_B T})} \,, \tag{5.4}$$

Where a and b are free parameters[3] and E_a is the activation energy. This simple activation model was fit to the intensity data, as shown in Fig. 5.14(d). The resulting activation barriers for CT quenching in the respective blends are summarized in Tab. 5.3, together with the yield of thermal CT quenching η_{th}, which was calculated from the ratio of the CT intensity at 10 K and at room temperature via

$$\eta_{th} = 1 - \frac{I[10\,\mathrm{K}]}{I[290\,\mathrm{K}]} \,. \tag{5.5}$$

Based on the previous statements regarding the manifold of CT energies and the disordered nature of organic systems, the value of E_a should be rather considered as an effective barrier, which may be subject to strong fluctuations according to the microscopic environment of the CT state. In particular for P3HT/PCBM, the physical meaning of the derived activation energy is questionable, because thermal activation of a presumably ultrafast dissociation channel should lead to a rather abrupt decrease of the CT intensity around the temperature corresponding to the activation energy. Furthermore, the relatively small activation energy of 18.5 meV for CT quenching in P3HT/PCBM is inconsistent with the CT quenching yield of only 53 %, which illustrates that about half of the emissive CT population is still present at room temperature, suggesting that only a small subset of CT states in this system can be associated with the relatively weak dissociation barrier obtained by the fit. For the PTB7/PCBM blends on the other hand, the thermal quenching yield of 55-75 % appears to be a realistic quantity, regarding the activation barriers on the order of 30 meV. However, also for PTB7/PCBM, it is important to consider that there is a manifold of underlying CT binding energies. For example, the values of E_a obtained for the quenching of the overall CT intensity deviate from the activation energies, which are obtained, when only the long-lived component of the CT emission is taken into account. Evaluation of the intensity of the long-lived CT component yields $E_a = 35\,\mathrm{meV}$ for the [1:1.5] blend and $E_a = 28\,\mathrm{meV}$ for the [1:3] blend (see Ref. [17]).

A major result of the phenomenological approach employing the activation model arises from the fact, that relatively small activation barriers for thermal CT quenching are present in both investigated material systems. The values of E_a are on the order of the product $k_B T$ at room temperature ($\approx 25\,\mathrm{meV}$) suggest that efficient dissociation of CT states at room temperature is possible in these systems, albeit a certain subset of the CT population in P3HT/PCBM seems to be more strongly trapped.

---

[3] The parameter a accounts for the PL intensity and b reflects the ratio of the radiative and non-radiative decay times, i.e. $b = \tau_r/\tau_{nr}$, see for example Ref. [173].

Table 5.3.: Activation energies E_a and the yield of thermal quenching (see Eq. 5.5) derived from temperature-dependent studies of the CT emission. The values are obtained by fitting Eq. 5.4 to the PL intensity data shown in Fig. 5.14(d).

Sample	E_a (meV)	η_{th} (%)
PTB7/PCBM [1:1.5]	32.1 ± 6.6	75.1
PTB7/PCBM [1:3]	28.0 ± 6.6	55.4
P3HT/PCBM [1:2]	18.5 ± 4.6	53.2

5.5. Discussion

The intermixing studies of different polymer/fullerene blends have evidenced a strong correlation between the material morphology and the PL properties. In both systems, the yield of the CT emission appears to be correlated with the occurrence of an amorphous polymer phase, which is intimately mixed with molecular dispersed fullerene or smaller fullerene agglomerates. The statement that CT emission is related to a disordered and intermixed polymer phase has also been made in previous work based on luminescence [8, 174, 175] and transient absorption studies [119, 120, 176, 177]. An interesting observation in this context is that the CT signatures probed by photoluminescence and electroluminescence are not mandatorily identical, as pointed out by Tvingstedt et al. [175]. They argue that CT states created after charge injection preferentially recombine in regions of higher molecular ordering (i.e. more extended donor or acceptor domains), because charge transport in the intermixed phase is less efficient. When the CT states are on the other hand generated via optical excitation, ordered and disordered phases of the blend are addressed to a similar extent and CT emission may preferentially occur in the intermixed phases, where the dissociation probability is likely to be reduced. For the peak energy of the CT emission in the P3HT/PCBM [1:2] blend at room temperature, an energy of 1.34 eV has been measured. This energy is in fact higher than the peak energy obtained from electroluminescence studies (1.03 eV [174]). Also for PTB7/PCBM, there is a discrepancy between the reported EL emission maximum (1.27 eV [178]) and the maximum of the CT emission, which is 1.34 eV at room temperature in the investigated [1:1.5] blend. The lower discrepancy between PL and EL emission in case of PTB7/PCBM however indicates that the photoexcited species formed by the respective method do not substantially alter from each other. This is a plausible result, because in PTB7/PCBM charge generation assumedly occurs to a large degree in the amorphous polymer phase, which therefore should reveal good charge transport properties, allowing injected carriers to reach the same interfacial sites as the optically created CT states. Thus, the presence of amorphous polymer phases does not necessarily give rise to major losses.

Another interesting observation made for the CT emission in PTB7/PCBM is the blue shift of the signature with increasing fullerene content. This finding contrasts with reports on other material systems, where the CT emission was found to red shift with increasing amount of PCBM [134, 171, 179–181]. The red-shift was originally attributed to an increase of the average dielectric constant with increasing fullerene fraction [179, 180]. However, Bernardo et al. stated that crystallization of the fullerene component might be the key feature to account for the full red-shift [134]. A reason for the blue shift of the CT emission with increasing PCBM fraction evidenced for PTB7/PCBM might be the fact that the emission energy is correlated with the separation of the charges within the CT state. A higher separation leads to weaker Coulombic interaction and thus to a higher emission energy. This hypothesis is corroborated by the observed faster decay of CT states in the PTB7 blend with higher PCBM fraction, suggesting that charges separate more efficiently when a higher portion of PCBM offers more percolation paths for the electrons to escape. This finding could also explain, why the optimum stochiometric ratio in copolymer/fullerene systems typically comprises an excess of PCBM. In P3HT/PCBM on the other hand, no blue shift of the CT emission is observed, suggesting that a higher PCBM fraction does not promote charge separation in the amorphous phase.

Regarding the energetics of the CT state it is also worth mentioning the energetic offset between the singlet and the CT emission, which differs strongly among the two studied material systems. In P3HT/PCBM the CT energy is 570 meV below the singlet level and in PTB7/PCBM it is only 250 meV. The lower energy offset implies reduced thermalization losses because of the more favorable energy level alignment. On the other hand, in several systems employing low-bandgap polymers, triplet generation from the CT state via $^3CT \rightleftharpoons {}^3CT \rightarrow T_1$ has to be considered as a relevant loss mechanism, when the triplet energy level T_1 of the polymer is below the CT level [178, 182, 183]. The triplet level of PTB7 is estimated to 0.9 eV [178], therefore triplet generation from the CT states is generally possible. However, the experimentally observed rate of the CT decay on the order of 1 ns^{-1} is much higher than the typically expected rate of intersystem crossing, therefore it is expected that the influence of triplet generation on CT decay dynamics is rather small.

The last important finding of this chapter is that the CT features probed in P3HT/PCBM and PTB7/PCBM reveal significant differences regarding their temperature dependence: In case of P3HT/PCBM, the peak energy of CT signature red-shifts with increasing temperature and the CT dynamics depends only weakly on temperature. In PTB7/PCBM on the other hand, a thermally induced blue-shift of the CT peak and faster decay at room temperature have been observed. To explain these discrepancies, it has been hypothesized that the relaxed and emissive CT states in the respective systems possess different tendencies to get quenched via exciton dissociation. Despite the presumably strong trapping character of the CT state in P3HT/PCBM, which is indicated by the temperature-independent CT dynamics, significant thermal quenching is observed in this system. This could be due to charge separation on a much shorter time scale via a 'hot' precursor state. Such an intermediate state could for example be a vibronically excited or a more delocalized state, which is isoenergetic with charge separated states. For PTB7/PCBM on the other hand, the faster dynamic decay of the CT emission with increasing temperature indicates that even the energetically relaxed CT state can undergo quenching with the help of thermal energy. The substantial difference of these processes is illustrated in the energy level scheme in Fig. 5.15.

The thermal activation barriers for CT quenching are on the order of 20-30 meV, suggesting that the CT states (or at least their precursor states) are only weakly bound, as required for an efficient OPV system. However, from thermal quenching studies it is difficult to make a statement about the question how precisely the experimentally derived activation energies actually reflect the energetics of the whole ensemble of CT states. It has already been pointed out that disorder at the interface leads to a manifold of CT binding energies and therefore it is likely, that a certain subset of the CT population reveals binding energies considerably larger than k_BT. Field-dependent TRPL studies are an instructive method to further investigate the mechanism and the underlying energetics of exciton separation. This will be carried out in the next chapter, which will exclusively focus on the PTB7/PCBM device with a [1:1.5] mixing ratio. Similar studies for P3HT/PCBM would be desirable as well, however, the superimposed and longer lived singlet emission makes the analysis of this system more challenging and furthermore, preliminary field-dependent experiments with a P3HT/PCBM device evidenced strong influence of a space charge zone on the quenching characteristics, leading to presumably inhomogeneous distribution of the electric field inside the device. Nevertheless, a comparative study of field-induced PL quenching in P3HT/PCBM should be subject of future work.

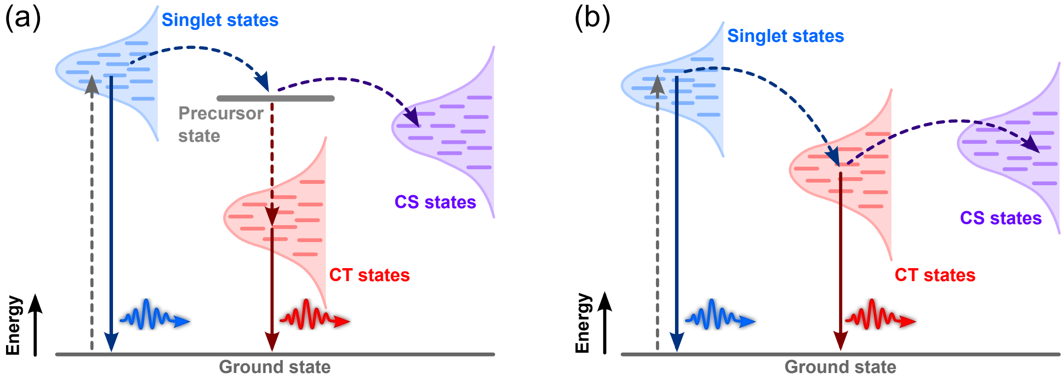

Figure 5.15.: Energetic scheme illustrating charge separation via an energetically excited precursor state (a) and via thermally relaxed CT states (b). When there is a 'hot' precursor state for charge generation, the CT states are expected to act as interfacial traps.

5.6. Summary

This chapter has focused on the intermixing effects in two BHJ systems, P3HT/PC$_{61}$BM and PTP7/PC$_{71}$BM, respectively. In the P3HT-based blends, the emission of the polymer has been found to decay by a factor of 10 faster than in the neat material due to quenching of the diffusive singlet excitons at the donor/acceptor interface. In addition to this dynamic quenching, which is driven by exciton diffusion, large portions of the singlet population are quenched on a sub-ps timescale. Similar findings were made for singlet excitons in the fullerene phase of the PTB7-based blends. The decay of the PTB7 signature in the blends on the other hand was faster than the instrument response time, indicating fast and efficient charge transfer from the polymer phase. Beside the singlet signatures, the TRPL data of the blends evidenced longer-lived broad and fainter signatures peaking around 1.3 eV, which have been attributed to CT states. In both systems, the emissive CT yield was found to be correlated with the occurrence of an amorphous polymer phase, which is intimately mixed with fullerene agglomerates. This has been evidenced by studying blends with different polymer/-fullerene mixing ratios and after varying the excitation conditions between selective excitation of the polymer phase and preferential excitation of the fullerene phase in case of PTB7/PCBM. Overall, the TRPL results are in good agreement with existent morphological studies. In both systems, the weak dependence of the CT dynamics on the excitation power indicates that the CT states are rather localized. This argument is further supported by considering the presumably low exchange and dipole interactions between the CT states impeding Förster and Dexter transfer. The CT signatures evidenced for P3HT/PCBM and PTB7/PCBM vary in terms of their temperature dependence: In P3HT/PCBM the CT dynamics is not significantly altered with increasing temperature, whereas the thermally induced dynamic quenching in case of PTB7/PCBM indicates that even the energetically relaxed CT state at the interface can be dissociated at room temperature.

Chapter 6

Field-induced luminescence quenching: Accessing exciton binding energies

In organic semiconductors, the strong Coulomb interactions and associated with this the stabilization of the excitonic states lead to the remarkable offset between the optical band gap and the threshold for charge generation, which is typically some 100 meV above the absorption edge [38]. Originally, the strong discrepancies between the optical and the electronic band gap were interpreted in terms of rapid polaron formation after excitation of conductive band states [64, 65]. However, the exciton picture is in much better agreement with experimental results, in particular with the phenomenon of spectral relaxation of the PL emission, as discussed in Ch. 4. The experimentally observed exciton binding energies in conjugated polymers are on the order of several hundreds of meV [38, 75, 76]. A common approach to access the exciton binding energy in experiments is to apply an electric field, in order to measure the field-dependent photocurrent yield [38, 97, 156], the field-induced changes in differential absorption [184] or the field-induced PL quenching [37, 75, 76, 185]. The threshold field at which charge extraction or PL quenching emerge is then related to the exciton binding energy. Further interpretation of the results requires a theoretical (and preferably analytical) model to predict the field and temperature dependency of the exciton separation process.

In the framework of this thesis, the field-induced luminescence quenching of a neat PTB7 device and a PTB7/PCBM blend device has been studied for different temperatures. A kinetic model based on a hopping mechanism [15] is applied to extract exciton binding energies from the recorded PL quenching data. A particular advantage of time-resolved studies is that they allow to test the validity of kinetic models, in particular regarding the predicted decay dynamics. After studying the quenching of singlet excitons in a neat polymer device, the same model is applied to CT states at the interface. For detailed studies of the PL quenching, the system PTB7/PCBM is chosen, as it allows for selective studies of different excited species (see Ch. 5). In particular, the rapidly decaying emission of singlet states in the blend does not strongly interfere with the CT emission, when the excitation wavelength is around 700 nm. From kinetic modeling, it turns out that the strong temperature dependence of the CT PL intensity, even in the absence of an electric field, can only be explained when the binding energy of electron-hole pairs at the interface is about one order of magnitude smaller than the binding energy of singlet excitons, i.e. the mutual Coulomb potential of geminate pairs is screened to a large extent at the interface. Furthermore, disorder plays an important role and has to be considered for an appropriate description of the exciton separation process.

The first part of this chapter introduces the procedure of kinetic modeling, which is based on Rubel's model of hopping dissociation from a one-dimensional Coulomb potential [15] (see Ch. 2.5.4). The experimental section first describes the applied methodology for field-induced luminescence quenching studies. Before discussing the actual results, it needs to be substantiated that the measured quenching phenomena are in fact due to exciton separation and do not result from other phenomena, such as exciton-charge annihilation or sample degradation. Subsequently, temperature- and field-dependent PL quenching measurements are presented, together with fits of the kinetic model and a discussion of the extracted parameters. The concluding discussion is particularly aimed at the important finding of weakly bound CT states at the interface and will put this result into the broader context of concurring theories about the underlying mechanisms of efficient charge generation in organic solar cells. Parts of the results presented here are planned to be published in Ref. [17].

6.1. Measurement and kinetic modeling of field-induced luminescence quenching

For field-dependent PL measurements, the experimental setup described in Ch. 3 was equipped with a programmable source meter in order to apply bias to the devices mounted in the cryostat. A device comprising a neat PTB7 film with a thickness of 120 nm was used to study the quenching of singlet excitons in the polymer. The excitation wavelength for the pristine film was set to 450 nm. A neat PCBM device on the other hand was found to be not stable enough for field-dependent studies. However, as evidenced in the previous chapter, the quenching of singlet excitons in PCBM can also be studied in PTB7/PCBM blends with appropriate excitaiton conditions. The blend device studied herein comprised a 72.5 nm active layer with a PCBM content of 60 % (weight). To study the quenching of PCBM excitons, the excitation wavelength was set to 400 nm. The quenching of CT states was probed using an excitation wavelength of 705 nm. The excitation intensities were set to sufficiently low values to avoid sample degradation, but high enough for an acceptable signal-to-noise ratio, i.e. to values around 0.1 $\mu\mathrm{Jcm}^{-2}$ to probe singlet excitons in PTB7 and PCBM and to 2.7 $\mu\mathrm{Jcm}^{-2}$ for CT states in the blend device, respectively. The excitation conditions allowed for reproducible studies of the same sample spot over the whole investigated temperature range.

In order to measure the field-induced luminescence quenching, the PL intensity was recorded for different electric fields and compared to a reference measurement without external field. The amount of quenching Q was then calculated via the ratio of the PL intensity of the biased device $I(F)$ and the PL intensity without external field $I(0)$:

$$Q_{exp}(F,T) = 1 - \frac{I(F,T)}{I(0,T)} \tag{6.1}$$

For kinetic modeling of the quenching process, a general consideration is the competition between field-induced exciton separation and recombination. The latter is assumed to be field-independent. As introduced in Ch. 2.5.2, the PL yield is given by the ratio of the competing rates of recombination and dissociation

$$\eta_{PL}(F,T) = \frac{k_r}{k_r + k_{nr} + k_D(F,T)} \; . \tag{6.2}$$

Here, k_r and k_{nr} are the rates of radiative and non-radiative recombination, which are assumed to have negligible field and temperature dependence and $k_D(F,T)$ denotes the field- and temperature-dependent dissociation rate. In the following section, the field and temperature dependent hopping rate suggested by Rubel et al. [15] (see Ch. 2.5.4, Eq. 2.38) is used to model the field-induced luminescence quenching. Theoretical quenching curves can then be obtained via the luminescence yield $\eta(F,T)$ presented in Eq. 6.2:

$$Q_{theo}(F,T) = 1 - \frac{\eta_{PL}(F,T)}{\eta_{PL}I(0,T)} \; . \tag{6.3}$$

To reduce the amount of fitting variables in the model described in Ch. 2.5.4 (see Eqns. 2.33, 2.34 and 2.38-2.40), several parameters were fixed to values known or estimated from the literature; i.e. the dielectric constant ε_r was estimated to 3 for PTB7, 3.9 for PCBM and 3.4 for the interface, in accordance with previous reports [15, 27, 76, 186, 187], and the parameter of the attempt-to-escape frequency ν_0 was estimated to a typically assumed extent of $1 \times 10^{13}\,\mathrm{s}^{-1}$ [15, 97]. Furthermore, the sum of the radiative and the non-radiative decay rates corresponds to the inverse of the experimentally determined PL lifetime, i.e. $k_r + k_{nr} = \tau_{PL}^{-1}$. Assuming temperature- and field-independent radiative and non-radiative decay rates, it is not necessary to know the actual radiative lifetime. Generally, it was possible to find good agreement between the experimental quenching data and the kinetic model by varying four parameters: The site separation r_0, the localization parameter α and the disorder parameters δr and σ. As the simulated dissociation rate is calculated from the average over a manifold of *randomly* created dissociation paths defined by δr and σ, fitting the kinetic model to experimental data is time-consuming (several hours). As a first approximation, good matches between experimental and modeled quenching data are obtained 'by hand', considering reasonable parameters of $r_0 \approx 1\,\mathrm{nm}$ and $\sigma \approx 50\,\mathrm{meV}$. A sufficiently high amount of simulation runs needs to be performed, to avoid random fluctuations of the averaged quenching curves. A number of M=10^4 runs was found to be sufficient for each data point $Q(F,T)$. Beside manual adjustment of the parameters, the standard deviation between experimental and theoretical data defined by

$$\Delta Q = \sqrt{\frac{1}{N-1} \sum_{F,T} \left[Q_{exp}(F,T) - Q_{theo}(F,T)\right]^2} \tag{6.4}$$

was minimized using an unconstrained downhill-simplex algorithm [188], available in *MATLAB* via the *fminsearch* function. Here, N defines the number of data points, Q_{exp} is the experimental and Q_{theo} the theoretical quenching data. For a series of field and temperature dependent measurements, the same set of parameters was used to fit the whole amount of PL quenching data $Q(F,T)$.

Before giving an adequate interpretation of the experimental results based on this approach, however, two issues need to be clarified: (i) Does the experimentally observed PL quenching in fact result from field-induced exciton separation and (ii) how does the externally applied electric field relate to the actual field experienced by the excitons? A brief discussion of both aspects shall be given herein, before the actual results of exciton quenching are discussed with regard to underlying binding energies and disorder scales.

6.1.1. Influences on luminescence quenching

Current/voltage (JV)-curves of the PTB7 and the blend device under illumination are presented in Fig. 6.1. The different work functions of the electrodes lead to pronounced non-ohmic JV-characteristics. Due to the high currents in forward direction, all field-dependent measurements were performed under reverse bias. However, even for the relatively low injected current under reverse bias, it should be excluded that the measured PL quenching results from exciton-charge annihilation. To ensure that exciton quenching is in fact driven by the electric field, control measurements were performed with voltage applied in forward direction. For example, a reverse bias of $-20\,\mathrm{V}$ leads to significant PL quenching in the neat PTB7 device (see Fig. 6.2(a)) and the corresponding current is 26 mA. The same current in forward direction is already reached at a bias of 1.6 V, however, this does not lead to any noticeable changes in the PL intensity and dynamics. Similar control measurements have been performed for the blend device under 400 and 705 nm excitation without evidencing any PL quenching resulting from the high currents in forward direction (Fig. 6.2(b) and (c)). Thus, the injected current seems not to impact the PL properties.

It turns out that similar conclusions can be drawn for the photocurrent. In order to investigate, whether photogenerated charges do influence the quenching characteristics, the excitation intensity was varied between 0.03 and 1 mW for the PTB7 device and between 1 and 10 mW for the PTB7/PCBM device and the PL intensity was recorded for different electric fields at room temperature. Due to the superimposed singlet emission at early times after excitation, the CT intensity was estimated from biexponential fits,

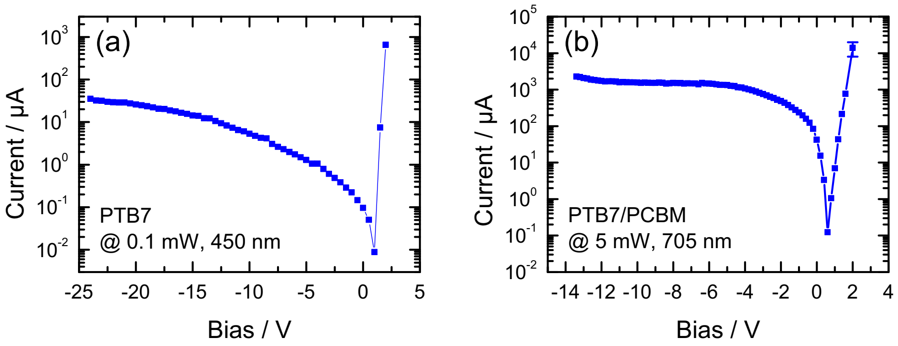

Figure 6.1.: JV curves of (a) the pristine PTB7 device and (b) the blend under illumination.

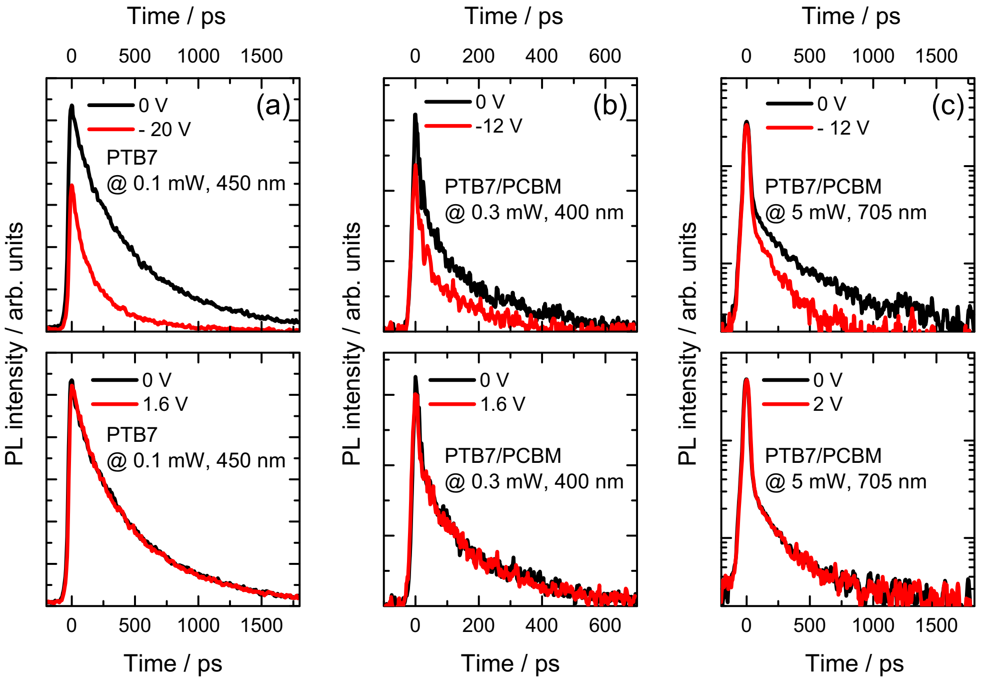

Figure 6.2.: PL transients under forward and reverse bias. The forward bias was chosen such that the resulting forward current is larger or equal to the value corresponding to a reverse bias with significant PL quenching. Panel (a): Neat PTB7 device; (b) PTB7/PCBM device excited at 400 nm, corresponding to preferential excitation of singlet excitons in PCBM and (c): PL transients of the PTB7/PCBM device excited at 705 nm, corresponding to selective excitation of the polymer/-fullerene mix phase with a higher yield of CT emission.

as introduced in Ch. 5. The amount of quenching Q was then calculated via Eq. 6.1 and the resulting quenching curves for different excitation intensities are presented in Fig. 6.3. Their slope is identical for all investigated excitation intensities, indicating that there is no growing influence of quenching due to free charges neither in the neat PTB7 device nor in the blend.

Another reason for luminescence quenching could be reduced oscillator strength, when the electronic structure is altered by the external field (*Stark effect*). When the radiative rate is decreased, the time-integrated PL intensity is reduced in the presence of non-radiative decay channels [189]. However, in case of PTB7, no significant impact on the oscillator strength and no pronounced Stark shift of the PL signatures are observed. Field-dependent PL spectra and transients recorded at 10 K are presented in Fig. 6.4. The spectra were reconstructed by multi-Gaussian fits, but based on this analysis, no red-shift of any feature larger than 8 meV could be identified. This is even less than the field-induced red-shift of 20 meV, which has been observed for a device based on the polymer MEH-PPV biased at $2 \times 10^8\,\mathrm{Vm}^{-1}$ [36, 189]. An obvious explanation for the negligible Stark shift arises from simple geometrical considerations: The polarizability and thus, the oscillator strength of single chromophores is highly anisotropic. As a consequence, absorption occurs preferentially in chromophores arranged parallel to the polarization of the excitation laser and likewise, the PL emission will be recorded preferentially from sites aligned in a plane parallel to the device electrodes. For chromophores comprising this orientation, however, the Stark shift is minimal, because

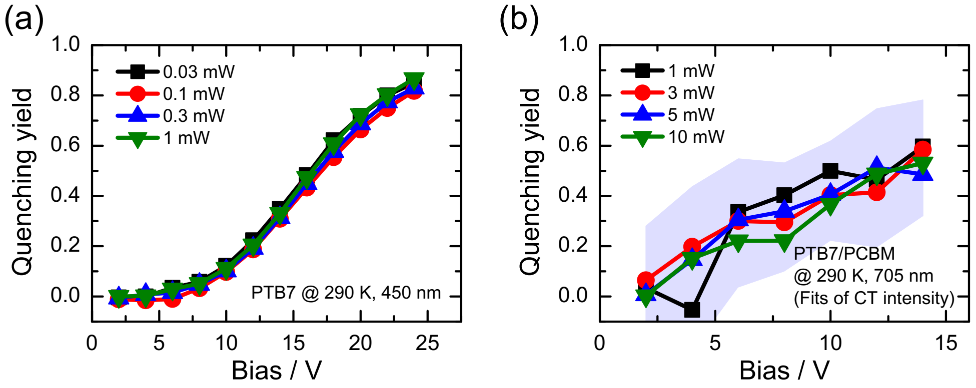

Figure 6.3.: Field-dependent PL quenching for different excitation intensities. (a): Pristine PTB7 device; (b): CT-quenching in the blend device. The contribution of CT emission to the overall PL of the blend was extracted via biexponential fits of the long-lived component of the CT emission. The shaded area correspondes to the uncertainty of the quenching yield, based on the standard errors of the fitting parameters. The figure is reprinted from the supporting information of Ref. [17].

they are arranged perpendicular to the electric field.

The PL intensity could also be altered due to sample degradation. A particular degradation mechanism for PTB7 is photo-oxidation via singlet oxygen, which is formed when triplet states are quenched by ambient O_2 [166, 190]. Under vacuum, which was 10^{-5}-10^{-6} mbar in the experiments presented here, this process is unlikely to occur. However, also high illumination intensities and long exposure times to electric fields were found to decrease the PL intensity irreversibly on a time scale of a few tens of seconds, indicating that either thermally or current-induced degradation increases the number of non-radiative recombination centers. In order to minimize this effect, the excitation intensities were set to sufficiently low values, as summarized in the description of Fig. 6.4. Furthermore, exposure times to an electric field were kept as short as possible, typically between 10 and 20 s for each bias step, with regard to an acceptable signal-to-noise ratio. In order to calculate the amount of PL quenching, control measurements without electric field were performed before and after each step in the bias sweep. The average of the PL intensities of the control measurements before and after a biased measurement was used as a reference value to calculate the PL quenching for the respective bias. The complete data sets of temperature and field dependent PL intensities including control measurements for the three investigated excitonic species are summarized in the appendix (Ch. B).

6.1.2. The role of intrinsic fields

The reasons for discrepancies between the externally applied and the actual electric field in the vicinity of the probed excitons are manifold. An obvious source of uncertainties is given by the limited accuracy in determining the sample thickness. In the experiments described here, the thickness of the active layers was measured with a profilometer, yielding a precision of $\Delta d = \pm 2.5$ nm. For a layer thickness of $d = 120$ nm (neat PTB7 device), this translates into an accuracy of $\Delta F/F = \Delta d/(d + \Delta d) = 2.0\,\%$ and for the 72.5 nm layer of the blend device the precision is 3.2 %.

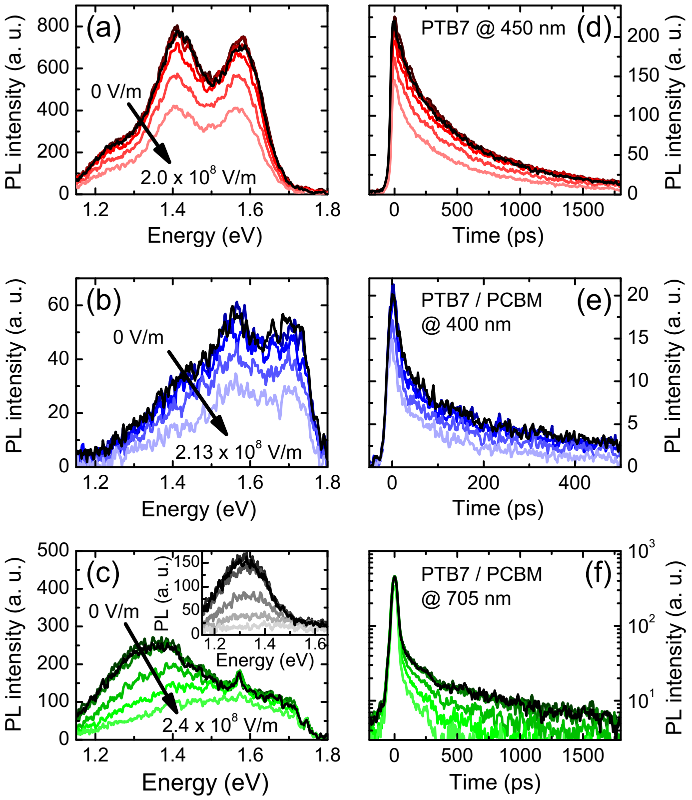

Figure 6.4.: Bias-dependent PL spectra (a)-(c) and transients (d)-(f) recorded at 10 K. Upper row: Pristine PTB7 device excited at 450 nm (2.76 eV) and 0.1 mW, corresponding to an energy fluence of ca. 0.1 µJcm^{-2}, middle row: Blend device excited at 400 nm (3.1 eV, 0.3 mW, 0.09 µJcm^{-2}), corresponding to preferential excitation of PCBM; lower row: Blend device excited at 705 nm (1.76 eV, 5 mW, 2.7 µJcm^{-2}). The resulting PL after 705 nm excitation is a superposition of singlet emission from PTB7 and CT emission. The inset in panel (c) shows the contribution of CT emission, which was obtained by integrating the PL spectra over the time range between 100 and 2000 ps after excitation, where the singlet emission has already decayed. The figure is reprinted from Ref. [17].

Beside this general uncertainty, further deviations have to be taken into account. According to the different work functions of the electrode materials, an intrinsic field emerges in the studied devices under illumination, which is typically between 5×10^6 Vm^{-1} and 1×10^7 Vm^{-1} [191]. The JV curves recorded under illumination presented in Fig. 6.1 indicate that the internal fields of the neat PTB7 and the blend device are on the same order of magnitude, when they are illuminated with the laser. Furthermore, it has been reported that the open-circuit voltage V_{OC} is temperature-dependent. For PTB7/PCBM, a linear decrease of V_{OC} with increasing temperature has been observed [192, 193], in good agreement with theoretical predictions based on the assumption of equal quasi-Fermi levels in metal-semiconductor-metal devices [194]. For varying the device temperature between 77 K and 295 K, Ebenhoch et al. [193] find a variation of the open circuit voltage of about 0.2 V. Assuming a linear correlation between V_{OC} and T and extrapolating the temperature-dependent shift of V_{OC} to 10 K yields an expectable change of V_{OC} on the order of 0.26 V over the investigated temperature range, corresponding to a variation of the intrinsic field of 3.5×10^6 Vm^{-1} for the PTB7/PCBM device when the sample temperature is varied between 10 and

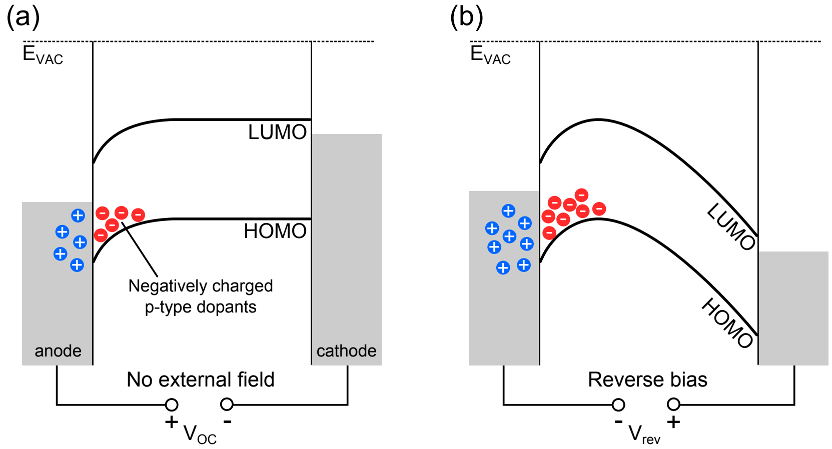

Figure 6.5.: Scheme of the energy level alignment in a p-type metal-semiconductor-metal structure with the formation of a space-charge-zone at the anode under open-circuit conditions (a). The space-charge zone is even enlarged when bias in reverse direction V_{rev} is applied to the device (b). Negative charges represent charged acceptor states.

290 K. The range of electric fields investigated here is more than one order of magnitude above the expected temperature-induced change of the intrinsic field related to the open circuit voltage.

Another limitation regarding the accuracy of the electric field might arise from space charge zones at the electrodes. It has been demonstrated that such space charge zones can lead to significant deviations from the intrinsic field, which is reflected by the different quenching characteristics for excitation of the anode and cathode, respectively [189]. For conjugated polymers, in particular for P3HT, high amounts of intrinsic dopants and connected with this high concentrations of p-type carriers have been evidenced [195, 196]. This could in turn lead to the formation of a depletion layer at the anode. The situation under open circuit conditions is illustrated in Fig. 6.5: At the junction between the metal electrode and the polymer layer, a certain amount of p-type carriers diffuses from the active layer into the metal, leaving behind some negatively charged defect states. As a consequence, a space charge zone is formed, inducing

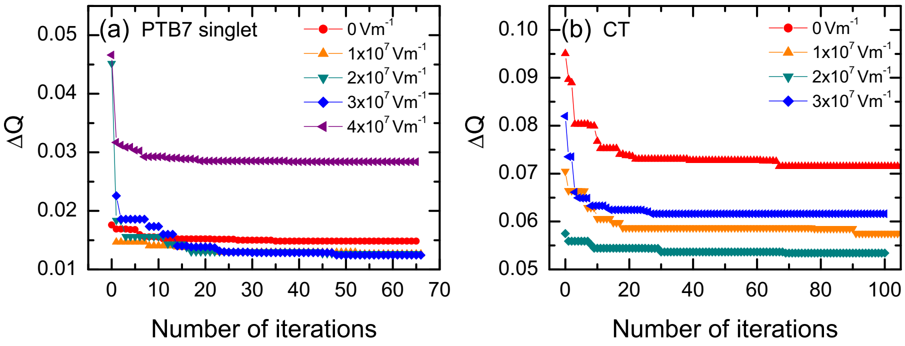

Figure 6.6.: Evolution of the standard deviation during optimization of the parameter set via downhill-simplex algorithm. In order to investigate the influence of the intrinsic field, the fit was performed for several values of F_0.

band bending in the region of the active layer close to the interface. In the presence of such a space charge zone, the electric field inside the device cannot be assumed to be homogeneous and the ability of excitons to dissociate depends on the region where they are created after absorption of light. Even when the device is operated at short circuit conditions, implying zero external field (Fig. 6.5(a)), excitations close to the anode may be quenched in the space-charge field. When a bias in reverse direction is applied, the space charge zone expands and partly compensates for the external field in certain regions of the active layer. In fact, the experimentally obtained quenching curves evidence a slight increase of the PL intensity at low external fields, which could be due to such compensation effects.

According to the variety of influences on the actual field distribution inside the devices and the lacking knowledge about the underlying parameters, it is not possible to include the actual field distribution into the simple kinetic modeling performed in this work. However, phenomenologically, the agreement between experimental and modeled data is significantly improved, when a constant built-in field F_0 on the order of $1 \times 10^7 - 3 \times 10^7\,\mathrm{Vm}^1$ is considered, which is opposed to the external field. The evolution of the standard deviation ΔQ during the optimization procedure for different intrinsic fields is shown in Fig. 6.6. The best match is obtained for $F_0 = 3 \times 10^7\,\mathrm{Vm}^{-1}$ in case of neat PTB7 and $F_0 = 2 \times 10^7\,\mathrm{Vm}^{-1}$ for the blend device. The corresponding fit results for different values of F_0 are presented in Fig. 6.7. A detailed discussion regarding the underlying fit parameters is given in Ch. 6.1.4 and 6.1.5.

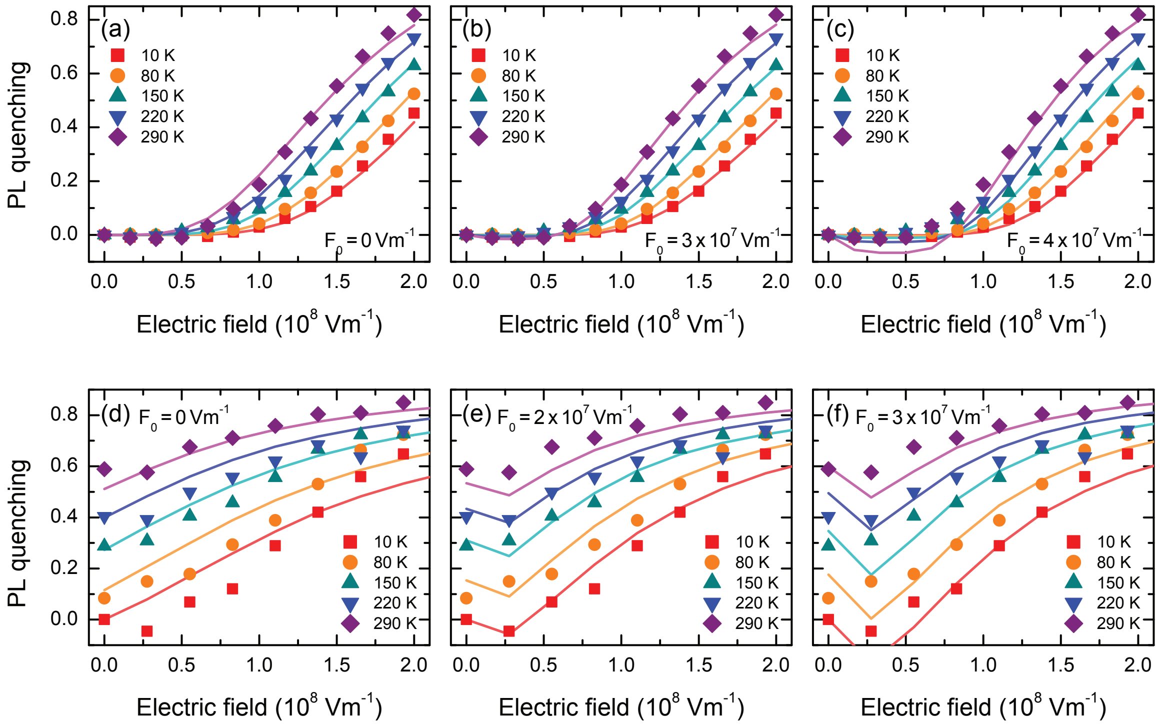

Figure 6.7.: Fits of the kinetic model to the experimental data, assuming various intrinsic fields F_0. (a)-(c): Quenching curves derived from the neat PTB7 device and (d)-(f): CT quenching data in the blend device.

6.1.3. The role of disorder

In order to reproduce the field- and temperature-dependent PL quenching data adequately with the kinetic model, it turns out that disorder needs to be taken into account. The discrepancies between experimental and modeled quenching are particularly large in the low-temperature regime. This is because the experimentally observed field-dependence of the PL quenching is relatively weak, even at temperatures around 10 K. Quenching curves recorded at low temperatures for the different probed excitonic species are shown in Fig. 6.8(a). At low temperatures, however, the kinetic models presented in Ch. 6.1 would predict an almost step-like increase of the quenching yield at a certain threshold field, which is related to the exciton binding energy. This is not observed in experiment, which strongly suggests that an underlying manifold of binding energies governs the actual quenching characteristics. This assumption is supported by the fact that organic semiconductors typically incorporate spatial and energetic disorder, leading to an individual vicinity for each photogenerated exciton. The discrepancies arising from disorder-free kinetic modeling are exemplified for the Onsager-Braun model (Ch. 2.5.3) in Fig. 6.8(b), which gives better agreement with the experimental data at room temperature but even at 290 K, the slope of the model function is too steep.

The influence of the disorder parameters in the kinetic model of Rubel et al. [15] is illustrated in Fig. 6.9 for a temperature of 80 K. Both the energetic and the spatial disorder lead to a significant flattening of the quenching curves. Additionally, increasing the energetic disorder parameter σ enhances the quenching probability at low electric fields. This implies that a higher fraction of excitons can already be quenched by the built-in field, which could be of particular relevance for CT states in OPV devices.

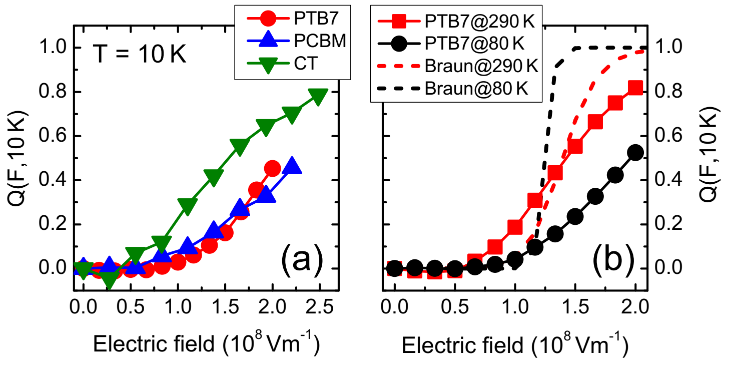

Figure 6.8.: (a) Experimental field-induced PL quenching data recorded for singlet and CT species at a temperature of 10 K and (b) quenching curves of the PTB7 singlet emission recorded at 80 K and 290 K in comparison to the slope predicted by the Onsager-Braun model (dotted curves) calculated from the dissociation rate presented in Eq. 2.32 using the parameters $\varepsilon_r = 3$ and $\mu\tau_r = 1 \times 10^{-17}\,\mathrm{V^2m^{-1}}$. The figure is reprinted with slight modifications from Ref. [17].

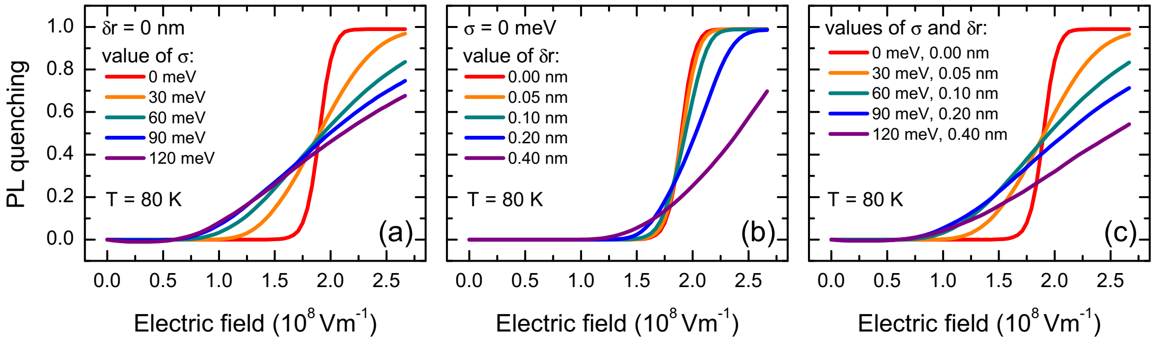

Figure 6.9.: Modeled PL quenching curves after Ref. [15] at a temperature of 80 K, using different values of the disorder parameters δr and σ: (a) Variation of σ for $\delta r = 0$ nm; (b) variation of δr fo $\sigma = 0$ meV and (c) simultaneous variation of σ and δr. The other parameters are similar to those in Tab. 6.1 for the PTB7 excitons.

6.1.4. Quenching of singlet states

The quenching of singlet excitons was investigated for a device comprising a neat PTB7 film and for a PTB7/PCBM blend device. The latter was excited at 400 nm, allowing for preferential excitation of the PCBM phase. Temperature-dependent quenching curves for both PTB7 and PCBM singlet excitons are presented in Fig. 6.10. Experimental data is represented by the symbols, whereas fits according to the kinetic model by Rubel et al. [15] are plotted as solid curves. The temperature dependence of the PCBM quenching curves is found to be weaker than for PTB7. The reason is that beside field-induced dissociation, another non-radiative quenching channel for excitons in the blend is dissociation at the PTB7/PCBM interface. As a consequence, the influence of the field-induced and temperature-dependent dissociation rate is weaker. As already evidenced in Ch. 5, the amount of interfacial quenching depends on the exciton diffusion rate and thus becomes more efficient with increasing temperature. This has been considered in the model by calculating the PL quenching yield from PL the decay times measured at the respective temperatures (see Tab. 6.1).0.6cm

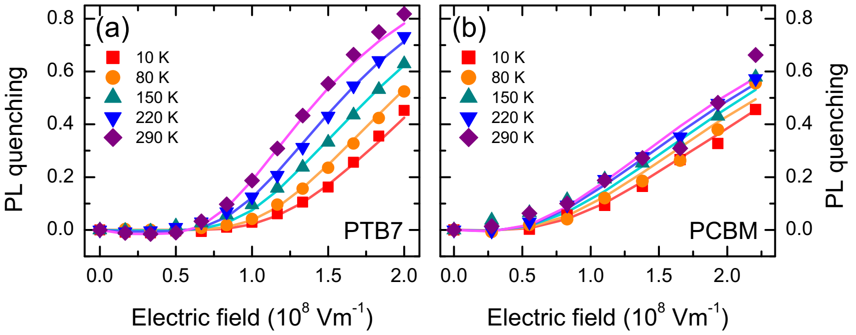

Figure 6.10.: Experimental PL data (symbols) of singlet exciton quenching in PTB7 (a) and PCBM (b) and best fits (solid lines) according to the model of Rubel et al. [15], based on the parameter sets summarized in Tab. 6.1. The figures are reprinted from Ref. [17] with slight modifications.

Table 6.1.: Model parameters for field-induced quenching of singlet excitons in PTB7 and PCBM, obtained from fits of the kinetic model by Rubel et al. [15] to experimental data. The parameters ε_r, ν_0, F_0, τ_{rad} and τ_{PL} were not varied during the fitting procedure, because they were either estimated from the literature or from experimental data. For PCBM, a diffusion-related faster decay of the PL with increasing temperature was taken into account by using different PL lifetimes: 110 ps at 10 K, 98 ps at 80 K, 94 ps at 150 K, 70 ps at 220 K and 65 ps at 290 K. The energy E_1 corresponds to the average exciton binding energy.

Parameter description	Parameter	PTB7	PCBM
Dielectric constant	ε_r	3	3.9
Attempt-to-escape frequency	ν_0 (s^{-1})	10^{13}	10^{13}
Intrinsic field	F_0 (Vm^{-1})	2×10^7	2×10^7
Radiative lifetime	τ_{rad} (ps)	500	390
PL lifetime	τ_{PL} (ps)	500	65...110
Site separation	r_0 (nm)	1.12	0.98
Localization length	α (nm)	0.52	0.54
Spatial disorder parameter	δr (nm)	0.07	0.23
Energetic disorder parameter	σ (meV)	52	99
Energy of first site	E_1 (meV)	420	377

The parameters for the quenching curves presented in Fig. 6.10 are summarized in Tab. 6.1. The value of E_1 in the last row denotes the energy of the first site of the model potential, calculated via Eq. 2.38 from r_0 and for $F = 0$. In an idealized material without intrinsic fields and disorder, a carrier would have to overcome the energy E_1 to get separated from the opposite charge. Thus, this energy can be interpreted as the exciton binding energy. However, this is an average value because the studied systems are subject to spatial and energetic disorder. The kinetic model yields reasonable values of binding energies of 420 meV for PTB7 and 377 meV for PCBM. The former value is in good agreement with values reported for other polymer systems [38, 76, 191].

In order to verify whether the applied kinetic model reproduces the experimentally observed PL dynamics, PL transients have been re-calculated via the convolution of the multiexponential decay with the Gaussian response function of the streak camera:

$$I(t,F,T) = \frac{1}{M}\int_{-\infty}^{\infty} \exp\left(-\frac{(t'-t)^2}{2w^2}\right)\sum_{i=1}^{M}\exp\left(-(k_r + k_{nr} + k_{D,i}(F,T))t'\right)\Theta(t')dt' \tag{6.5}$$

The width (FWHM) of the response function is ca. 25 ps, corresponding to the rise time of the PL transients recorded in experiment. Thus, the standard deviation w in Eq. 6.5 is $w = 25\,\text{ps}/2\sqrt{2\ln 2} \approx 10\,\text{ps}$. The value M is the number of simulation runs, each producing a unique disordered model potential with an individual field-dependent quenching rate $k_{D,i}(F,T)$. The inverse of the sum $k_r + k_{nr} + k_{D,i}(F,T)$ corresponds to the PL lifetime of the biased device. The experimentally obtained PL decay time enters

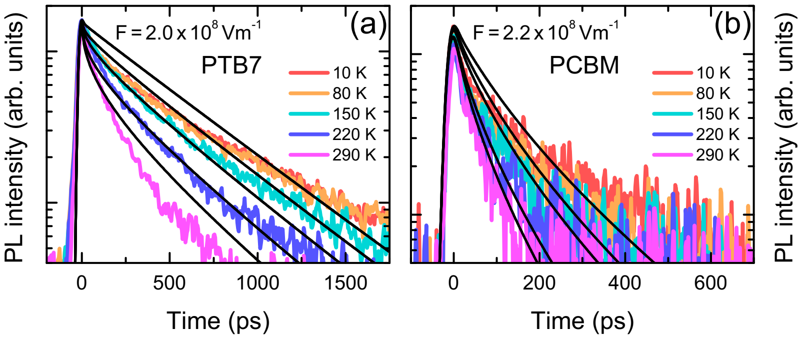

Figure 6.11.: PL transients for PTB7 (a) and PCBM (b) for temperatures between 10 and 290 K. The black curves are simulated data reconstructed from the parameters listed in Tab. 6.1 and the coloured curves represent experimental data. Panel (a) is reprinted from Ref. [17] with slight modifications.

the model via the inverse of the sum $k_r + k_{nr}$. The heavyside function $\Theta(t)$ induces a rise of the PL transient at $t = 0$. Exemplary simulated PL transients for various temperatures and for the highest applied field are presented in Fig. 6.11, together with experimental data. Generally, the kinetic model reproduces the field-induced changes of the PL-dynamics well, but in particular at low temperatures the decay of the experimentally recorded transients shows a pronounced multiexponential slope, which is not reproduced by the model. This is not surprising, because the influence of spectral diffusion, which has been discussed in Ch. 4, is not considered in the applied kinetic model, but becomes relevant at low temperatures. Another reason for multi-exponential decay in case of PCBM could be the varying cluster sizes in blends with PTB7 [11, 12], leading to a broad distribution of times the excitons need to diffuse to an interface, where they are quenched. At low temperatures, this process is slowed down, thus, the dispersion of diffusion-related non-radiative decay times is increased.

6.1.5. Quenching of charge transfer states

In the previous section, the experimentally determined quenching data of singlet states is in good agreement with the kinetic model based on the picture of hopping dissociation from a one-dimensional, disordered Coulomb potential. An essential difference between the singlet and CT states is, however, that the CT emission is already quenched with the help of thermal energy (see Ch. 5), whereas the intensity of the singlet emission is not significantly altered over the investigated range of temperatures. Without any further assumptions regarding the nature of the donor/acceptor interface, it turns out that the kinetic model applied so far cannot account for the strong temperature dependence of the CT intensity in the absence of an electric field. The high yield of thermal quenching indicates that the CT states are only weakly bound with regard to the singlet states, with binding energies on the order of $k_B T$ at room temperature. This implies that the Coulomb potential at the donor-acceptor interface is significantly flattened compared to the potential faced by singlet excitons. The simplistic approximation for the electrostatic potential described by 2.40 does not account for such screening effects. However, as further detailed in the discussion section (Ch. 6.2), the assumption of a shallow potential at the donor-acceptor interface is well-grounded [16, 52, 96, 155, 197–199]. In this work, no sophisticated treatment of the interfacial potential has been carried out. However, regardless of the underlying reasons for the weaker binding energy of electron-hole pairs at the donor/acceptor interface, screening can be empirically implemented by diminishing the depth of the potential in Eq. 2.40 by a factor f. The site energies are then given by

$$E_j(F) = E_j^0(\sigma) - f\frac{e^2}{4\pi\varepsilon_0\varepsilon_r r_j} - eFr_j \ . \tag{6.6}$$

Good agreement with the experimentally observed thermal quenching is obtained for $f \approx 0.1$. Experimental data and the corresponding fits are presented in Fig. 6.12(a). In order to illustrate the temperature dependence of the PL yield, the measured PL intensities have been related to the CT intensity at 10 K, i.e. the experimental and modeled PL quenching are calculated via

$$Q(F,T) = 1 - \frac{I(F,T)}{I(0\,\mathrm{Vm}^{-1}, 10\,\mathrm{K}}) \ . \tag{6.7}$$

The parameters resulting from the fit assuming an intrinsic field of $2 \times 10^7\,\mathrm{Vm}^{-1}$ are summarized in Tab. 6.2. The underlying model potential used for simulation of the CT quenching is presented in Fig. 6.12(b), together with the model potentials used to simulate the quenching of singlet states. For the purpose of demonstration, the disorder parameters were set to zero. From the plot of the model potentials it becomes evident, that the CT states can be dissociated by small activation energies, implying that a high quenching yield is already achieved by the built-in field. Using a screening factor of $f = 0.1$, the potential depth characterized by the energy of the first site reduces to 46 meV.

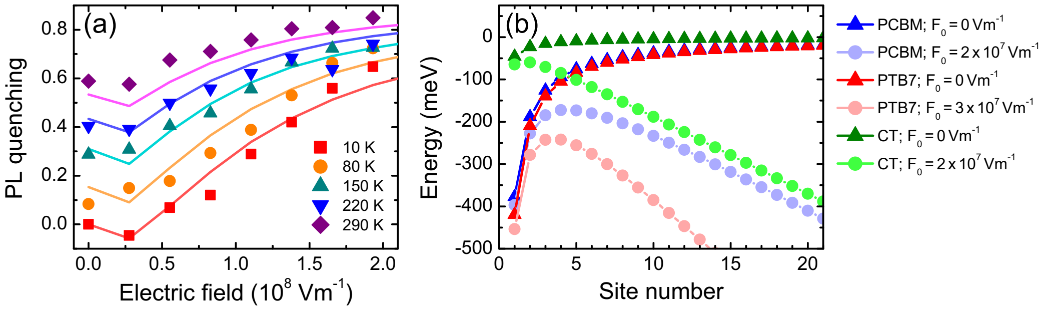

Figure 6.12.: Experimental quenching data obtained for the CT states (symbols in panel (a)) and best fit to these data employing the modified kinetic model (solid lines). Panel (b) shows the underlying (disorder-free) Coulomb potential for CT states in comparison to the unscreened potentials of singlet states in PTB7 and PCBM. The circles indicate the slope of the respective potentials assuming a small built-in field.

Table 6.2.: Model parameters for field-induced PL quenching of CT states in PTB7/PCBM, obtained from fits of the kinetic model by Rubel et al. [15] to experimental quenching data. In order the match the strong temperature and the weak field dependence of the CT intensity, the model was modified as described in the text. For the fit, only the parameters r_0, α, δr and σ were varied.

Parameter description	Parameter	Value
Dielectric constant	ε_r	3.4
Attempt-to-escape frequency	ν_0 (s^{-1})	10^{13}
Intrinsic field	F_0 (Vm^{-1})	2×10^7
Radiative lifetime	τ_{rad} (ps)	400
PL lifetime	τ_{PL} (ps)	400
Site separation	r_0 (nm)	0.92
Localization length	α (nm)	0.51
Spatial disorder parameter	δr (nm)	0.46
Energetic disorder parameter	σ (meV)	60
Energy of first site	E_1 (meV)	46

Such a small value of E_1 implies that the criterion for CT dissociation in the kinetic model needs to be revisited. In case of the singlet excitons, the criterion for dissociation has been considered to be fulfilled, when the escaping charge has reached site number 30, where the site energy induced by the Coulomb potential is within the range of disorder-induced fluctuations. For the CT states, however, the potential is flat and thus, the charges get separated already after few hops. In fact, it turns out that the strong temperature dependence of the field-dependent quenching curves can only be reproduced adequately by the model, when dissociation occurs already at the second site. Longer dissociation paths would underestimate the temperature dependence, as illustrated in Fig. 6.13(a) for a number of 10 sites. This can be understood by taking into account the disorder-induced fluctuations of the potential energy. As the CT potential depth of $E_1 = 46\,\mathrm{meV}$ is on the order of random fluctuations ($\sigma = 60\,\mathrm{meV}$), the quenching is governed by the disorder scale rather than by the depth of the Coulomb potential, which can thus be screened by random fluctuations already at the second site. When on the other hand more sites are considered for dissociation, it becomes more likely that this path incorporates some 'deeper' wells, which may inhibit thermally activated hopping dissociation. However, the strong temperature dependence and the weak field dependence of the experimental quenching curves suggest that only a small number of sites (i.e. two) is involved in the dissociation process.

Another reason for the weak field dependence of the CT quenching could be the strong localization of CT states. Considering that their ability to orient in the electric field is constrained with respect to the donor/acceptor interface, the actually applied field reduces to an effective field, depending on the angle between the field direction and CT orientation. Assuming that the CT states in the bulk heterojunction material are randomly arranged as a result of the random arrangement of donor/acceptor interfaces, the effect of localization can be considered by multiplying the actual field (which is the

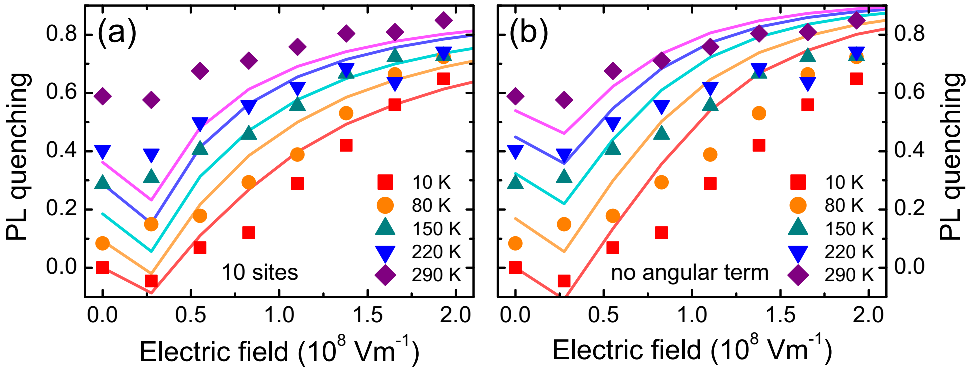

Figure 6.13.: 'Misfits' to the experimental quenching data, demonstrating that the field-dependence of the quenching curves is too strong and the temperature dependence is underestimated, when the dissociation path is too long, here exemplified for a number of 10 sites (a). Similar discrepancies arise, when the constrained orientation of the CT states is not taken into account (b).

externally applied field diminished by the built-in field) with an angular pre-factor, yielding

$$F_{CT} = |F - F_0| \cos\theta \ , \tag{6.8}$$

where θ is a random angle from the interval $\pm\pi$. This modification implies that the recombination probability of the CT states can even be enhanced, when their orientation is antiparallel with regard to the direction of the electric field. When, on the other hand, no angular dependence is considered, the slope of the modeled quenching curves is steeper and no good match with the experimental data is obtained, even for high disorder parameters (see Fig. 6.13(b)).

With the above-mentioned modifications of the kinetic model, good agreement between experimental and modeled quenching data based on the measured CT intensities is obtained. Finally, the CT dynamics resulting from these considerations is simulated and compared to the experimentally recorded decay characteristics of the CT states. As demonstrated in Fig. 6.14, both the field and the temperature-dependent PL dynamics are satisfactorily reproduced based on the parameters summarized in Tab. 6.2. It turns out that the spatial disorder parameter δr plays an essential role for the multiexponential decay characteristics. This parameter is higher than for the singlet states and implies that there is a manifold of recombination times at the interface, depending on the spatial separation of the donor and acceptor sites. This can be considered by modifying the recombination time with a tunneling term [15], which incorporates the randomly created offset x_1 of site number 1 from the opposite charge at the origin:

$$\tau_{eff} = \tau_{PL} \exp\left(\frac{2x_1}{\alpha}\right) \tag{6.9}$$

An important implication of the good agreement between experimental and modeled transients is that the field-induced dissociation rate obtained by the kinetic model de-

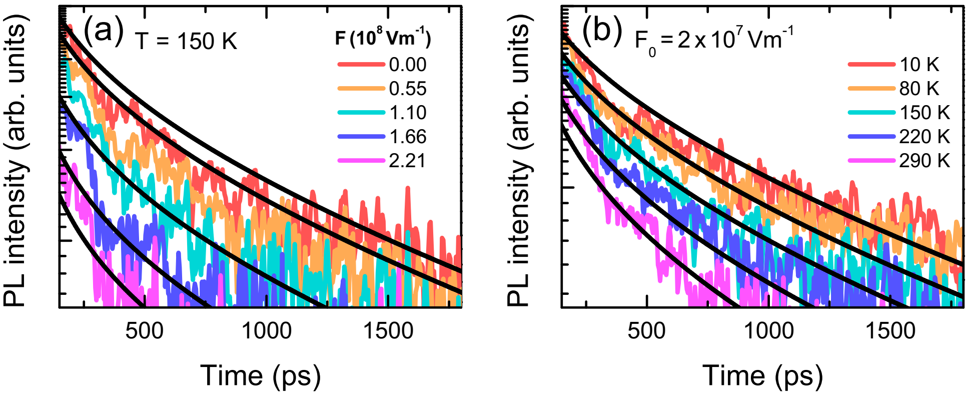

Figure 6.14.: PL transients of the CT emission at various electric fields (a) and without external field for different temperatures (b). The transients are shown from 150 ps after excitation due to the superimposed singlet emission at early times in the experimental data. Modeled transients are presented as black curves. The decay of both experimental and modeled transients is shown over one order of magnitude.

scribes in fact the dissociation from the energetically *relaxed* and emissive CT states, which are characterized by a manifold of spatial separations and weak binding energies. On the other hand, the important role of a 'hot' precursor state, which is often mentioned in the context of the question how excitons dissociate at donor/acceptor interface, is challenged by these results.

6.2. Discussion

In the previous section, experimental field and temperature dependent luminescence quenching data has been analyzed in terms of a kinetic model based on field-assisted dissociation of excitons via a hopping mechanism. A particular goal of these efforts was to relate the observed field-dependent quenching characteristics to the underlying exciton binding energies. In previous work on luminescence quenching, the well-established Onsager-Braun model has often been considered to estimate exciton binding energies from the threshold field for quenching [75, 76, 185]. These approaches give reasonable values for the binding energies of singlet excitons in polymer systems on the order of 300-400 meV. In this work, the binding energy of excitons in PTB7 has been estimated to 420 meV and is thus consistent with the results for other polymers. On the other hand, a weaker binding energy according to the 'push-pull' character of the alternating monomer units in PTB7, which has been suggested by others [151] cannot be confirmed here.

A general drawback of the above-mentioned PL quenching studies is that they were carried out only at room temperature and they do not account for the presence of disorder, which, however, has been found to dominate the quenching characteristics in the low temperature regime. Decisively, even for a temperature of 10 K, the field-dependent quenching curves presented in Ch. 6.1.4 reveal a particularly shallow slope, which can only be described by the model, when disorder is taken into account. In the

Onsager-Braun model, the possibility to implement disorder is limited to the initial separation parameter r_0. In the approach by Rubel et al. [15], however, spatial and energetic disorder can be explicitly considered by addressing each site with an individual and randomly selected offset from its spatial position and potential energy in the disorder-free case. It turns out that good agreement between experimental and simulated quenching data can be achieved with this empirical model. The parameters summarized in Ch. 6.1.4 are consistent with previously reported values, e.g. for the dielectric constant ε_r [15, 27, 76, 186, 187], the attempt-to-escape-frequency ν_0 [15, 97] and the parameter of energetic disorder σ [186, 193, 200, 201]. It should also be emphasized that the same parameters were used to model the whole set of field and temperature dependent quenching data.

At the donor/acceptor interface the situation is different. In order to account for the high yield of thermal CT quenching even without electric field, special assumptions concerning the interface have to be included into kinetic modeling. In the contemporary literature there is an ongoing discussion about the question, why electron-hole pairs dissociate so efficiently in polymer/fullerene systems, giving rise to the high performance of OPV devices. In fact, the extracted photocurrent in highly-performing OPV devices has been found to be independent of the applied electric field [124, 202], evidencing that geminate recombination at the interface is not the 'bottleneck' in the charge generation and extraction process. The approaches to understand the underlying mechanisms of exciton separation are manifold, as for example detailed in Refs. [51] and [52].

At present, there is no consensus in the research community whether charge separation occurs via energetically 'hot', i.e. vibronically or electronically excited states, or if a 'cold' process involving the energetically relaxed and emissive CT states can be efficient as well. Experimental evidence for the presence of a 'hot' separation mechanism in some polymer/fullerene systems is given by transient absorption studies, which have demonstrated ultrafast charge generation on a sub-ps timescale [120, 150–152]. The important role of vibronic excess energy in combination with charge delocalization has also been demonstrated theoretically employing quantum dynamical simulations [84, 155]. Delocalized states could in particular arise from fullerene clustering [85, 132, 134, 155], which is further supported by the observation that ultrafast charge generation is absent in bulk-heterojunctions based on non-fullerene acceptors [203]. The role of excess energy in the process of charge generation has also been investigated by Vandewal et al. [86]. They made the important observation that the external quantum yield of efficient OPV devices did not depend on the energy of the exciting photons and, most importantly, excitation above the optical gap and direct excitation of the energetically relaxed CT states yielded similar quantum efficiencies. This finding is consistent with previous work where the carrier yield for above-gap and CT excitation has been probed by means of time-resolved terahertz spectroscopy [87]. An important conclusion based on these results is that, at least in some efficient OPV systems, the relaxed CT states are weakly bound, as they reveal the ability to dissociate without the help of excess energy. So the striking question is: What actually causes the weak exciton binding energy at the interface? In this context, Arkhipov et al. [16] have investigated influences on the interfacial Coulomb potential theoretically. They found that this potential can be significantly screened by an interfacial dipolar layer due to partial charge transfer between donor and acceptor molecules in the dark. The model has been refined later by employing more sophisticated calculations of the interfacial potential, such as taking into account a random distribution of interfacial dipoles [204], revisiting the actual position of interfacial electron-hole pairs with respect to these dipoles [96] and calculating the electrostatic potential beyond the commonly used harmonic approximation [198]. The presence of an interfacial dipolar layer has also been confirmed experimentally by means of photoelectron spectroscopy [88, 97]. Recently, the concept of interfacial dipoles has been successfully applied to model the field-dependent photocurrent yield in OPV devices [97, 156].

It is beyond the scope of this work to investigate the precise reasons for the experimentally observed, weakly bound emissive CT states. However, from the discussion above it turns out that weakly-bound CT states have also been evidenced by other methods. Furthermore, theoretical studies confirm that the statement of a screened Coulomb potential at the donor-acceptor interface is well-grounded. The main contribution of this work is that the time-resolved quenching studies document efficient exciton separation via a 'cold' hopping mechanism. Empiric modeling of the CT intensity quenching and the multiexponential PL dynamics in the PTB7/PCBM system shows that the complex decay characteristics could in fact result from a manifold of CT states with different site separations and binding energies. Importantly, the entire dissociation and recombination dynamics can be described with the assumption that the emissive and *relaxed* CT state is the starting point in the dissociation process and there is no need to assume that quenching occurs predominantly through a hot precursor state, as suggested in other work [13, 171, 205]. However, the situation may strongly depend on the material system. Moreover, 'hot' and 'cold' dissociation mechanisms are not mutually exclusive.

Overall, temperature and field dependent TRPL studies have proven to be an effective tool to probe the trapping character of CT states, allowing for conclusions if charge generation from relaxed CT states is efficient or not. On the other hand, the emissive CT states represent only a subset of the manifold of intermediate states in the charge generation process. Further complementary studies i.e. transient absorption spectroscopy or studies of the photocurrent yield are necessary to estimate the relevance of the 'cold' separation mechanism for the whole amount of generated charges. Beside these general considerations, the field and temperature dependent data can be used as a robust test for kinetic modeling and on the other hand the analytic and empirical model tested in the framework of this thesis has been found to be in good agreement with the experimental data, using a set of physically reasonable parameters. For studies of the carrier or exciton dynamics, the development of analytic models is of general interest, as they are less time-consuming compared to Monte Carlo simulations [38, 78, 130, 191, 205–208].

6.3. Summary

In this chapter, the energetics of singlet and CT states in the polymer/fullerene system PTB7/PCBM has been studied by means of field-dependent and time-resolved luminescence quenching experiments in the temperature range between 10 and 290 K. The PL quenching has been found to be independent of the photocurrent and the injected current, furthermore no evidence for reduced oscillator strength of the optical transition has been found, suggesting, that the observed PL quenching results in fact from exciton dissociation in the applied electric field. The PL quenching data was analyzed based on an empiric and analytical kinetic model [15], yielding binding energies of 420 meV and 377 meV for singlet excitons in PTB7 and PCBM, respectively. For an appropriate description, intrinsic fields of 2-3 $\times$ $10^7\,\mathrm{Vm}^{-1}$ and energetic disorder of σ=52 meV for PTB7 and σ=99 meV for PCBM have been taken into account. The strong temperature dependence of the CT intensity has been interpreted in terms of a weak binding energy on the order of k_BT at room temperature. The relatively weak dependence of the quenching yield on the electric field on the other hand indicates that the CT states are strongly localized and thus constrained regarding their orientation in the electric field. When both is considered in the kinetic model, the average binding energy of the CT states can be estimated to 46 meV. Modeling suggests, that the underlying spatial disorder for CT states is significantly higher than the spatial disorder of the singlet states. The manifold of distances between the donor and acceptor sites in the CT manifold essentially accounts for the observed multiexponential decay kinetics. The good agreement between the experimentally observed and the modeled dynamics of the CT emission implies that the temperature- and field-induced separation of CT states in PTB7/PCBM can be described via a ’cold’ hopping process, whereas no evidence is found that a ’hot’ precursor state plays a significant role for CT quenching.

Chapter 7

Conclusions and outlook

The major conclusions based on this work can be summarized as follows:

- The time-dependent Stokes shift of the PL in the neat polymers P3HT and PTB7, which has been discussed in Chapter 4, is consistent with the picture of exciton relaxation in a disordered system. A peculiarity in case of PTB7 is the absence of any saturation behavior of the PL red shift with increasing time after excitation, which should arise from thermal equilibrium between upward and downward hops in a Gaussian density of states. This finding challenges an underlying Gaussian density of states in case of PTB7, as the strong red-shift indicates the presence of a higher amount of low-energetic tail states. The Gaussian Disorder Model is a very popular tool to model the transport properties of organic systems, however, the results on PTB7 suggest that the underlying density of states should be studied more carefully.
- Blending the polymers with the fullerene derivative PCBM (see Chapter 5) significantly changes the PL properties with regard to the neat materials. The major observations are a faster decay of the emission arising from singlet excitons, as a result of dissociation at the donor-acceptor interface, and the presence of a faint and long lived emission in the near-infrared, which is attributed to CT state emission. This assignment is justified with the emission energy, which is related to the energy level offset at the interface, and the measured decay times, which are consistent with decay constants obtained from transient absorption studies [119]. Furthermore, the CT emission is quenched with the help of thermal energy at room temperature, which strongly indicates that the underlying binding energies are weak. Such characteristics are expected for CT states in highly performing organic solar cells, as strongly bound CT states would be a serious loss channel. Another important finding is that for both studied blend systems P3HT/PCBM and PTB7/PCBM, respectively, the intensity of the CT emission is correlated with the presence of an intimately mixed polymer/fullerene phase. In P3HT/PCBM with an excess of PCBM, a long-lived subset of the CT states seems to be more strongly bound and thus gives rise to losses, as the decay is not remarkably altered up to room temperature. In PTB7/PCBM on the other hand, the CT dynamics depend more strongly on temperature, suggesting that even the CT states created in the highly disordered PTB7/PCBM mix phase can undergo efficient dissociation.

- The issue of CT dissociation in PTB7/PCBM is further addressed with field-dependent TRPL measurements, as presented in Chapter 6. In a first step, the quenching of the singlet emission is investigated and analyzed in terms of a kinetic model suggested by Rubel et al. [15], which is based on hopping dissociation via several intermediate sites in a disordered Coulomb potential. The model gives an accurate description of the luminescence quenching data, when the underlying energetic disorder is taken into account. This is a particular advantage with regard to the commonly used Onsager-Braun model. The exciton binding energies extracted from the modeling approach are 420 meV for PTB7 and 377 meV for PCBM, respectively. In a next step the model is applied to the quenching data of the CT emission. It turns out that good agreement between the experimental and modeled quenching data can only be obtained when the interfacial potential is assumed to be highly screened, leading to weakly bound CT states, for which the model yields an average binding energy of 46 meV. This result is consistent with the thermal quenching studies in Chapter 5 and is further supported by the assumption of a dipolar layer at the donor/acceptor interface suggested by Arkhipov et al. [16]. This finding suggests that charge separation from the energetically relaxed CT states can be very efficient and a separation mechanism involving either vibronically or electronically excited CT states is not mandatory to explain the high internal quantum yields of some organic solar cell materials.

The TRPL studies carried out in this work have proven to be a useful tool to probe the underlying loss processes, which accompany charge generation in organic solar cell devices. However, the results should always be discussed in the context of complementary studies, such as for example transient absorption or pump-push photocurrent measurements to understand the relevance of the investigated processes. In case of P3HT/PCBM, Guo et al. have reported geminate losses on a time scale similar to the CT dynamics measured in this work [119]. For PTB7/PCBM, delayed charge generation on a 100 ps time scale has been reported [151], which is again consistent with the measured CT decay time. Transient absorption studies also evidence that a high portion of charges in these systems is generated on a sub-ps time scale, suggesting that several processes contribute to charge generation. However, beside the general statement that dissociation of energetically relaxed CT states is efficient in PTB7/PCBM, the 'shallow' trapping character of interfacial CT states could also be beneficial for the transport properties and reduce the amount of bimolecular recombination. Moreover, the observed efficient separation route via relaxed CT states leads to further implications for the energetics at the interface: When excess energy is not required for exciton separation, a smaller offset between the donor and acceptor energy levels at the interface could be sufficient to drive charge separation. This is corroborrated by work of Veldman et al., who found that in principle an energy difference of 0.1 eV between the donor band gap and the CT energy is sufficient [104] for efficient CT dissociation.

Another issue that should be investigated in greater detail in future work is the localization of CT states. The present data suggests that the CT states are rather immobile along the interface, or, at least, that the observed spectral relaxation and dynamics of the CT emission are rather the result of an energy-dependent separation process. However, it cannot be excluded that the CT states reveal a certain mobility, for example driven by uncorrelated asynchronous hopping transport [168]. Such a process could be beneficial for charge generation, as it allows CT states to diffuse into areas where they can be more easily separated. On the other hand, higher diffusivity could also lead to a higher probability to get trapped in recombination centers. These questions regarding the CT mobility could be further addressed by time-resolving the polarization anisotropy of the CT emission.

A general problem regarding the accuracy of the field-dependent studies arises from the fact that the distribution of the electric field in the active layer is not known and thus it is assumed to be homogeneous. However, the PL quenching studies have shown that space charge zones are present in the devices and hence, the electric field is overestimated when it is set equal to the applied field. The impact of space charge zones inside the devices could be further investigated by varying the sample thickness or tuning the excitation wavelength, which would vary the absorption depth. Both approaches would lead to a variation of the number of excitons created in the space charge zone. Beside this intrinsic built-in field there is also the possibility that singlet or CT excitons cause some dynamic screening of the external field. This could in particular be the case at low temperatures where high numbers of emissive CT states are created. The mentioned effects lead to uncertainties regarding interpretation of field-dependent luminescence quenching studies. On the other hand luminescence quenching can be a instructive tool to probe the actual field distribution inside a device when the precise correlation between the emission intensity and the electric field is known [189].

Overall, organic semiconductors are promising candidates to meet the requirements for third-generation photovoltaics with the potential to reach even higher photoconversion efficiencies than nowadays, when the underlying loss processes are better understood [27]. They compete against the perovskites, a material class, which is in particular promising according to the much higher achievable photoconversion efficiencies. Organic semiconductors on the other hand offer the possibility to customize the material properties, according to the variety of synthesis routes available in organic chemistry and they can be prepared easily on flexible substrates. In this work, only material systems based on fullerene acceptors have been discussed. A new and interesting development in the field of organic photovoltaics is however the usage of small molecule acceptors, which bear the advantage that they absorb in the visible range of the solar spectrum, whereas the absorption of the fullerene derivative PCBM is in the blue or the UV range, where the solar flux is rather low. Recently, a photoconversion efficiency of 11 % has been reported for a solar cell based on a small molecule acceptor [3]. For detailed studies of the loss processes in these systems, the same methodology can be applied like for the fullerene based materials [209]. In the context of the growing demand of photovoltaics, the next years in the research field of third generation photovoltaics are exciting, as they may reveal a more sophisticated picture about the most promising material systems, also regarding long-term stability. Beside these efforts, more detailed research on the photophysics of organic light harvesting systems is certainly a topic of broad fundamental interest.

A Calculation of the excitation fluence

The photon and energy flux in the excitation spot of the laser can be estimated, when the spot size, the aperture size of the entrance slits, the time-averaged output power and the laser wavelength are known. Furthermore, the two lenses in front of the spectrometer (see Ch. 3.2 lead to a magnification of the original PL spot by a factor of two.

The number of photons per laser pulse N can be calculated by dividing the deposited energy per laser cycle by the photon energy at a given wavelength:

$$N = \frac{P \cdot T \cdot \lambda}{hc} \tag{A.1}$$

Here, P is the average output power of the laser, T is the period of the Ti:Sa oscillator (12.5 ns), h is Planck's constant and c denotes the speed of light. It is now important to account for the fact that only a part of the PL intensity emerging from the excitation spot is depicted on the cathode of the streak camera. The actual area selected from the excitation spot is determined by the aperture size of the horizontal and vertical entrance slits. The situation is illustrated in Fig. A.1(a). The parameter r_{eff} is used to characterize the depicted spot area and it is related to the slit width d via $r_{eff} = \frac{d}{4}$. The additional factor of $\frac{1}{2}$ emerges because the size of the excitation spot is magnified by a factor of two by the lenses in front of the spectrometer. The number of photons N_{eff} in the depicted area of the excitation spot can now be approximated by integrating over the photon density n inside the circular area with the radius r_{eff}:

$$N_{eff} = 2\pi n \int\limits_0^{r_{eff}} \exp\left(-2\left(\frac{1.18 \cdot r}{w}\right)^2\right) r \,\mathrm{d}r \tag{A.2}$$

Here, w is the diameter of the excitation spot (full width at half maximum), which is related to the two-fold standard deviation via a factor of 1.18. The variable n denotes the photon density, which is obtained by dividing the total number of photons N by the Gaussian spot area, i.e.

$$n = \frac{N}{2\pi \int\limits_0^{\infty} \exp\left(-2\left(\frac{1.18\cdot}{w}\right)^2\right) r \,\mathrm{d}r} \,. \tag{A.3}$$

From the number of photons, the photon flux Φ_{ph} is obtained via

$$\Phi_{ph} = \frac{N_{eff}}{\pi r_{eff}^2} \tag{A.4}$$

and the energy flux Φ_E is given by

$$\Phi_E = \Phi_{ph} \cdot \frac{hc}{\lambda} \ . \tag{A.5}$$

It should be noted that further assumptions about the absorptivity of the material and intensity losses at the sample surface or cryostat window have to be made to enhance the accuracy of the presented approach. For this work, the calculation of the excitation fluence was implemented in a LabVIEW script, where Eqns. A.2 and A.3 were solved numerically. The issue of estimating the excitation fluence is treated in greater depth in Ref. [138].

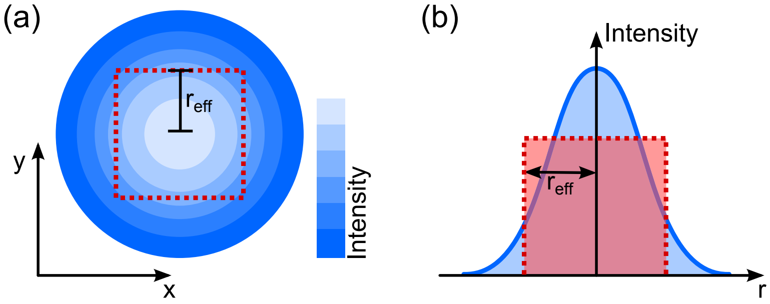

Figure A.1.: Panel (a): Color-coded two-dimensional intensity profile of the laser spot. The area of this spot which is investigated experimentally is indicated by the square. The average excitation intensity is calculated via Eq. A.2 and the resulting effective intensity profile is sketched in panel (b).

B Supporting experimental data

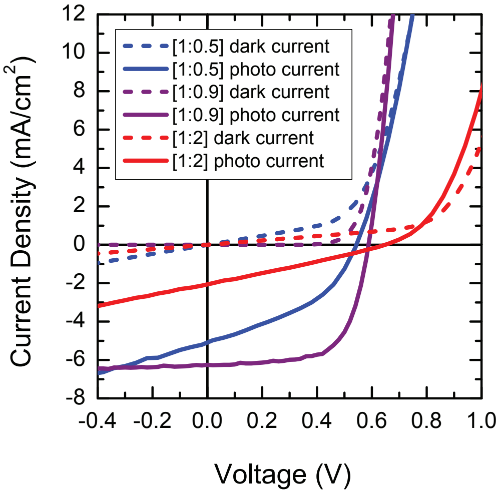

Figure B.1.: Current density versus voltage curves of the investigated P3HT/PCBM devices with varying PCBM content.

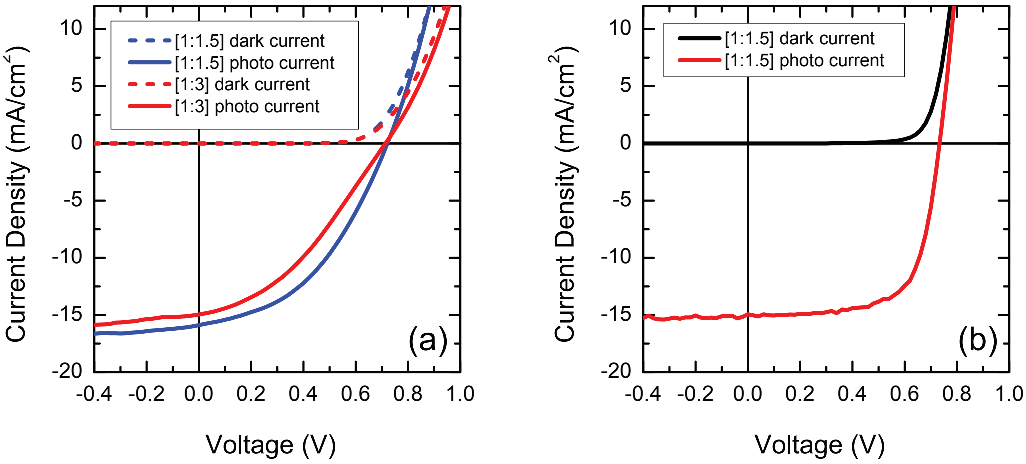

Figure B.2.: Current density versus voltage curves of the investigated PTB7/PCBM devices with varying fullerene content. The curves in panel (a) correspond to the first batch of samples investigated in Ch. 5 and the curve in panel (b) is representative for the second batch of samples, which was fabricated for the field-dependent studies presented in Ch. 6.

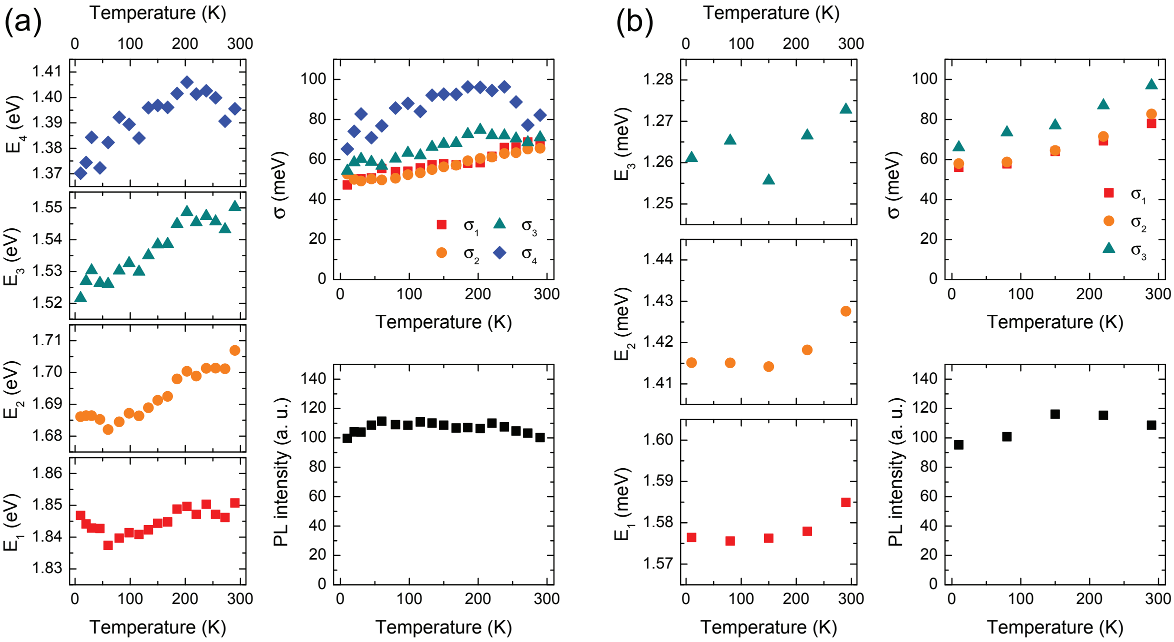

Figure B.3.: Parameters describing the temperature-dependent PL spectra of P3HT (a) and PTB7 (b), as labeled. The values of E_i denote the peak maxima obtained from multi-Gaussian fits, σ is the disorder parameter and the PL intensity was obtained by integrating the intensity of the recorded PL spectra.

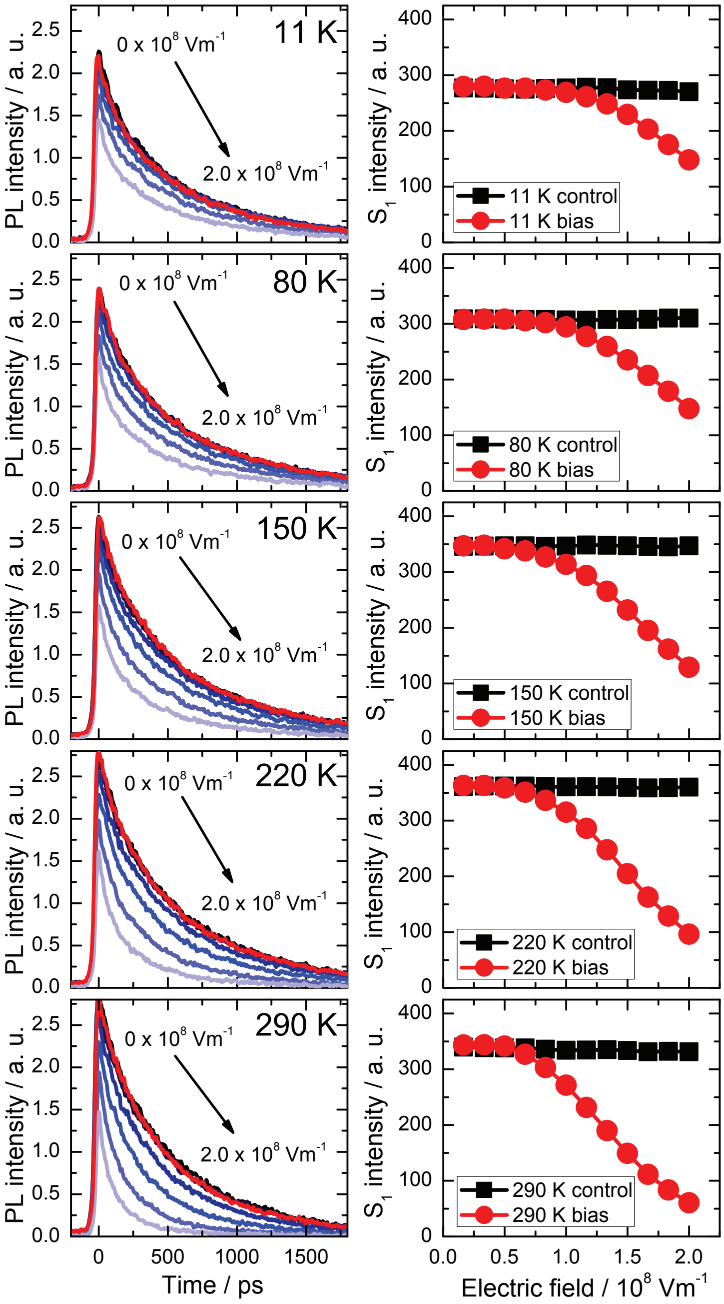

Figure B.4.: Left column: Selected PL transients from bias sweeps of the PTB7 device at different temperatures. The red curves correspond to the control measurements without bias after the sweeps. The range of applied fields is indicated in the plots. The device was excited at 450 nm (2.76 eV) and the excitation power was set to 0.1 mW, corresponding to an energy fluence of about 0.1 µJcm^{-2}. Right column: Integrated PL intensities extracted from the measurements. Black squares represent the intensities derived from control measurements before and after the respective bias step and red circles correspond to the PL intensities when bias is applied to the device. The figure is reprinted from the supporting information in Ref. [17].

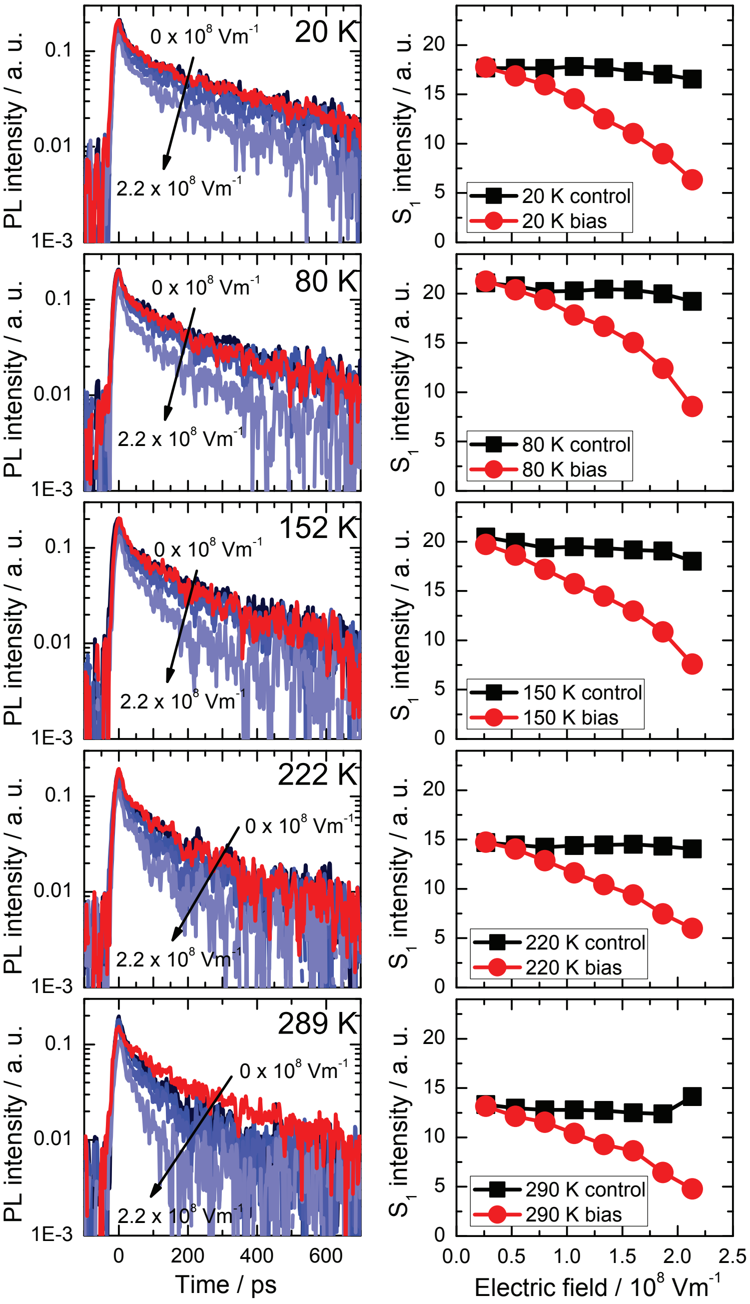

Figure B.5.: Left column: Selected PL transients from bias sweeps of the PTB7/PCBM device at different temperatures. The red curves correspond to the control measurements without bias after the sweeps. The range of applied fields is indicated in the plots. Excitation conditions: 400 nm (3.1 eV), leading to preferential excitation of the PCBM phases. The excitation power was set to 0.3 mW, corresponding to an energy fluence of about 0.08 µJcm^{-2}. Right column: Integrated PL intensities extracted from the measurements. Black squares represent the intensities derived from control measurements before and after the respective bias step and red circles correspond to the PL intensities when bias is applied to the device. The figure is reprinted from the supporting information in Ref. [17].

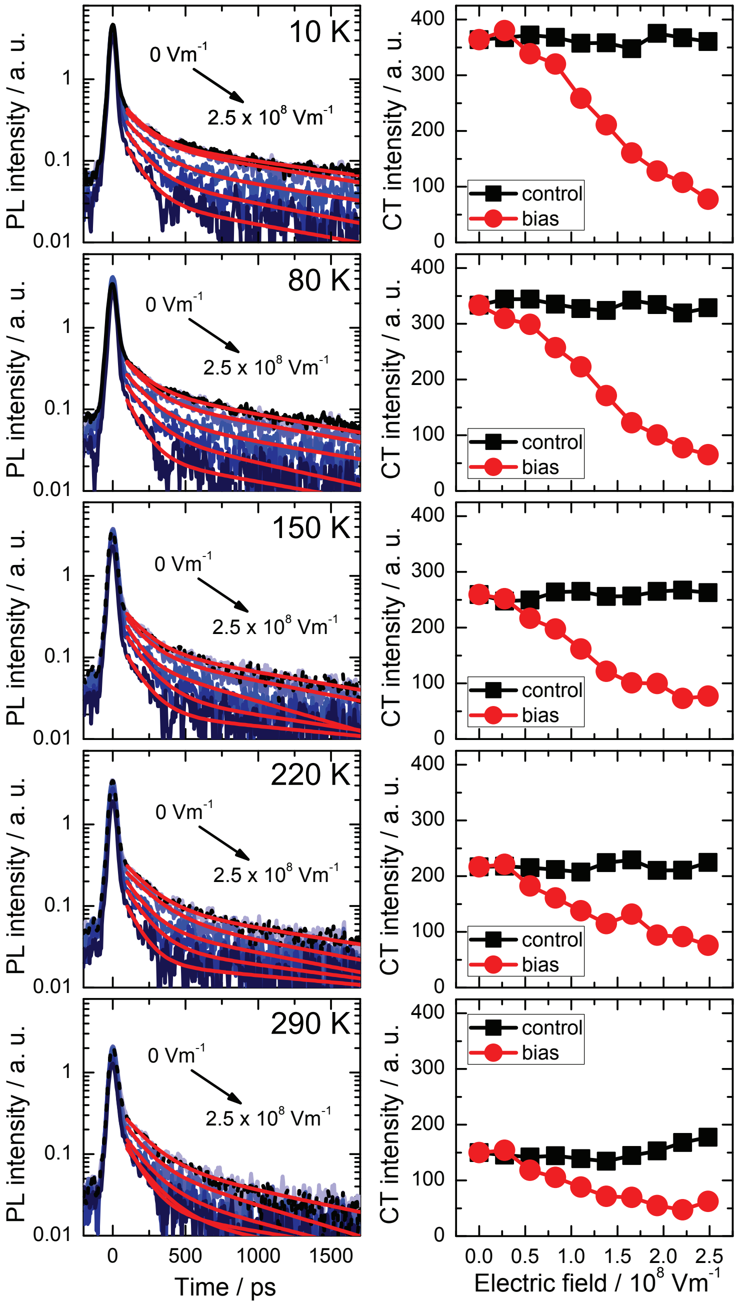

Figure B.6.: Left column: Selected PL transients from bias sweeps of the PTB7/PCBM device at different temperatures. The black curves correspond to the control measurements without bias after the sweeps. The range of applied fields is indicated in the plots. The excitation wavelength was set to 705 nm (1.76 eV), allowing for selective excitation of the polymer phase and an excitation power of 5 mW was chosen (the corresponding energy fluence is ca. 2.7 µJcm^{-2}). The CT intensity was approximated with the integral over a biexponential model function fitted to the long-lived component of the recorded PL transients (red curves). Right column: Integrated PL intensities extracted from the fits. Black squares represent the intensities derived from control measurements before and after the respective bias step and red circles correspond to the PL intensities when bias is applied to the device. The figure is reprinted from the supporting information in Ref. [17].

C Matlab-script for modeling of field-induced luminescence quenching

```
% parameters for optimization
r0=1.12e-9;                 % Separation of neighboring sites (m)
alpha=0.52e-9;              % Localization parameter (m)
dr=0.07e-9;                 % Spatial disorder parameter (m)
sigma_meV=52;               % Energetic disorder parameter (meV)
sigma_J=sigma_meV/6.242e21; % Energetic disorder parameter (J)
p=[r0 alpha dr sigma_J];    % Parameter set for optimization

% experimental PL quenching data
data_exp=load('PTB7data.dat');

% externally applied electric field (0...24V for a 120nm film)
F_exp=[0:2:24]'/120e-9;

% Settings for optimization procedure "fminsearch"
options=optimset('Display','iter','MaxIter',50);

% Optimization of function "fiterr"
p=fminsearch(@fiterr, p,options,F_exp,data_exp);

% Calculate theoretical quenching curves from best parameter set
[delta, qdata]=fiterr(p,F_exp,data_exp);

% Plot optimized quenching curves and experimental data
plot(F_exp,qdata,F_exp,data_exp);

p(4)=p(4)*6.242e21;     % Energetic disorder parameter in meV

% Export modeled quenching data and optimized parameter set
save 'qdata.dat' qdata -ASCII
save 'params_PTB7.dat' p -ASCII

function [delta, qdata] =fiterr(p, F_exp, data_exp)

% Constants (SI-units!)
eps_r=3.0;                  % relative dielectric constant
eps_0=8.85418781762e-12;    % vacuum permittivity
k_B=1.38064852e-23;         % Boltzmann constant
e=1.6021766208e-19;         % elementary charge

% Fixed parameters
v0=1e13;                    % attempt-to-escape frequency
trad=0.5e-9;                % radiative decay rate
tex=0.5e-9;                 % experimental PL decay time
F0=2e7;                     % intrinsic field
f=1;                        % potential screening factor (~0.1 for CT states)
F=abs(F_exp-F0);            % effective field

% Free parameters
r0=p(1);
alpha=p(2);
dr=p(3);
sigma_J=p(4);

% Investigated temperatures
Tvec=[10 80 150 220 290];
```

```
% Model settings
m=1e4;                      % no. of simulation runs
n=31;                       % number of relevant sites

for g=1:1:length(Tvec) % loop for different temperatures
T=Tvec(g);

    for k=1:1:m        % loop for averaging between random model potentials

        % Enable this to account for random field direction (for CT)
        % theta=rand(1)*2*pi-pi;
        % F=abs(F*cos(theta));

        % Create random position and energy offsett
        xr=rand(1,n)*2*dr-dr;   % spatial disorder (uniformly distributed)
        xE=sigma_J.*randn(1,n); % energetic disorder (normally distributed)

        % Weight decay times by a tunneling term
        trad_mod=trad*exp(2*xr(1)/alpha);
        tex_mod=tex*exp(2*xr(1)/alpha);

        % Calculation of potential energy E and site-to-site hopping rate
        for j=2:1:n
           rj=(j-1)*r0+xr(j-1);
           rj1=j*r0+xr(j);
           Ej=xE(j-1)-f*e^2/(4*pi*eps_0*eps_r*rj)-e*F*rj;     % E(j)
           Ej1=xE(j)-f*e^2/(4*pi*eps_0*eps_r*rj1)-e*F*rj1;   % E(j+1)
           % site-to-site Miller-Abrahams-hopping-rate
           aj=v0*exp(-(2*(rj1-rj)/alpha)-((Ej1-Ej)+abs(Ej1-Ej))/(2*k_B*T));
            if j==2
               E1=ones(n-1,1)*Ej';  % Energy of the first site
            end
            E(j-1,:)=Ej';
            a(j-1,:)=aj';
        end

        % Field-dependent dissociation rate (Rubel et al., PRL, 2008)
        kdiss=(sum((1./a).*exp((E-E1)/(k_B*T)))).^(-1);

        % Sum over dissociation probabilities for individual potentials
        if k==1
            p=(trad_mod^(-1))./(tex_mod^(-1)+kdiss);
        else
            p=p+(trad_mod^(-1))./(tex_mod^(-1)+kdiss);
        end

    end

    % Calculate field-dependent dissociation probability and quenching
    p=p/m;

    q=1-p/p(1);

    % Enable this to calculate quenching relative to 10 K intensity (for CT)
    %   if g==1
    %    p10K=p(1);
    %   end
    % q=1-p/p10K;

qdata(:,g)=q';

end

% Calculate standard deviation (function to be minimized)
[cols rows]=size(data_exp);
delta=sqrt(sum(sum((data_exp-qdata).^2))/(cols*rows-1));
```

D List of abbreviations

Frequently used abbreviations

Abbreviation	Description
A	Acceptor
AM	Air mass
BHJ	Bulk heterojunction
CS state	Charge separated state
CT state	Charge transfer state
D	Donor
DET	Dexter energy transfer
DOS	Density of states
ET	Electron transfer
FF	Fill factor
FRET	Förster resonant energy transfer
FWHM	Full width at half maximum
HOMO	Highest occupied molecular orbital
IC	Internal conversion
ISC	Intersystem crossing
J_{sc}	Short circuit current
JV curve	Current density/voltage curve
LCAO	Linear combination of atomic orbitals
LUMO	Lowest unoccupied molecular orbital
ND:YAG laser	Neodym-doped yttrium aluminium garnet laser
OPV	Organic photovoltaics
PCE	Power conversion efficiency
PL	Photoluminescence
RR	Regioregular
RRa	Regiorandom
SHG	Second harmonic generation
SSH model	Su-Schrieffer-Heeger model
Ti:Sa laser	Titanium:sapphire laser
TRPL	Time-resolved photoluminescence
V_{oc}	Open circuit voltage
XT	Exciton transfer

Chemicals

Abbreviation	Description
Al	Aluminum
BDT	Benzodithiophene
DIO	Diiodooctane
ITO	Indium tin oxide
MDMO-PPV	Poly[(2-methoxy-5-(3',7'-dimethyloctyloxy))-1,4-phenylenevinylene]
P3HT	Poly(3-hexylthiophene)
$PC_{61}BM$	[6,6]-phenyl-C_{61} butyric acid methyl ester
$PC_{71}BM$	[6,6]-phenyl-C_{71} butyric acid methyl ester
PCDTBT	Poly[N-9-heptadecanyl-2,7-carbazole-alt-5,5-(4,7-di-2-thienyl-2,1,3-benzothiadiazole)]
PEDOT:PSS	Poly(3,4-ethylenedioxythiophene)-poly(styrenesulfonate)
PPV	Poly(p-phenylenevinylene)
PTB7	Thieno-[3,4-b]thiophene-*alt*-benzodithiophene
TT	Thienothiophene

Bibliography

[1] Z. He, C. Zhong, S. Su, M. Xu, H. Wu, and Y. Cao. "Enhanced power-conversion efficiency in polymer solar cells using an inverted device structure". *Nature Photonics* 6 (9) (2012), pp. 591–595.

[2] M. A. Green, K. Emery, Y. Hishikawa, W. Warta, and E. D. Dunlop. "Solar cell efficiency tables (version 48)". *Progress in Photovoltaics: Research and Applications* 24 (7) (2016), pp. 905–913.

[3] W. Zhao, D. Qian, S. Zhang, S. Li, O. Inganäs, F. Gao, and J. Hou. "Fullerene-Free Polymer Solar Cells with over 11% Efficiency and Excellent Thermal Stability". *Advanced Materials* 28 (26) (2016), pp. 4734–4739.

[4] S. T. Hoffmann, H. Bässler, J. M. Koenen, M. Forster, U. Scherf, E. Scheler, P. Strohriegl, and A. Köhler. "Spectral diffusion in poly(para-phenylene)-type polymers with different energetic disorder". *Physical Review B* 81 (11) (2010), p. 115108.

[5] S. T. Hoffmann, S. Athanasopoulos, D. Beljonne, H. Bässler, and A. Köhler. "How do triplets and charges move in disordered organic semiconductors? A Monte Carlo study comprising the equilibrium and nonequilibrium regime". *The Journal of Physical Chemistry C* 116 (31) (2012), pp. 16371–16383.

[6] S. Athanasopoulos, S. T. Hoffmann, H. Bässler, A. Köhler, and D. Beljonne. "To hop or not to hop? Understanding the temperature dependence of spectral diffusion in organic semiconductors". *The Journal of Physical Chemistry Letters* 4 (10) (2013), pp. 1694–1700.

[7] T. Erb, U. Zhokhavets, G. Gobsch, S. Raleva, B. Stühn, P. Schilinsky, C. Waldauf, and C. J. Brabec. "Correlation Between Structural and Optical Properties of Composite Polymer/Fullerene Films for Organic Solar Cells". *Advanced Functional Materials* 15 (7) (2005), pp. 1193–1196.

[8] M. Hallermann, I. Kriegel, E. Da Como, J. M. Berger, E. von Hauff, and J. Feldmann. "Charge Transfer Excitons in Polymer/Fullerene Blends: The Role of Morphology and Polymer Chain Conformation". *Advanced Functional Materials* 19 (22) (2009), pp. 3662–3668.

[9] B. A. Collins, E. Gann, L. Guignard, X. He, C. R. McNeill, and H. Ade. "Molecular miscibility of polymer-fullerene blends". *The Journal of Physical Chemistry Letters* 1 (21) (2010), pp. 3160–3166.

[10] S. S. van Bavel, M. Bärenklau, G. de With, H. Hoppe, and J. Loos. "P3HT/-PCBM Bulk Heterojunction Solar Cells: Impact of Blend Composition and 3D Morphology on Device Performance". *Advanced Functional Materials* 20 (9) (2010), pp. 1458–1463.

[11] B. A. Collins, Z. Li, J. R. Tumbleston, E. Gann, C. R. Mcneill, and H. Ade. "Absolute measurement of domain composition and nanoscale size distribution explains performance in PTB7:PC$_{71}$BM solar cells". *Advanced Energy Materials* 3 (1) (2013), pp. 65–74.

[12] G. J. Hedley, A. J. Ward, A. Alekseev, C. T. Howells, E. R. Martins, L. A. Serrano, G. Cooke, A. Ruseckas, and I. D. W. Samuel. "Determining the optimum morphology in high-performance polymer-fullerene organic photovoltaic cells." *Nature Communications* 4 (2013), p. 2867.

[13] A. P. Arndt, M. Gerhard, A. Quintilla, I. A. Howard, M. Koch, and U. Lemmer. "Time-Resolved Charge-Transfer State Emission in Organic Solar Cells: Temperature and Blend Composition Dependence of Interfacial Traps". *The Journal of Physical Chemistry C* 119 (24) (2015), pp. 13516–13523.

[14] M. Gerhard, A. P. Arndt, I. A. Howard, A. Rahimi-Iman, U. Lemmer, and M. Koch. "Temperature- and Energy-Dependent Separation of Charge-Transfer States in PTB7-Based Organic Solar Cells". *The Journal of Physical Chemistry C* 119 (51) (2015), pp. 28309–28318.

[15] O. Rubel, S. D. Baranovskii, W. Stolz, and F. Gebhard. "Exact Solution for Hopping Dissociation of Geminate Electron-Hole Pairs in a Disordered Chain". *Physical Review Letters* 100 (19) (2008), p. 196602.

[16] V. I. Arkhipov, P. Heremans, and H. Bässler. "Why is exciton dissociation so efficient at the interface between a conjugated polymer and an electron acceptor?" *Applied Physics Letters* 82 (25) (2003), pp. 4605–4607.

[17] M. Gerhard, A. P. Arndt, M. Bilal, U. Lemmer, M. Koch, and I. A. Howard. "Field-induced exciton dissociation in PTB7-based organic solar cells" (2016). In preparation.

[18] Deutsche Koordinierungsstelle des Weltklimarats IPCC. "Kernbotschaften des Fünften Sachstandsberichts des IPCC Klimaänderung 2013: Naturwissenschaftliche Grundlagen" (2013).

[19] V. Quaschning. "Sektorkopplung durch die Energiewende". *Hochschule für Technik und Wirtschaft, Berlin* (2016).

[20] Arbeitsgemeinschaft Energiebilanzen des Bundesministeriums für Wirtschaft und Energie. "Primärenergieverbrauch in Deutschland" (2015).

[21] G. Lanzani. *The Photophysics behind Photovoltaics and Photonics.* WILEY-VCH, 2012. ISBN: 978-3-527-41054-5.

[22] Web article: "Bernard Verspieren", *Oullins Mali Aqua Viva.* 2011. URL: `http://www.oullinsmali.fr/bernard-verspieren/`.

[23] Web article: "Marokko statt Desertec". 2015. URL: `http://www.tagesspiegel.de/wirtschaft/solarstrom-aus-der-wueste-marokko-statt-desertec/11793588.html`.

[24] J. Nelson. *The Physics of Solar Cells*. Imperial College Press, 2003. ISBN: 1-86094-340-3.

[25] D. M. Chapin, C. S. Fuller, and G. L. Pearson. “A new silicon p-n junction photocell for converting solar radiation into electrical power”. *Journal of Applied Physics* 25 (5) (1954), pp. 676–677.

[26] N. Armaroli and V. Balzani. “Solar Electricity and Solar Fuels: Status and Perspectives in the Context of the Energy Transition”. *Chemistry A - European Journal* 22 (1) (2016), pp. 32–57.

[27] M. C. Scharber and N. S. Sariciftci. “Efficiency of bulk-heterojunction organic solar cells”. *Progress in Polymer Science* 38 (12) (2013), pp. 1929–1940.

[28] A. Köhler and H. Bässler. *Electronic Processes in Organic Semiconductors*. WILEY-VCH, 2015. ISBN: 978-3-527-33292-2.

[29] H. Kallman and M. Pope. “Bulk Conductivity in Organic Crystals”. *Nature* 186 (4718) (1960), pp. 31–33.

[30] W. Helfrich and W. G. Schneider. “Recombination Radiation in Anthracene Crystals”. *Physical Review Letters* 14 (7) (1965), pp. 229–231.

[31] M. Sano, M. Pope, and H. Kallmann. “Electroluminescence and Band Gap in Anthracene”. *The Journal of Chemical Physics* 43 (8) (1965), pp. 2920–2921.

[32] C. K. Chiang, C. R. Fincher, Y. W. Park, A. J. Heeger, H. Shirakawa, E. J. Louis, S. C. Gau, and A. G. MacDiarmid. “Electrical conductivity in doped polyacetylene”. *Physical Review Letters* 39 (17) (1977), pp. 1098–1101.

[33] C. W. Tang and S. A. VanSlyke. “Organic electroluminescent diodes”. *Applied Physics Letters* 51 (12) (1987), pp. 913–915.

[34] J. H. Burroughes, D. D. C. Bradley, A. R. Brown, R. N. Marks, K. Mackay, R. H. Friend, P. L. Burns, and A. B. Holmes. “Light-emitting diodes based on conjugated polymers”. *Nature* 347 (6293) (1990), pp. 539–541.

[35] U. Rauscher, H. Bässler, D. D. C. Bradley, and M. Hennecke. “Exciton versus band description of the absorption and luminescence spectra in poly(p-phenylenevinylene)”. *Physical Review B* 42 (16) (1990), pp. 9830–9836.

[36] R. Kersting, U. Lemmer, M. Deussen, H. Bakker, R. Mahrt, H. Kurz, V. Arkhipov, H. Bässler, and E. Göbel. “Ultrafast Field-Induced Dissociation of Excitons in Conjugated Polymers”. *Physical Review Letters* 73 (10) (1994), pp. 1440–1443.

[37] M. Scheidler, U. Lemmer, R. Kersting, S. Karg, W. Riess, B. Cleve, R. Mahrt, H. Kurz, H. Bässler, E. Göbel, and P. Thomas. “Monte Carlo study of picosecond exciton relaxation and dissociation in poly(phenylenevinylene)”. *Physical Review B* 54 (8) (1996), pp. 5536–5544.

[38] S. Barth and H. Bässler. “Intrinsic Photoconduction in PPV-Type Conjugated Polymers”. *Physical Review Letters* 79 (22) (1997), pp. 4445–4448.

[39] H. Bässler and B. Schweitzer. “Site-selective fluorescence spectroscopy of conjugated polymers and oligomers”. *Accounts of Chemical Research* 32 (2) (1999), pp. 173–182.

[40] G. A. Chamberlain. “Organic solar cells: A review”. *Solar Cells* 8 (1) (1983), pp. 47–83.

[41] W. Rieß, S. Karg, V. Dyakonov, M. Meier, and M. Schwoerer. “Electroluminescence and photovoltaic effect in PPV Schottky diodes”. *Journal of Luminescence* 60-61 (1994), pp. 902–905.

[42] N. S. Sariciftci, L. Smilowitz, A. J. Heeger, and F. Wudl. “Photoinduced electron transfer from a conducting polymer to buckminsterfullerene.” *Science* 258 (1992), pp. 1474–1476.

[43] N Sariciftci, D Braun, C Zhang, V Srdanov, G Stucky, A Heeger, and F Wudl. “Semiconducting polymer-buckminsterfullerene heterojunctions: Diodes, photodiodes, and photovoltaic cells”. *Applied Physics Letters* 62 (1993), p. 585.

[44] G. Yu, J. Gao, J. C. Hummelen, F. Wudl, and A. J. Heeger. “Polymer Photovoltaic Cells: Enhanced Efficiencies via a Network of Internal Donor-Acceptor Heterojunctions”. *Science* 270 (5243) (1995), pp. 1789–1791.

[45] M. Pope and C. E. Swenberg. *Electronic Processes in Organic Crystals*. Oxford, 1982. ISBN: 0-19-851334-8.

[46] P. W. Atkins and J. de Paula. *Physikalische Chemie*. WILEY-VCH, 2006. ISBN: 978-3-527-31546-8.

[47] M. Schwoerer and H. C. Wolf. *Organic Molecular Solids*. WILEY-VCH, 2007. ISBN: 978-3-527-40540-4.

[48] H. Rand, Barry P., Richter. *Organic Solar Cells: Fundamentals, Devices, and Upscaling*. CRC Press, 2014. ISBN: 978-981-4463-66-9.

[49] T. M. Clarke and J. R. Durrant. “Charge Photogeneration in Organic Solar Cells.” *Chemical Reviews* 110 (11) (2010), pp. 6736–6767.

[50] C. Deibel, T. Strobel, and V. Dyakonov. “Role of the Charge Transfer State in Organic Donor-Acceptor Solar Cells”. *Advanced Materials* 22 (37) (2010), pp. 4097–4111.

[51] S. Few, J. M. Frost, and J. Nelson. “Models of charge pair generation in organic solar cells”. *Physical Chemistry Chemical Physics* 17 (4) (2015), pp. 2311–2325.

[52] H. Bässler and A. Köhler. “Hot or cold: how do charge transfer states at the donor/acceptor interface of an organic solar cell dissociate?” *Physical Chemistry Chemical Physics* 17 (43) (2015), pp. 28451–28462.

[53] K. Watanabee and M. Zelikoff. “Absorption Coefficients of Water Vapor in the Vacuum Ultraviolet”. *Journal of the Optical Society of America* 43 (9) (1953), pp. 756–759.

[54] J. Franck. “Elementary processes of photochemical reactions”. *Transactions of the Faraday Society* 21 (1925), pp. 536–542.

[55] E. Condon. “A theory of intensity distribution in band systems”. *Physical Review* 28 (6) (1926), pp. 1182–1201.

[56] S. D. Colson, D. M. Hanson, R. Kopelman, and G. W. Robinson. “Direct Observation of Entire Exciton Band of First Excited Singlet States of Crystalline Benzene and Naphthalene”. *The Journal of Chemical Physics* 48 (5) (1968), pp. 2215–2231.

[57] F. Dubin, R. Melet, T. Barisien, L. Legrand, R. Grousson, M. Schott, and V. Voliotis. “Coherent exciton state in an organic quantum wire”. *Nature Physics* 2 (1) (2006), pp. 32–35.

[58] J. Frenkel. “On the transformation of light into heat in solids”. *Physical Review* 37 (1) (1931), pp. 17–44.

[59] A. S. Davydov. “Theory of absorption spectra of molecular crystals”. *Ukrainian Journal of Physics* 53 (2) (2008), pp. 210–218. Translated and reprinted from *Zh. Eksp. Teor. Fiz.* 18 (2), pp. 210218 (1948).

[60] R. R. Lunt, J. B. Benziger, and S. R. Forrest. “Relationship between crystalline order and exciton diffusion length in molecular organic semiconductors”. *Advanced Materials* 22 (11) (2010), pp. 1233–1236.

[61] G. D. Scholes, G. R. Fleming, A. Olaya-Castro, and R. van Grondelle. “Lessons from nature about solar light harvesting”. *Nature Chemistry* 3 (10) (2011), pp. 763–774.

[62] T. Förster. “Zwischenmolekulare Energiewanderung und Fluoreszenz”. *Annalen der Physik* 6 (2) (1948), pp. 55–75.

[63] D. L. Dexter. “A Theory of Sensitized Luminescence in Solids”. *The Journal of Chemical Physics* 21 (5) (1953), pp. 836–850.

[64] W. P. Su, J. R. Schrieffer, and A. J. Heeger. “Solitons in polyacetylene”. *Physical Review Letters* 42 (25) (1979), pp. 1698–1701.

[65] W. P. Su, J. R. Schrieffer, and A. J. Heeger. “Soliton excitations in polyacetylene”. *Physical Review B* 22 (4) (1980), pp. 2099–2111.

[66] A. J. Heeger, S. Kivelson, J. R. Schrieffer, and W. P. Su. “Solitons in conducting polymers”. *Reviews of Modern Physics* 60 (3) (1988), pp. 781–850.

[67] M. Furukawa, K. Mizuno, A. Matsui, S. D. D. V. Rughooputh, and W. C. Walker. “Time-Resolved Excitonic Luminescence Processes in Poly(phenylene-vinylene)”. *Journal of the Physical Society of Japan* 58 (8) (1989), pp. 2976–2987.

[68] J. Torras, J. Casanovas, and C. Alemán. “Reviewing extrapolation procedures of the electronic properties on the π-conjugated polymer limit”. *The Journal of Physical Chemistry A* 116 (28) (2012), pp. 7571–7583.

[69] H. C. Longuet-Higgins and L. Salem. “The alternation of bond lengths in long conjugated chain molecules”. *Proceedings of the Royal Society A* 251 (1265) (1959), pp. 172–185.

[70] R. E. Peierls. *Quantum theory of solids*. Oxford, 1955. ISBN: 9780198507819.

[71] G. N. Lewis and M. Calvin. “The Color of Organic Substances”. *Chemical Reviews* 25 (2) (1939), pp. 273–328.

[72] W. Kuhn. “Über das Absorptionsspektrum der Polyene”. *Helvetica Chimica Acta* 31 (6) (1948), pp. 1780–1799.

[73] J. Gierschner, J. Cornil, and H.-J. Egelhaaf. “Optical bandgaps of π-conjugated organic materials at the polymer limit: Experiment and theory”. *Advanced Materials* 19 (2) (2007), pp. 173–191.

[74] J. Roncali. “Synthetic Principles for Bandgap Control in Linear π-Conjugated Systems”. *Chemical Reviews* 97 (1) (1997), pp. 173–206.

[75] C. Deibel, D. Mack, J. Gorenflot, A. Schöll, S. Krause, F. Reinert, D. Rauh, and V. Dyakonov. “Energetics of excited states in the conjugated polymer poly(3-hexylthiophene)”. *Physical Review B* 81 (8) (2010), p. 085202.

[76] J. Kern, S. Schwab, C. Deibel, and V. Dyakonov. “Binding energy of singlet excitons and charge transfer complexes in MDMO-PPV:PCBM solar cells”. *Physica Status Solidi Rapid Research Letters* 5 (10-11) (2011), pp. 364–366.

[77] B. Yang, Y. Yi, C.-r. Zhang, S. G. Aziz, V. Coropceanu, and J.-L. Brédas. “Impact of Electron Delocalization on the Nature of the Charge- Transfer States in Model Pentacene/C_{60} Interfaces: A Density Functional Theory Study”. *The Journal of Physical Chemistry C* 118 (48) (2014), pp. 27648–27656.

[78] H Bässler. “Charge Transport in Disordered Organic Photoconductors a Monte Carlo Simulation Study”. *Physica Status Solidi B* 175 (1) (1993), pp. 15–56.

[79] J. L. Brédas, D. Beljonne, V. Coropceanu, and J. Cornil. “Charge-transfer and energy-transfer processes in π-conjugated oligomers and polymers: A molecular picture”. *Chemical Reviews* 104 (11) (2004), pp. 4971–5003.

[80] W. J. D. Beenken and T. Pullerits. “Excitonic coupling in polythiophenes: Comparison of different calculation methods”. *The Journal of Chemical Physics* 120 (5) (2004), p. 2490.

[81] B. Movaghar, B. Ries, and M. Grünewald. “Diffusion and relaxation of energy in disordered systems: Departure from mean-field theories”. *Physical Review B* 34 (8) (1986), pp. 5574–5582.

[82] R. A. Marcus. “On the Theory of Oxidation-Reduction Reactions Involving Electron Transfer. I”. *The Journal of Chemical Physics* 24 (5) (1956), pp. 966–978.

[83] J. Jortner. “Temperature dependent activation energy for electron transfer between biological molecules”. *The Journal of Chemical Physics* 64 (12) (1976), p. 4860.

[84] H. Tamura and I. Burghardt. “Ultrafast charge separation in organic photovoltaics enhanced by charge delocalization and vibronically hot exciton dissociation”. *Journal of the American Chemical Society* 135 (44) (2013), pp. 16364–16367.

[85] B. M. Savoie, A. Rao, A. A. Bakulin, S. Gelinas, B. Movaghar, R. H. Friend, T. J. Marks, and M. A. Ratner. “Unequal partnership: asymmetric roles of polymeric donor and fullerene acceptor in generating free charge”. *Journal of the American Chemical Society* 136 (7) (2014), pp. 2876–2884.

[86] K. Vandewal, S. Albrecht, E. T. Hoke, K. R. Graham, J. Widmer, J. D. Douglas, M. Schubert, W. R. Mateker, J. T. Bloking, G. F. Burkhard, A. Sellinger, J. M. J. Fréchet, A. Amassian, M. K. Riede, M. D. McGehee, D. Neher, and A. Salleo. “Efficient charge generation by relaxed charge-transfer states at organic interfaces”. *Nature Materials* 13 (1) (2014), pp. 63–68.

[87] P. D. Cunningham and L. M. Hayden. “Carrier Dynamics Resulting from Above and Below Gap Excitation of P3HT and P3HT/PCBM Investigated by Optical-Pump Terahertz-Probe Spectroscopy”. *The Journal of Physical Chemistry C* 112 (21) (2008), pp. 7928–7935.

[88] W. Osikowicz, M. P. De Jong, and W. R. Salaneck. “Formation of the interfacial dipole at organic-organic interfaces: C 60/polymer interfaces”. *Advanced Materials* 19 (23) (2007), pp. 4213–4217.

[89] S. D. Baranovskii, M. Wiemer, A. V. Nenashev, F. Jansson, and F. Gebhard. “Calculating the Efficiency of Exciton Dissociation at the Interface between a Conjugated Polymer and an Electron Acceptor”. *The Journal of Physical Chemistry Letters* 3 (9) (2012), pp. 1214–1221.

[90] J. Frenkel. “On Pre-Breakdown Phenomena in Insulators and Electronic Semi-Conductors”. *Physical Review* 54 (8) (1938), pp. 647–648.

[91] M. D. Tabak and P. J. Warter. “Field-Controlled Photogeneration and Free-Carrier Transport in Amorphous Selenium Films”. *Physical Review* 173 (3) (1968), pp. 899–907.

[92] C. L. Braun. “Electric field assisted dissociation of charge transfer states as a mechanism of photocarrier production”. *The Journal of Chemical Physics* 80 (9) (1984), pp. 4157–4161.

[93] L. Onsager. “Deviations from Ohm’s Law in Weak Electrolytes”. *The Journal of Chemical Physics* 2 (9) (1934), pp. 599–615.

[94] L. Onsager. “Initial Recombination of Ions”. *Physical Review* 54 (8) (1938), pp. 554–557.

[95] A. Miller and E. Abrahams. “Impurity Conduction at Low Concentrations”. *Physical Review* 120 (3) (1960), pp. 745–755.

[96] M. Wiemer, A. V. Nenashev, F. Jansson, and S. D. Baranovskii. “On the efficiency of exciton dissociation at the interface between a conjugated polymer and an electron acceptor”. *Applied Physics Letters* 99 (1) (2011), p. 013302.

[97] C. Schwarz, S. Tscheuschner, J. Frisch, S. Winkler, N. Koch, H. Bässler, and A. Köhler. “Role of the effective mass and interfacial dipoles on exciton dissociation in organic donor-acceptor solar cells”. *Physical Review B* 87 (15) (2013), p. 155205.

[98] A. Nenashev, S. Baranovskii, M. Wiemer, F. Jansson, R. Österbacka, A. Dvurechenskii, and F. Gebhard. “Theory of exciton dissociation at the interface between a conjugated polymer and an electron acceptor”. *Physical Review B* 84 (3) (2011), p. 035210.

[99] C. W. Tang. “Two-layer organic photovoltaic cell”. *Applied Physics Letters* 48 (2) (1986), pp. 183–185.

[100] H. Hoppe and N. S. Sariciftci. “Organic solar cells: An overview”. *Journal of Materials Research* 19 (7) (2011), pp. 1924–1945.

[101] W. Shockley and H. J. Queisser. “Detailed balance limit of efficiency of p-n junction solar cells”. *Journal of Applied Physics* 32 (3) (1961), pp. 510–519.

[102] M. D. Archer and J. R. Bolton. “Requirements for ideal performance of photochemical and photovoltaic solar energy converters”. *The Journal of Physical Chemistry* 94 (21) (1990), pp. 8028–8036.

[103] T. Kirchartz, K. Taretto, and U. Rau. “Efficiency limits of organic bulk heterojunction solar cells”. *The Journal of Physical Chemistry C* 113 (41) (2009), pp. 17958–17966.

[104] D. Veldman, S. C. J. Meskers, and R. A. J. Janssen. “The energy of charge-transfer states in electron donor-acceptor blends: insight into the energy losses in organic solar cells”. *Advanced Functional Materials* 19 (12) (2009), pp. 1939–1948.

[105] K. Vandewal, K. Tvingstedt, A. Gadisa, O. Inganäs, and J. V. Manca. “On the origin of the open-circuit voltage of polymer/fullerene solar cells”. *Nature Materials* 8 (11) (2009), pp. 904–909.

[106] O. J. Korovyanko, R. Österbacka, X. M. Jiang, Z. V. Vardeny, and R. A. J. Janssen. “Photoexcitation dynamics in regioregular and regiorandom polythiophene films”. *Physical Review B* 64 (6) (2001), p. 235122.

[107] H. Ohkita and S. Ito. “Transient absorption spectroscopy of polymer-based thin-film solar cells”. *Polymer* 52 (20) (2011), pp. 4397–4417.

[108] Y.-J. Cheng, S.-H. Yang, and C.-S. Hsu. “Synthesis of Conjugated Polymers for Organic Solar Cell Applications”. *Chemical Reviews* 109 (11) (2009), pp. 5868–5923.

[109] E. E. Havinga, W. ten Hoeve, and H. Wynberg. “A new class of small band gap organic polymer conductors”. *Polymer Bulletin* 29 (1992), pp. 119–126.

[110] E. E. Havinga, W. ten Hoeve, and H. Wynberg. “Alternate donor-acceptor small-band-gap semiconducting polymers; Polysquaraines and polycroconaines”. *Synthetic Metals* 55 (1) (1993), pp. 299–309.

[111] A. Ajayaghosh. “Donor-Acceptor Type Low Band Gap Polymers: Polysquaraines and Related Systems”. *Chemical Society Reviews* 32 (4) (2003), pp. 181–191.

[112] G. Brocks and A. Tol. “Small Band Gap Semiconducting Polymers Made from Dye Molecules:Polysquaraines”. *The Journal of Physical Chemistry* 100 (5) (1996), pp. 1838–1846.

[113] F. Wudl, M. Kobayashi, and A. J. Heeger. “Poly(isothianaphthene)”. *The Journal of Organic Chemistry* 49 (18) (1984), pp. 3382–3384.

[114] C. Kitamura, S. Tanaka, and Y. Yamashita. "Design of Narrow-Bandgap Polymers. Syntheses and Properties of Monomers and Polymers Containing Aromatic-Donor and o-Quinoid-Acceptor Units". *Chemistry of Materials* 8 (2) (1996), pp. 570–578.

[115] N. Kleinhenz, L. Yang, H. Zhou, S. C. Price, and W. You. "Low-band-gap polymers that utilize quinoid resonance structure stabilization by thienothiophene: Fine-tuning of HOMO level". *Macromolecules* 44 (4) (2011), pp. 872–877.

[116] M. T. Dang, L. Hirsch, and G. Wantz. "P3HT:PCBM, Best Seller in Polymer Photovoltaic Research". *Advanced Materials* 23 (31) (2011), pp. 3597–3602.

[117] P. Brown, D. Thomas, A. Köhler, J. Wilson, J.-S. Kim, C. Ramsdale, H. Sirringhaus, and R. Friend. "Effect of interchain interactions on the absorption and emission of poly(3-hexylthiophene)". *Physical Review B* 67 (6) (2003), p. 064203.

[118] M. Al-Ibrahim, H.-K. Roth, Z. Uladzimir, G. Gobsch, and S. Sensfuss. "Flexible large area polymer solar cells based on poly(3-hexylthiophene)/fullerene". *Solar Energy Materials and Solar Cells* 85 (1) (2004), pp. 13–20.

[119] J. Guo, H. Ohkita, H. Benten, and S. Ito. "Charge Generation and Recombination Dynamics in Poly (3-hexylthiophene)/Fullerene Blend Films with Different Regioregularities and Morphologies". *Journal of the American Chemical Society* 132 (17) (2010), pp. 6154–6164.

[120] I. A. Howard, R. Mauer, M. Meister, and F. Laquai. "Effect of morphology on ultrafast free carrier generation in polythiophene:fullerene organic solar cells". *Journal of the American Chemical Society* 132 (42) (2010), pp. 14866–14876.

[121] F. Padinger, R. S. Rittberger, and N. S. Sariciftci. "Effects of Postproduction Treatment on Plastic Solar Cells". *Advanced Functional Materials* 13 (1) (2003), pp. 85–88.

[122] M. Reyes-Reyes, K. Kim, and D. L. Carroll. "High-efficiency photovoltaic devices based on annealed poly(3-hexylthiophene) and 1-(3-methoxycarbonyl)-propyl-1-phenyl-(6,6)C_{61} blends". *Applied Physics Letters* 87 (8) (2005). p. 083506.

[123] N. Blouin, A. Michaud, D. Gendron, S. Wakim, E. Blair, R. Neagu-Plesu, M. Belletête, G. Durocher, Y. Tao, and M. Leclerc. "Toward a rational design of poly(2,7-carbazole) derivatives for solar cells". *Journal of the American Chemical Society* 130 (2) (2008), pp. 732–742.

[124] S. H. Park, A. Roy, S. Beaupré, S. Cho, N. Coates, J. S. Moon, D. Moses, M. Leclerc, K. Lee, and A. J. Heeger. "Bulk heterojunction solar cells with internal quantum efficiency approaching 100 %". *Nature Photonics* 3 (5) (2009), pp. 297–302.

[125] Y. Liang, Z. Xu, J. Xia, S.-T. Tsai, Y. Wu, G. Li, C. Ray, and L. Yu. "For the bright future-bulk heterojunction polymer solar cells with power conversion efficiency of 7.4 %". *Advanced Materials* 22 (20) (2010), E135–E138.

[126] L. Lu and L. Yu. “Understanding low bandgap polymer PTB7 and optimizing polymer solar cells based on It”. *Advanced Materials* 26 (26) (2014), pp. 4413–4430.

[127] Y. Zou, A. Najari, P. Berrouard, S. Beaupré, B. R. Aïch, Y. Tao, and M. Leclerc. “A Thieno[3,4-c] pyrrole-4,6-dione-Based Copolymer for Efficient Solar Cells”. *Journal of the American Chemical Society* 132 (15) (2010), pp. 5330–5331.

[128] H.-Y. Chen, J. Hou, S. Zhang, Y. Liang, G. Yang, Y. Yang, L. Yu, Y. Wu, and G. Li. “Polymer solar cells with enhanced open-circuit voltage and efficiency”. *Nature Photonics* 3 (2009), pp. 649–653.

[129] S. Sapp and S. Luebben. “New Conducting and Semiconducting Polymers for Organic Photovoltaics”. *MRS Proceedings* 1270 (2007), pp. 1–7.

[130] T. Offermans, P. A. van Hal, S. C. J. Meskers, M. M. Koetse, and R. A. J. Janssen. “Exciplex dynamics in a blend of π-conjugated polymers with electron donating and accepting properties: MDMO-PPV and PCNEPV”. *Physical Review B* 72 (4) (2005), p. 045213.

[131] K. Tajima, Y. Suzuki, and K. Hashimoto. “Polymer Photovoltaic Devices using Fully Regioregular Poly[(2-methoxy-5-(3’,7’-dimethyloctyloxy))-1,4-phenylenevinylene]”. *The Journal of Physical Chemistry C Letters* 112 (23) (2008), pp. 8507–8510.

[132] F. C. Jamieson, E. B. Domingo, T. McCarthy-Ward, M. Heeney, N. Stingelin, and J. R. Durrant. “Fullerene crystallisation as a key driver of charge separation in polymer/fullerene bulk heterojunction solar cells”. *Chemical Science* 3 (2) (2012), pp. 485–492.

[133] S. Shoaee, S. Subramaniyan, H. Xin, C. Keiderling, P. S. Tuladhar, F. Jamieson, S. A. Jenekhe, and J. R. Durrant. “Charge photogeneration for a series of thiazolo-thiazole donor polymers blended with the fullerene electron acceptors PCBM and ICBA”. *Advanced Functional Materials* 23 (26) (2013), pp. 3286–3298.

[134] B. Bernardo, D. Cheyns, B. Verreet, R. D. Schaller, B. P. Rand, and N. C. Giebink. “Delocalization and dielectric screening of charge transfer states in organic photovoltaic cells”. *Nature Communications* 5 (3245) (2014), pp. 1–7.

[135] L. Ye, W. Jiang, W. Zhao, S. Zhang, D. Qian, Z. Wang, and J. Hou. “Selecting a Donor Polymer for Realizing Favorable Morphology in Efficient Non-fullerene Acceptor-based Solar Cells”. *Small* 10 (22) (2014), pp. 4658–4663.

[136] J. Zhao, Y. Li, H. Lin, Y. Liu, K. Jiang, C. Mu, T. Ma, J. Y. L. Lai, H. Hu, D. Yu, and H. Yan. “High-efficiency non-fullerene organic solar cells enabled by a difluorobenzothiadiazole-based donor polymer combined with a properly matched small molecule acceptor”. *Energy and Environmental Science* 8 (2) (2015), pp. 520–525.

[137] *Hamamatsu Photonics*. “Guide to Streak Cameras” (2008). Application note.

[138] A. A. Chernikov. “Time-Resolved Photoluminescence Spectroscopy of Semiconductors for Optical Applications Beyond the Visible Spectral Range”. PhD thesis. Philipps-Universität Marburg, 2011.

[139] *Hamamatsu Photonics.* "Universal Streak Camera C5680 Series" (2003). Application note.

[140] G. Li, Y. Yao, H. Yang, V. Shrotriya, G. Yang, and Y. Yang. ""Solvent annealing" effect in polymer solar cells based on poly(3-hexylthiophene) and methanofullerenes". *Advanced Functional Materials* 17 (10) (2007), pp. 1636–1644.

[141] C. Gourdon and P. Lavallard. "Exciton transfer between localized states in $\mathrm{CdS}_{1-x}\mathrm{Se}_x$ alloys". *Physica Status Solidi B* 153 (2) (1989), pp. 641–652.

[142] O. Rubel, W. Stolz, and S. D. Baranovskii. "Spectral dependence of the photoluminescence decay in disordered semiconductors". *Applied Physics Letters* 91 (2) (2007), p. 021903.

[143] T. Niebling, O. Rubel, W. Heimbrodt, W. Stolz, S. D. Baranovskii, P. J. Klar, and J. F. Geisz. "Spectral and time dependences of the energy transfer of bound optical excitations in GaP(N)". *Journal of Physics: Condensed Matter* 20 (1) (2008), p. 015217.

[144] M. R. Hammond, R. J. Kline, A. A. Herzing, L. J. Richter, D. S. Germack, H.-w. Ro, C. L. Soles, D. A. Fischer, T. Xu, L. Yu, M. F. Toney, and D. M. Delongchamp. "Molecular Order in High-Efficiency Polymer/Fullerene Bulk Heterojunction Solar Cells". *ACS Nano* 5 (10) (2011), pp. 8248–8257.

[145] S. D. Baranovskii. "Theoretical description of charge transport in disordered organic semiconductors". *Physica Status Solidi (B)* 251 (3) (2014), pp. 487–525.

[146] A. Merdasa, A. J. Jiménez, R. Camacho, M. Meyer, F. Würthner, and I. G. Scheblykin. "Single Lévy states - disorder induced energy funnels in molecular aggregates". *Nano Letters* 14 (12) (2014), pp. 6774–6781.

[147] J. Orenstein and M. A. Kastner. "Thermalization and recombination in amorphous semiconductors". *Solid State Communications* 40 (1) (1981), pp. 85–89.

[148] D. Ouadjaout and Y. Marfaing. "Localized excitons in II-VI semiconductor alloys: Density-of-states model and photoluminescence line-shape analysis". *Physical Review B* 41 (17) (1990), pp. 96–105.

[149] J. G. Müller, U. Lemmer, G Raschke, M Anni, U. Scherf, J. M. Lupton, and J Feldmann. "Linewidth-limited energy transfer in single conjugated polymer molecules". *Physical Review Letters* 91 (26) (2003), p. 267403.

[150] M. Tong, N. E. Coates, D. Moses, A. J. Heeger, S. Beaupré, and M. Leclerc. "Charge carrier photogeneration and decay dynamics in the poly(2,7-carbazole) copolymer PCDTBT and in bulk heterojunction composites with $\mathrm{PC}_{70}\mathrm{BM}$". *Physical Review B* 81 (12) (2010), p. 125210.

[151] J. M. Szarko, B. S. Rolczynski, S. J. Lou, T. Xu, J. Strzalka, T. J. Marks, L. Yu, and L. X. Chen. "Photovoltaic Function and Exciton/Charge Transfer Dynamics in a Highly Efficient Semiconducting Copolymer". *Advanced Functional Materials* 24 (1) (2013), pp. 10–26.

[152] G. Grancini, M. Maiuri, D. Fazzi, A. Petrozza, H.-J. Egelhaaf, D. Brida, G. Cerullo, and G. Lanzani. "Hot exciton dissociation in polymer solar cells". *Nature Materials* 12 (1) (2013), pp. 29–33.

[153] K. Chen, A. J. Barker, M. E. Reish, K. C. Gordon, and J. M. Hodgkiss. “Broadband ultrafast photoluminescence spectroscopy resolves charge photogeneration via delocalized hot excitons in polymer:fullerene photovoltaic blends.” *Journal of the American Chemical Society* 135 (49) (2013), pp. 18502–18512.

[154] L. G. Kaake, D. Moses, and A. J. Heeger. “Coherence and Uncertainty in Nanostructured Organic Photovoltaics”. *The Journal of Physical Chemistry Letters* 4 (14) (2013), pp. 2264–2268.

[155] M. Huix-Rotllant, H. Tamura, and I. Burghardt. “Concurrent Effects of Delocalization and Internal Conversion Tune Charge Separation at Regioregular PolythiopheneFullerene Heterojunctions”. *The Journal of Physical Chemistry Letters* 6 (9) (2015), pp. 1702–1708.

[156] S. Tscheuschner, H. Bässler, K. Huber, and A. Köhler. “A Combined Theoretical and Experimental Study of Dissociation of Charge Transfer States at the Donor-Acceptor Interface of Organic Solar Cells”. *The Journal of Physical Chemistry B* 119 (32) (2015), pp. 10359–10371.

[157] Y. Kim, S. A. Choulis, J. Nelson, D. D. C. Bradley, S. Cook, and J. R. Durrant. “Composition and annealing effects in polythiophene/fullerene solar cells”. *Journal of Materials Science* 40 (6) (2005), pp. 1371–1376.

[158] A. R. Marsh, J. M. Hodgkiss, S. Albert-Seifried, and R. H. Friend. “Effect of annealing on P3HT:PCBM charge transfer and nanoscale morphology probed by ultrafast spectroscopy”. *Nano Letters* 10 (3) (2010), pp. 923–930.

[159] J. Peet, J. Y. Kim, N. E. Coates, W. L. Ma, D. Moses, A. J. Heeger, and G. C. Bazan. “Efficiency enhancement in low-bandgap polymer solar cells by processing with alkane dithiols”. *Nature Materials* 6 (7) (2007), pp. 497–500.

[160] I. W. Hwang, S. Cho, J. Y. Kim, K. Lee, N. E. Coates, D. Moses, and A. J. Heeger. “Carrier generation and transport in bulk heterojunction films processed with 1,8-octanedithiol as a processing additive”. *Journal of Applied Physics* 104 (3) (2008), p. 033706.

[161] J. K. Lee, W. L. Ma, C. J. Brabec, J. Yuen, J. S. Moon, J. Y. Kim, K. Lee, G. C. Bazan, and A. J. Heeger. “Processing additives for improved efficiency from bulk heterojunction solar cells”. *Journal of the American Chemical Society* 130 (11) (2008), pp. 3619–3623.

[162] S. Albrecht, W. Schindler, J. Kurpiers, J. Kniepert, J. C. Blakesley, I. Dumsch, S. Allard, K. Fostiropoulos, U. Scherf, and D. Neher. “On the Field Dependence of Free Charge Carrier Generation and Recombination in Blends of PCPDTBT/$PC_{70}BM$: Influence of Solvent Additives”. *The Journal of Physical Chemistry Letters* 3 (5) (2012), pp. 640–645.

[163] A. Zusan, B. Gieseking, M. Zerson, V. Dyakonov, R. Magerle, and C. Deibel. “The Effect of Diiodooctane on the Charge Carrier Generation in Organic Solar Cells Based on the Copolymer PBDTTT-C”. *Scientific Reports* 5 (8268) (2015), pp. 1–8.

[164] J. Piris, T. E. Dykstra, A. A. Bakulin, P. H. M. van Loosdrecht, W. Knulst, M. T. Trinh, J. M. Schins, and L. D. A. Siebbeles. "Photogeneration and Ultrafast Dynamics of Excitons and Charges in P3HT/PCBM Blends". *The Journal of Physical Chemistry C* 113 (32) (2009), pp. 14500–14506.

[165] Website of *Sigma Aldrich*. 2016. URL: `http://www.sigmaaldrich.com/catalog/product/aldrich/684465?lang=de\&region=DE`.

[166] J. Razzell-Hollis, J. Wade, W. C. Tsoi, Y. Soon, J. Durrant, and J.-S. Kim. "Photochemical stability of high efficiency PTB7:PC$_{70}$BM solar cell blends". *Journal of Materials Chemistry A* 2 (47) (2014), pp. 20189–20195.

[167] E. Cohen and M. D. Sturge. "Fluorescence line narrowing, localized exciton states, and spectral diffusion in the mixed semiconductor CdS$_x$Se$_{1-x}$". *Physical Review B* 25 (6) (1982), pp. 3828–3840.

[168] P. B. Deotare, W. Chang, E. Hontz, D. N. Congreve, L. Shi, P. D. Reusswig, B. Modtland, M. E. Bahlke, C. K. Lee, A. P. Willard, V. Bulović, T. Van Voorhis, and M. A. Baldo. "Nanoscale Transport of Charge Transfer States in Organic Donor-Acceptor Blends". *Nature Materials* 14 (11) (2015), pp. 1130–1134.

[169] D. W. Gehrig, I. A. Howard, and F. Laquai. "Charge Carrier Generation Followed by Triplet State Formation, Annihilation, and Carrier Recreation in PBDTTT-C:PC$_{60}$BM Photovoltaic Blends". *The Journal of Physical Chemistry C* 119 (24) (2015), pp. 13509–13515.

[170] J. Aragó and A. Troisi. "Dynamics of the excitonic coupling in organic crystals". *Physical Review Letters* 114 (2) (2015), p. 026402.

[171] D. Jarzab, F. Cordella, J. Gao, M. Scharber, H.-J. Egelhaaf, and M. A. Loi. "Low-Temperature Behaviour of Charge Transfer Excitons in Narrow-Bandgap Polymer-Based Bulk Heterojunctions". *Advanced Energy Materials* 1 (4) (2011), pp. 604–609.

[172] S. Cook, R. Katoh, and A. Furube. "Ultrafast Studies of Charge Generation in PCBM:P3HT Blend Films following Excitation of the Fullerene PCBM". *The Journal of Physical Chemistry C* 113 (6) (2009), pp. 2547–2552.

[173] R. Westphaling, T. Breitkopf, S. Bauer, and C. Klingshirn. "Photoluminescence quantum efficiency and dynamics in ZnSe$_{1-x}$Te$_x$ and CdS$_{1-x}$Se$_x$ mixed crystals". *Journal of Luminescence* 72-74 (1997), pp. 980–982.

[174] K. Tvingstedt, K. Vandewal, A. Gadisa, F. Zhang, J. Manca, and O. Inganäs. "Electroluminescence from charge transfer states in polymer solar cells". *Journal of the American Chemical Society* 131 (33) (2009), pp. 11819–11824.

[175] K. Tvingstedt, K. Vandewal, F. Zhang, and O. Inganäs. "On the dissociation efficiency of charge transfer excitons and Frenkel excitons in organic solar cells: A luminescence quenching study". *The Journal of Physical Chemistry C* 114 (49) (2010), pp. 21824–21832.

[176] I.-W. Hwang, C. Soci, D. Moses, Z. Zhu, D. Waller, R. Gaudiana, C. Brabec, and A. Heeger. "Ultrafast Electron Transfer and Decay Dynamics in a Small Band Gap Bulk Heterojunction Material". *Advanced Materials* 19 (17) (2007), pp. 2307–2312.

[177] F. Etzold, I. A. Howard, R. Mauer, M. Meister, T.-D. Kim, K.-S. Lee, N. S. Baek, and F. Laquai. "Ultrafast exciton dissociation followed by nongeminate charge recombination in PCDTBT:PCBM photovoltaic blends." *Journal of the American Chemical Society* 133 (24) (2011), pp. 9469–9479.

[178] M. K. Etherington, J. Wang, P. C. Y. Chow, and N. C. Greenham. "Recombination pathways in polymer:fullerene photovoltaics observed through spin polarization measurements". *Applied Physics Letters* 104 (6) (2014), p. 063304.

[179] M. A. Loi, S. Toffanin, M. Muccini, M. Forster, U. Scherf, and M. Scharber. "Charge Transfer Excitons in Bulk Heterojunctions of a Polyfluorene Copolymer and a Fullerene Derivative". *Advanced Functional Materials* 17 (13) (2007), pp. 2111–2116.

[180] D. Veldman, O. Ipek, S. C. J. Meskers, J. Sweelssen, M. M. Koetse, S. C. Veenstra, J. M. Kroon, S. S. van Bavel, J. Loos, and R. A. J. Janssen. "Compositional and electric field dependence of the dissociation of charge transfer excitons in alternating polyfluorene copolymer/fullerene blends". *Journal of the American Chemical Society* 130 (24) (2008), pp. 7721–7735.

[181] F. Piersimoni, S. Chambon, K. Vandewal, R. Mens, T. Boonen, A. Gadisa, M. Izquierdo, S. Filippone, B. Ruttens, J. D'haen, N. Martin, L. Lutsen, D. Vanderzande, P. Adriaensens, and J. V. Manca. "Influence of fullerene ordering on the energy of the charge-transfer state and open-circuit voltage in polymer:fullerene solar cells". *The Journal of Physical Chemistry C* 115 (21) (2011), pp. 10873–10880.

[182] T. Basel, U. Huynh, T. Zheng, T. Xu, L. Yu, and Z. V. Vardeny. "Optical, Electrical, and Magnetic Studies of Organic Solar Cells Based on Low Bandgap Copolymer with Spin $\frac{1}{2}$ Radical Additives". *Advanced Functional Materials* 25 (12) (2015), pp. 1895–1902.

[183] A. Rao, P. C. Y. Chow, S. Gélinas, C. W. Schlenker, C.-Z. Li, H.-L. Yip, A. K.-Y. Jen, D. S. Ginger, and R. H. Friend. "The role of spin in the kinetic control of recombination in organic photovoltaics". *Nature* 500 (7463) (2013), pp. 435–439.

[184] V. Gulbinas, Y. Zaushitsyn, V. Sundström, D. Hertel, H. Bässler, and A. Yartsev. "Dynamics of the electric field-assisted charge carrier photogeneration in ladder-type poly(para-phenylene) at a low excitation intensity". *Physical Review Letters* 89 (10) (2002), p. 107401.

[185] M. Hallermann, S. Haneder, and E. Da Como. "Charge-transfer states in conjugated polymer/fullerene blends: Below-gap weakly bound excitons for polymer photovoltaics". *Applied Physics Letters* 93 (5) (2008), p. 053307.

[186] V. D. Mihailetchi, K. J. van Duren, P. W. M. Blom, J. C. Hummelen, R. A. J. Janssen, J. M. Kroon, M. T. Rispens, W. J. H. Verhees, and M. M. Wienk. "Electron transport in a methanofullerene". *Advanced Functional Materials* 13 (1) (2003), pp. 43–46.

[187] L. J. A. Koster, S. E. Shaheen, and J. C. Hummelen. "Pathways to a new efficiency regime for organic solar cells". *Advanced Energy Materials* 2 (10) (2012), pp. 1246–1253.

[188] J. C. Lagarias, J. A. Reeds, M. H. Wright, and P. E. Wright. "Convergence Properties of the Nelder–Mead Simplex Method in Low Dimensions". *SIAM Journal on Optimization* 9 (1) (1998), pp. 112–147.

[189] U. Lemmer. "Dynamik optischer Anregungen in π-konugierten Polymeren". PhD thesis. Philipps-Universität Marburg, 1995.

[190] Y. W. Soon, H. Cho, J. Low, H. Bronstein, I. McCulloch, and J. R. Durrant. "Correlating triplet yield, singlet oxygen generation and photochemical stability in polymer/fullerene blend films". *Chemical Communications* 49 (13) (2013), pp. 1291–1293.

[191] C. Deibel, T. Strobel, and V. Dyakonov. "Origin of the Efficient Polaron-Pair Dissociation in Polymer-Fullerene Blends". *Physical Review Letters* 103 (3) (2009), p. 036402.

[192] D. Rauh, C. Deibel, and V. Dyakonov. "Charge density dependent nongeminate recombination in organic bulk heterojunction solar cells". *Advanced Functional Materials* 22 (16) (2012), pp. 3371–3377.

[193] B. Ebenhoch, S. A. J. Thomson, K. Genevičius, G. Juška, and I. D. Samuel. "Charge carrier mobility of the organic photovoltaic materials PTB7 and $PC_{71}BM$ and its influence on device performance". *Organic Electronics* 22 (2015), pp. 62–68.

[194] L. J. A. Koster, V. D. Mihailetchi, R. Ramaker, and P. W. M. Blom. "Light intensity dependence of open-circuit voltage of polymer:fullerene solar cells". *Applied Physics Letters* 86 (12) (2005), p. 123509.

[195] Z. Liang, A. Nardes, D. Wang, J. J. Berry, and B. A. Gregg. "Defect engineering in π-conjugated polymers". *Chemistry of Materials* 21 (20) (2009), pp. 4914–4919.

[196] L. G. Kaake, P. F. Barbara, and X. Y. Zhu. "Intrinsic charge trapping in organic and polymeric semiconductors: A physical chemistry perspective". *The Journal of Physical Chemistry Letters* 1 (3) (2010), pp. 628–635.

[197] G. D'Avino, S. Mothy, L. Muccioli, C. Zannoni, L. Wang, J. Cornil, D. Beljonne, and F. Castet. "Energetics of electron-hole separation at P3HT/PCBM heterojunctions". *The Journal of Physical Chemistry C* 117 (25) (2013), pp. 12981–12990.

[198] M. Wiemer, M. Koch, U. Lemmer, A. B. Pevtsov, and S. D. Baranovskii. "Efficiency of exciton dissociation at internal organic interfaces beyond harmonic approximation". *Organic Electronics* 15 (10) (2014), pp. 2461–2467.

[199] G. D'Avino, L. Muccioli, Y. Olivier, and D. Beljonne. "Charge separation and recombination at polymer-fullerene heterojunctions: Delocalization and hybridization effects". *The Journal of Physical Chemistry Letters* 7 (3) (2016), pp. 536–540.

[200] F. Steiner, S. Foster, A. Losquin, J. Labram, T. D. Anthopoulos, J. M. Frost, and J. Nelson. “Distinguishing the Influence of Structural and Energetic Disorder on Electron Transport in Fullerene Multi-Adducts”. *Materials Horizons* 2 (1) (2014), pp. 113–119.

[201] F. Gao, S. Himmelberger, M. Andersson, D. Hanifi, Y. Xia, S. Zhang, J. Wang, J. Hou, A. Salleo, and O. Inganäs. “The Effect of Processing Additives on Energetic Disorder in Highly Efficient Organic Photovoltaics: A Case Study on PBDTTT-C-T:$PC_{71}BM$”. *Advanced Materials* 27 (26) (2015), pp. 3868–3873.

[202] J. Kniepert, I. Lange, J. Heidbrink, J. Kurpiers, T. J. K. Brenner, L. J. A. Koster, and D. Neher. “The Effect of Solvent Additive on Generation, Recombination and Extraction in PTB7:PCBM Solar Cells: A Conclusive Experimental and Numerical Simulation Study”. *The Journal of Physical Chemistry C* 119 (15) (2015), pp. 8310–8320.

[203] D. W. Gehrig, I. A. Howard, V. Kamm, H. Mangold, and D. Neher. “Efficiency-Limiting Processes in Low-Bandgap Polymer:Perylene Diimide Photovoltaic Blends”. *The Journal of Physical Chemistry C* 118 (35) (2014), pp. 20077–20085.

[204] M. Koehler, M. C. Santos, and M. G. E. Da Luz. “Positional disorder enhancement of exciton dissociation at donor/acceptor interface”. *Journal of Applied Physics* 99 (5) (2006), p. 053702.

[205] M. L. Jones, B. Chakrabarti, and C. Groves. “Monte Carlo simulation of geminate pair recombination dynamics in organic photovoltaic devices: Multi-exponential, field-dependent kinetics and its interpretation”. *The Journal of Physical Chemistry C* 118 (1) (2014), pp. 85–91.

[206] P. Peumans and S. R. Forrest. “Separation of geminate charge-pairs at donoracceptor interfaces in disordered solids”. *Chemical Physics Letters* 398 (1-3) (2004), pp. 27–31.

[207] C. Groves, R. A. Marsh, and N. C. Greenham. “Monte Carlo modeling of geminate recombination in polymer-polymer photovoltaic devices”. *The Journal of Chemical Physics* 129 (11) (2008), p. 114903.

[208] M. L. Jones, R. Dyer, N. Clarke, and C. Groves. “Are hot charge transfer states the primary cause of efficient free-charge generation in polymer:fullerene organic photovoltaic devices? A kinetic Monte Carlo study”. *Physical Chemistry Chemical Physics* 16 (38) (2014), pp. 20310–20320.

[209] M. Gerhard, D. Gehrig, I. A. Howard, A. P. Arndt, M. Bilal, A. Rahimi-Iman, U. Lemmer, F. Laquai, and M. Koch. “Loss mechanisms in organic solar cells based on perylene diimide acceptors studied by time-resolved photoluminescence”. *Proceedings of SPIE* 9895 (2016).

Wissenschaftlicher Werdegang

Eva Marina Gerhard, geboren am 12. Januar 1987 in Bad Arolsen

2006 **Allgemeine Hochschulreife**: Alte Landesschule Korbach

Studium und Promotion (Philipps-Universität Marburg)

2006 - 2009 **Bachelorstudium**

Thema der Bachelorarbeit:
Photolumineszenz-Spektroskopie neuartiger quaternärer III/V-Heterostrukturen

Betreuer: Dr. Habil. Wolfgang Stolz

2009 - 2011 **Masterstudium**

Thema der Masterarbeit:
Charakterisierung photoleitender Antennen für Anwendungen im Terahertz-Bereich
(angefertigt am Fraunhofer Heinrich-Hertz-Institut für Nachrichtentechnik, Berlin)

Betreuer: Prof. Dr. Martin Koch

2011 - 2016 **Wissenschaftliche Mitarbeiterin**

In der Arbeitsgruppe der Experimentellen Halbleiterphysik und Terahertz-Systemtechnik von Prof. Dr. Martin Koch

Seit 2016 **Post-Doc**

In der Einzelmolekülspektroskopie-Gruppe von Prof. Dr. Ivan Scheblykin, *Department of Chemical Physics*, Universität Lund, Schweden

Weitere Tätigkeiten

Juli - Sept. 2007	**Industriepraktikum** bei ContiTech (Werk Korbach)
Aug. - Sept. 2008 und Feb. - April 2010	**Studentische Hilfskraft** bei der zentralen, allgemeinen Studienberatung der Philipps-Universität Marburg
2010 - 2011	**HIWI-Tätigkeit** begleitend zur Masterarbeit

Publikationsliste

Veröffentlichungen in Fachzeitschriften (peer-reviewed)

M. Gerhard, A. P. Arndt, Mühenad Bilal, U. Lemmer, M. Koch und I. A. Howard, „Field-induced exciton dissociation in PTB7-based Organic Solar Cells“, in Vorbereitung

M. Gerhard, A. P. Arndt, I. A. Howard, A. Rahimi-Iman, U. Lemmer und M. Koch, „Temperature and Energy-Dependent Separation of Charge-Transfer States in PTB7-Based Organic Solar Cells“, *The Journal of Physical Chemistry C* 119 (51), 28309-28318, 2015

A. P. Arndt, M. Gerhard, A. Quintilla, I. A. Howard, M. Koch und U. Lemmer, „Time-Resolved Charge-Transfer State Emission in Organic Solar Cells: Temperature and Blend Composition Dependence of Interfacial Traps“, *The Journal of Physical Chemistry C* 119 (24), 13516-13523, 2015

A. Hangleiter, Z. Jin, M. Gerhard, D. Kalincev, T. Langer, H. Bremers, U. Rossow, M. Koch, M. Bonn und D. Turchinovich, „Efficient formation of excitons in a dense electron-hole plasma at room temperature“, *Physical Review B* (92), 241305, 2015

T. Langer, A. Chernikov, D. Kalincev, M. Gerhard, H. Bremers, U. Rossow, M. Koch und A. Hangleiter, „Room-temperature excitonic recombination in GaInN/GaN quantum wells“, *Applied Physics Letters* 103 (20), 202106, 2013

R. J. B. Dietz, B. Globisch, M. Gerhard, A. Velauthapillai, D. Stanze, H. Roehle, M. Koch, T. Göbel und M. Schell, „64 μW pulsed THz emission from growth optimized InGaAs/InAlAs heterostructures with separated photoconductive and trapping regions“, *Applied Physics Letters* 103 (6), 061103, 2013

M. Scheller, M. Stecher, M. Gerhard und M. Koch, „Versatile spectrally shapeable multi-mode terahertz system“, *Applied Physics B: Laser and Optics* 106 (1), 81-84, 2012

R. J. B. Dietz, M. Gerhard, D. Stanze, M. Koch, B. Sartorius und M. Schell, „THz generation at 1.55 μm excitation: Six-fold increase in THz conversion efficiency by separated photoconductive and trapping regions“, *Optics Express* 19 (27), 25911-25917, 2011

M. Scheller, M. Stecher, M. Gerhard und M. Koch, „Hybrid Continuous Wave Terahertz Spectroscopy“, *Optics Express* 18 (15), 15887-15892, 2010

KONFERENZBEITRÄGE MIT PROCEEDINGS-VERÖFFENTLICHUNG

M. Gerhard, D. Gehrig, I. A. Howard, A. P. Arndt, M. Bilal, A. Rahimi-Iman, U. Lemmer, F. Laquai und M. Koch, „Loss mechanisms in organic solar cells based on perylene diimide acceptors studied by time-resolved photoluminescence“, *Proceedings of SPIE* 9895, 2016 (Vortrag auf der *SPIE Photonics Europe*, Brüssel, Belgien 2016)

M. Gerhard, A. P. Arndt, A. Quintilla, A. Rahimi-Iman, U. Lemmer und M. Koch, „Time-resolved spectroscopy of charge transfer phenomena in organic solar cells“, *Proceedings of SPIE 9360*, 2015 (Vortrag auf der *SPIE Photonics West*, San Francisco, USA, 2015)

A. Hangleiter, T. Langer, M. Gerhard, D. Kalincev, A. Kruse, H. Bremers, U. Rossow und M. Koch, „Efficiency droop in nitride LEDs revisited: impact of excitonic recombination processes“, *Proceedings of SPIE 9363* (SPIE Photonics West, San Francisco, USA, 2015)

WEITERE BEITRÄGE

M. Gerhard, A. P. Arndt, I. A. Howard, A. Rahimi-Iman, U. Lemmer und M. Koch, „Efficient dissociation of excitons at donor/acceptor interfaces in organic solar cells“ (Poster auf der *ICII*, Marburg, 2016)

M. Gerhard A. P. Arndt, I. A. Howard, M. Bilal, A. Rahimi-Iman, U. Lemmer und M. Koch, „Efficient dissociation of charge transfer states in PTB7-based organic solar cells“(Poster auf der DPG-Früjahrstagung, Regensburg, 2016)

A. P. Arndt, M. Gerhard, A. Quintilla, I. A. Howard, M. Koch und U. Lemmer, „Charge transfer states as traps in organic solar cells“(*SPIE Organic Photonics and Electronics*, San Diego, USA, 2015)

A. P. Arndt, M. Gerhard, A. Quintilla, I. A. Howard, M. Koch und U. Lemmer, „Charge transfer states as traps in organic solar cells“(*HOPV*, Rom, Italien, 2015)

M. Gerhard, A. P. Arndt, I. A. Howard, A. Quintilla, A. Rahimi-Iman, U. Lemmer und M. Koch, „Charge transfer states as interfacial traps in organic solar cells: A time-resolved spectroscopic study“(Vortrag auf dem Tag der Materialwissenschaften, Marburg, 2015)

M. Gerhard, A. P. Arndt, A. Quintilla, A. Rahimi-Iman, U. Lemmer und M. Koch, „Luminescence quenching due to charge transfer in organic solar cells“(Poster auf dem 578. WE-Heraeus Seminar *Charge-Transfer Effects in Organic Heterostructures: Fundamentals and Applications*, Bad Honnef, 2014)

M. Gerhard, A. P. Arndt, A. Quintilla, U. Lemmer und M. Koch, „Time-resolved spectroscopy of interfacial states in P3HT/PCBM blends“(Poster auf der DPG-Frühjahrstagung, Dresden, 2014)

Danksagung

Zum Schluss möchte ich allen herzlich danken, die mich während meiner Promotion direkt oder indirekt unterstützt haben.

- Prof. Dr. Martin Koch danke ich herzlich für die Aufnahme in die AG Experimentelle Halbleiterphysik und die Betreuung dieser Arbeit. Ebenso danke ich Prof. Dr. Uli Lemmer vom Karlsruher Institut für Technologie für die Übernahme des Zweitgutachtens und den damit verbundenen Aufwand.
- Es gibt noch mehr Menschen am KIT, die mir sehr geholfen haben: Mein besonderer Dank gilt Dr. Ian Howard für seine fachliche Unterstützung und die vielen hilfreichen Diskussionen. Andreas Arndt danke ich ebenfalls für jede Menge Diskussionen, sein Motivationstalent, schöne Proben und epische Messkampagnen. Auch Dr. Aina Quintilla möchte ich für die gute Zusammenarbeit herzlich danken.
- Eine Abhandlung über all die Dinge, die bei der zeitaufgelösten Photolumineszenz-Spektroskopie schief gehen können, würde den für Kapitel 3 vorgesehenen Rahmen bei Weitem übersteigen. Hier gilt die Devise *learning by doing* und im Team funktioniert das am besten. In diesem Sinne danke ich Dr. Alexey Chernikov und Dr. Khaled Shakfa für die Einarbeitung an der Streak-Kamera und die ständige Bereitschaft, ihr Wissen zu teilen. Ronja Woscholski danke ich für die Möglichkeit, die unmöglichsten Probleme zu teilen und besonders für den Einsatz ihrer übermenschlichen LabVIEW-Fähigkeiten zum Wohle der Allgemeinheit. Dimitri Kalincev und Markus Stein sei ebenfalls herzlich gedankt für die gute Zusammenarbeit im Labor.
- Den Studenten Mühenad Bilal und Marc Halbich danke ich für schöne Messdaten und für die vielen Fragen, die mir selbst nie in den Sinn gekommen wären.
- Sina Lippert danke ich für die tolle und niemals langweilige gemeinsame Zeit im Büro, für therapeutische Gespräche und für Ausflüge in die Welt des Vierwellen-Mischens, sowie in verschiedenste Gastronomie-Betriebe der Marburger Oberstadt.
- Bei der Stammbesetzung von Raum 02011A darf auch Martin Wiemer nicht fehlen, ihm möchte ich ebenfalls herzlich danken, nicht nur für die gesellige Atmosphähre, sondern auch für einige erhellende Gespräche über Exzitonen und dafür, dass er entscheidend zum Überleben meiner Bananenpflanzen beigetragen hat.

- Dr. Gunter Urbasch danke ich für das akribische Korrekturlesen von Teilen dieser Arbeit und ferner auch für diverse Zeitreisen in die aufregende Vergangenheit des Laborbaus II, die bei mir stets den latenten Wunsch zurückließen, dort einmal vor 20 Jahren vorbeigeschaut zu haben.
- I also would like to to express my gratitude to our guest student Dylan Renaud for his close reading and language support. Thanks a lot!
- Maya Strobel und Anne Ehlers sei herzlich gedankt für die kompetente Unterstützung bei allen möglichen bürokratischen und organisatorischen Herausforderungen.
- Bei Rüdiger Rink bedanke ich mich für die Nachhilfestunden in Vakuumtechnik und dafür, dass die Dinge am Laufen blieben. Außerdem danke ich ihm und dem gesamten Team der feinmechanischen Werkstatt für die technische Umsetzung meiner Skizzen und die dafür notwendige Kreativität.
- Ebenso gilt mein Dank Carsten Schindler und der übrigen Belegschaft der Elektronik-Werkstatt für die gute Beratung und die immer wieder von Neuem überraschenden Einsichten zu der Frage, was sich alles noch reparieren lässt.
- Ich danke außerdem allen Mitgliedern der AG Koch herzlich für die angenehme Arbeitsatmosphähre, flache Hierarchiestrukturen und diverse Special-Events (Grillen, Elba, Kanu fahren,...), die immer mit viel Spaß verbunden waren. Ohne Anspruch auf Vollständigkeit danke ich neben den oben bereits genannten Personen besonders Ralf Gente, Fan Zhang, Norman Born, Dalia Al-Nakdali, Steffen Schumann, Christoph Möller, Oday Abdulmunem Mazin, David Jahn, Arash Rahimi-Iman, Michael Drexler, Christian Lammers, Philipp Richter, Ole Peters, Bernd Heinen, und Ajanth Velauthapillai für die schöne Zeit.
- Meinen Freunden danke ich ebenfalls für allerlei Abenteuer und Aktivitäten, dies gilt besonders für die Marburger Truppe (Kathrin, Karsten, Philipp, Immo, Simon, Benni) und auch Lena, Leif, Felix und Kathi danke ich für wunderbare (Kurz-)Urlaube.
- Schließlich gilt mein besonderer Dank meinen Eltern Regine und Erwin Gerhard und meinen Schwestern für die beständige und bedingungslose Unterstützung all meiner Vorhaben. Meiner Schwester Aline danke ich ferner herzlich für die notwendige Ablenkung und die Einsicht, dass man komplexe Brettspiele auch durch eine Promotion in den Naturwissenschaften nicht leichter gewinnt.

Tschüß Marburg, es war eine tolle Zeit!